A Direct Measurement of the W Boson Decay Width in Proton-Antiproton Collisions at 1.8 TeV

by

William Joseph Ashmanskas

A.B. (Harvard University) 1992
M.A. (University of California, Berkeley) 1994

A dissertation submitted in partial satisfaction of the

requirements for the degree of

Doctor of Philosophy
in

Physics

in the

GRADUATE DIVISION

of the

UNIVERSITY OF CALIFORNIA, BERKELEY

Committee in charge:

Professor Marjorie D. Shapiro, Chair
Professor Mark W. Strovink
Professor Joseph Cerny

Spring 1998

The dissertation of William Joseph Ashmanskas is approved:

Marjorie Shapiro   May 11 1998

Chair   Date

Mark Strovink   May 11, 1998

                        Date

Joseph Cerny   May 11, 1998

                        Date

University of California, Berkeley

Spring 1998

A Direct Measurement of the W Boson Decay Width in Proton-Antiproton Collisions at 1.8 TeV

Abstract

A Direct Measurement of the W Boson Decay Width in Proton-Antiproton Collisions at 1.8 TeV

by

William Joseph Ashmanskas

Doctor of Philosophy in Physics

University of California, Berkeley

Professor Marjorie D. Shapiro, Chair

We present a direct measurement of the W boson total decay width, Γ_W, using 90 pb^{-1} of high-p_T electron data collected by the Collider Detector at Fermilab during the 1994–1995 run of the Fermilab Tevatron $p\bar{p}$ collider. We normalize predicted signal and background transverse mass (M_T) distributions to 49843 $W \rightarrow e\nu$ candidates in the region $M_T < 200$ GeV and fit the high-M_T region to extract Γ_W. By fitting the 456 events in the region 100 GeV $\leq M_T < 200$ GeV, we find $\Gamma_W = 2.25^{+0.13}_{-0.12}$ (stat) ± 0.11 (syst) GeV.

Marjorie Shapiro
Chair

May 11 1998
Date

1

Dedicated to my wife,

Kirsten Leigh Parkinson.

Acknowledgements

Throughout my years as a student, I have been fortunate to have many outstanding mentors. When I was in high school, Judy Masselam, Mark Rodriguez, and Paul Bamberg inspired me to learn as much about science, math, and computer science as I could manage—for no other reason than the pleasure of understanding. My interest in particle physics began with a terrific undergraduate course taught by Bob Cousins when he visited Harvard during 1990–91. During the two following summers, George Brandenburg and Melissa Franklin showed me how much fun working in high-energy physics could be. From Richard Kadel and Aseet Mukherjee, whose approaches to problem solving are about as different as two people's can be, I absorbed a wealth of knowledge about particle detectors, charged particle tracking, and the nuts and bolts of experimental physics; I would have gladly spent twice as long working with each of them.

Since my first visit to Berkeley, I have benefited from the knowledge, common sense, and thoughtfulness of my advisor, Marjorie Shapiro. When I have had questions about physical phenomena, particle detectors, simulation techniques, or data analysis, or have needed advice on coping with a laborious statistical mechanics course, writing a thesis, finding a job, or even finding an apartment, Marjorie's door has always been open. She insisted that I choose for myself what I was really interested in doing—even at times when I would have preferred the safety of being told what to do—but once I had decided, she consistently offered thoughtful advice on making it work. I don't think any student in this field could find a better advisor.

People often describe the size of particle physics experiments as a disadvantage. One sure advantage, however, is the large number of talented people from whom one has an opportunity to learn. I am grateful to Barry Wicklund, Peter Berge, John Kadyk, Hans Wenzel, Jerry Przybylski, and Tom Weber for frequently taking the time to explain things to me.

I am indebted to Henry Frisch and Young-Kee Kim for suggesting this measurement as a possible thesis topic. (I am also extremely grateful to Henry for wandering down Grant Street in Chinatown on November 22, 1997.)

I would like to thank my dissertation committee, Marjorie Shapiro, Mark Strovink, and Joe Cerny, for taking the time to read and to comment on this thesis. Kevin Einsweiler, Larry Nodulman, Sacha Kopp, and John Wahl have also provided valuable feedback on this thesis and the note that preceded it.

The CDF Collaboration

F. Abe,[17] H. Akimoto,[36] A. Akopian,[31] M. G. Albrow,[7] S. R. Amendolia,[27] D. Amidei,[20] J. Antos,[33] S. Aota,[36] G. Apollinari,[31] T. Asakawa,[36] W. Ashmanskas,[18] M. Atac,[7] F. Azfar,[26] P. Azzi-Bacchetta,[25] N. Bacchetta,[25] W. Badgett,[20] S. Bagdasarov,[31] M. W. Bailey,[22] J. Bao,[39] P. de Barbaro,[30] A. Barbaro-Galtieri,[18] V. E. Barnes,[29] B. A. Barnett,[15] M. Barone,[9] E. Barzi,[9] G. Bauer,[19] T. Baumann,[11] F. Bedeschi,[27] S. Behrends,[3] S. Belforte,[27] G. Bellettini,[27] J. Bellinger,[38] D. Benjamin,[35] J. Benlloch,[19] J. Bensinger,[3] D. Benton,[26] A. Beretvas,[7] J. P. Berge,[7] J. Berryhill,[5] S. Bertolucci,[9] B. Bevensee,[26] A. Bhatti,[31] K. Biery,[7] M. Binkley,[7] D. Bisello,[25] R. E. Blair,[1] C. Blocker,[3] A. Bodek,[30] W. Bokhari,[19] V. Bolognesi,[2] G. Bolla,[29] D. Bortoletto,[29] J. Boudreau,[28] L. Breccia,[2] C. Bromberg,[21] N. Bruner,[22] E. Buckley-Geer,[7] H. S. Budd,[30] K. Burkett,[20] G. Busetto,[25] A. Byon-Wagner,[7] K. L. Byrum,[1] J. Cammerata,[15] C. Campagnari,[7] M. Campbell,[20] A. Caner,[27] W. Carithers,[18] D. Carlsmith,[38] A. Castro,[25] D. Cauz,[27] Y. Cen,[30] F. Cervelli,[27] P. S. Chang,[33] P. T. Chang,[33] H. Y. Chao,[33] J. Chapman,[20] M. -T. Cheng,[33] G. Chiarelli,[27] T. Chikamatsu,[36] C. N. Chiou,[33] L. Christofek,[13] S. Cihangir,[7] A. G. Clark,[10] M. Cobal,[27] E. Cocca,[27] M. Contreras,[5] J. Conway,[32] J. Cooper,[7] M. Cordelli,[9] C. Couyoumtzelis,[10] D. Crane,[1] D. Cronin-Hennessy,[6] R. Culbertson,[5] T. Daniels,[19] F. DeJongh,[7] S. Delchamps,[7] S. Dell'Agnello,[27] M. Dell'Orso,[27] R. Demina,[7] L. Demortier,[31] M. Deninno,[2] P. F. Derwent,[7] T. Devlin,[32] J. R. Dittmann,[6] S. Donati,[27] J. Done,[34] T. Dorigo,[25] A. Dunn,[20] N. Eddy,[20] K. Einsweiler,[18] J. E. Elias,[7] R. Ely,[18] E. Engels, Jr.,[28] D. Errede,[13] S. Errede,[13] Q. Fan,[30] G. Feild,[39] C. Ferretti,[27] I. Fiori,[2] B. Flaugher,[7] G. W. Foster,[7] M. Franklin,[11] M. Frautschi,[35] J. Freeman,[7] J. Friedman,[19] H. Frisch,[5] Y. Fukui,[17] S. Funaki,[36] S. Galeotti,[27] M. Gallinaro,[26] O. Ganel,[35] M. Garcia-Sciveres,[18] A. F. Garfinkel,[29] C. Gay,[11] S. Geer,[7] D. W. Gerdes,[15] P. Giannetti,[27] N. Giokaris,[31] P. Giromini,[9] G. Giusti,[27] L. Gladney,[26] D. Glenzinski,[15] M. Gold,[22] J. Gonzalez,[26] A. Gordon,[11] A. T. Goshaw,[6] Y. Gotra,[25] K. Goulianos,[31] H. Grassmann,[27] L. Groer,[32] C. Grosso-Pilcher,[5] G. Guillian,[20] R. S. Guo,[33] C. Haber,[18] E. Hafen,[19] S. R. Hahn,[7] R. Hamilton,[11] R. Handler,[38] R. M. Hans,[39] F. Happacher,[9] K. Hara,[36] A. D. Hardman,[29] B. Harral,[26] R. M. Harris,[7] S. A. Hauger,[6] J. Hauser,[4] C. Hawk,[32] E. Hayashi,[36] J. Heinrich,[26] B. Hinrichsen,[14] K. D. Hoffman,[29] M. Hohlmann,[5] C. Holck,[26] R. Hollebeek,[26] L. Holloway,[13] S. Hong,[20] G. Houk,[26] P. Hu,[28] B. T. Huffman,[28] R. Hughes,[23] J. Huston,[21] J. Huth,[11] J. Hylen,[7] H. Ikeda,[36] M. Incagli,[27] J. Incandela,[7] G. Introzzi,[27] J. Iwai,[36] Y. Iwata,[12] H. Jensen,[7] U. Joshi,[7] R. W. Kadel,[18] E. Kajfasz,[25] H. Kambara,[10] T. Kamon,[34] T. Kaneko,[36] K. Karr,[37] H. Kasha,[39] Y. Kato,[24] T. A. Keaffaber,[29] K. Kelley,[19] R. D. Kennedy,[7] R. Kephart,[7] P. Kesten,[18] D. Kestenbaum,[11] H. Keutelian,[7] F. Keyvan,[4] B. Kharadia,[13] B. J. Kim,[30] D. H. Kim,[7a] H. S. Kim,[14] S. B. Kim,[20] S. H. Kim,[36] Y. K. Kim,[18] L. Kirsch,[3] P. Koehn,[23] K. Kondo,[36] J. Konigsberg,[8] S. Kopp,[5] K. Kordas,[14] A. Korytov,[8] W. Koska,[7] E. Kovacs,[7a] W. Kowald,[6]

M. Krasberg,[20] J. Kroll,[7] M. Kruse,[30] T. Kuwabara,[36] S. E. Kuhlmann,[1] E. Kuns,[32] A. T. Laasanen,[29] S. Lami,[27] S. Lammel,[7] J. I. Lamoureux,[3] M. Lancaster,[18] T. LeCompte,[1] S. Leone,[27] J. D. Lewis,[7] P. Limon,[7] M. Lindgren,[4] T. M. Liss,[13] J. B. Liu,[30] Y. C. Liu,[33] N. Lockyer,[26] O. Long,[26] C. Loomis,[32] M. Loreti,[25] J. Lu,[34] D. Lucchesi,[27] P. Lukens,[7] S. Lusin,[38] J. Lys,[18] K. Maeshima,[7] A. Maghakian,[31] P. Maksimovic,[19] M. Mangano,[27] J. Mansour,[21] M. Mariotti,[25] J. P. Marriner,[7] A. Martin,[39] J. A. J. Matthews,[22] R. Mattingly,[19] P. McIntyre,[34] P. Melese,[31] A. Menzione,[27] E. Meschi,[27] S. Metzler,[26] C. Miao,[20] T. Miao,[7] G. Michail,[11] R. Miller,[21] H. Minato,[36] S. Miscetti,[9] M. Mishina,[17] H. Mitsushio,[36] T. Miyamoto,[36] S. Miyashita,[36] N. Moggi,[27] Y. Morita,[17] A. Mukherjee,[7] T. Muller,[16] P. Murat,[27] H. Nakada,[36] I. Nakano,[36] C. Nelson,[7] D. Neuberger,[16] C. Newman-Holmes,[7] C-Y. P. Ngan,[19] M. Ninomiya,[36] L. Nodulman,[1] S. H. Oh,[6] K. E. Ohl,[39] T. Ohmoto,[12] T. Ohsugi,[12] R. Oishi,[36] M. Okabe,[36] T. Okusawa,[24] R. Oliveira,[26] J. Olsen,[38] C. Pagliarone,[27] R. Paoletti,[27] V. Papadimitriou,[35] S. P. Pappas,[39] N. Parashar,[27] S. Park,[7] A. Parri,[9] J. Patrick,[7] G. Pauletta,[27] M. Paulini,[18] A. Perazzo,[27] L. Pescara,[25] M. D. Peters,[18] T. J. Phillips,[6] G. Piacentino,[27] M. Pillai,[30] K. T. Pitts,[7] R. Plunkett,[7] L. Pondrom,[38] J. Proudfoot,[1] F. Ptohos,[11] G. Punzi,[27] K. Ragan,[14] D. Reher,[18] A. Ribon,[25] F. Rimondi,[2] L. Ristori,[27] W. J. Robertson,[6] T. Rodrigo,[27] S. Rolli,[37] J. Romano,[5] L. Rosenson,[19] R. Roser,[13] T. Saab,[14] W. K. Sakumoto,[30] D. Saltzberg,[5] A. Sansoni,[9] L. Santi,[27] H. Sato,[36] P. Schlabach,[7] E. E. Schmidt,[7] M. P. Schmidt,[39] A. Scribano,[27] S. Segler,[7] S. Seidel,[22] Y. Seiya,[36] G. Sganos,[14] M. D. Shapiro,[18] N. M. Shaw,[29] Q. Shen,[29] P. F. Shepard,[28] M. Shimojima,[36] M. Shochet,[5] J. Siegrist,[18] A. Sill,[35] P. Sinervo,[14] P. Singh,[28] J. Skarha,[15] K. Sliwa,[37] F. D. Snider,[15] T. Song,[20] J. Spalding,[7] T. Speer,[10] P. Sphicas,[19] F. Spinella,[27] M. Spiropulu,[11] L. Spiegel,[7] L. Stanco,[25] J. Steele,[38] A. Stefanini,[27] K. Strahl,[14] J. Strait,[7] R. Ströhmer,[7a] D. Stuart,[7] G. Sullivan,[5] K. Sumorok,[19] J. Suzuki,[36] T. Takada,[36] T. Takahashi,[24] T. Takano,[36] K. Takikawa,[36] N. Tamura,[12] B. Tannenbaum,[22] F. Tartarelli,[27] W. Taylor,[14] P. K. Teng,[33] Y. Teramoto,[24] S. Tether,[19] D. Theriot,[7] T. L. Thomas,[22] R. Thun,[20] R. Thurman-Keup,[1] M. Timko,[37] P. Tipton,[30] A. Titov,[31] S. Tkaczyk,[7] D. Toback,[5] K. Tollefson,[30] A. Tollestrup,[7] H. Toyoda,[24] W. Trischuk,[14] J. F. de Troconiz,[11] S. Truitt,[20] J. Tseng,[19] N. Turini,[27] T. Uchida,[36] N. Uemura,[36] F. Ukegawa,[26] G. Unal,[26] J. Valls,[7a] S. C. van den Brink,[28] S. Vejcik, III,[20] G. Velev,[27] R. Vidal,[7] R. Vilar,[7a] M. Vondracek,[13] D. Vucinic,[19] R. G. Wagner,[1] R. L. Wagner,[7] J. Wahl,[5] N. B. Wallace,[27] A. M. Walsh,[32] C. Wang,[6] C. H. Wang,[33] J. Wang,[5] M. J. Wang,[33] Q. F. Wang,[31] A. Warburton,[14] T. Watts,[32] R. Webb,[34] C. Wei,[6] H. Wenzel,[16] W. C. Wester, III,[7] A. B. Wicklund,[1] E. Wicklund,[7] R. Wilkinson,[26] H. H. Williams,[26] P. Wilson,[5] B. L. Winer,[23] D. Winn,[20] D. Wolinski,[20] J. Wolinski,[21] S. Worm,[22] X. Wu,[10] J. Wyss,[25] A. Yagil,[7] W. Yao,[18] K. Yasuoka,[36] Y. Ye,[14] G. P. Yeh,[7] P. Yeh,[33] M. Yin,[6] J. Yoh,[7] C. Yosef,[21] T. Yoshida,[24] D. Yovanovitch,[7] I. Yu,[7] L. Yu,[22] J. C. Yun,[7] A. Zanetti,[27] F. Zetti,[27] L. Zhang,[38] W. Zhang,[26] and S. Zucchelli[2]

(CDF Collaboration)

[1] *Argonne National Laboratory, Argonne, Illinois 60439*

[2] *Istituto Nazionale di Fisica Nucleare, University of Bologna, I-40127 Bologna, Italy*

[3] *Brandeis University, Waltham, Massachusetts 02264*

[4] *University of California at Los Angeles, Los Angeles, California 90024*

[5] *University of Chicago, Chicago, Illinois 60638*

[6] *Duke University, Durham, North Carolina 28708*

[7] *Fermi National Accelerator Laboratory, Batavia, Illinois 60510*

[8] *University of Florida, Gainesville, FL 33611*

[9] *Laboratori Nazionali di Frascati, Istituto Nazionale di Fisica Nucleare, I-00044 Frascati, Italy*

[10] *University of Geneva, CH-1211 Geneva 4, Switzerland*

[11] *Harvard University, Cambridge, Massachusetts 02138*

[12] *Hiroshima University, Higashi-Hiroshima 724, Japan*

[13] *University of Illinois, Urbana, Illinois 61801*

[14] *Institute of Particle Physics, McGill University, Montreal H3A 2T8, and University of Toronto, Toronto M5S 1A7, Canada*

[15] *The Johns Hopkins University, Baltimore, Maryland 21218*

[16] *Institut für Experimetelle Kernphysik, Universität Karlsruhe, 76128 Karlsruhe, Germany*

[17] *National Laboratory for High Energy Physics (KEK), Tsukuba, Ibaraki 315, Japan*

[18] *Ernest Orlando Lawrence Berkeley National Laboratory, Berkeley, California 94720*

[19] *Massachusetts Institute of Technology, Cambridge, Massachusetts 02139*

[20] *University of Michigan, Ann Arbor, Michigan 48109*

[21] *Michigan State University, East Lansing, Michigan 48824*

[22] *University of New Mexico, Albuquerque, New Mexico 87132*

[23] *The Ohio State University, Columbus, OH 43320*

[24] *Osaka City University, Osaka 588, Japan*

[25] *Universita di Padova, Istituto Nazionale di Fisica Nucleare, Sezione di Padova, I-36132 Padova, Italy*

[26] *University of Pennsylvania, Philadelphia, Pennsylvania 19104*

[27] *Istituto Nazionale di Fisica Nucleare, University and Scuola Normale Superiore of Pisa, I-56100 Pisa, Italy*

[28] *University of Pittsburgh, Pittsburgh, Pennsylvania 15270*

[29] *Purdue University, West Lafayette, Indiana 47907*

[30] *University of Rochester, Rochester, New York 14628*

[31] *Rockefeller University, New York, New York 10021*

[32] *Rutgers University, Piscataway, New Jersey 08854*

[33] *Academia Sinica, Taipei, Taiwan 11530, Republic of China*

[34] *Texas A&M University, College Station, Texas 77843*

[35] *Texas Tech University, Lubbock, Texas 79409*

[36] *University of Tsukuba, Tsukuba, Ibaraki 315, Japan*

[37] *Tufts University, Medford, Massachusetts 02155*

[38] *University of Wisconsin, Madison, Wisconsin 53806*

[39] *Yale University, New Haven, Connecticut 06511*

Contents

List of Tables

List of Figures

Chapter 1

Theoretical Context and Overview

People seem to have an innate desire to understand the world in which they live. What are the constituents of air, water, and earth? Why does the sun shine? In searching for answers to questions such as these, scientists have been guided by emerging patterns. The fractions of elements that combine to form a chemical compound are ratios of small integers. Densities of many gases (at a given temperature and pressure) are approximately integer multiples of one-half the density of hydrogen gas. Elements can be arranged in an orderly table by atomic weight and by chemical properties. These patterns and others led to the nineteenth-century atomic model of chemistry. (Many physicists were not convinced of the atomic hypothesis until Einstein invoked it to explain Brownian motion—the random motion of a (small) macroscopic object, such as a speck of dust, suspended in a liquid.)

The knowledge that matter is composed of atoms leads to a more fundamental question: What is the nature of atoms? The model that emerged in the early twentieth century placed light, negatively charged electrons in orbit around a massive nucleus that contains positively charged protons and electrically neutral neutrons. The quantum-mechanical description of such a system elegantly explains the structure of the periodic table of the elements.

This model leads to further questions: How are neutrons and protons related? What force overcomes the electrical repulsion of protons in the nucleus? Are the electrons, protons, and neutrons themselves pieces in a different kind of periodic table?

Particle physics endeavors to find and to study the most fundamental building blocks of matter and the forces by which they interact. The picture that has evolved thus far has many intriguing properties: particles with fractional electric charge, particles that are just like electrons but heavier, particles that can only be found in bound states with other particles. Below, we briefly describe the present state of the art in particle physics, known as the Standard Model.

1.1 The Standard Model

There are four known forces in nature: gravity, the electromagnetic force, the weak nuclear force (responsible for β decay), and the strong nuclear force (whose residual effects bind the protons and neutrons in the nucleus). While gravity is extremely important in the macroscopic world, at the subatomic level its effects are negligible in comparison with the other three forces, so we neglect it in the following discussion.[1] In relativistic quantum mechanics (the analog of Newtonian mechanics for the subatomic world), forces are described as the exchange of particles.

The Standard Model comprises two theories: the Glashow-Weinberg-Salam [1, 2, 3] (GWS) model of the weak and electromagnetic interactions and quantum chromodynamics [4, 5, 6] (QCD), which describes the strong interaction. In the Standard Model, the electromagnetic force is carried by the massless photon; the weak force is carried by the three massive $W^{\pm}$ and Z^0 particles; and the strong force is carried by eight massless gluons.

The known particles can be divided into two classes: fermions, which have half-integer spin (intrinsic angular momentum) and obey the Pauli exclusion principle; and bosons, which have integer spin. All force carriers are bosons. Electrons, protons, and neutrons are all fermions. Every fermion has a corresponding antiparticle, of opposite electric charge: the positron, antiproton, and antineutron are antiparticles of the electron, proton, and neutron.[2] While electrons appear to be fundamental particles, protons and neutrons are in fact bound states of three quarks (*uud* and *udd*, respectively).

While only two quarks, u and d, are present in ordinary matter, there are in fact six known quarks, d, u, s, c, b, and t, whose masses range from ~ 0.005 GeV to 175 GeV.[3] In addition to the proton and neutron, dozens of other bound states of three quarks—collectively known as baryons—exist, but all have much shorter lifetimes than the proton (which appears to be stable: $\tau > 10^{31}$ years) and the neutron ($\tau \approx 15$ minutes, or longer when bound inside a nucleus). Many bound states of a quark and an antiquark—called mesons—also exist, but all are short-lived ($< 10^{-7}$ seconds). Whereas the electromagnetic force couples to electric charge, the strong force couples to a quantity called color charge, which (unlike electric charge) comes in three varieties, called red, green, and blue.[4] Quarks are either red, blue, or green; antiquarks are either anti-red, anti-blue, or anti-green. A

---

[1] Gravitational effects are expected to be important in particle physics in the 10^{19} GeV energy region, while today's particle accelerators explore the 10^2 GeV energy region.

[2] In recent years, experiments have produced small numbers of antihydrogen atoms from antiprotons and positrons [7].

[3] Particle physicists measure energy, momentum, and mass in the same units—electron volts. In these units, the proton mass is 0.938×10^9 eV, or 0.938 GeV.

[4] These have nothing to do with visible light. They could just as well have been called chocolate, vanilla, and strawberry.

net color of zero can be made by combining a particle and antiparticle of opposite color (e.g. red and anti-red) or by combining equal amounts of red, green, and blue. Thus, colorless bound states can be formed from three quarks, from three antiquarks, or from a quark and an antiquark. A peculiar property of the strong force is that its strength increases as the distance between two particles of nonzero color charge increases. Thus, quarks never appear in isolation. We can assign each quark a "baryon number" $B = +1/3$ and each antiquark $B = -1/3$. For reasons that are not understood, baryon number is (additively) conserved by all known interactions.[5]

The electron, an essential constituent of ordinary matter, turns out to be only one of three charged leptons. The muon and the tau lepton are like the electron but 200 times and 2500 times heavier, respectively. In addition, there are three corresponding neutral leptons, the electron neutrino, the muon neutrino, and the tau neutrino, whose masses are very small—possibly zero. Leptons are assigned "lepton number" $L = +1$ and antileptons are assigned $L = -1$; the sum of L values is conserved by all known interactions. In fact, separate lepton numbers for each generation, L_e, L_μ, and L_τ, appear to be individually conserved. While there is no known reason for L conservation, if L is conserved then L_e, L_μ, and L_τ will be separately conserved if neutrinos are massless.

Both quarks and leptons couple to the photon in proportion to their electric charge. The Z^0 boson couples to fermions in proportion to a combination of electric charge and another property called weak isospin (T_3). The $W^\pm$ boson couples to the left-handed component of each fermion with equal strength (with a coupling that is closely related to the electron's electric charge) and does not couple at all to the right-handed component of each fermion.[6] The W is the only particle whose interactions change particle flavor—changing a charged lepton to a neutral lepton or an up-type ($T_3 = +1/2$) quark to a down-type ($T_3 = -1/2$) quark. Only specific pairs of fermions (called isospin doublets) are connected by interaction with a W: (ν_e, e), (ν_μ, μ), (ν_τ, τ), (u, d'), (c, s'), and (t, b'), where

$$
\begin{pmatrix} d' \\ s' \\ b' \end{pmatrix} = \begin{pmatrix} V_{ud} & V_{us} & V_{ub} \\ V_{cd} & V_{cs} & V_{cb} \\ V_{td} & V_{ts} & V_{tb} \end{pmatrix} \begin{pmatrix} d \\ s \\ b \end{pmatrix}
$$

The change of basis V_{ij} is called the CKM matrix [8, 9]. Another particle, the Higgs boson, as yet undiscovered, couples to the $W^\pm$, Z^0, γ, and all fermions; the coupling to each fermion is in proportion to its mass. We summarize the couplings of γ, $W^\pm$,

---

[5] Since the universe appears to be dominated by matter, rather than antimatter, and thus has a very large total baryon number, it is speculated that some yet undiscovered B-violating process was at work in the early universe.

[6] For massless particles, handedness refers to the relative alignment of a particle's spin and its momentum. For massive particles, the definition is more subtle, but becomes equivalent as the particle's velocity approaches the speed of light.

	f_L	f_R
γ	eQ	eQ
$W^{\pm}$	$g_W/\sqrt{2}$	0
Z^0	$g_Z(Q\sin^2\theta_W - T_3)$	$g_Z Q \sin^2\theta_W$

Table 1.1: Standard Model electroweak boson-fermion couplings. Note $g_W = e/\sin\theta_W$ and $g_Z = e/\sin\theta_W\cos\theta_W$. f_L and f_R refer to left-handed and right-handed fermions.

quarks (spin 1/2)			Q	T_3^L
u 5 MeV	c 1.3 GeV	t 175 GeV	$+2/3$	$+1/2$
d 20 MeV	s 200 MeV	b 4.3 GeV	$-1/3$	$-1/2$
leptons (spin 1/2)			Q	T_3^L
ν_e < 15 eV	ν_μ < 0.2 MeV	ν_τ < 24 MeV	0	$+1/2$
e 0.511 MeV	μ 106 MeV	τ 1.78 GeV	-1	$-1/2$
gauge bosons (spin 1)				Higgs boson (spin 0)
γ $W^{\pm}$ 0 80.3 GeV	Z^0 91.187 GeV	g 0		(H^0) > 60 GeV

Table 1.2: Standard Model particle content. The approximate mass of each particle is listed below its name. For fermions, the electric charge (Q) is given, as well as the weak isospin assignment (T_3) for the left-handed fermion. (Right-handed fermions have $T_3 = 0$, and right-handed neutrinos may not exist.) The Higgs boson is undiscovered; if it exists, its mass must be between 60 GeV and about 1000 GeV. Each quark comes in three distinct color states.

and Z^0 to fermions in Table 1.1.

Some properties of the known particles (and of the unknown Higgs boson) are summarized in Table 1.2. The particles in this table are, as far as we know, fundamental particles.[7] The fact that each set of quarks and leptons is repeated three times, however, suggests that someday a deeper connection may be found, as with the various elements in the periodic table. Although there are three generations each of quarks and leptons, there is no known connection between generation i $(i = 1, 2, 3)$ of quarks and generation i of leptons.

---

[7] For instance, quarks appear to be point-like, down at least to the level of $\sim 10^{-17}$ cm.

The tidy arrangement of known particles and interactions into Tables 1.1 and 1.2 is the result of many decades of experimental and theoretical work.[8] We can trace the theory of weak interactions back to 1930, when Pauli introduced the neutrino to explain the broad electron energy spectrum observed in nuclear β decay. In 1933, Fermi modeled weak interactions as a vector coupling of two fermionic currents, by analogy with quantum electrodynamics. To model the short-range behavior of the weak force, Fermi replaced the dimensionless coupling ($\alpha \approx \frac{1}{137}$) and long-range interaction ($\frac{1}{q^2}$) of QED with the dimensionful coupling of a point-like interaction ($G \approx \frac{10^{-5}}{M_p^2}$). The same[9] Fermi coupling constant G explained nuclear β decay rates, , $\propto G^2(\Delta E)^5$, and the decay rate of the muon, , $\propto G^2 M_\mu^5$. In 1956, motivated by a puzzle in which two particles of opposite parity appeared to have the same mass and lifetime,[10] Lee and Yang, in a thorough analysis of the experimental literature, found no evidence for the widely-held belief that weak interactions conserve parity (mirror symmetry). In 1957, C.S. Wu *et al* [11] observed a large parity-violating asymmetry in β decay of polarized Co^{60} nuclei; shortly thereafter, parity violation was observed at accelerators in the $\pi^\pm \to \mu\nu \to e\nu\nu$ decay chain by Garwin, Lederman, and Weinrich [12] and by Friedman and Telegdi [13]. These experiments, and others in which the helicities of β decay products were measured, established the $V - A$ (vector minus axial-vector) form of the leptonic coupling in weak interactions, proposed by Feynman and Gell-Mann and by Sudarshan and Marshak, to replace the vector coupling of the original Fermi model. The $V - A$ coupling explains, among many other things, why $\frac{\Gamma(\pi^\pm \to e\nu)}{\Gamma(\pi^\pm \to \mu\nu)} \sim 10^{-4}$. The study of strange particle decays in the 1950s and 60s required another extension to Fermi's theory: introduction of the Cabibbo mixing angle, $\theta_C \approx 0.22$, relating strangeness-changing and strangeness-conserving weak hadronic currents.[11] With these modifications, the Fermi theory survives as a useful phenomenological model for low-energy ($q^2 \ll M_W^2$) weak interactions.

In the early 1960s, particle theorists searched for a model of weak interactions that would make sensible predictions at high energy and beyond first order in perturbation theory (the latter property is called renormalizability). An aesthetic desire to unify the weak and electromagnetic forces within a single symmetry group led Glashow, Weinberg, and Salam to the solution.

Both QCD and the GWS model are "gauge theories," based on symmetry groups $SU(3)$ and $SU(2) \otimes U(1)$, respectively. In a gauge theory, the force-carrying particles (gauge bosons) correspond to the generators of the gauge symmetry group, and the allowed set of couplings (interactions) between particles is fixed by the requirement that the Lagrangian be locally invariant under symmetry group transformations.[12]

---

[8] We have found the historical review by Cahn and Goldhaber [10] very useful.

[9] Up to a few-percent correction due to the Cabbibo angle, introduced much later.

[10] They were the same particle, now called K^+.

[11] The Cabibbo mixing angle is the two-generation analog of the CKM matrix.

[12] In quantum electrodynamics, whose gauge group is $U(1)$, this "minimal coupling" prescription

The GWS model describes the interactions of massless leptons and quarks with four massless vector bosons: B^0, corresponding to the one generator of $U(1)$, and W^0, $W^\pm$, corresponding to the three generators of $SU(2)$. Particle mass terms are excluded because they break the electroweak gauge symmetry. The parity-violating $V-A$ form of the weak interaction is incorporated by assigning left-handed fermions to weak-isospin doublets ($T_3 = \pm 1/2$) and right-handed fermions to weak-isospin singlets ($T_3 = 0$). The masses are then generated dynamically through interactions with an additional particle, the Higgs boson. It was suspected by Weinberg, and proven by 't Hooft in 1971, that including the masses in this manner would leave the theory renormalizable. The Higgs mechanism mixes the B^0 and W^0 states into a massless state A (the photon) and a massive state Z^0 (the Z boson):

$$\begin{aligned} A_\mu &= \cos\theta_W B^0_\mu + \sin\theta_W W^0_\mu \\ Z_\mu &= \cos\theta_W W^0_\mu - \sin\theta_W B^0_\mu \end{aligned}$$

While the mixing angle θ_W is not specified by the theory, the same mixing angle relates both the masses and the couplings of the W and Z bosons: $M_W/M_Z = \cos\theta_W$ and $g_W/g_Z = \cos\theta_W$. The W coupling g_W is also related to the fundamental unit e of electric charge: $e = g_W \sin\theta_W$.[13] The point-like Fermi coupling G corresponds to the exchange of a massive vector boson, $\frac{g_W^2}{q^2 - M_W^2} \to g_W^2/M_W^2$ at low q^2.[14]

Since its birth in the 1960s, the Glashow-Weinberg-Salam model of electroweak interactions has survived a remarkable series of experimental tests. Its prediction of weak neutral currents, introduced on theoretical grounds alone, was confirmed with the observation of $\nu_\mu N \to \nu_\mu +$hadrons scattering in the Gargamelle bubble chamber at CERN in 1973 [14]. A central prediction of the theory—that the mixing angle θ_W relating weak and electromagnetic charges also relates the masses of the W and Z bosons—was spectacularly confirmed when the W and Z were discovered [15] in 1983 at the first $p\bar{p}$ collider, CERN's $Sp\bar{p}S$, at the masses predicted from neutrino-scattering data and the muon lifetime.

Experimental tests of the Standard Model have now reached a level of precision at which loop diagrams must be considered. For instance, once the remarkably precise experimental values for $\alpha^{-1} = 137.0359895(61)$, $G_F = 1.16639(1) \times 10^{-5}$ GeV^{-2}, and $M_Z = 91.1867(20)$ GeV [16] are specified, the W mass can be predicted. The prediction, however, includes radiative corrections proportional to $(\frac{m_{\text{top}}}{M_Z})^2$ and $\log(\frac{M_{\text{higgs}}}{M_Z})$ [17]. Measuring the W mass directly at the 1% level probes these radiative corrections. Similarly, measuring $\frac{\Gamma(Z \to b\bar{b})}{\Gamma(Z \to \text{hadrons})}$ at the 1% level probes loop

---

replaces p_μ with $p_\mu - eA_\mu$ in the Lagrangian, giving the electron-photon coupling term.

[13] These relations are modified somewhat by loop corrections. The relation $g_W/g_Z = M_W/M_Z$ receives a roughly 1% correction due to the mass of the top quark and a several-percent correction due to the running of α_{EM} as a function of q^2.

[14] Including the constants, $\frac{G}{\sqrt{2}} = \frac{g_W^2}{8M_W^2}$.

corrections proportional to $(\frac{m_{\text{top}}}{M_Z})^2$, and is potentially sensitive to the presence of new particles—such as a charged Higgs boson $H^{\pm}$ predicted by many supersymmetric models—that would reveal their existence through loop effects [18]. For a recent review of the Electroweak Standard Model, see Ref. [16].

Despite its tremendous success, the Standard Model must be incomplete. The Higgs boson has not yet been found, and it is likely that many other new particles will be discovered along with it.[15]

1.2 Γ_W in the Standard Model

At tree level (lowest order in perturbation theory) in the Standard Model, the partial width $\Gamma (W \to e\nu)$ is calculated to be $\Gamma_{e\nu} = \frac{g^2 M_W}{48\pi}$,[16] which we can rewrite as

$$\Gamma_{e\nu} = \frac{G_F M_W^3}{6\pi\sqrt{2}} \tag{1.1}$$

using $\frac{G_F}{\sqrt{2}} = \frac{g^2}{8M_W^2}$. When experimental values for G_F (measured in muon decay) and M_W (measured at S$\bar{\text{p}}$pS, the Tevatron, and LEP II) are used in Equation 1.1, Standard Model radiative corrections are calculated by Rosner *et al* [20] to be less than $\frac{1}{2}$%, and the predicted partial width is [20, 21]

$$\Gamma_{e\nu} = 226 \pm 1 \text{ MeV} \tag{1.2}$$

where the uncertainty is dominated by the experimental precision on M_W. With three leptonic decay channels and two hadronic decay channels (times three colors), the branching ratio $B(W \to e\nu)$ is naively $\frac{1}{9}$. Including the QCD correction factor $1 + \frac{\alpha_s(M_W)}{\pi} + 1.409(\frac{\alpha_s}{\pi})^2 - 12.77(\frac{\alpha_s}{\pi})^3$ for the quark modes, the Standard Model prediction for the total width is [20, 21]

$$\Gamma_W = 2.09 \pm 0.01 \text{ GeV} \tag{1.3}$$

(Note that the QCD loop effects are a 2.5% correction.)

Because radiative corrections to the W boson propagator—such as $t\bar{b}$, WH, and $W\gamma$ loops—affect Γ_W and M_W in the same manner, these corrections are absorbed into M_W when the measured W mass is used in Equation 1.1. Thus, within the Standard Model, Γ_W is extremely well predicted. The measurement described in this dissertation is an experimental test of that prediction.

---

[15] Fundamental particles of spin 0 create theoretical problems. Solutions to these problems, such as supersymmetry and technicolor, predict large spectra of new particles.

[16] See Appendix H in Perkins's textbook [19] for an explicit calculation.

1.3 Overview of the analysis

This measurement uses a relatively novel method, outlined in Ref. [20] and first employed in Ref. [22] by CDF, to measure Γ_W directly from the $M_T(e,\nu)$ lineshape. Many authors[17] have noted that a Γ_W measurement from the M_T lineshape is possible, and most M_W measurements to date have quoted a fitted value for Γ_W, but these values have usually been quoted either with large systematic errors or (equivalently) with no estimate of systematic errors. The trick that makes the lineshape method feasible is to observe that the Breit-Wigner (width) component of the high M_T lineshape falls off much more slowly than the Gaussian (resolution) component.[18] By comparing the $M_T \gg M_W$ region to the peak region, one is sensitive to Γ_W but relatively insensitive to the systematic uncertainties in detector resolution—particularly calorimeter response to $p_T(W)$—that make a measurement of Γ_W in the region $M_T \approx M_W$ difficult. Figure 1.1 illustrates the variation of the M_T lineshape with Γ_W.

Historically, most W width measurements have used a different method. The most precise experimental values for Γ_W to date have been extracted from the ratio

$$
\begin{aligned}
R &= \frac{\sigma \cdot B(\overline{p}p \to W \to l\nu)}{\sigma \cdot B(\overline{p}p \to Z \to ll)} \\
&= \frac{\sigma(\overline{p}p \to WX)}{\sigma(\overline{p}p \to ZX)} \cdot \frac{\Gamma(W \to l\nu)}{\Gamma(Z \to ll)} \cdot \frac{\Gamma_Z}{\Gamma_W} \\
&= \frac{\sigma(W)}{\sigma(Z)} \cdot \frac{\Gamma_Z}{\Gamma(Z \to ll)} \cdot B(W \to l\nu)
\end{aligned}
$$

by using the LEP value of $\frac{\Gamma(Z \to ll)}{\Gamma_Z}$ and a theoretical calculation of $\frac{\sigma(W)}{\sigma(Z)}$ to obtain the branching ratio $B(W \to l\nu)$. One then divides the Standard Model value for $\Gamma(W \to l\nu)$ by this branching ratio to find Γ_W. Because $\Gamma(W \to e\nu)$ is taken from a calculation, R is usually interpreted as a measurement of the branching ratio $\frac{\Gamma_W}{\Gamma(W \to e\nu)}$ rather than a measurement of the W coupling strength g_W.[19] Since numerically $R \approx 11$, the R method determines Γ_W with a statistical precision dominated by the number of available Z events: $\frac{\sigma_R}{R} \approx \frac{1}{\sqrt{N_{Z \to ee}}} \approx 1.4\%$ for a 90 pb^{-1} data sample [25].

The direct Γ_W measurement complements the standard R measurement in several ways:

- Theoretical input for $\frac{\sigma(W)}{\sigma(Z)}$ and $\Gamma(W \to e\nu)$ are not needed

---

[17] For example, Barger *et al* [23] and Smith *et al* [24].

[18] This idea was introduced to CDF by Henry Frisch, Sacha Kopp, and David Saltzberg.

[19] A large deviation of g_W from the Standard Model expectation, however, would also affect $\frac{\sigma(W)}{\sigma(Z)}$, so in effect the R measurement is testing both the branching ratio and the coupling strength.

- Sources of systematic error are different: understanding acceptance for $ee/e\nu$ final states vs. understanding spectral shape for $e\nu$ final state

- The measurement is in principle sensitive to vertex enhancements that may cancel in the ratio $\frac{\Gamma_{e\nu}}{\Gamma_{\text{tot}}}$ [20]

- It explores the region above the W pole, where new phenomena such as $W' \to e\nu$ may appear[21]

- Experimentally, it is desirable to have more than one method of measuring a given particle property

- Having a second method will be especially important if the R measurement encounters a systematic limit in the next collider run

From a more practical point of view, this analysis uses the same data and many of the same methods as the W mass analysis, and thus provides a set of useful cross-checks on that measurement. The W mass and width are thus intertwined both theoretically and experimentally.

This dissertation, documenting a measurement of the W boson decay width from the $M_T(e, \nu)$ lineshape, is organized as follows: Chapter 2 reviews W and Z production and decay at a hadron collider. Chapter 3 describes the experimental setup used in this measurement. In Chapter 4, we describe the selection of W, Z, and inclusive electron candidate events. Chapter 5 describes the Monte Carlo simulation of W and Z lineshapes and the tuning of this simulation from data. In Chapter 6, we estimate the rates and kinematic shapes of background processes that can fake the $W \to e\nu$ signature. In Chapter 7, we fit the data to simulated lineshapes to extract $,_W$ and investigate sources of systematic error. In Chapter 8, we conclude.

---

[20] We are not aware of any models that predict such enhancements at a rate to which we would be sensitive, but in a future collider run the precision of this measurement may approach the level of the Standard Model radiative corrections discussed in Ref. [20].

[21] Of course this particular phenomenon is already ruled out in the region $110 \leq M_T < 200 \, \text{GeV}$ in which this measurement is performed, but this is one example of an effect that would alter the measured lineshape.
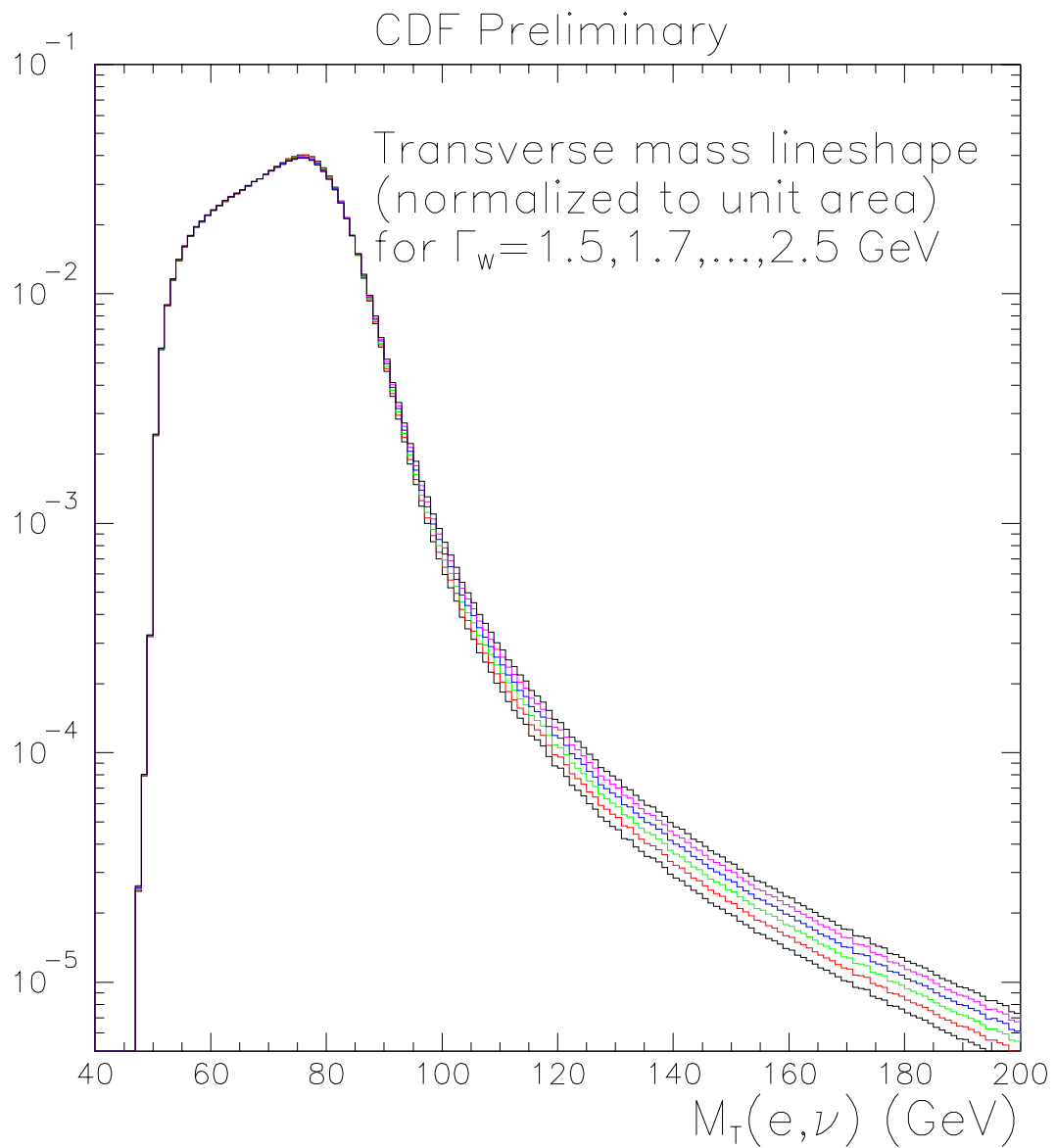
Figure 1.1: Simulated $M_T(e, \nu)$ lineshapes, normalized to unit area, for $\Gamma_W = 1.5, 1.7, \ldots, 2.5$ GeV. Detector response, kinematic cuts, and fiducial cuts are simulated.

Chapter 2

W and Z Production and Decay at a $p\overline{p}$ Collider

Perhaps the most familiar particle colliders are e^+e^- machines, in which every collision proceeds through a known initial state, $e^+e^- \to \gamma^*/Z^*$, at a fixed center-of-momentum energy $\sqrt{s} = 2E_{\text{beam}}$.

By contrast, the particles colliding in a $p\overline{p}$ machine are a broad-band beam of quarks, antiquarks, and gluons. The initial state particles can be $q\overline{q}$, qg, $\overline{q}g$, or gg, and the range of attainable intermediate-state masses, $\sqrt{\hat{s}}$, is distributed roughly exponentially, from 0 to $\sqrt{s} = 2E_{\text{beam}}$. Thus, a wide range of states can be produced, making these machines ideal for new-particle searches.

To predict the rate of a process, such as $p\overline{p} \to W \to e\nu$, one calculates the parton-level cross section, $\hat{\sigma}$, as a function of the quark momenta, and then convolves with the distribution of quark momenta inside the proton,

$$\sigma = \sum_{a,b} \int dx_1 \; dx_2 \; f_{a/p}(x_1, Q^2) \; f_{b/\overline{p}}(x_2, Q^2) \; \hat{\sigma}_{ab}(\hat{s})$$

where $\hat{s} = \tau s = x_1 x_2 s$ [26]. The probability density functions f are called parton distribution functions (PDFs). The distributions are functions of x, the fraction of the hadron momentum carried by the parton, and of a scale Q^2, which we take to equal $\hat{s}$. Modern PDFs are constructed from HERA ep collider data, fixed-target μN, eN, and νN scattering data, and to a lesser extent Tevatron $p\overline{p}$ collider data [27].

We can integrate over $y = \frac{1}{2}\log(\frac{x_1}{x_2})$ and define a parton luminosity,

$$\begin{aligned}
\frac{dL_{ab}}{d\tau} &= \int_0^1 dx_1 \int_0^1 dx_2 \; f_{a/p}(x_1, \tau s) \; f_{b/\overline{p}}(x_2, \tau s) \; \delta(x_1 x_2 - \tau) \\
&= \int_{\log\sqrt{\tau}}^{-\log\sqrt{\tau}} dy \; f_{a/p}(\sqrt{\tau}e^y, \tau s) \; f_{b/\overline{p}}(\sqrt{\tau}e^{-y}, \tau s)
\end{aligned}$$

which describes the $\tau = \frac{\hat{s}}{s}$ spectrum produced by the broad-band beam of partons in the proton and antiproton beams. Figure 2.1 shows the parton luminosity vs. mass, $\frac{dL_{ab}}{d\sqrt{\hat{s}}} = \frac{2\sqrt{\hat{s}}}{s}\frac{dL_{ab}}{d\tau}$, from the MRS-R2 PDF for $a = u$, $b = \overline{d}$, $\sqrt{s} = 1.8$ TeV. Most parton-level cross sections fall asymptotically as $\frac{1}{\hat{s}}$. This behavior of $\hat{\sigma}$ and the rapidly falling parton luminosity are the reason that low-mass states are much more copiously produced than high-mass states.
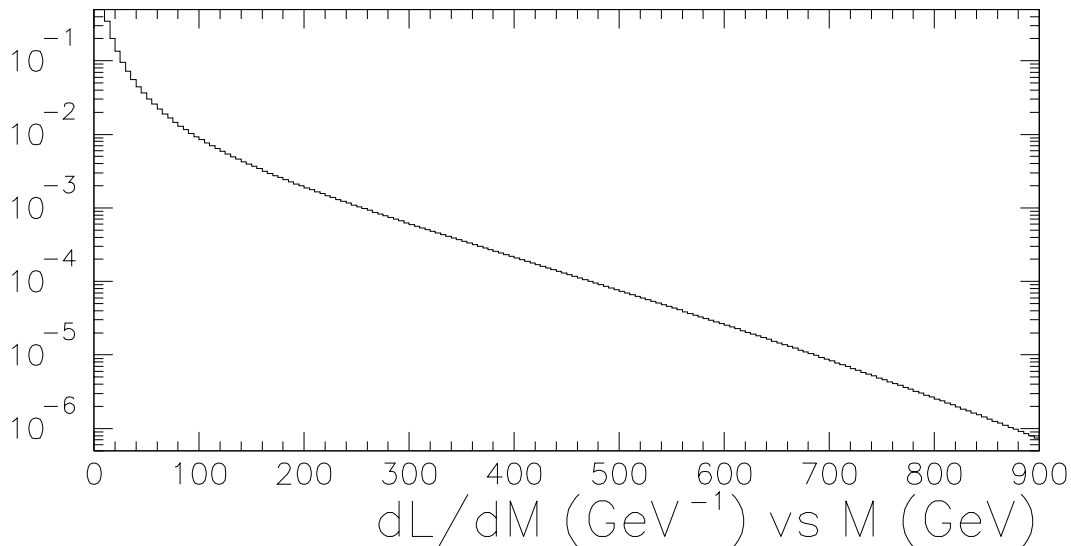
Figure 2.1: Parton luminosity $dL_{u\overline{d}}/d\sqrt{\hat{s}}$ vs. invariant mass $\sqrt{\hat{s}}$ of the $u\overline{d}$ system, for finding an up quark in the proton and a down antiquark in the antiproton at $\sqrt{s} = 1.8$ TeV. We use the MRS-R2 parton distribution functions.

The diagram for the lowest-order process for W and Z production and leptonic decay at a $p\overline{p}$ collider is shown in Figure 2.2. The parton-level cross section for $q\overline{q}' \to W^+ \to e^+\nu$ is [28]

$$\hat{\sigma}_{ij}(\hat{s}) = \frac{1}{3}\,\frac{|V_{ij}|^2}{3\pi}\left(\frac{G_F M_W^2}{\sqrt{2}}\right)^2 \frac{\hat{s}}{(\hat{s} - M_W^2)^2 + (\hat{s},\,_W/M_W)^2}$$

The factor $\frac{1}{3}$ in front accounts for the fact that the colliding partons must have the same color. The resonance shape is the relativistic Breit-Wigner distribution, the $\hat{s}$-dependent factor in $\hat{\sigma}$ above. Figure 2.3 shows the lowest-order Tevatron $p\overline{p} \to W^+ \to e^+\nu$ cross-section as a function of $\sqrt{\hat{s}}$, using the MRS-R2 PDFs.

Because the W couples only to left(right)-handed (anti)fermions, a W^+ produced by a u from the proton and a $\overline{d}$ from the antiproton will be polarized along the antiproton $(-\hat{z})$ direction. The same $V - A$ coupling causes the $e^\pm$ to be emitted preferentially in the direction of the $W^\pm$ polarization $(\mp\hat{z})$, giving $\frac{dN}{d\cos\theta} = \frac{3}{8}(1 \mp \cos\hat{\theta})^2$
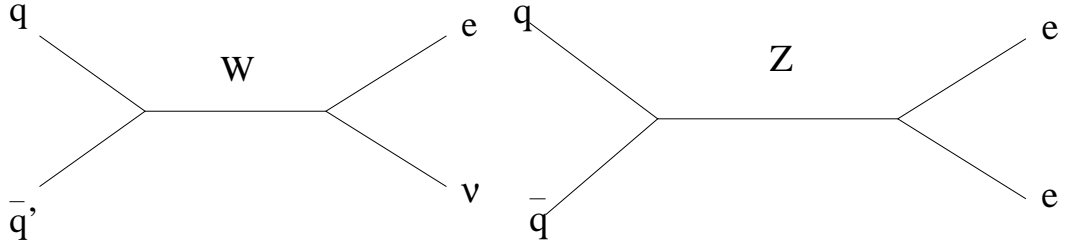
Figure 2.2: Lowest-order diagrams for W and Z production and leptonic decay at a $p\overline{p}$ collider. For W^+ production, q is u or c and $\overline{q}'$ is the corresponding linear combination $V_{ud}\overline{d} + V_{us}\overline{s}$ or $V_{cd}\overline{d} + V_{cs}\overline{s}$. For Z production, q is u, d, s, or c, and $\overline{q}$ is $\overline{u}$, $\overline{d}$, $\overline{s}$, or $\overline{c}$, respectively.

$$\overline{\sigma}(m) \; dL/dM \; (nb/GeV) \; vs \; M \; (GeV)$$
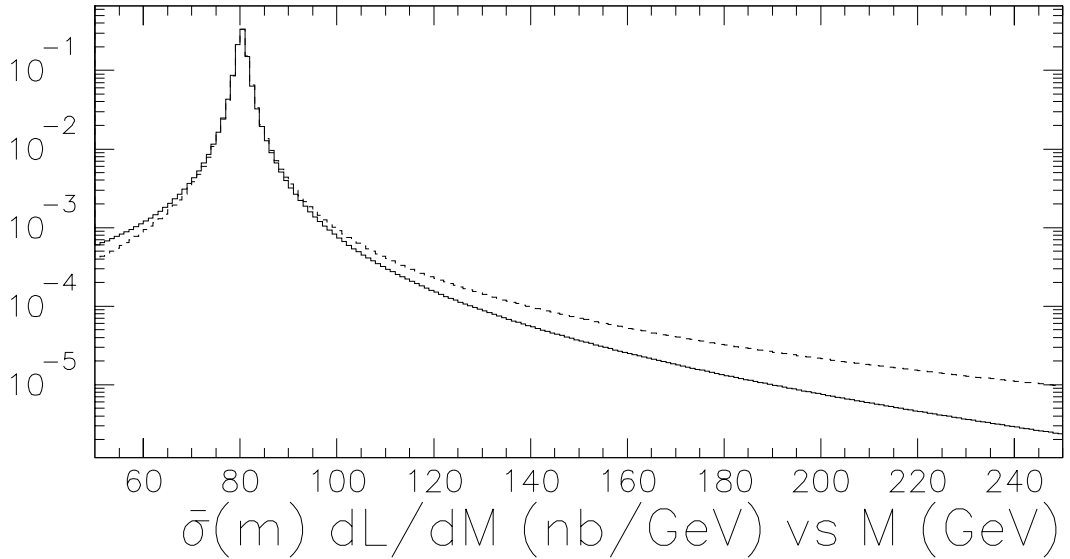
Figure 2.3: The solid curve is the parton-level cross section $\hat{\sigma}$ for $u\overline{d} \to W^+ \to e^+\nu$, weighted by the $u\overline{d}$ parton luminosity, $\frac{dL}{d\sqrt{\hat{s}}} = \frac{2\sqrt{\hat{s}}}{s}\frac{dL_{u\overline{d}}}{d\tau}$, for $\sqrt{s} = 1.8$ TeV from the MRS-R2 parton distribution functions. In the dashed curve, we show the effect of the parton luminosity by replacing $\frac{dL}{d\sqrt{\hat{s}}}$ with $\frac{1}{\sqrt{\hat{s}}}$ (so that we compare two quantities with equivalent dimension). The dashed curve has been normalized to the area under the solid curve, which is about 1 nanobarn.

for $W^\pm$ when (anti)quarks come exclusively from the (anti)proton.[1] Averaging over charge, $\frac{dN}{d\cos\hat{\theta}} = \frac{3}{8}(1 + \cos^2\hat{\theta})$, where $\hat{\theta}$ is measured in the frame of the colliding partons. In the lab frame, this distribution is modified by boosts along $\hat{z}$:

---

[1] Some fraction of the time, $\overline{q}(q)$ will come from the (anti)proton, reversing the sign of the charge asymmetry. Thus, Tevatron measurements of the W charge asymmetry are used as constraints on the sea-quark distributions, as well as the relative momentum fractions carried by u and d quarks, in PDFs.

$\eta_e = \hat{\eta}_e + y$.

Two corrections to the lowest-order model are important to describe W and Z events at the level required by this measurement. The first is to account for final-state photon radiation, as illustrated in Figure 2.4. These effects, calculated by Berends and Kleiss [29], reduce observed electron energies when photons and electrons land in different calorimeter cells, and they increase the probability that the electron will be accompanied by a photon conversion $\gamma \to e^+ e^-$ and thus fail the track isolation requirement described in Section 3.4.5.
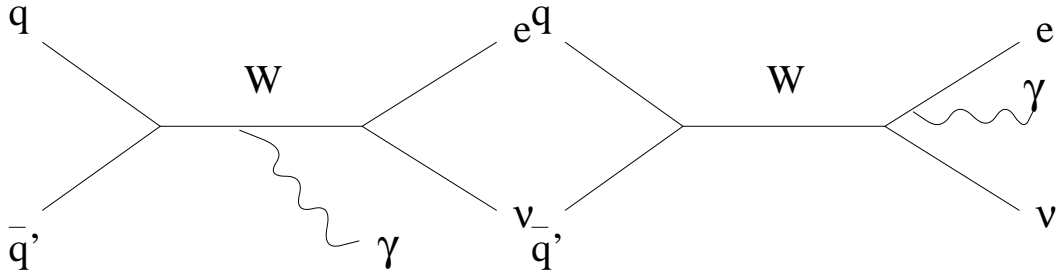
Figure 2.4: Diagrams in which the final state contains a photon radiated by the electron or the virtual W.

The second correction is to account for the transverse momentum of the W and Z. In the diagrams of Figure 2.2, the W and Z are produced at rest. Figure 2.5 shows two examples of diagrams in which a W is produced with non-zero transverse momentum. High-p_T W and Z bosons are accompanied by a small number of high-p_T gluons, which produce collimated jets. Those events are qualitatively different from the low-p_T W and Z bosons relevant to this measurement, which are accompanied by a large number of very low-p_T gluons. At high p_T, conventional perturbation theory reliably predicts the W and Z p_T spectra as a power series in α_s; this calculation has been performed to order α_s^2 in Ref. [30]. At low p_T ($p_T \ll M$), powers of $\alpha_s \log^2(M^2/p_T^2)$ arise [31], which have been calculated using resummation techniques [32, 33, 34]. The resummation is typically performed as a Fourier integral in b, a conjugate variable to p_T; at large b, α_s blows up, so perturbation theory must be replaced with a phenomenological model. Ladinsky and Yuan [35] have fit previously published fixed-target and collider data to a three-parameter model of the nonperturbative regime: $g_1 = 0.11^{+0.04}_{-0.03}$ GeV^2, $g_2 = 0.58^{+0.1}_{-0.2}$ GeV^2, $g_3 = -1.5 \pm 0.1$ GeV^{-1}. Recently Ellis et al [36, 37] have performed the resummation procedure in p_T-space rather than in b-space, which eliminates dependence on non-perturbative models except at the very lowest p_T values.

The total inelastic cross-section at the Tevatron is about $\sigma_{\mathrm{MB}} \approx 50$ mb,[2] while

---

[2] MB stands for "minimum bias," because these are the events recorded when the trigger is set to accept any inelastic collision—without the usual bias for events containing leptons, photons, missing energy, energetic jets, etc. Lowercase mb stands for millibarns. 1 b = (10 fm)^2 = 10^{-24} cm^2.
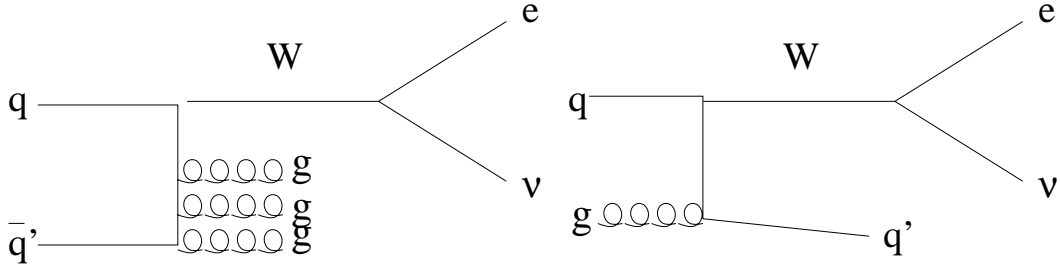
Figure 2.5: A W or Z produced by $q\overline{q}$ can be accompanied by one or more gluons. A W or Z produced by qg is accompanied by a quark and possible gluons. Because the gluon distribution falls more rapidly with x than the quark distributions, the $qg \to W$ process is less important than the $q\overline{q} \to W$ process at Tevatron energies.

$\sigma \cdot B(Z \to ee)$ is about 0.2 nb ($\sigma \cdot B(W \to e\nu)$ is about 2.4 nb). Thus, a rejection factor of order 10^8 is required to isolate a sample of leptonic W and Z events at the Tevatron. A factor of order 10^5 can be obtained simply because the W and Z are so massive: CDF has measured $\sigma(jjX) = 280 \pm 135$ nb for $70 < M_{jj} < 100$ GeV [38]. The remaining rejection is due to the striking signatures of leptonic W and Z decays. An electron typically appears as a single charged particle in the tracking volume, produces a shower only a few centimeters wide,[3] and deposits its energy early in the calorimeter;[4] a jet, by contrast, typically contains many charged and neutral particles, spread over many calorimeter cells, which penetrate more of the calorimeter material before losing their energy.[5] Some jets contain b and c quarks, whose decay products often include real electrons. Electrons from these sources can be statistically separated from electrons produced in W and Z decay, however, because the latter are much more isolated from other particles in the event. A neutrino leaves no signal at all in the detector, but because the colliding $p\overline{p}$ system carries negligible momentum in the laboratory frame, one can infer the presence of a neutrino from an energy imbalance in the calorimeter. In practice, only the component of this energy imbalance transverse to the beamline is used, because a significant fraction of the proton and antiproton longitudinal momenta escape undetected at very small angles to the beamline,[6] and because the partons colliding in the hard-scattering process have a broad distribution of longitudinal momenta. Jet energy resolution effects can mimic the neutrino signature, but this happens infrequently. We can estimate from Figure C.2 in Appendix C that of dijet events

---

[3] The transverse dimension of an electromagnetic shower is characterized by the Molière radius, whose value in lead (a typical absorber in EM calorimeters) is 1.2 cm.

[4] The longitudinal development of an EM shower is characterized by the radiation length, whose value in lead is 0.56 cm.

[5] A hadronic interaction length in lead is about 30 times larger than a radiation length.

[6] CDF's calorimetry only extends down to 2° from the beamline. Even if all remnants of the $p\overline{p}$ collision could be observed, a longitudinal imbalance would be difficult to distinguish from a fluctuation, since sampling calorimeters have resolutions of the form $\sigma_E \sim \sqrt{E}$.

likely to fake the signature of an electron from W decay, the probability also to satisfy the neutrino signature with a large energy imbalance is only 2–3%.

Because only the transverse components of the neutrino momentum are inferred, one uses transverse quantities in $W \to e\nu$ events: the electron and neutrino transverse momentum vectors $\vec{p}_T^{\,e}$ and $\vec{p}_T^{\,\nu}$,[7] the "transverse mass," $M_T = \sqrt{(|\vec{p}_T^{\,e}| + |\vec{p}_T^{\,\nu}|)^2 - (\vec{p}_T^{\,e} + \vec{p}_T^{\,\nu})^2}$, and the W transverse momentum p_T^W. For the special case $p_T^W = 0$, the transverse components of the electron and neutrino momenta are back-to-back, with $p_T^e = p_T^\nu = \frac{M}{2}\sin\theta^*$, so $M_T = M\sin\theta^*$, where θ^* is the electron polar angle in the W rest frame. The transverse mass distribution, graphed in Figure 2.6, is

$$
\begin{aligned}
\frac{d\sigma}{d(M\sin\theta^*)} &= \int dM\, \frac{d\sigma}{dM}\, \frac{1}{M}\, \frac{dN}{d\sin\theta^*} \\
&= \int dM\, \frac{d\sigma}{dM}\, \frac{1}{M}\, \frac{d\cos\theta^*}{d\sin\theta^*}\, \frac{dN}{d\cos\theta^*} \\
&= \int dM\, \frac{dL}{dM}\, \frac{\hat{\sigma}(M)}{M}\, \tan\theta^*(1 + \cos^2\theta^*) \\
&= \int dM\, \frac{dL}{dM}\, \frac{\hat{\sigma}(M)}{M}\, \frac{\sin\theta^*(2 - \sin^2\theta^*)}{\sqrt{1 - \sin^2\theta^*}}
\end{aligned}
$$

which is a convolution of the sharply peaked mass spectrum ($M = \sqrt{\hat{s}}$) shown in Figure 2.3 with the singular $\sin\theta^*$ distribution. Because the singularity is a result of the change of variables from $\cos\theta^*$ to $\sin\theta^*$, it is known as a "Jacobian peak." Since M_T is to first order independent of $\frac{p_T^W}{M_W}$, the M_T spectrum (without resolution effects) has a similar appearance for the general case $p_T^W \neq 0$.

Since the discovery of the W boson in 1982-83, the size of W samples available for study at hadron colliders has increased more than a thousand-fold, providing a laboratory for precise measurements of W properties. Since 1996, W bosons have also been produced (in pairs: $e^+e^- \to W^+W^-$) at LEP, near Geneva; while the W event samples at LEP are not large, precise knowledge of the e^+e^- initial state allows much more information to be extracted from each event. Table 2.1 lists approximate numbers of $W \to e\nu$ decays observed by experiments at $Sp\overline{p}S$, the Tevatron, and LEP-II, including predictions for upcoming accelerator runs.

---

[7] Experimentally, the measured values of $\vec{p}_T^{\,e}$ and $\vec{p}_T^{\,\nu}$ are usually called "transverse energy" $\vec{E}_T$ and "missing transverse energy" $\vec{\cancel{E}}_T$, because of the manner in which they are measured.

Year	Where	$W \to e\nu$ recorded
1982	UA1	6
1982-83	UA1	52
1985	UA2	250
1988-89	CDF	1700
1988-90	UA2	2100
1992-93	CDF	12000
1992-93	DØ	10000
1994-95	CDF	50000
1994-95	DØ	60000
1996	LEP-II (161 GeV)	30
1996	LEP-II (172 GeV)	100
1999 (?)	LEP-II (500 pb^{-1} at 180 GeV)	7000
2000 (?)	CDF-II (2 fb^{-1})	1000000

Table 2.1: Approximate numbers of $W \to e\nu$ decays recorded by various experiments. We have combined the four LEP-II experiments. Event counts have been estimated from values in Refs. [15, 39, 40, 41, 42, 43, 44, 45, 46].
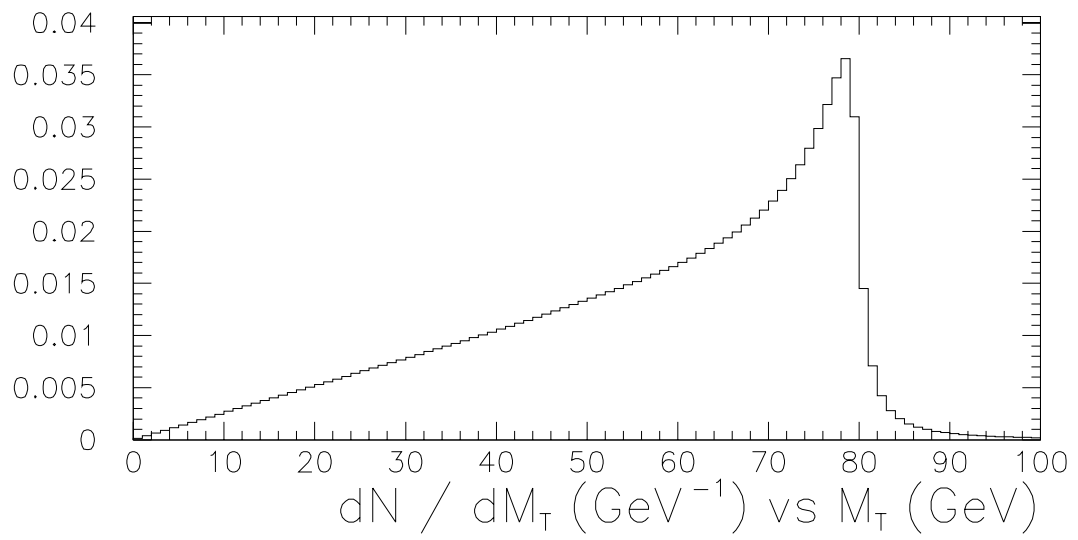
Figure 2.6: Jacobian peak.

Chapter 3

Experimental Setup

3.1 Tevatron

The Tevatron is a circular proton synchrotron 1000.00 meters in radius, located at Fermilab, near Chicago. When the Tevatron operates in $p\overline{p}$ collider mode, six bunches of 2×10^{11} protons circulate clockwise (as seen from above) and six bunches of 2–9×10^{10} antiprotons circulate counterclockwise, with beam energies of 900 GeV.[1] Bunches collide, at a center-of-momentum energy $\sqrt{s} = 1800$ GeV, every $\frac{2\pi \text{ km}}{6 \times 3 \times 10^8 \text{ m/sec}} = 3.5$ μsec at locations "B0" and "D0," where the CDF and DØ detectors reside. The bunches are $\sigma_L \approx 60$ cm (rms) in length and $\sigma_R \approx 40$ μm in radius when they collide.

A continuous period of collider operation (a "store") lasts typically 10 hours. A store can be terminated deliberately, when the beams have diminished after many hours to a fraction of their initial intensities, or by accident, when a superconducting magnet quenches. The initiation of a store (a "shot") takes typically 2.5 hours. The luminosity,

$$L = \frac{f N_{\text{bunch}} N_p N_{\overline{p}}}{4\pi \sigma_R^2}$$

(where $f \approx 48$ kHz is the revolution frequency), is limited by the 6×10^{10}/hour rate at which antiprotons can be accumulated between shots.

During the 1994-95 running period (Run Ib), the average instantaneous luminosity was 8×10^{30} cm^{-2}sec^{-1}, implying (using $\sigma_{\text{MB}} = 50$ mb) that on average there were 1.4 inelastic $p\overline{p}$ collisions per bunch crossing. The CDF experiment recorded 90 pb^{-1} of data in roughly 10^7 seconds of live time.

Whereas one may expect a bunch length $\sigma_L \approx 60$ cm to distribute $p\overline{p}$ interactions over a length of 60 cm/$\sqrt{2}$, this length is in fact about 30 cm. The beam profile σ_R

---

[1]Many of the Tevatron operational parameters listed here were found in Ref. [47]. The beam profile information was found in Refs. [48, 49].

varies along the beam axis (z coordinate): $\sigma_R^2 \propto 1 + (z/\beta^*)^2$, where $\beta^* \approx 35$ cm. Thus, the density of $p\overline{p}$ collisions along z has the form

$$\frac{N_p(z)N_{\overline{p}}(z)}{\sigma_R(z)^2} \propto \frac{\left(e^{-\frac{z^2}{2\sigma_L^2}}\right)^2}{1 + (z/\beta^*)^2}$$

whose rms is 29 cm, to be compared with 42 cm for the numerator alone.

3.2 CDF detector

The CDF detector [50] is a solenoidal magnetic spectrometer surrounded by 4π calorimetry, designed to study a broad range of final states in $p\overline{p}$ collisions. Below, we first define the CDF coordinate system and then describe the parts of the detector relevant to this measurement.
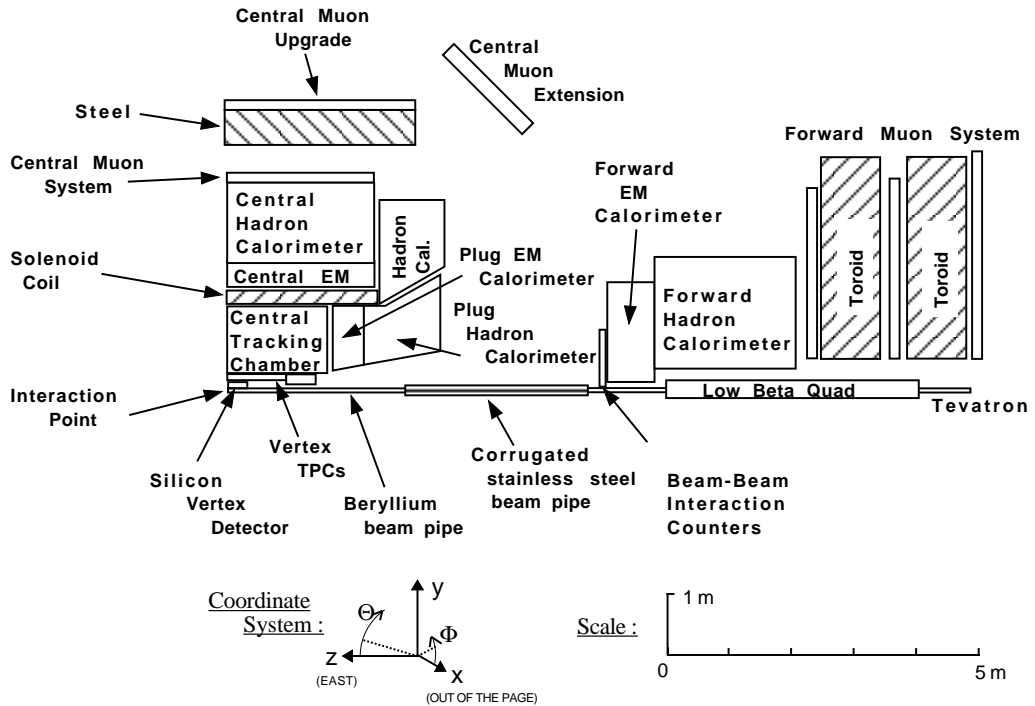
Figure 3.1: An elevation view of the $y > 0$, $z < 0$ quarter of the CDF detector.

3.2.1 Coordinate system

CDF uses a right-handed coordinate system in which $\hat{x}$ points away from the center of the Tevatron (north), $\hat{y}$ points up, and $\hat{z}$ points along the proton beam direction

20

(east). Distances are measured in centimeters from the center of the detector. The z-axis coincides with the nominal Tevatron beamline.

As the detector has approximate cylindrical symmetry, it is convenient to introduce a cylindrical coordinate system in which r is the distance from the z-axis and ϕ ($0 \leq \phi < 2\pi$) is the azimuthal angle, such that $(x, y) = (r \cos \phi, r \sin \phi)$. We also define a polar angle θ ($0 \leq \theta \leq \pi$), such that $r = z \tan \theta$.

Rapidity $y = \frac{1}{2} \log(\frac{E+p_z}{E-p_z})$ occurs frequently as a unit of relativistic phase space. In the ultrarelativistic limit $E = p$, we can rewrite e^{2y} as the purely geometrical expression $\frac{\sqrt{1+\cot^2\theta}+\cot\theta}{\sqrt{1+\cot^2\theta}-\cot\theta} = (\cot\theta + \sqrt{1+\cot^2\theta})^2$, so another convenient variable to use in a collider experiment is pseudorapidity $\eta = \log(\cot\theta + \sqrt{1+\cot^2\theta}) = \log(\cot\frac{\theta}{2})$.[2] Since the most frequent processes in $p\bar{p}$ collisions distribute particles uniformly in pseudorapidity, CDF's calorimetry (described below) is uniformly segmented in η.

Momenta, energies, and masses are measured in GeV. The transverse (x-y) component of an energy or momentum vector, analogous to the r coordinate, is denoted E_T or p_T as a scalar, and $\vec{E}_T$ or $\vec{p}_T$ as a vector in the x-y plane.

As a charged particle follows a helical trajectory in a uniform magnetic field, CDF uses five helix parameters, $c, \phi_0, d_0, z_0, \lambda$, to describe a particle trajectory. The curvature, c, has a magnitude equal to the inverse diameter of the helix (projected into the x-y plane) and is signed such that a particle having $c > 0$ orbits counterclockwise; as it happens, CDF's magnetic field is oriented such that a positively-charged particle has $c > 0$. ϕ_0 is the angle (in the x-y plane) of the particle's motion at its closest approach to the z-axis. d_0 is the distance of closest approach to the z-axis, signed so that the (x, y) point of closest approach is $(-d_0 \sin\phi_0, d_0 \cos\phi_0)$. z_0 is the particle's z position at its point of closest approach to the z-axis. $\lambda = \cot\theta$ is $\frac{p_z}{p_T}$. For magnetic field $\vec{B} = B\hat{z}$, $p_T = \frac{0.299792458B}{2|c|}$, where p_T is in GeV, B is in Gauss, and c is in cm^{-1}.

3.2.2 Solenoid

A 14116 Gauss solenoidal magnetic field is maintained in the region $r < 150$ cm, $|z| < 250$ cm by circulating a 4650 A current through 1164 turns of a superconducting coil. The field is oriented along $+\hat{z}$ and is uniform at the 0.1% level in the region $|z| < 150$ cm in which track measurements are made. The small nonuniformities, mapped out during detector construction, are treated as a perturbation in the track fitting software. NMR probes monitor B continuously during data taking, and any deviation from the nominal value is applied as a correction to measured

---

[2] An alternate derivation, $y = \frac{1}{2} \log(\frac{E+p_z}{E-p_z}) \to \frac{1}{2} \log(\frac{1+\cos\theta}{1-\cos\theta})$, $\tanh y = \frac{e^{2y}-1}{e^{2y}+1} = \cos\theta$, yields the equivalent definition $\eta = \tanh^{-1}(\cos\theta)$.

track momenta. In this magnetic field, a $p_T = 30$ GeV particle deviates only 1.6 cm from a straight path by $r = 150$ cm, while a $p_T = 0.3$ GeV particle produced at the origin does not escape the magnetic field radially. The solenoid presents 0.85 radiation lengths (X_0) to a particle passing at normal incidence.

3.2.3   VTX

The VTX is a set of 28 time projection chambers, each 9.4 cm in length, providing 24 z measurements ($\sigma \approx 200$ μm) between $r = 6.5$ cm and $r = 21$ cm for $85 < |z| < 132$ cm and 16 z measurements between $r = 11.5$ cm and $r = 21$ cm for $|z| < 85$ cm. Each module is segmented octagonally in ϕ; adjacent modules are offset $11.25°$ in ϕ to allow three-dimensional reconstruction of track segments that cross module boundaries.

The principal purpose of the VTX is to locate $p\overline{p}$ interaction vertices along the beam axis. A z-vertex measurement is needed to calculate the transverse component of calorimeter energies: for each calorimeter cell i, $E_T^i = E_{\text{total}}^i \sin\theta_i$, where θ_i depends upon z_{vertex}. The positions of z-vertices are also used as seeds in the r-z component of CTC track reconstruction. A z-vertex measurement is also necessary for determining the beam position in the x-y plane, as the Tevatron beamline has a significant slope, which varies from store to store, with respect to the z axis.

The presence or absence of VTX hits can be used to distinguish electrons and photons in the high-η region in which CTC information is not available, and to identify electrons originating from photon conversion in the CTC inner cylinder ($r \approx 28$ cm).

Finally, the number of reconstructed VTX vertices per event is closely correlated with the number of $p\overline{p}$ interactions per bunch crossing, so it is sometimes used as a measure of luminosity.

3.2.4   CTC

The central tracking chamber (CTC) [51] is a 6156-channel cylindrical drift chamber that measures charged particle trajectories in the region $31 < r < 132$ cm, $|z| < 150$ cm. Eighty-four sense layers are arranged into five axial superlayers, which measure $r\phi$ at 12 radii spaced 0.707 cm apart, interleaved with four stereo superlayers, which measure $r\phi \pm z\tan(2.5°)$ at six radii. The CTC geometry is illustrated in Figure 3.2. Each superlayer is divided into cells, each of which contains a row of sense (anode) wires and is bounded by two rows of field (cathode) wires, as shown in Figure 3.3. The wire planes are tilted $45°$ with respect to the radial direction; cells overlap such that a particle traveling radially crosses an average of 1.2 sense wire planes in each axial superlayer.

Drift electrons follow approximately azimuthal trajectories (the Lorentz angle is chosen to match the $45°$ cell tilt) at 51 μm/nsec. The maximum drift distance
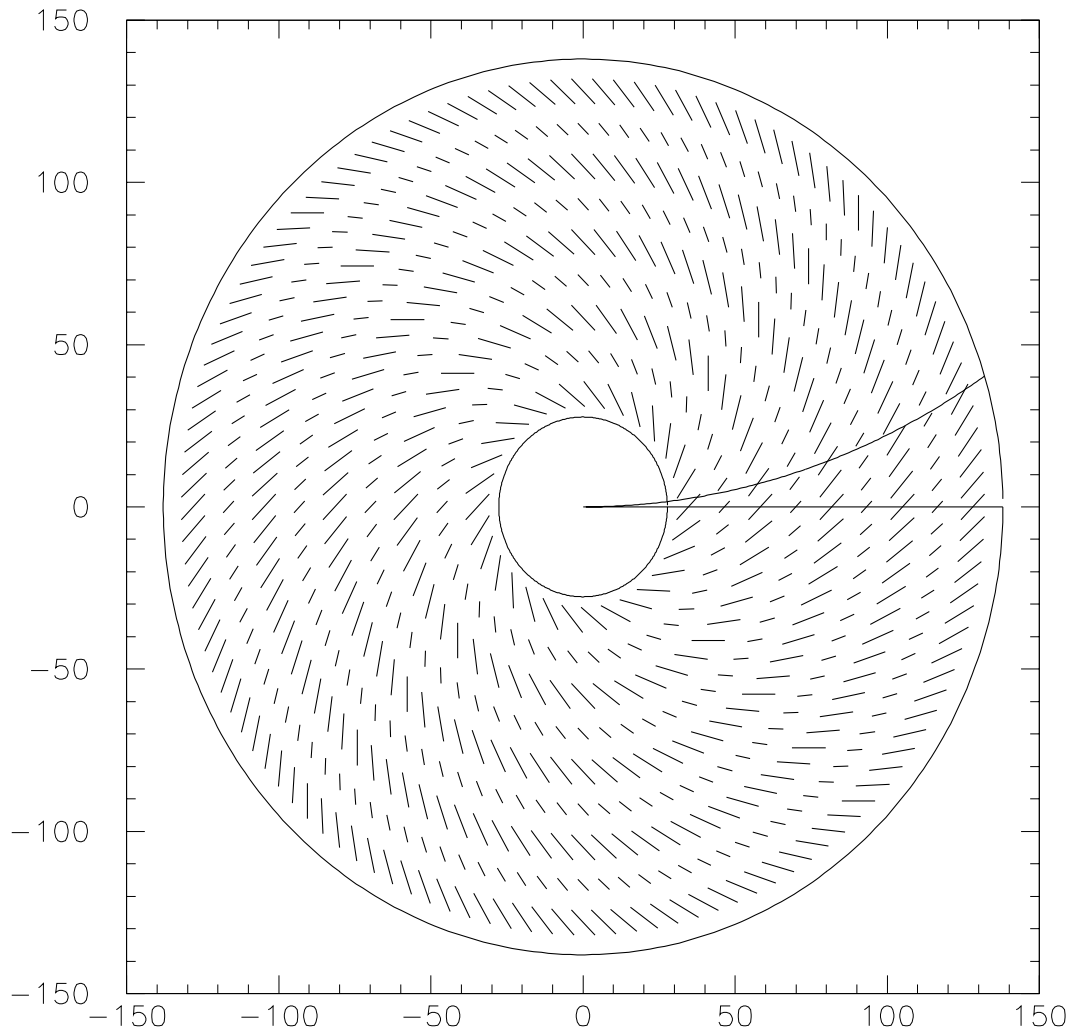
Figure 3.2: Locations (y vs. x, in cm) of sense wire planes on the CTC endplates, as seen from the east side of the detector. Field wire planes are not shown. In a right-handed coordinate system, the cells are tilted 45° counterclockwise with respect to the radial direction. (Many published illustrations draw the endplates as seen from the west, which we find counterintuitive.) Also drawn are a straight track at $\phi_0 = 0, d_0 = 0$ and a 1 GeV positive track at $\phi_0 = 0, d_0 = 0$.

is about 4 cm, or 800 nsec. Leading and trailing edge times of sense-wire signals are recorded in 2 nsec bins by multiple-hit TDCs. The distribution of pulse widths gives a typical two-track separation of 0.2 cm.

The tilted-cell geometry greatly simplifies the problem of drift-velocity calibration, as every high-p_T track samples the full range of drift distances within each superlayer. The corollary that a high-p_T track always produces at least one hit per superlayer with a short (< 80 nsec) drift time is exploited in an elegant trigger design [52].
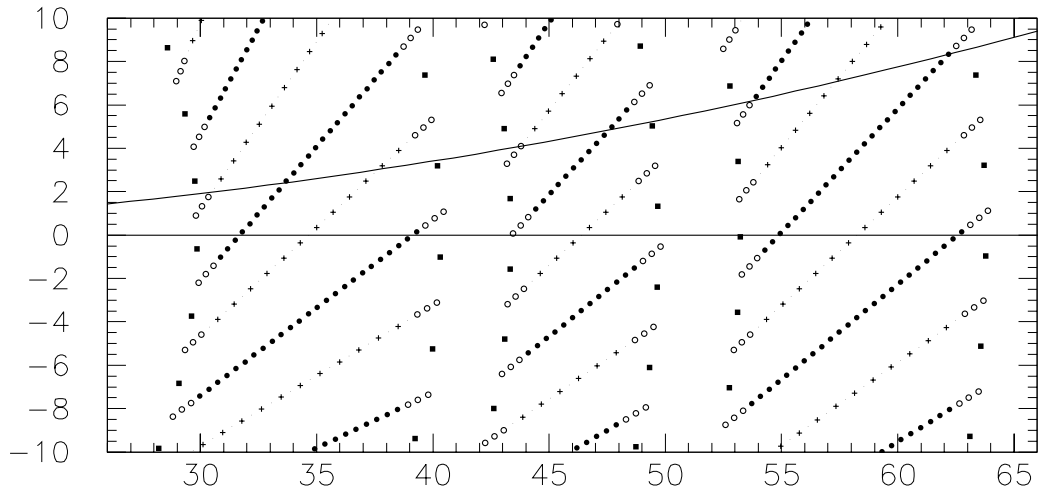
Figure 3.3: Nominal endplate locations (y vs. x, in cm) of CTC wires near $\phi = 0$ in superlayers 0, 1, and 2. Sense, potential, field, guard, and shaper wires are drawn as plus signs, dots, filled circles, open circles, and squares, respectively. The tracks from Figure 3.2 are also shown.

Hit residuals from helical track fits vary from 250 μm in the inner layers to 160 μm in the outer layers. (The z resolution for a stereo layer is a factor $1/\tan(2.5°)$ larger.) To predict actual track parameter resolutions, however, e.g. to obtain vertex or mass resolutions or to combine CTC and SVX information, one must scale the hit resolutions by an empirical factor of 1.5–2.5, for which no satisfactory explanation has ever been found.

CTC resolutions observed in Run Ib data are $\frac{\sigma_{p_T}}{p_T^2} = 0.09\%$ GeV^{-1}, $\sigma_{d_0} = 0.04$ cm, $\sigma_{z_0} = 0.7$ cm.[3] The momentum resolution is measured in $Z \to \mu\mu$ decays [71], after constraining the tracks to originate from the beamline. As the rule of thumb $\sigma_{1/p_T} \sim \frac{\sigma_{\text{hit}}}{\sqrt{N_{\text{hits}}}BL^2}$ illustrates, increasing the length over which track measurements are made from 100 cm to 130 cm improves momentum resolution by nearly a factor of two.

The CTC serves many purposes in this measurement. The presence of a high-p_T track that matches an electromagnetic shower is an essential part of CDF electron identification, even in the trigger (described below). We also use the absence of other CTC tracks near the electron to discriminate W and Z electrons from background. CTC tracks are used to identify $Z \to ee$ events that fake the $W \to e\nu$ signature when one electron lands in a region of poor calorimeter response. The CTC provides the direction vector for electron energies, needed to compute transverse energies or invariant masses. Comparing CTC momenta and CEM energies for electrons is the basis of the tower-to-tower calibration of the CEM.

---

[3] These resolutions use an improved set of calibration constants; the original calibration gives 0.10% GeV^{-1}, 0.07 cm, and 1.0 cm, respectively.

3.2.5 SVX

The silicon vertex detector (SVX') [53] is a four-layer, 46080-channel silicon microstrip detector, with 60 μm strip pitch (55 μm in the outermost layer). In the region $1.1 < |z| < 26.6$ cm, it provides $r\phi$ measurements with 13 μm resolution at radii of 2.9, 4.3, 5.7, and 7.9 cm. The impact parameter resolution for tracks combining CTC and SVX information is well described by $\sigma_\delta = 10 \ \mu$m $+ \frac{40}{p_T} \ \mu$m GeV.[4]

While the SVX plays a significant role in the study of heavy quark decays at CDF, this measurement uses it merely to determine the average Tevatron beam position on a run-by-run basis, so that a beam constraint can be used to improve the CTC momentum resolution.

3.2.6 Calorimetry

Electromagnetic and hadronic calorimetry covers the pseudorapidity region $|\eta| < 4.2$ ($2° < \theta < 178°$) in projective towers that cover $\Delta\eta \times \Delta\phi = 0.1 \times 15°$ in the central region ($|\eta| < 1.1$) and $0.1 \times 5°$ in the plug and forward regions. The nearly 4π solid angle coverage is important for this measurement, in which the presence of a neutrino is inferred from an imbalance of transverse energy in the calorimetry.

As Figure 3.1 shows, CDF calorimetry is divided into several independent subsystems. Central (CEM), plug (PEM), and forward (FEM) electromagnetic shower detectors cover $|\eta| < 1.1$, $1.1 < |\eta| < 2.4$, and $2.2 < |\eta| < 4.2$, respectively, with 16–26 radiation lengths (X_0) of lead absorber. Behind these shower detectors are central (CHA), end wall (WHA), plug (PHA), and forward (FHA) hadronic calorimeters, covering $|\eta| < 0.9$, $0.7 < |\eta| < 1.3$, $1.3 < |\eta| < 2.4$, and $2.3 < |\eta| < 4.2$, respectively, with 4–8 nuclear interaction lengths of steel. The CEM, CHA, and WHA consist of alternating layers of absorber and plastic scintillator; the scintillation light is measured with two photomultiplier tubes per tower. The PEM, PHA, FEM, and FHA are alternating layers of absorber and multi-wire proportional chambers; the chamber cathodes are divided into pads to form the tower geometry.

CDF has several regions of low calorimeter response ("cracks"), through which energetic particles can escape undetected: the $\theta = 90°$ region between the east and west halves of the CEM, the azimuthal boundaries between CEM wedges, the $\theta \approx 30°$ region between the CEM and PEM, and the $\theta \approx 10°$ region between the PEM and FEM. Fortunately, all but the $10°$ region are well covered by the CTC, which can identify escaping charged particles in the crack regions. Figure 3.4 illustrates the tower geometry and uses the QFL simulation program to show regions in which mean electron response is less than 50%.

---

[4] While addition in quadrature has more physical motivation, CDF has historically added the detector and multiple-scattering terms linearly to describe the SVX impact-parameter resolution.
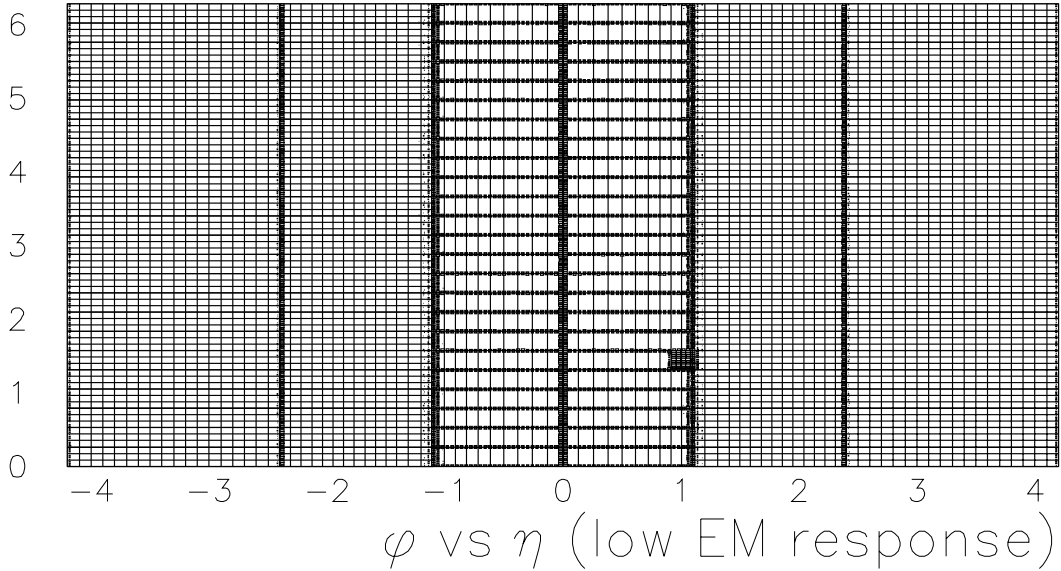
Figure 3.4: The grid, ϕ vs. η, shows the tower segmentation of the CDF calorimetry. The shading indicates regions in which electron or photon response is less than 50% in the QFL detector simulation program. The regions of low response are $|\eta| \approx 2.4$ ($10°$ region), $|\eta| \approx 1.1$ ($30°$ region), $|\eta| \approx 0$ ($90°$ region), the azimuthal boundaries between CEM wedges (ϕ cracks), and the CEM chimney tower, through which the solenoid is accessed.

3.2.7 CEM

The central electromagnetic calorimeter (CEM) [54] provides electron and photon energy measurements in the region $|\eta| < 1.1$, with a resolution $\sigma_E/E = 13.5\%/\sqrt{E_T(\text{GeV})} \oplus 1.5\%$.[5] It is constructed as four arches, northeast, southeast, northwest, and southwest, each of which contains 12, $15°$ wedges. A wedge consists of alternating layers of polystyrene scintillator and aluminum-clad lead, divided into ten towers in η. To maintain a constant thickness (in X_0), compensating the $\sin\theta$ variation between towers, some lead layers are replaced with acrylic; the number of lead layers varies from 30 in the innermost ($|\eta| \approx 0.06$) tower to 20 in the outermost ($|\eta| \approx 1.0$, $\sin\theta \approx 0.64$) tower. Light from each tower is collected by sheets of acrylic wavelength shifter at both azimuthal tower boundaries and guided to two phototubes per tower. The outer two towers in one wedge (called the "chimney towers") are missing to allow solenoid access, leaving 478 instrumented towers. Figure 3.5 is an illustration of a CEM wedge.

At a depth of 5.9 X_0 (including the solenoid), which is approximately the depth at which shower energy deposition peaks, the central strip chambers (CES) measure

---

[5] The first term is called the "stochastic term" and the second term is called the "constant term." The former is an intrinsic limitation due to shower fluctuations and PMT photoelectron fluctuations, while the latter is limited by the amount of data available for calibration.
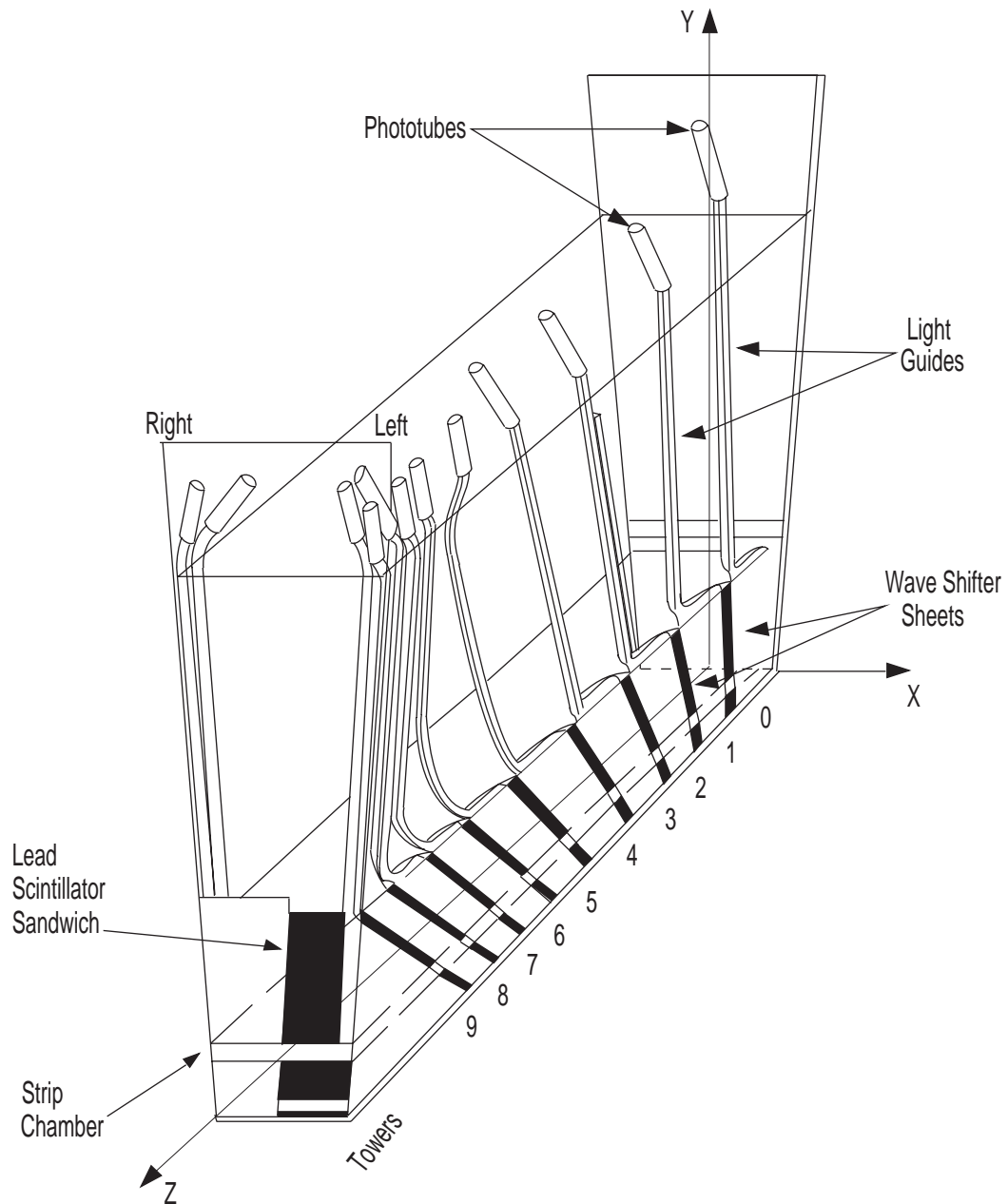
Figure 3.5: A CEM wedge. The local coordinate system, in which x points azimuthally, is illustrated. The mostly empty region between the lead/scintillator sandwich and the phototubes is where the CHA resides.

the transverse shower shape with 1.4–2 cm segmentation, to be compared with the approximately 25 cm × 50 cm tower segmentation. The CES module in each wedge is a multi-wire proportional chamber with 64 anode wires oriented parallel to the beam axis, spaced 0.73 cm apart, and split at $|z| \approx 121$ cm; adjacent anode wires

are ganged together for readout, so the azimuthal segmentation is 1.45 cm. The cathodes are segmented into 128 strips with $\Delta z = 1.67$ cm for $|z| < 121$ cm and $\Delta z = 2.01$ cm for $|z| > 121$ cm. Since an electron or photon shower typically spans several CES channels in each dimension, the position resolution is quite good: When CTC tracks from W electrons are extrapolated to the CES ($r \approx 184$ cm), the CES and CTC shower positions match to 0.22 cm (rms) in azimuth and 0.46 cm (rms) in z. Both CES/CTC position match and CES shower shape are useful electron identification variables.

Between the outer radius of the CTC and the start of the CEM, a particle traverses $1.1/\sin\theta\ X_0$ in the solenoid and other material, giving a photon a high probability of converting to e^+e^- before the CEM. This fact is exploited by the central pre-radiator (CPR), a set of multiwire proportional chambers located between the solenoid and the CEM.

Phototube gains are calibrated once per store using a Xenon flasher system. After long shutdowns, tower-to-tower gains are calibrated with radioactive sources to the 2% level, which is adequate for use in the trigger.

3.3   Trigger and DAQ

As we noted in Chapter 2, a large amount of filtering is required to extract $W \to e\nu$ (2.4 nb) and $Z \to ee$ (0.2 nb) from the 50 mb minimum-bias cross section. Most of this filtering is done by CDF's three-level trigger system [55, 56].

At a typical Run Ib luminosity of 8×10^{30} cm^{-2} sec^{-1}, the average number of $p\overline{p}$ interactions per bunch crossing is 1.4, giving a typical minimum-bias event rate of 215 kHz, 75% of the 286 kHz bunch-crossing rate.

Using custom electronics to process analog calorimeter signals and identify muon-chamber track segments, the Level 1 trigger makes its decision in less than the 3.5 μsec crossing time, accepting typically 100 μb, or a rate of 800 Hz (at 8×10^{30} cm^{-2} sec^{-1}). The Level 1 trigger thus provides a typical rejection factor of 350 with no dead time.[6]

For each event accepted by Level 1, the Level 2 trigger system uses analog calorimeter signals, muon track segments, and tracks from the CTC track processor (CFT). It forms clusters of energy in the calorimeter (corresponding to jets, electrons, or photons), calculates $\vec{E}_T$ imbalance in the calorimeter, and correlates CFT tracks with electron or muon candidates. Combinations of interesting objects, such as two central electron/photon candidates, a central electron candidate matched to a track, or a central electron/photon candidate in coincidence with a large $\vec{E}_T$ imbalance, can be used in the trigger decision. This decision takes typically 40 μsec,

---

[6]Many of the numbers quoted in this section come from Ref. [57] and from the LUMMON output for run 65816.

which causes the detector to miss about 3% of bunch crossings at a Level 1 trigger rate of 800 Hz. Level 2 accepts typically 2 μb, or 15 Hz (at typical luminosity), providing a rejection factor around 50.

For each event accepted by Level 2, the full detector (about 10^5 electronics channels) is read out by the data acquisition system. This process takes typically 3 msec, which causes the detector to miss roughly an additional 5% of bunch crossings at a Level 2 trigger rate of 15 Hz. The data are sparsified and formatted into an event record about 100 kilobytes in length, then transmitted to the Level 3 trigger, which is a farm of commercial computers running software reconstruction algorithms on the full event data. Level 3 provides a rejection factor of 3–4, accepting typically 600 nb, or 5 Hz at a luminosity of 8×10^{30} cm^{-2} sec^{-1}. All events passing Level 3 are spooled to tape for later processing. About 5% of events, called "Stream A," are cached on disk for rapid processing—usually within hours of being recorded; Stream A comprises the Level 3 triggers for high-p_T leptons, photons, and jets, large $\not{E}_T$, and $J/\psi \to \mu\mu$ candidates. A fraction of Level 3 output is monitored in real time to search for detector malfunctions, to derive calibration constants, to display events graphically, and to identify extremely unusual events.

3.3.1 Central electron triggers

We briefly describe the particular criteria imposed by the trigger to select the W and Z events used in this measurement. The Level 1 calorimeter trigger requires a single trigger tower[7] signal above threshold (8 GeV for the CEM) in E_T;[8] to facilitate trigger efficiency measurements, this threshold is reduced to 4 GeV (for CHA and all EM calorimeters) every 40th bunch crossing [58]. A separate dielectron trigger requires two CEM trigger towers above a 4 GeV E_T threshold. These triggers combined accept a cross section of approximately 40 μb.[9]

At Level 2, a $Z \to ee$ trigger, a $W \to e\nu$ trigger, and an inclusive electron trigger search for CEM clusters with $E_T > 16$ GeV and hadronic energy fraction below 12.5%. The Z trigger requires two such clusters. The W trigger requires one such cluster, a transverse energy imbalance exceeding 20 GeV, and a > 4 GeV CES anode signal [59] in the CEM trigger tower, which suppresses triggers caused by sporadic discharges of single photomultiplier tubes. The inclusive electron trigger, which also serves as a backup trigger for both W and Z events, requires a CEM cluster matched in azimuth to a > 12 GeV CFT track. Another backup trigger, potentially

---

[7] In the L1 and L2 triggers, adjacent towers in η are paired to reduce the number of signals. Since the scintillation light from each CEM tower is collected by two separate phototubes, each CEM trigger tower signal, covering $\Delta\eta \times \Delta\phi = 0.2 \times 15°$, is the sum of four phototube signals.

[8] In the L1 and L2 triggers, $\sin\theta$ for $E_T = E\sin\theta$ is the nominal value, computed using $z_0 = 0$.

[9] Of the 49843 events passing the $W \to e\nu$ selection in Chapter 4, in which no explicit Level 1 or Level 2 trigger requirements are imposed, only 10 fail the Level 1 calorimeter trigger (OR'ed, as is required, with the 4 GeV $\times 40$ prescaled trigger).

of interest for off-shell $W \to e\nu$ events, requires a CEM cluster with $E_T > 50$ GeV and hadronic energy fraction below 12.5%, with no other requirements. These four triggers combined accept a cross section of approximately 200 nb.

The Level 2 W and Z triggers demonstrate an important CDF strategy: Triggers overlap to ensure that important signals are not missed. Of the 49843 W events we select in Chapter 4, 99.8% pass either the $\not{E}_T$ trigger or the CFT trigger at Level 2.[10] Of the 46190 events passing the CFT trigger, 95.3% pass the $\not{E}_T$ trigger; of the 47551 events passing the $\not{E}_T$ trigger, 92.6% pass the CFT trigger. In the absence of correlated sources of inefficiency, one expects the two triggers combined to be 99.7% efficient—much better than either one alone.

At Level 3, there are several high-p_T electron triggers. The $Z \to ee$ trigger requires one CEM electron with $E_T > 22$ GeV and $E_{\mathrm{hadron}}/E_{\mathrm{EM}} < 0.125$, a corresponding CTC track with $p_T > 13$ GeV, and a second CEM, PEM, or FEM electron with $E_T > 20$, 15, or 10 GeV, respectively. The $W \to e\nu$ trigger requires a CEM electron with $E_T > 22$ GeV and $E_{\mathrm{hadron}}/E_{\mathrm{EM}} < 0.125$, a corresponding CTC track with $p_T > 13$ GeV, and $\not{E}_T > 22$ GeV. A "no track" backup W trigger removes the W trigger's track requirement, imposes more stringent versions of the W trigger's other requirements—$E_T > 25$ GeV, $E_{\mathrm{hadron}}/E_{\mathrm{EM}} < 0.05$, $\not{E}_T > 25$ GeV—and adds several additional electron identification requirements.[11] The "no track" trigger prevents good W events from being lost if CTC tracking efficiency is slightly lower in Level 3 than offline—for instance because better calibration constants are available offline; it also provides a way to measure track-finding efficiency with $W \to e\nu$ events. The inclusive electron trigger requires a CEM electron with $E_T > 18$ GeV, $E_{\mathrm{hadron}}/E_{\mathrm{EM}} < 0.125$, several other electron identification requirements,[12] and a corresponding track with $p_T > 13$ GeV. A backup inclusive electron trigger requires $E_T > 50$ GeV and a corresponding track with $p_T > 25$ GeV but makes no other requirements on the electron. These triggers combined accept a cross section of approximately 8 nb, a factor of nearly 10^7 below the 50 mb minumum bias cross section.[13]

---

[10]Incidentally, none of the 112 events failing both of these triggers has $M_T > 100$ GeV.

[11]The additional requirements are $\chi_s^2 < 20$ (described below), Lshr3 < 0.2 (a check that energy shared with neighboring towers in η is consistent with an electron), and $E_{\mathrm{border}} < 2.5$ GeV (a calorimeter isolation requirement).

[12]Lshr3 < 0.2, $\chi_s^2 < 10$, $|\Delta x_{\mathrm{track,CES}}| < 3$ cm, and $|\Delta z_{\mathrm{track,CES}}| < 5$ cm.

[13]Of the 49843 events passing the $W \to e\nu$ selection in Chapter 4, which requires either the W trigger or the "no track" trigger at Level 3, 90% pass the "no track" trigger, but it is rarely needed: Only 297 events (0.6%) fail the W trigger.

3.4 Data handling

3.4.1 Offline reconstruction

Typically within hours of being recorded, Stream A events are processed by a farm[14] of 32 commercial UNIX-based computers running Fortran reconstruction software developed by CDF physicists [46]. A processor typically spends 20 seconds per event combining raw digitizations with calibration constants, suppressing known noise sources, and clustering detector-level objects—drift chamber and scintillator hit times and phototube, MWPC, and silicon strip pulse heights—into objects of interest in physics analysis—charged-particle trajectories, interaction vertices, jets, electron, photon, and muon candidates, and so on.

Offline reconstruction differs from Level 3 reconstruction in three ways. First, since more time is available, a thorough reconstruction of the data from each detector component is performed offline for every event, computing much more than is necessary to make a trigger decision. Second, some calibration constants are derived in parallel with data-taking, and are thus not available in Level 3. Third, whereas the goal of Level 3 is irreversible data reduction through event filtering, the goal of offline reconstruction is to combine the raw data from each event with compact, high-level quantities that can be analysed quickly.[15]

The full Stream A output for Run Ib, about 200 kilobytes per event, is stored on 133, 8 mm tapes.

3.4.2 Central electron datasets

From the full set of Stream A output, events passing Level 3 electron triggers are selected, and for these events, high-level event information (about 30 kilobytes per event) is extracted and written to disk at Fermilab [60]. The data on disk are divided (non-exclusively) into three data sets: 497446 inclusive electron events, 232909 W electron events, and 282181 Z electron events.

Running on Fermilab computers for 2–3 days, we reduce these three data sets to 1.2 kilobytes per event, keeping all events. The reduced data sets, containing information about electrons, muons, tracks, vertices, $\not{E}_T$, trigger decisions, etc., are stored in Berkeley, where they are repeatedly analyzed to extract summary information, at a cost of several minutes per iteration.

---

[14] Since high-energy physics data are naturally divided into events, which in nearly all HEP computing tasks are treated independently (except for statistical summary information), HEP computing can almost always be sped up linearly with parallel processing.

[15] The offline reconstruction also writes a version of the output that contains only the compact, high-level quantities, without the raw data.

3.4.3 Inferred electron and neutrino momenta

Electron energy

Because CEM electrons deposit 80–100% of their energy in a single tower, nearly all of which is deposited in a single wedge, the clustering algorithm used for CEM electrons is straightforward. A CEM electron (or photon) cluster comprises a seed tower (the tower containing most of the energy) and the two neighboring ("shoulder") towers in η.[16] The search for seed towers proceeds sequentially through the 48 CEM wedges. In each wedge, towers with CEM energy above a 3 GeV threshold are sorted by energy. If any such towers are found, the one with highest energy forms a seed; the seed's shoulder tower(s) are marked ineligible to become seed towers; and the search through the wedge continues in decreasing order by energy. The electron energy is the sum of the energies in the seed tower and its shoulder tower(s). Because light transmitted to each light guide decreases exponentially with distance, each CEM tower energy is computed from the geometric mean of the two phototube pulse heights for that tower. Corrections to this energy are noted below.

By design, the CEM minimizes azimuthal leakage of electron showers. Thus, reconstructed electron energies never include energy deposited in neighboring wedges. The test-beam response map and in-situ calibration procedure (described in Section 3.4.6) account on average for leakage by flattening electron response over the entire fiducial region of a wedge.

Electron direction vector

All CTC tracks[17] are extrapolated to the calorimeter to determine whether they impact any of the electron cluster's towers. The number of such tracks, called N_{3D}, is stored for possible use as an electron identification variable. If $N_{3D} = 0$, the cluster is not considered an electron candidate in this measurement. Otherwise, the highest-p_T track impacting the electron cluster is deemed "the electron track." The electron track's helix parameters (without any beamline or vertex constraints) then define the electron direction: $\vec{E} = \frac{E}{\sqrt{1+\cot^2\theta}}(\cos\phi_0, \sin\phi_0, \cot\theta)$.

---

[16] If the seed tower is the inner ($|\eta| \approx 0.06$) or outer ($|\eta| \approx 1.0$) tower of a wedge, then only one shoulder tower is included.

[17] Actually only tracks for which the CTC finds and uses both axial and stereo hit data, so that all five helix parameters are determined.

Recoil energy, ΣE_T, and $\not{E}_T$

We define the recoil energy vector $\vec{u}$ and the total transverse energy ΣE_T as vector and scalar sums of tower transverse energies:

$$\vec{u} = \sum_i E_i \sin\theta_i (\cos\phi_i, \sin\phi_i)$$

$$\Sigma E_T = \sum_i E_i \sin\theta_i$$

where i indexes all towers of all calorimeters, out to $|\eta| < 3.6$.[18] Towers with total energies below thresholds of $(100, 150, 200, 185, 445, 730)$ MeV in the (CEM, PEM, FEM, CHA/WHA, PHA, FHA) are excluded from the sum. For each tower i, $\sin\theta_i$ is computed using the z-vertex closest to the electron track, or using the electron track z_0 if there is no z-vertex within 5 cm of the electron track.[19]

The electron seed and shoulder towers, as well as the CHA/WHA towers behind them, are excluded from the sum. If the shower has $|x_{\text{CES}}| > 6$ cm,[20] then the azimuthal neighbors of the seed and shoulder towers are also excluded. Energies in excluded towers are replaced by an average value of approximately 30 MeV per tower.[21] If there are multiple electron candidates, then $\vec{u}$ and ΣE_T are computed with both one and two electrons subtracted. When we select W candidates, we use $\vec{u}$ and ΣE_T with one electron subtracted; when we select Z candidates, we use $\vec{u}$ and ΣE_T with two electrons subtracted.

In W events, we compute $\vec{\not{E}}_T = -(\vec{E}_T + \vec{u})$.

3.4.4 Fiducial requirements

Because CDF calorimetry is designed with a tower geometry projecting from the origin, we impose a z-vertex fiducial cut at 60 cm (about 2σ) to limit the range of angles at which particles impact the calorimeter.

Because the outer layers of the CTC have the lowest occupancy, the best resolution, and the largest weight in determining p_T,[22] we impose a fiducial cut at the outer CTC superlayer: We require that $|z| < 150$ cm when the track reaches a radius of 130 cm.

CDF has a standard set of CEM electron fiducial criteria, designed to eliminate known regions of poor response, and codified in a software library procedure called

---

[18] The sum does not extend to $|\eta| < 4.2$ because the azimuthal symmetry of the last six η annuli of the FEM is broken by the presence of accelerator quadrupole magnets.

[19] If there are several electrons, we use the central electron with the largest transverse energy.

[20] in CES local coordinates, in which x is an azimuthal coordinate centered within a tower

[21] for EM and hadron summed, not individually

[22] if the track is constrained to originate at the beamline

FIDELE. The procedure rejects $|x_{CES}| > 21$ cm to avoid azimuthal boundaries, rejects $|z_{CES}| < 9$ cm to avoid the $90°$ region, rejects the outermost tower in the chimney wedge, and rejects the outermost tower (the $|\eta| \approx 1.0$ tower) in other wedges.

We note that the W mass analysis tightens the $|x|$ cut to 18 cm and the $|z|$ cut to 12 cm, to stay even farther away from wedge boundaries. We discuss only the $|x|$ cut because it is a larger effect on the acceptance (14% vs. 1.5%). Figure 3.6 shows test beam response [61, 62] for 50 GeV electrons near the azimuthal boundary of a wedge. The steep drop in response clearly occurs outside of the standard fiducial region $|x| < 21$ cm. We also observe that the E/p resolution is 4.98% for $|x| < 18$ and 5.15% for $18 < |x| < 21$, which implies (after subtracting out the p resolution) that the E resolution is only about 10% worse for $18 < |x| < 21$ than for $|x| < 18$. Thus, we believe that the usual fiducial cuts are adequate for this measurement. When we refer hereafter to the CEM fiducial volume, we mean the CDF standard fiducial volume, not the W mass modified fiducial volume.
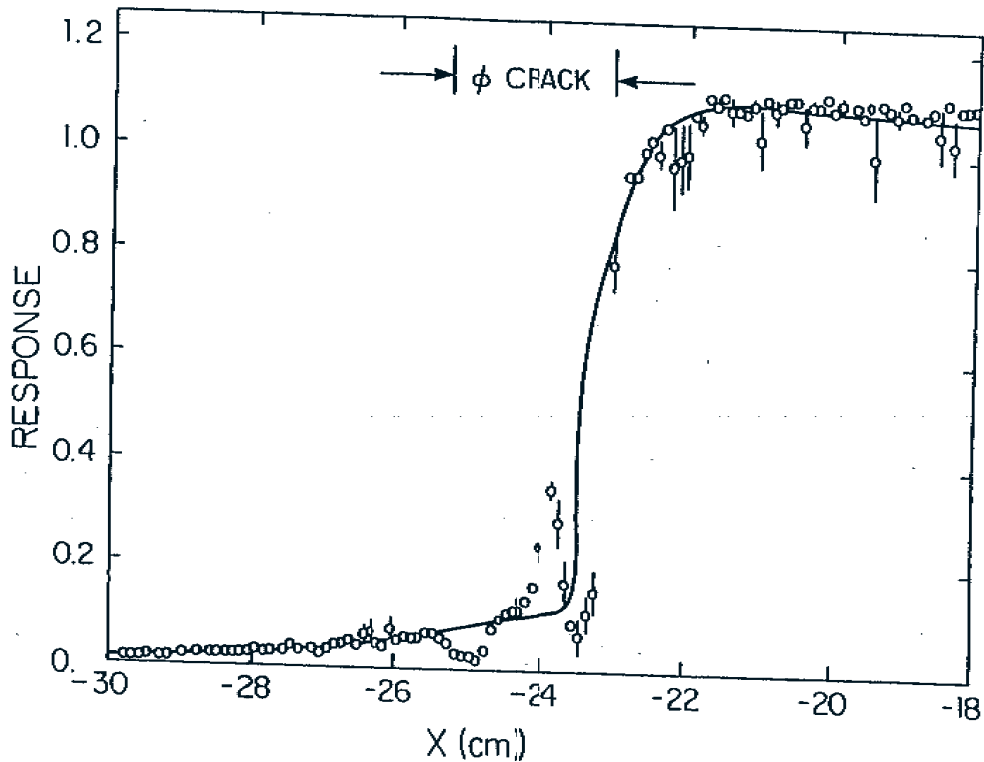
Figure 3.6: CEM ϕ crack response in test beam.

3.4.5 Electron identification

We use several electron identification variables to separate W and Z electrons from multijet backgrounds. The figures in Chapter 4 demonstrate that these variables are highly effective.

Since hadrons typically interact later in the calorimeter than electrons, the ratio $E_{\text{hadron}}/E_{\text{EM}}$ of hadron calorimeter energy (summed over the towers behind the CEM seed and shoulder towers) to electromagnetic calorimeter energy can be used to purify an electron sample. Because the depth at which a high-energy electron or photon deposits its energy increases slowly (logarithmically) with energy, we impose an energy-dependent cut: $E_{\text{hadron}}/E_{\text{EM}} < 0.055 + 0.045 \frac{E}{100 \text{ GeV}}$. This requirement has been demonstrated [63] to have high efficiency for test beam electrons over a wide range of energies.

Jets that appear to be electrons because a $\pi^{\pm}$ leaves a charged track and an overlapping π^0 leaves an electromagnetic shower can be suppressed by requiring a good position match between the track and the shower. We require the shower z position, measured with CES cathode strip data, and CTC track position to match within 5 cm. This is not a very stringent requirement: The rms mismatch for W electrons is 0.46 cm. A similar requirement can be imposed in the azimuthal (x) view, using the CES anode wire data, but we avoid this requirement for two reasons: First, the (charge-weighted) Δx distribution can be pulled away from zero by bremsstrahlung, since electrons bend in the magnetic field while photons do not; second, each wire channel spans five towers in η, so the wire data can be sensitive to the presence of underlying event particles in towers well outside of the electron cluster.

Eleven CES cathode channels, centered on the electron shower, are clustered to determine the shower z position discussed above. The distribution of pulse heights within these channels can be compared with test beam profiles. The quantity χ_s^2 is a measure of consistency between the observed shower and a test beam electron shower. We require $\chi_s^2 < 20$. A corresponding CES anode variable, χ_w^2, is available, but we do not use it, for the same reasons that we do not use the CES $|\Delta x|$ variable.

We define a track isolation variable N_{cone}[23] as the number of tracks of (un-constrained) $p_T > 1$ GeV that lie in a cone $\Delta R < 0.25$[24] around the electron track and have z_0 within 5 cm of the electron's z vertex. A related variable that is sometimes used is N_{3D}, mentioned in Section 3.4.3; we prefer the N_{cone} variable because it rejects more background while preserving more signal, as one can infer from the numbers in Table 5.2. The N_{cone} variable is the basis of the dijet background determination in Section 6.2.2.

---

[23] We thank David Saltzberg for suggesting the N_{cone} variable.
[24] ΔR is $\sqrt{(\Delta\eta)^2 + (\Delta\phi)^2}$.

Ref. [64] contains an excellent description of many electron identification variables used in CDF.

3.4.6 Corrections applied to the data

The CTC and CEM are complementary in many ways. The CEM measures a quantity proportional to momentum, while the CTC measures the reciprocal of momentum. The CEM is charge symmetric, while the CTC is not. CTC response is relatively uniform over a large area, while CEM response can vary tower by tower. CTC cells are much smaller than CEM wedges, so CEM and CTC position-dependent systematic effects tend to be easily separated. For these reasons, the quantity E/p—the ratio of CEM energy to CTC momentum—is an important ingredient in the calibration of both the CEM and the CTC.

As we discuss in Appendix D, systematic effects in the CEM tend to produce errors of the form $E \rightarrow E^{\text{true}}(1 + \epsilon)$ (independent of charge) while CTC wire-position offsets tend to produce charge-dependent errors of the form $p_T \rightarrow p_T^{\text{true}}(1 + q\epsilon)$.[25] Thus, the CEM is used to align the CTC (by subtracting E/p for positives and negatives), and the CTC is used to calibrate the CEM (by averaging E/p for positives and negatives).

Track-level CTC corrections

By comparing E/p for positive and negative electrons as a function of ϕ_0, z_0, and $\cot\theta$, the following track-level CTC alignment corrections are derived [65, 66]:

$$\frac{q}{p_T^{\text{BC}}} \rightarrow \frac{q}{p_T^{\text{BC}}} \quad - \quad 0.000056$$
$$- \quad 0.00040 \, \sin(\phi_0 - 3.0)$$
$$- \quad 0.00028 \, (\cot\theta + z_0/81.3 \text{ cm})$$

where p_T^{BC} is beam-constrained transverse momentum in GeV. Physically, the constant term and $\cot\theta$- and z_0-dependent terms correspond to separate distortions of the east and west CTC endplates (illustrated in Appendix D), while the ϕ-dependent term may correspond to a displacement of the SVX—and hence the SVX-derived beamline—with respect to the CTC axis. We correct p_T^{BC} in this way, but we note that p_T^{BC} has very limited use in this measurement: We require $p_T^{\text{BC}} > 15$ GeV in W, Z, and inclusive electron selection in Chapter 4, and we use p_T^{BC} in calculating masses when we eliminate $Z \rightarrow ee$ events from the W sample in Section 6.1.1. In Appendix D, we verify the numerical magnitudes of these corrections, investigate their origin in terms of CTC geometry, and show that they can be handled much more cleanly if CTC hit data are available.

---

[25] Momentum scale errors are a separate issue, investigated with a large $J/\psi \rightarrow \mu\mu$ sample.

CEM calibration

After CTC momenta are corrected as described above, E/p is used to remove systematic effects in CEM measurements [65], using both the W electrons and a large sample of low-energy ($E_T > 8$ GeV) inclusive electrons. The basic strategy is to plot the mean of E/p in the window $0.8 < E/p < 1.25$ against variables in which one expects to find systematic effects. The 1994-95 run is divided into four time periods, two of which are bounded by long accelerator shutdowns. Within each of these periods, a relative gain factor is derived for each of the 478 CEM towers, with a statistical precision of 0.3–0.7% (depending on time period) for towers in the fiducial volume.[26] An arch-dependent linear slope in time is also derived for each time period. Time-independent corrections are derived within each wedge as a function of x_{CES} and z_{CES}.

Before the corrections derived from the data are applied, a response map derived from test beam electrons [61, 62] is applied. Whereas tower energies are derived from the geometric mean of the two phototube pulse heights in the $p\bar{p}$ data, tower energies in the test beam data were derived from the arithmetic mean; the test beam response map is thus corrected by a factor $\cosh(x_{\mathrm{CES}}/\lambda)$, where $\lambda \approx 80$ cm is the scintillator attentuation length.

If these corrections (map and calibration combined) were not applied, the CEM constant term would increase from 1.5% to about 4.5%.

---

[26] The rms tower-to-tower correction is about 2.5%.

Chapter 4

Event Selection

This analysis employs three electron-based data sets, selected from three groups of Level-3 central-electron triggers. We use a sample of 2206 $Z \to ee$ candidates to constrain a theoretical model of W and Z p_T spectra and to map out the calorimeter response to hadrons recoiling against the boson p_T; a 2012-event subset of these Z candidates is used to measure the calorimeter response to high-p_T electrons. We use a sample of 127040 electron candidate events, with no $\not{E}_T$ requirement, to model multijet events that can mimic the $W \to e\nu$ signature. Finally, we use a sample of 49843 $W \to e\nu$ candidate events to measure , $_W$.

While the W and Z samples do not overlap, the inclusive electron sample contains 99.5% of the events in the $Z \to ee$ sample and 95.3% of the events in the $W \to e\nu$ sample.[1]

The W and Z selection criteria in this analysis are, by design, similar to those of the CDF W mass analysis [00], with two significant exceptions. First, because this measurement is statistically limited, we use the standard CDF electron fiducial criteria (discussed in Section 3.4.4), rather than the more restrictive W mass fiducial cuts, which would force us to discard 14% of the W sample and 27% of the Z sample. Second, because this measurement studies the tail of the W signal region, we impose more stringent electron ID requirements to keep multijet backgrounds as small as possible. The general similarity between the two analyses provides a number of consistency checks, which we exploit throughout this dissertation.

4.1 $Z \to ee$ candidate selection

Table 4.1 lists the $Z \to ee$ selection criteria. We start from the 282182-event Run Ib EZA dataset described in Section 3.4.2. We keep only runs in which the detector

---

[1]A $Z \to ee$ event has two chances to pass the inclusive trigger's electron-identification requirements, while a $W \to e\nu$ event has only one.

	Cut	# pass	% fail	if last
A	Run Ib Z electron dataset	282181	—	—
B	No known detector problems	273377	3.1	2.8
C	Passes any $Z \to ee$ trigger	273141	0.09	0.0
D	Passes central electron Z trigger	213344	21.9	0.0
E	Central electron reconstructed	213341	0.001	—
F	First electron in CEM fiducial volume	197151	7.6	7.7
G	$E_T > 25$ GeV	153235	22.3	0.5
H	Electron track $p_T^{\mathrm{BC}} > 15$ GeV	89022	41.9	4.0
I	z-vertex in fiducial region	80710	9.3	4.5
J	CTC fiducial volume	78377	2.9	2.4
K	Second CEM electron candidate exists	40755	48.0	—
L	Second electron in CEM fiducial volume	37349	8.4	6.7
M	$E_T > 25$ GeV	28549	23.6	0.3
N	Electron track $p_T^{\mathrm{BC}} > 15$ GeV	10862	38.0	3.3
O	CTC fiducial volume	10571	2.9	2.5
P	$|z_0^{\mathrm{ele1}} - z_0^{\mathrm{ele2}}| < 5$ cm	9934	6.0	0.6
Q	$\cos(\phi_0^{\mathrm{ele1}} - \phi_0^{\mathrm{ele2}}) < 0.95$	9356	5.8	0.0
R	70 GeV $< M^{ee} < 110$ GeV	5515	41.1	5.5
S	$p_T^{ee} < 50$ GeV	5320	3.5	3.0
T	Tracks have opposite electric charge	3849	27.7	0.05
U	Identification cuts, first electron	2206	42.7	8.5
V	Identification cuts, second electron	2012	8.9	8.9

Table 4.1: $Z \to ee$ candidate events passing successive selection criteria. The last column gives the fraction (%) of events failing a given cut if that cut is applied after all other cuts. Electron ID cuts are detailed in Tables 4.2 and 4.3.

	Cut	# pass	% fail	if last
A	Table 4.1, lines A–S	5320	—	—
B	$E_{\mathrm{hadron}}/E_{\mathrm{EM}}$ consistent with electron	2823	46.9	1.3
C	Track/CEM position match (z-view)	2715	3.8	0.1
D	Transverse shower shape (z-view)	2499	8.0	1.8
E	Electron track is isolated	2214	11.1	8.3
F	Tracks have opposite charge	2206	0.4	0.4

Table 4.2: $Z \to ee$ candidate events passing successive electron ID cuts applied to first electron. (The electrons are ordered randomly.) The last column gives the fraction (%) of events failing a given cut if that cut is applied after all other cuts. See Section 3.4.5 for definitions of the electron ID variables.

39

	Cut	# pass	% fail	if last
A	Table 4.2, lines A–E	2214	—	—
B	$E_{\mathrm{hadron}}/E_{\mathrm{EM}}$ consistent with electron	2171	1.9	1.3
C	Track/CEM position match (z-view)	2169	0.1	0.1
D	Transverse shower shape (z-view)	2134	1.6	1.5
E	Electron track is isolated	2013	5.7	5.6
F	Tracks have opposite charge	2012	0.05	0.05

Table 4.3: $Z \to ee$ candidate events passing successive electron ID cuts applied to second electron. The last column gives the fraction (%) of events failing a given cut if that cut is applied after all other cuts.

and trigger were believed to be in good working order, then verify that each event in fact passes one of the EZA Level-3 triggers. We next look specifically for a CEM electron trigger, and check that events contain a central electron candidate. If an event contains two central electron candidates, we select one of them at random to be labeled "the first electron."

We require the first electron to be in the CEM fiducial volume, as described in Section 3.4.4. Using the energy measured in the CEM and the trajectory measured in the CTC, and applying the corrections described in Section 3.4.6, we define the electron energy vector $\vec{E}$ and require $E_T > 25$ GeV, which exceeds the Level-3 trigger threshold by about four times the CEM resolution. We next require p_T^{BC}, measured by the CTC, to exceed 15 GeV, which exceeds the Level-3 $p_T > 13$ GeV requirement by several times the p_T resolution. We also impose fiducial-volume cuts at the beamline and at the outer radius of the CTC, as described in Section 3.4.4.

We then look for a second central electron and impose the same E_T, p_T^{BC}, and CEM and CTC fiducial requirements. Since two electrons from Z decay must originate from the same point at the beamline, we check that the electrons were constrained to the same z-vertex, or to two z-vertices less than 5 cm apart.[2]

To eliminate a class of background events in which the reconstruction software finds two electron candidates in a single electromagnetic jet, we require the two electrons to be separated by at least $18.2°$ in azimuth ($\cos \Delta\phi < 0.95$); since in these events the same track is often assigned to both electron candidates, it is convenient to remove them before calculating M^{ee}. Figure 4.1 shows the distribution of dielectron invariant mass, M^{ee}, for events passing the above cuts. We require 70 GeV $< M^{ee} <$ 110 GeV; the $Z \to ee$ resonance (, $_Z = 2.49$ GeV) is well contained within this window. Because this measurement studies low-p_T Z and W events, which are qualitatively different from the $Z, W +$ jets events found at high p_T, we require $p_T^{ee} < 50$ GeV.[3]

5320 events satisfy these selection criteria. In 3849 of these events, the two electrons have opposite charge; using the like-sign pairs as an estimate of dijet backgrounds, we estimate that about 40% of the 3849 opposite-sign events are dijet background. Figure 4.2 shows M^{ee} distributions for opposite-sign and like-sign pairs after this initial $Z \to ee$ selection.

Up to this point, we define "electron candidate" very loosely, as a high-E_T

---

[2] About 2.5% of events in the final sample have $0 < |\Delta z_{\mathrm{vertex}}| < 5$ cm. They are strongly peaked near M_Z, hence not background. This sample of events has a significantly high average luminosity and a significantly low average number of stereo hits per track. Since there is no corresponding cut to make in the W sample, we choose not to require $\Delta z_{\mathrm{vertex}} = 0$.

[3] The recoil energy $\vec{u}$ in a low-p_T Z or W event resembles a minimum-bias event, whereas collimated jets recoil against high-p_T Z and W bosons. This measurement's resolution model (described in Section 5.5) exploits the similarity with minimum-bias events. (In W events, we require $u < 20$ GeV.)
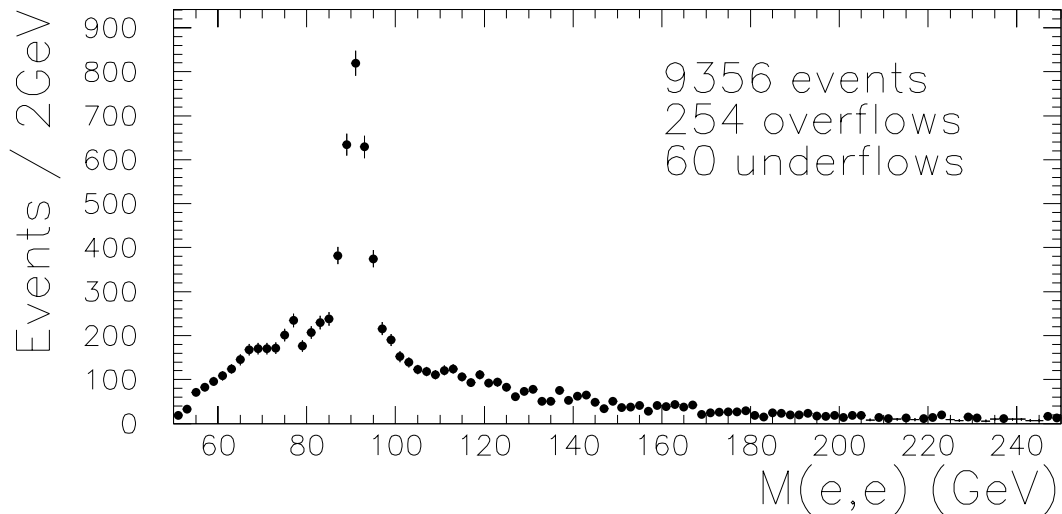
Figure 4.1: M^{ee} spectrum after minimal event selection (Table 4.1, lines A–Q).
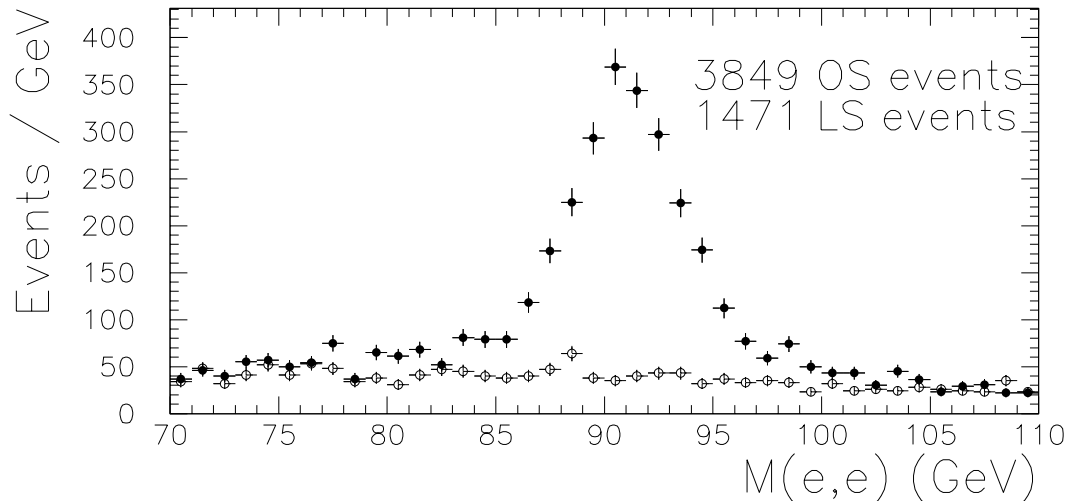
Figure 4.2: M^{ee} spectra (opposite sign, solid points; like sign, open points) before electron ID requirements (Table 4.1, lines A–S).

electromagnetic shower having $E_{\mathrm{hadron}}/E_{\mathrm{EM}} < 0.125^{(4)}$ and an associated high-p_{T} track. As a result, we observe an unacceptably high background rate.

As detailed in Table 4.2, we next impose on the first electron the identification criteria described in Section 3.4.5, after which 2206 opposite-sign and 8 like-sign events remain. The estimated opposite-sign background fraction, LS/OS, is 0.4%— two orders of magnitude lower than the 40% before the ID cuts. We will refer to the 2206 opposite-sign events as "the $Z \to ee$ sample." Figure 4.3 shows the M^{ee}

$^{(4)}$Implicit in the reconstruction software's definition of electron candidate, and applied in the Level-2 trigger hardware.

spectrum for this sample.
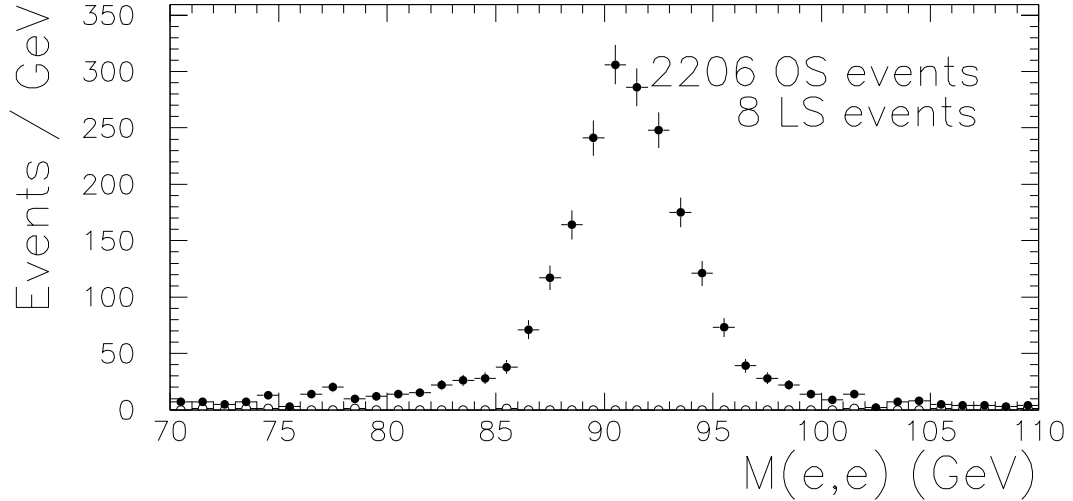
Figure 4.3: M^{ee} spectra (opposite sign, solid points; like sign, open points) after electron ID requirements on one leg (Table 4.1, lines A–U).

Imposing electron identification criteria on the second electron, as detailed in Table 4.3, improves the estimated signal-to-background by another order of magnitude, leaving 2012 opposite-sign events and only one like-sign event—hence an estimated 0.05% background fraction. We will refer to the 2012 opposite-sign events as "the tight $Z \to ee$ sample." Figure 4.4 shows the M^{ee} spectrum for this sample.
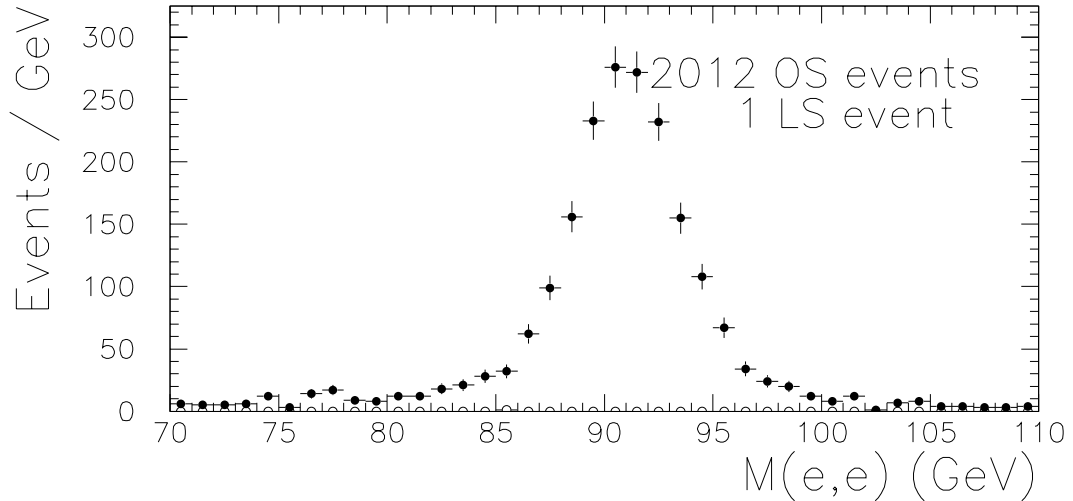
Figure 4.4: M^{ee} spectra (opposite sign, solid points; like sign, open points) after electron ID requirements on both legs (Table 4.1, lines A–V).

	Cut	# pass	% fail	if last
A	Run Ib inclusive central electron dataset	497446	—	—
B	No known detector problems	482763	3.0	2.9
C	Passes either CEM inclusive electron trigger	482707	0.01	—
D	Passes 18 GeV CEM inclusive electron trigger	426923	11.6	2.4
E	Central electron found by reconstruction software	426922	0.0002	—
F	Electron in CEM fiducial volume	379962	11.0	9.8
G	$E_T > 25$ GeV	175450	53.8	50.1
H	Electron track $p_T^{\mathrm{BC}} > 15$ GeV	159481	9.1	5.9
I	z-vertex in fiducial region	150705	5.5	5.3
J	CTC fiducial volume	147508	2.1	2.1
K	CTC impact parameter < 0.5 cm	145982	1.0	0.8
L	$Z \to ee$ removal	140896	3.5	3.7
M	$E_{\mathrm{hadron}}/E_{\mathrm{EM}}$ consistent with electron	128126	9.1	8.8
N	Track/CEM position match (z-view)	127096	0.8	0.8
O	Transverse shower shape (z-view)	127040	0.04	0.04

Table 4.4: Inclusive electron events passing successive selection cuts. The last column gives the fraction (%) of events failing a given cut if that cut is applied after all other cuts.

4.2   Inclusive electron candidate selection

Table 4.4 lists the selection criteria for the inclusive electron sample used to study multijet backgrounds. We start from the 497446-event Run Ib EIA dataset described in Section 3.4.2. We eliminate runs with known detector problems, verify that the event passes the inclusive electron trigger, and look for a central electron candidate. If several central electron candidates are found, we choose the one with highest E_T.

The selection continues in parallel with the $W \to e\nu$ candidate selection described below, except that the $\not{E}_T$, u, track isolation, and $M_T < 200$ GeV requirements are not imposed. Figure 4.5 shows the $\not{E}_T$ spectrum for the 127041 surviving events.

4.3 $W \to e\nu$ candidate selection

Table 4.5 lists the $W \to e\nu$ selection criteria. We start from the 232909-event Run Ib EWA dataset described in Section 3.4.2. We eliminate runs with known detector problems, verify that the event passes the $W \to e\nu$ trigger, and look for a central electron candidate. If several central electron candidates are found, we choose the one with highest E_T.

	Cut	# pass	% fail	if last
A	Run Ib W central electron dataset	232909	—	—
B	No known detector problems	225402	3.2	2.9
C	Passes CEM $W \to e\nu$ trigger	225051	0.16	0.0
D	Central electron found by reconstruction software	225048	0.001	—
E	Electron in CEM fiducial volume	201995	10.2	8.2
F	$E_T > 25$ GeV	187249	7.3	4.1
G	Electron track $p_T^{\mathrm{BC}} > 15$ GeV	118870	36.5	4.2
H	z-vertex in fiducial region	105338	11.4	5.6
I	CTC fiducial volume	103030	2.2	2.5
J	$\not{E}_T > 25$ GeV	70143	31.9	5.1
K	$u < 20$ GeV	58182	17.1	8.3
L	CTC impact parameter < 0.5 cm	57900	0.5	0.2
M	$Z \to ee$ removal	57201	1.2	1.2
N	$E_{\mathrm{hadron}}/E_{\mathrm{EM}}$ consistent with electron	55741	2.6	1.0
O	Track/CEM position match (z-view)	54813	1.7	1.0
P	Transverse shower shape (z-view)	53643	2.1	1.4
Q	Electron track is isolated	49851	7.1	7.1
R	$M_T < 200$ GeV	49843	0.02	0.02

Table 4.5: $W \to e\nu$ candidate events passing successive selection cuts. The last column gives the fraction (%) of events failing a given cut if that cut is applied after all other cuts.
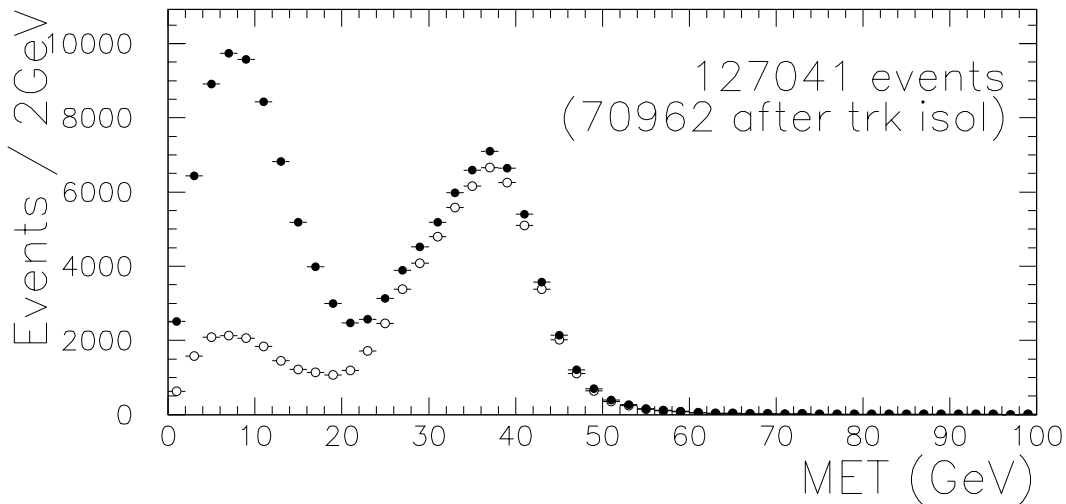
Figure 4.5: The solid points show the $\not{E}_T$ spectrum for inclusive electrons passing cuts A–O in Table 4.4. The W peak near $\frac{1}{2}M_W$ is prominent; multijet background peaks at low $\not{E}_T$. For comparison, the open points show the $\not{E}_T$ spectrum for the subset of these events in which the electron track is isolated.

We impose fiducial cuts and require $E_T > 25$ GeV, $p_T^{\mathrm{BC}} > 15$ GeV. We compute the recoil transverse energy vector $\vec{u}$, as described in Section 3.4.3, define $\vec{\not{E}}_T = -(\vec{E_T} + \vec{u})$, and require $\not{E}_T > 25$ GeV, $u < 20$ GeV. The E_T, p_T^{BC}, and $\not{E}_T$ cuts are selected to be several resolutions above the trigger thresholds. As shown in Figure 4.6, the u cut reduces multijet backgrounds substantially, while preserving about 90% of W signal; in addition, the transverse mass resolution is much better at low u. To reject cosmic rays, we require the electron track to pass within 0.5 cm of the beamline. We reject $Z \to ee$ decays in which one electron lands in a region of low calorimeter response, by searching for a second high-p_T track that can be combined with the first electron to make a mass near M_Z. Finally, to reduce multijet backgrounds, we impose the electron identification cuts described in Section 3.4.5. 49851 events remain, of which 49843 have $M_T < 200$ GeV. Figure 4.7 plots $M_T(e, \nu)$ for this sample, and Figure 4.8 is a graphical display of an event satisfying all criteria.

4.4 Checks of $W \to e\nu$ event selection

We perform checks of the rejection rates of most of the requirements imposed on $W \to e\nu$ candidates, to ensure that each step of the selection is well understood. These checks are summarized in Table 4.6 and described below.

We simulate $W \to e\nu$ events using the CDF detector simulation program QFL, as described in Chapter 5, to predict inefficiencies for all fiducial requirements, the p_T^{BC} cut, and the Z-removal procedure. The larger z-vertex inefficiency in the data is expected, because the actual z-vertex distribution has longer tails than a Gaussian

46

Cut	data % fail	% predict	how
CEM fiducial volume	8.2	6.7	simulation
$E_T > 25$ GeV	4.1	—	Figure 5.23
$p_T^{\mathrm{BC}} > 15$ GeV	4.2	3.8	simulation
z-vertex fiducial volume	5.6	2.4	simulation
CTC fiducial volume	2.5	2.6	simulation
$\not{E}_T > 25$ GeV	5.0	—	Figure 5.23
$u < 20$ GeV	8.3	8.2	Z data+sim+bkg
CTC impact parameter	0.2	0.2	Z data
Z removal	1.2	1.1	simulation
$E_{\mathrm{hadron}}/E_{\mathrm{EM}}$	1.0	1.3	Z data
$\Delta z_{\mathrm{track,CES}}$	1.0	0.1	Z data
transverse shower profile	1.4	1.5	Z data
track isolation cut	7.1	7.3	W data+sim+bkg

Table 4.6: Comparison of cut failure rates in data (for each cut if it is applied after all others) with expectations.

distribution. The 94.4% efficiency we observe for $|z\text{-vertex}| < 60$ cm is consistent with $95.6 \pm 1.0\%$ found in Ref. [49].[5]

While we do not explicitly calculate the number of events expected to fail the E_T or $\not{E}_T$ cuts, we note (see Figure 5.23) that the E_T and $\not{E}_T$ shapes are modeled well by the simulation, even near 25 GeV.

We use the $Z \to ee$ data to check inefficiencies of the CTC impact parameter, $E_{\text{hadron}}/E_{\text{EM}}$, $\Delta z_{\text{track,CES}}$, and transverse shower profile criteria. We find disagreement only in the $\Delta z_{\text{track,CES}}$ cut. We believe that most of these events are caused by CTC mismeasurements in the r-z view: relaxing the $|z_0^{\text{ele1}} - z_0^{\text{ele2}}|$ requirement in the $Z \to ee$ selection raises the $\Delta z_{\text{track,CES}}$ inefficiency in $Z \to ee$ events to 0.8%.

We check the u requirement using a combination of Z data, simulation, and background shape prediction, as follows. Since the W and Z p_T spectra are not identical, we use the Z data (without the $p_T < 50$ GeV cut) only to predict that the $u > 35$ GeV fraction is 3.3%. Then we use the W simulation (which only generates $p_T < 50$ GeV) to predict that 20 GeV $< u < 35$ GeV is 4.75% of $u < 35$ GeV, and combine to obtain 7.9%. Finally, we account for an estimated 450 multijet background events, about half of which have $u > 20$ GeV, to obtain 8.4%, in good agreement with 8.3% seen in the data.

The track isolation requirement rejects 7.1% of data events. We expect a 4.8% inefficiency for real W events, as described in Section 5.3. From Table 6.2, we expect about three background events to fail the track isolation cut for every one that passes, and from Table 6.3, we expect 450 ± 110 dijet background events that pass. Thus, we predict a $\frac{3 \times 450}{49843} = 2.7 \pm 0.7\%$ rate of track isolation failures due to backgrounds. Averaging 75% inefficiency for $4 \times 450 = 1800$ multijet background events with 4.8% inefficiency for the remaining $49843 - 450 = 48043$ events, we predict $7.3 \pm 0.7\%$, in good agreement with the observed rate. The predicted contribution from tridents (bremsstrahlung photons that produce e^+e^- pairs) alone rises from 1.3% at $E_T \approx 40$ GeV to 2.5% at $E_T \approx 100$ GeV.

---

[5]For a detailed comparison of CEM fiducial cut failures in data and in QFL, see Table A.1 in Appendix A.
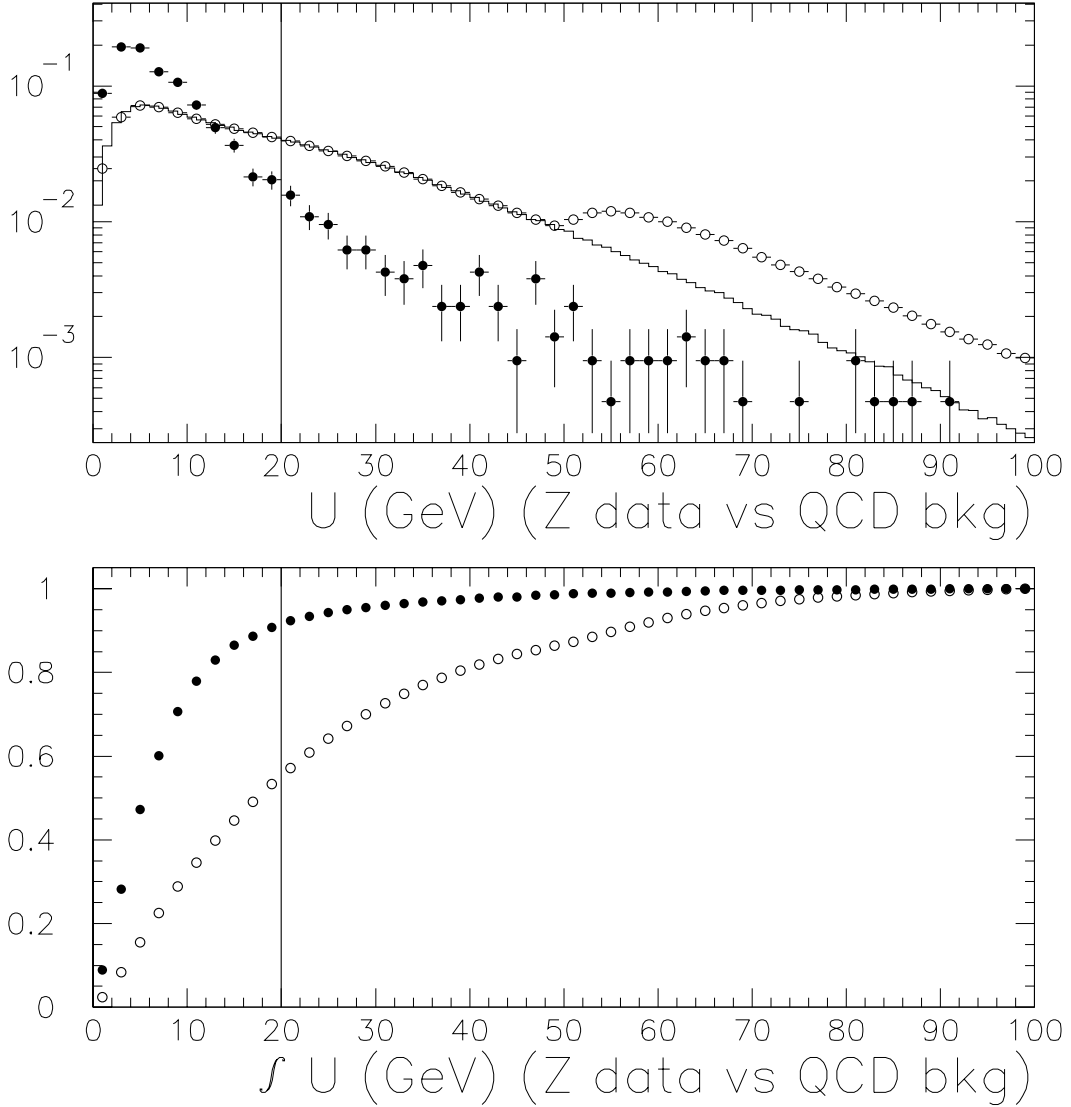
Figure 4.6: (Top) Distributions of recoil energy (u) for $Z \to ee$ data (solid points), whose p_T spectrum is similar to that of W events, and for a background sample of photon conversion data (open points). (Note logarithmic y-axis.) Both distributions are normalized to unity. The structure in the background shape near $u = 50$ GeV is a result of the $E_T > 25$ GeV and $\not{E}_T > 25$ GeV cuts. For $u < 50$ GeV, $\vec{E}_T$ and $\vec{\not{E}}_T$ must point in opposite directions; for $u > 50$ GeV, $\vec{E}_T$ and $\vec{\not{E}}_T$ can be either aligned or antialigned. To illustrate this point, the solid histogram shows the subset of the background for which $\vec{E}_T \cdot \vec{\not{E}}_T < 0$. (Bottom) The integrated distributions. The figure illustrates that a $u < 20$ GeV cut is useful for rejecting background while preserving about 90% of the signal in W events.
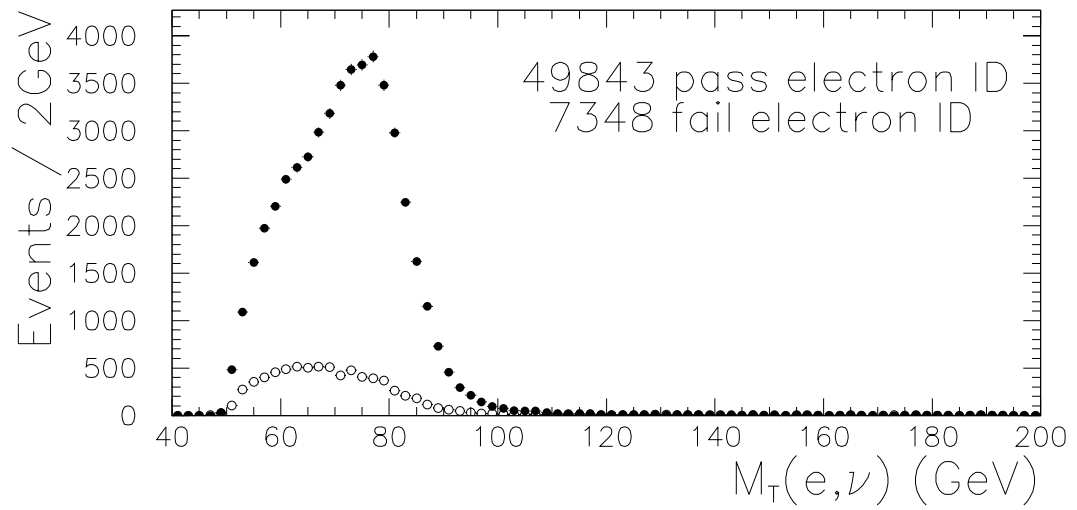
Figure 4.7: The solid points show the $M_T(e, \nu)$ spectrum for events passing all cuts in Table 4.5. For comparison, the open points show the M_T spectrum for events failing one or more of the electron ID cuts (lines N–Q).

CDF Preliminary
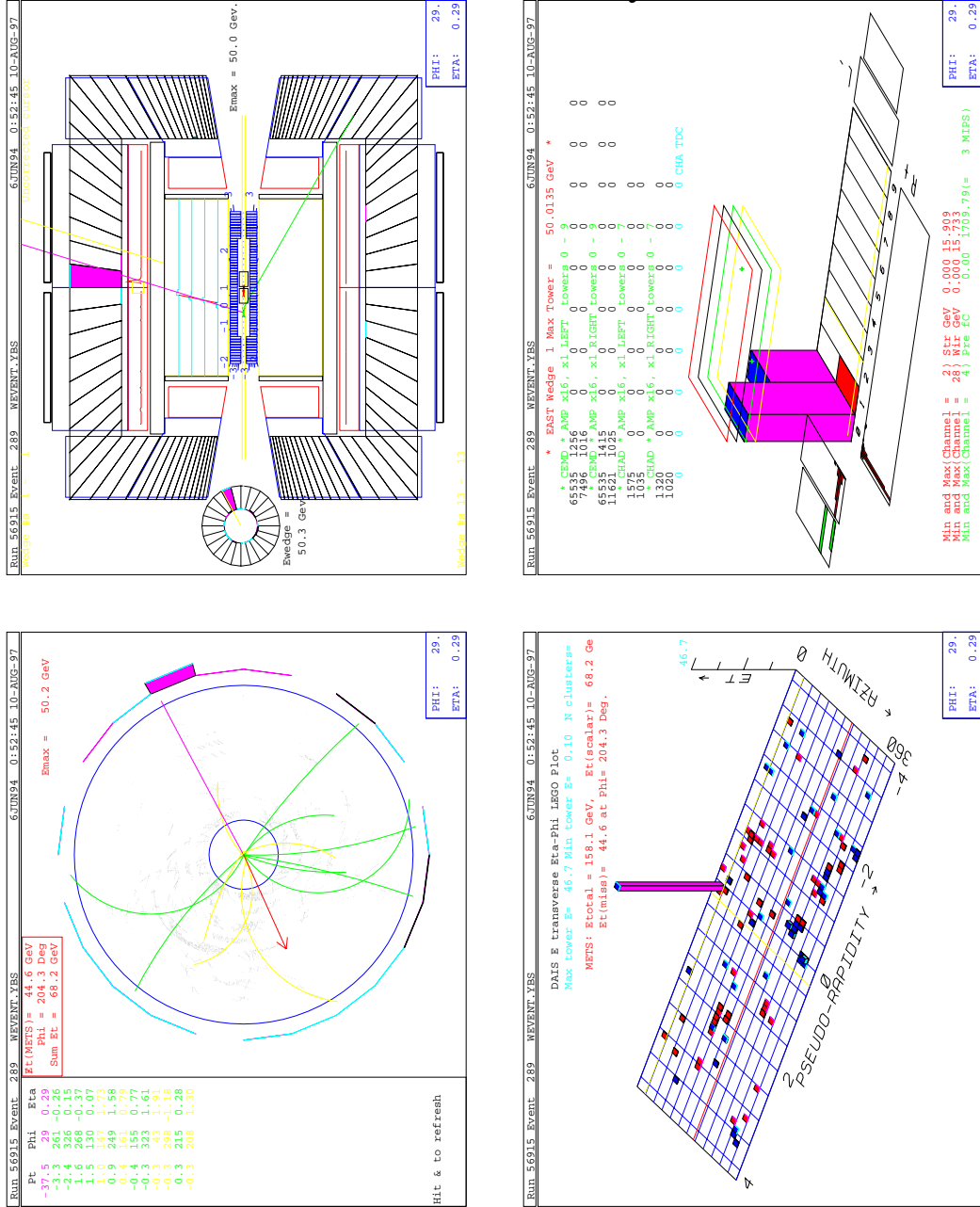
Figure 4.8: A typical event passing all cuts in Table 4.5.

51

Chapter 5

W and Z Lineshape Simulation

This analysis extracts a measured value for $, _W$ from the observed $M_T(e, \nu)$ line-shape. A crucial component in such an analysis is a prediction of the M_T distribution as a function of $, _W$. Following the standard practice of high-energy physics, we predict this spectrum using Monte Carlo methods.

We need several ingredients to model the M_T lineshape. We must generate W bosons with correct distributions of (in general off-shell) mass, longitudinal momentum, polarization, and transverse momentum, and decay them properly, including radiative decays $W \to e\nu\gamma$. We must then place each event into the CDF detector, modeling the spread in z of $\overline{p}p$ collisions, and trace the initial-state particles through the detector, simulating the detector's response to electrons, photons, and recoiling hadrons. The kinematic and geometric acceptance cuts applied to the data must be applied consistently to simulated events. Finally, contributions of important background processes must be included in the spectra.

We describe these ingredients below in more detail.

5.1 Event generation

The first stage of the Monte Carlo calculation, called "event generation," produces a list of initial-state particles—electrons, positrons, photons, and neutrinos—and their true, unsmeared momenta.

We use a zeroth-order $(p_T(W) = 0)$ generator, TOYGEN [67], developed by the UA2 collaboration and currently used in the CDF W mass analysis [68, 00]. TOYGEN produces weighted $\overline{p}p \to W \to e\nu\gamma$ events with boson mass $M = \sqrt{\hat{s}} = \sqrt{x_1 x_2 s}$ and rapidity $y = \mathrm{arcsinh}(\frac{p_z}{M}) = \frac{1}{2}\log(\frac{x_1}{x_2})$, with distribution

$$\frac{d\sigma}{dx_1 dx_2} \propto \sum_{ij} f_{i/p}(x_1) f_{j/\overline{p}}(x_2) \cdot |V_{ij}|^2 \cdot \frac{\hat{s}}{(\hat{s} - M_W^2)^2 + (\frac{\hat{s}\Gamma_W}{M_W})^2} \qquad (5.1)$$

where i, j sum over quark flavors and V_{ij} is the CKM matrix. For the present analysis, the most important feature of Equation 5.1 is the $\hat{s}$ dependence, which is a convolution of the "momentum-dependent" Breit-Wigner distribution[1] (the last factor in 5.1) with the falling parton luminosity (the first factor). We use the parton distribution functions (the functions $f_i(x)$) from set MRS-R2 [27].

The momenta of e, ν, γ are distributed according to a calculation by Berends and Kleiss [29]. The W is then boosted, with a new p_z chosen to preserve longitudinal rapidity $y = \frac{1}{2} \log(\frac{E+p_z}{E-p_z})$, so that its p_T distribution $\frac{dN}{dp_T dy}$ is given by the NLO Arnold-Kauffman [31] calculation, with nonperturbative (low $p_T(W)$) component parameterized by Ladinsky and Yuan [35]. A reweighting technique, described in Section 5.4.3, accounts for the variation of $\frac{dN}{dp_T}$ with $\sqrt{\hat{s}}$.

TOYGEN also generates $Z \to ee\gamma$ events, using the same calculations for radiative decay and boson p_T.

The initial states generated by TOYGEN contain only electrons, neutrinos, and photons, boosted from the W or Z rest frame to the laboratory frame. No particle-by-particle description is provided of recoil energy, initial-state gluon radiation, or additional minimum-bias events from the $p\bar{p}$ bunch crossings in which the W and Z bosons are produced. Such a particle-level description is difficult to calculate theoretically, because perturbation theory does not apply, and difficult to simulate reliably, because the detector's response to individual low-momentum hadrons is difficult to measure. Instead, we use an empirical model described below.

5.2 Detector simulation overview

Two detector simulation programs are used in this analysis. For most results, we use the SSD simulation, developed by this author and described in Appendix B. Its advantages are that it runs relatively quickly, that it is easily modified or extended, and that this author understands exactly what set of effects it simulates. We also use the standard CDF detector simulation, QFL, to perform some checks of the electron and photon simulation, and to simulate lost-Z backgrounds. The advantages of QFL are that it has been well tested by a large number of physicists and that it simulates several effects not found in SSD.[2] Where possible, we look for agreement between the simple simulation, the comprehensive simulation, and the data.

Because the generator does not produce a list of recoil particles, neither simulation directly models the effect of hadrons recoiling against the boson p_T. When using either simulation, we draw the recoil energy vector, $\vec{u}$, from a model that is tuned with minimum-bias and Z data. Given a value of the true $\vec{p}_T(W)$ vector, the

---

[1] David Saltzberg informs us that the real names behind this distribution are Matthews and Salam.

[2] Most significantly, QFL uses a more sophisticated model of calorimeter response.

model generates an observed recoil vector $\vec{u}$ from a distribution. The recoil model is described in detail in Section 5.5.

Both simulation programs output data in a format that closely resembles the format of the real data, allowing the same analysis program to process both real and simulated events. We have found that this approach eliminates an enormous number of trivial sources of error in comparing data and simulation.

All electron ID variables are simulated in QFL, while SSD simulates only the track isolation variable. Since the track isolation cut is the most stringent electron identification criterion that we apply (see Table 4.5), it is important to model it carefully. Neither simulation directly models the contribution of underlying-event particles to the track isolation variable; as described in Section 5.3, we use the W data to simulate this effect.

Estimated backgrounds from $W \rightarrow \tau\nu \rightarrow e\nu\nu$, $Z \rightarrow ee$, and QCD multijet events are added to the $M_T(e,\nu)$ spectrum by hand. Background determination is discussed in Chapter 6.

5.3 Simulating N_{cone} with W events

Since the N_{cone} track isolation variable, defined in Section 3.4.5, plays an important role in this measurement, it is useful to have a technique to model its effect on W and Z signal distributions. We consider two contributions to the N_{cone} distribution for W and Z signal: e^+e^- pair production by bremsstrahlung photons, which is modeled within both the SSD and the QFL detector simulations, and underlying event contributions, which we simulate using the "W list" technique described in this section.[3]

Figure 5.1 shows N_{cone} distributions for TOYGEN Z electrons simulated with SSD. The fraction outside the $N_{\mathrm{cone}} = 0$ bin is 1.4%. Below we will combine this information with the W list result.

For each of the 49843 events in the W sample, we write to a binary file u, $\phi(\vec{u})$, $\phi(\vec{E}_T)$; (η, ϕ) for each track of $p_T > 1$ GeV within 5 cm in z of the electron vertex; and the run and event number for debugging.[4] We read this binary file (about 1.5 MB) into a data structure in memory, then arrange the data into 40 u bins, from 0 to 20 GeV. To simulate the N_{cone} variable for a Monte Carlo W event, we randomly choose an event from the correct u bin, and rotate the W list event so that $\phi(\vec{u})$ is the same for the two events. If the real electron in the W list event is within 30° of the MC electron, we choose a different W list event from the same u bin. Since the

---

[3] While overlaying Monte Carlo particles and real data events is a well known simulation technique in hadron collider physics, our use of this method was inspired by the work of Andrew Gordon in Ref. [69].

[4] Most of these quantities are in practice stored as 16-bit integers, to save space.
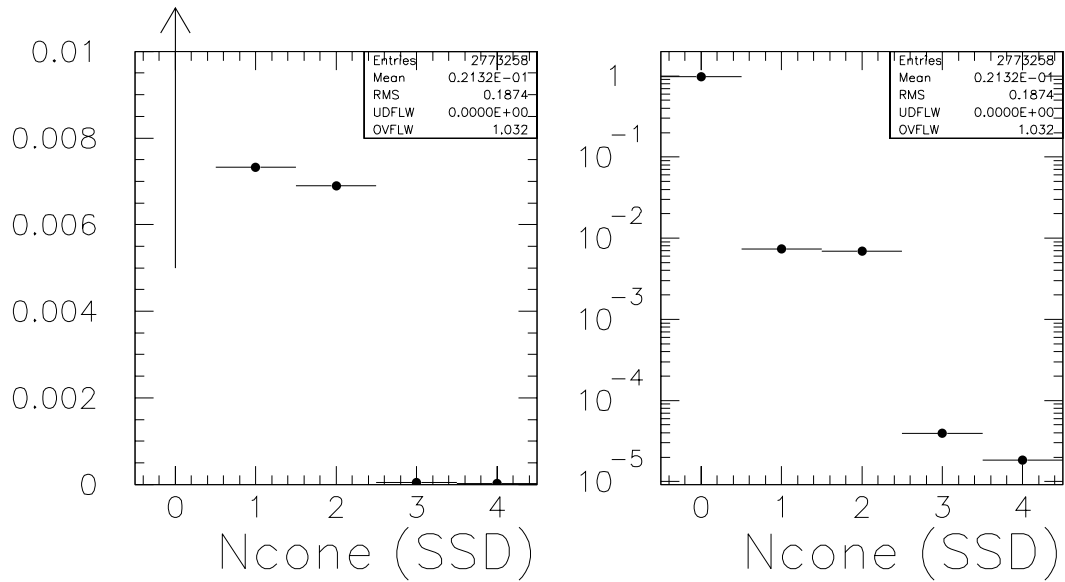
Figure 5.1: N_{cone} distribution for TOYGEN Z events simulated with SSD. The $N_{\mathrm{cone}} > 0$ fraction is 1.4%. Note that the $N_{\mathrm{cone}} = 0$ point is off-scale in the left-hand plot. These results are in excellent agreement with an earlier study that simulated W electrons with QFL [70].

p_T and $|\Delta z_0|$ cuts on the tracks have already been made in writing the W list, we simply count tracks in a cone around the MC electron to simulate N_{cone}.[5]

Figure 5.2 shows some predictions of this simulation of the underlying event's contribution to N_{cone}. The predicted inefficiency is 3.4%, which we can combine with the SSD prediction to obtain 4.8%, in good agreement with the 5 ± 1% inefficiency observed in the Z data.

While it would be straightforward to extend this technique to model the ineffi-ciencies of the shower shape (χ_s^2) and $E_{\mathrm{hadron}}/E_{\mathrm{EM}}$ cuts, by overlaying QFL electron showers with data from the underlying event, we decided that it would make no sense to do so for this measurement: As Table 4.5 shows, each of the other electron ID cuts removes 1–1.5% of W events (if it is applied last), while the track isolation cut rejects 7%. We model the most important variable, N_{cone}, very well, and that seems adequate.

Table 5.1 summarizes the results of the SSD and W list N_{cone} predictions and combines them into a single predicted N_{cone} distribution for W and Z signal elec-trons.

Because the N_{cone} cut uses a fixed track p_T threshold of 1 GeV, we expect high-energy electrons, whose secondary particles are proportionally more energetic, to

---

[5]Recall that the definition of N_{cone} is the number of tracks of $p_T > 1$ GeV in a cone of $\Delta R = 0.25$ around the electron, with z_0 within 5 cm of the electron vertex.
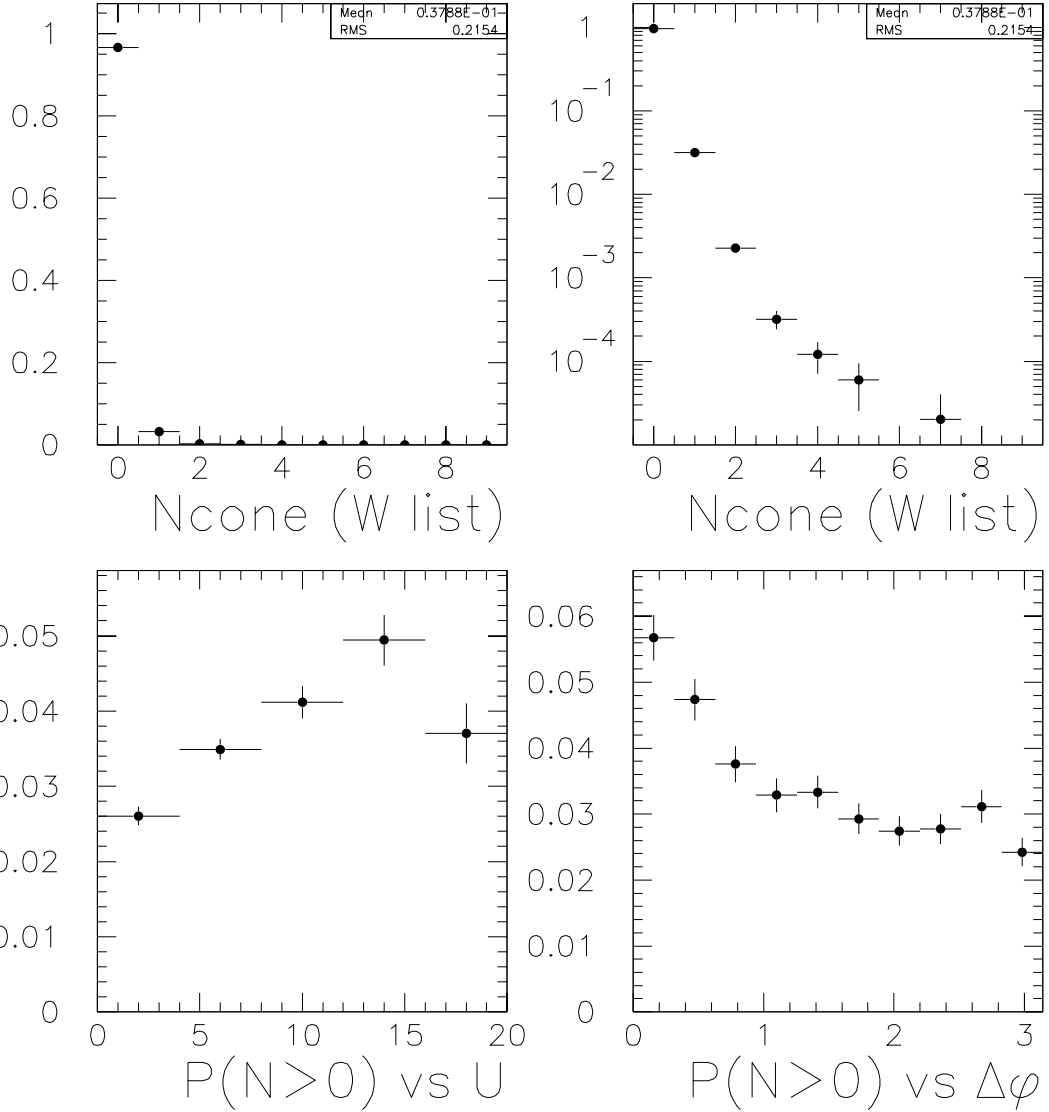
Figure 5.2: (Top) N_{cone} distribution predicted by W list. The $N_{\text{cone}} > 0$ fraction is 3.4%. (Bottom) Probability to have $N_{\text{cone}} > 0$ (SSD contribution is not included) vs. u and $\Delta\phi(\vec{E}_T, \vec{u})$.

fail the N_{cone} cut more frequently than low-energy electrons. The N_{cone} inefficiency predicted by the combined SSD and W-list simulation increases from 4.8% for $M_T <$ 100 GeV to 6% for $M_T = 200$ GeV. The physical processes that cause this decrease in efficiency—bremsstrahlung and pair production—are well understood, and the model successfully predicts the N_{cone} inefficiency observed in both the Z data and the W data.[6] Thus, we feel that we can trust the simulation to model this modest

---

[6] Note the good agreement between the N_{cone} distribution predicted in Table 5.1 and the W signal rate predicted for each N_{cone} bin at the end of Section 6.2.2.

N_{cone}	SSD	W list	combined
0	0.9857	0.9657	0.9519
1	0.0072	0.0315	0.0380
2	0.0070	0.0027	0.0096
> 2	0.0001	0.0001	0.0005

Table 5.1: Prediction for W and Z signal electron N_{cone} distribution, combining results from the SSD simulation (which models the contribution from bremsstrahlung and pair-production) and the W list (which models the underlying event contribution).

dependence on electron energy.

5.4   Tuning the simulation

The $M_T(e, \nu)$ lineshape simulation requires a number of inputs, many of which have associated uncertainties. These inputs include electron energy scale, electron resolution, W p_T distribution, and calorimeter response to the hadronic energy recoiling against the W. The ability to constrain these quantities from the data (usually the $Z \to ee$ sample) will set the scale for many of the systematic errors we assign to the measured W width.

5.4.1   Electron energy scale

We check the electron energy scale in the $Z \to ee$ sample (after the corrections described in Section 3.4.6) with a one-parameter binned log-likelihood fit, using 40 mass bins from 70 GeV to 110 GeV.[7] We compute the log-likelihood for a Monte Carlo template of a given energy scale to produce the observed set of $Z \to ee$ events, and fit a parabola to $-2\log(L)$ vs. energy scale.

Since effects sensitive to electron ID cuts, such as underlying event energy, hard bremsstrahlung, and leakage into the hadronic calorimeter, may affect the electron response, we use the "tight $Z \to ee$ sample," in which electron ID cuts are applied to both electrons. We find $M_Z = 91.240 \pm 0.068$ GeV, i.e. that we must multiply the Monte Carlo energies by 1.00059 ± 0.00075 to match the data. (See Figure 5.3.)

As a check of the fitting procedure, we fit the unscaled Monte Carlo distribution and find a scale factor of 1.00001 ± 0.00003. The Monte Carlo statistical error is a factor of 25 smaller than the data statistical error. (The fitting templates use 1.35 million MC events, after all cuts.)

---

[7]Since the fitted energy scale and constant term are completely uncorrelated (see figures in Ref. [71]), we do not need to do a two-parameter simultaneous fit to both.

Cuts	M_Z (GeV)	scale ($\frac{\text{data}}{\text{MC}}$)	# OS	# LS
$\Delta z_{\text{track,CES}}$, N_{cone}, $E_{\text{hadron}}/E_{\text{EM}}$, $\chi_s^2 < 20$	91.240 ± 0.068	1.00059 ± 0.00075	2012	1
$\Delta z_{\text{track,CES}}$, N_{cone}, $E_{\text{hadron}}/E_{\text{EM}}$, $\chi_s^2 < 10$	91.281 ± 0.069	1.00104 ± 0.00076	1929	1
$\Delta z_{\text{track,CES}}$, N_{cone}, $E_{\text{hadron}}/E_{\text{EM}}$, $\chi_s^2 + \chi_w^2 < 20$	91.293 ± 0.075	1.00117 ± 0.00082	1639	0
$\Delta z_{\text{track,CES}}$, N_{cone}, $E_{\text{hadron}}/E_{\text{EM}}$	91.244 ± 0.067	1.00063 ± 0.00074	2077	1
$\Delta z_{\text{track,CES}}$, N_{cone}	91.193 ± 0.066	1.00007 ± 0.00073	2128	3
$\Delta z_{\text{track,CES}}$, N_{3D}	91.156 ± 0.072	0.99967 ± 0.00079	1823	10
$\Delta z_{\text{track,CES}}$, N_{3D}, $|x_{\text{cal}}| < 18$ cm	91.136 ± 0.082	0.99944 ± 0.00090	1376	5
$\Delta z_{\text{track,CES}}$, N_{3D}, $|x_{\text{cal}}| < 18$ cm, $|z_{\text{cal}}| > 12$ cm	91.105 ± 0.084	0.99911 ± 0.00092	1329	5
N_{3D}, $|x_{\text{cal}}| < 18$ cm, $|z_{\text{cal}}| > 12$ cm	91.089 ± 0.084	0.99893 ± 0.00092	1343	9
N_{3D}, no P_T^Z cut, $|x_{\text{cal}}| < 18$ cm, $|z_{\text{cal}}| > 12$ cm	91.112 ± 0.082	0.99919 ± 0.00090	1384	9

Table 5.2: Dependence of CEM energy scale (inferred from Z mass) on electron selection criteria. These cuts are applied to both electrons.

We have found that making other reasonable choices of electron selection criteria can change the observed energy scale at the 0.1% level. In particular, the scale factor that we fit is 0.16% (about 1.6σ, since the errors are nearly 100% correlated) higher than the $M_Z = 91.095 \pm 0.090$ GeV reported in Ref. [71]. Table 5.2 shows the dependence of the fitted M_Z on electron selection criteria. Using cuts similar to those in Ref. [71], we find a result in much better agreement, $M_Z = 91.112 \pm 0.082$ GeV.

We will divide the observed CEM energies by a factor 1.0006. In addition to the statistical error of 0.08%, we conservatively assign a systematic error of 0.17% for the unexplained variation of M_Z with electron selection cuts, even though some of this variation may be statistical in origin, or may cancel when W and Z electrons are selected using identical criteria. Adding these values in quadrature, the uncertainty we assign to the CEM energy scale is 0.2%.

Cuts	κ	# OS	# LS
(both legs) $\Delta z_{\mathrm{track,CES}}$, N_{cone}, $E_{\mathrm{hadron}}/E_{\mathrm{EM}}$, χ_s^2	$1.47^{+0.22}_{-0.25}\%$	2012	1
(one leg) $\Delta z_{\mathrm{track,CES}}$, N_{cone}, $E_{\mathrm{hadron}}/E_{\mathrm{EM}}$, χ_s^2	$1.71^{+0.20}_{-0.22}\%$	2206	8
(both legs) $\Delta z_{\mathrm{track,CES}}$, N_{3D}, $\|x_{\mathrm{cal}}\| < 18$ cm, $\|z_{\mathrm{cal}}\| > 12$ cm	$1.49^{+0.28}_{-0.33}\%$	1329	5
(one leg) $\Delta z_{\mathrm{track,CES}}$, N_{3D}, $\|x_{\mathrm{cal}}\| < 18$ cm, $\|z_{\mathrm{cal}}\| > 12$ cm	$1.71^{+0.23}_{-0.25}\%$	1826	79

Table 5.3: Dependence of CEM constant term κ (inferred from $Z \to ee$ mass spectrum) on electron selection criteria.

5.4.2 Electron resolution

Fitting the same $Z \to ee$ mass distribution, we find the CEM constant term to be $\kappa = 1.47^{+0.22}_{-0.25}\%$, consistent with the $1.64 \pm 0.3\%$ reported in Ref. [71], but with a slightly lower central value. (See Figure 5.3.) We find that applying ID cuts to only one electron gives results closer to those found in Ref. [71]. Table 5.3 shows the value of κ obtained for various sets of selection criteria. We add the 0.2% difference in quadrature with the 0.25% statistical error and take κ to be $1.5 \pm 0.3\%$.

Figure 5.4 shows $Z \to ee$ mass spectra for data and Monte Carlo, using $\kappa = 1.5\%$, $M_Z = 91.1863$ GeV [16], and , $_Z = 2.49$ GeV, with data CEM energies divided by 1.0006.

5.4.3 $W\ p_T$ distribution

Nonperturbative parameters

In the Ladinsky-Yuan [35] parameterization introduced in Chapter 2, the p_T spectrum at a given $\tau = \hat{s}/s$ is most sensitive to g_2, while g_1 and g_3 control the variation with τ. Thus, we vary the g_2 parameter to obtain the best fits to the $Z\ p_T^{ee}$ and
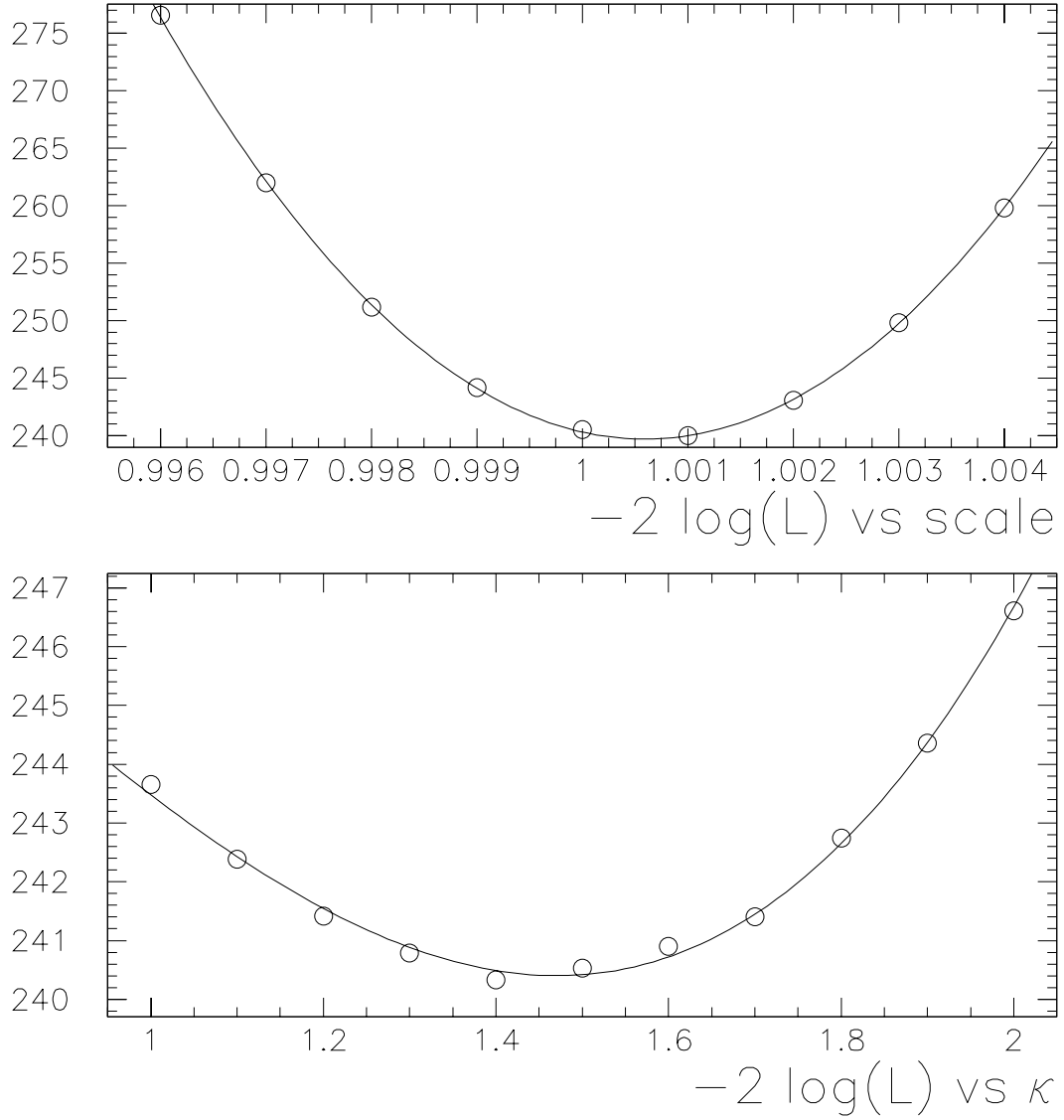
Figure 5.3: (Top) $-2\log(L)$ vs. CEM energy scale for $Z \to ee$ data. The fitted energy scale is 1.00059 ± 0.00075. (Bottom) $-2\log(L)$ vs. CEM constant term κ. The fitted resolution is $1.47^{+0.22}_{-0.25}\%$.

$\Delta\phi^{ee}$ spectra (while leaving g_1 and g_3 at the LY fitted values of 0.1 and -1.5, respectively). The p_T^{ee} fit gives $g_2 = 0.69^{+0.10}_{-0.09}$, and the $\Delta\phi$ fit gives $g_2 = 0.46^{+0.11}_{-0.10}$.[8] (See Refs. [72] and [73] for other fits to these parameters.) Figure 5.5 shows the sensitivity of p_T^{ee} and $\Delta\phi^{ee}$ distributions to g_2, Figure 5.6 plots $-2\log(L)$ vs. g_2, and Figure 5.7 compares the Z data with the best fits. We average the results of the two fits and take $g_2 = 0.6 \pm 0.2$, which agrees well with the LY value $g_2 = 0.58^{+0.1}_{-0.2}$.

---

[8] We thank Hans Jensen for the suggestion to fit the $\Delta\phi$ distribution.
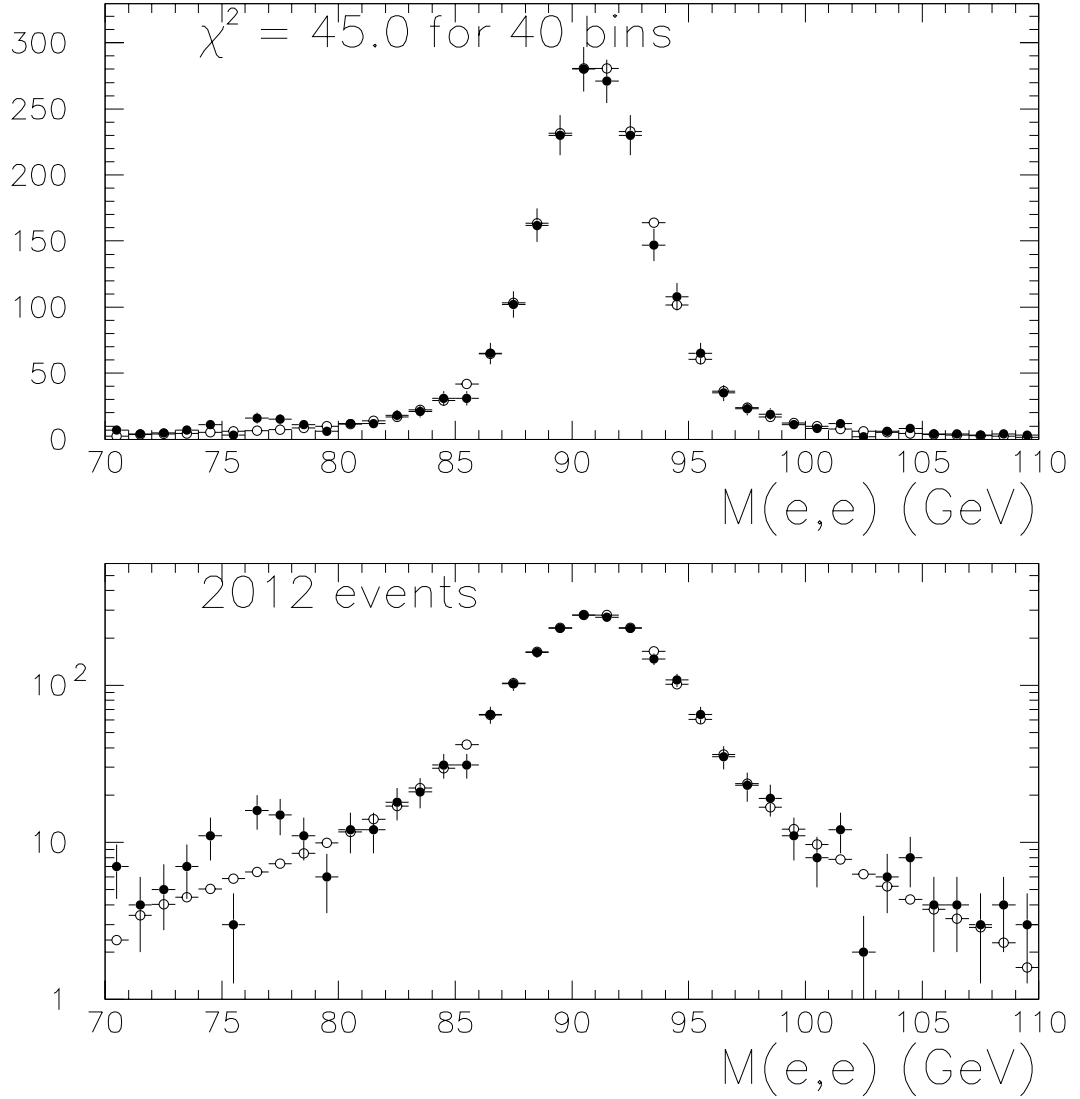
Figure 5.4: (Top) $Z \rightarrow ee$ mass distribution, for data (solid points) and simulation (open circles), using $M_Z = 91.186$ GeV and $\kappa = 1.5\%$, with the data CEM energies divided by 1.0006. (Bottom) Same as above, on a semilogarithmic scale. The data and simulation agree well: χ^2 is 45.0 for 37 degrees of freedom, and the Kolmogorov-Smirnov (KS) confidence level is 66%.

We briefly investigate systematic effects in determining g_2 from the $Z \rightarrow ee$ data, and the largest potential effect we find is modeling the electron acceptance in ϕ. If we fit the p_T^{ee} spectrum for Monte Carlo data with $|x| < 18$ cm fiducial cuts, generated at $g_2 = 0.60$, to templates made with $|x| < 21$ cm fiducial cuts, we mismeasure g_2 to be 0.45. Varying the CEM constant term from $\kappa = 1.0\%$ to $\kappa = 2.0\%$, for generated $g_2 = 0.6$, and fitting to templates with $\kappa = 1.5\%$, we find that the fitted g_2 varies from 0.58 to 0.65. Varying the CEM energy scale from 0.9950 to 1.0050, we find that the fitted g_2 varies from 0.59 to 0.62. Ignoring the

magnetic field in extrapolating electrons to the calorimeter and doubling the ϕ_0 resolution in the simulation both produce biases smaller than 0.01 in g_2. Varying skew parameter s (see below) by 0.0028 GeV^{-1} changes the measured g_2 by 0.04. Except for using inconsistent fiducial cuts, which would be a mistake rather than a legitimate source of error, the biases considered are much smaller than the quoted uncertainty of 0.2.

For the fit to the $\Delta\phi$ distribution, doubling the ϕ_0 resolution in the simulation also biases g_2 by less than 0.01, while comparing $|x| < 18$ cm data to $|x| < 21$ cm templates produces a much larger bias—a fitted g_2 value of 0.28.
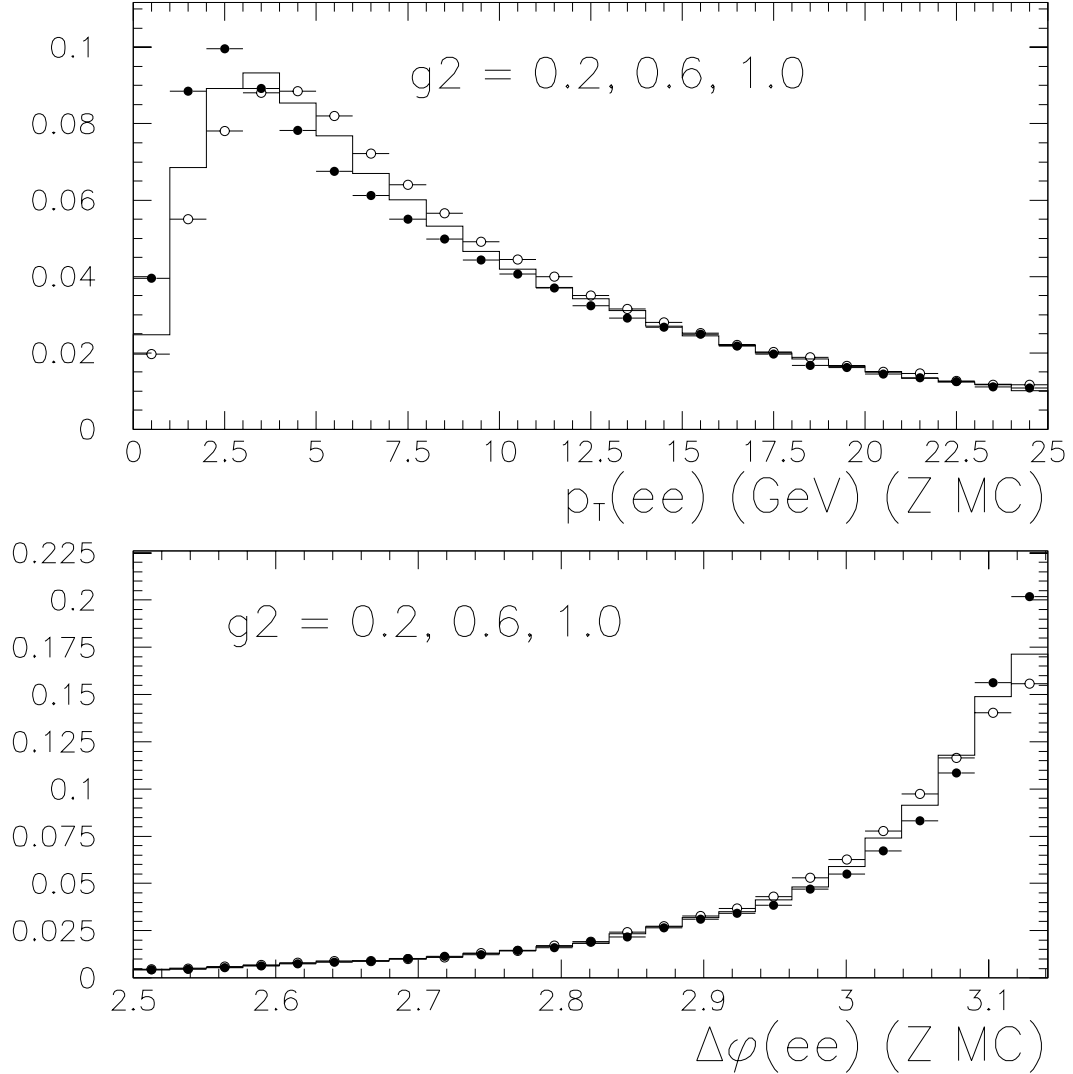
Figure 5.5: (Top) Simulated p_T^{ee} spectra for $Z \to ee$ with nonperturbative parameter g_2 taking values 0.2 (solid points), 0.6 (histogram), and 1.0 (open circles). Higher values of g_2 produce harder p_T spectra. (Bottom) Simulated $\Delta\phi^{ee}$ distributions for g_2 values 0.2, 0.6, and 1.0. Smaller values of g_2 produce a larger peak at $p_T \approx 0$ and thus $\Delta\phi \approx \pi$.
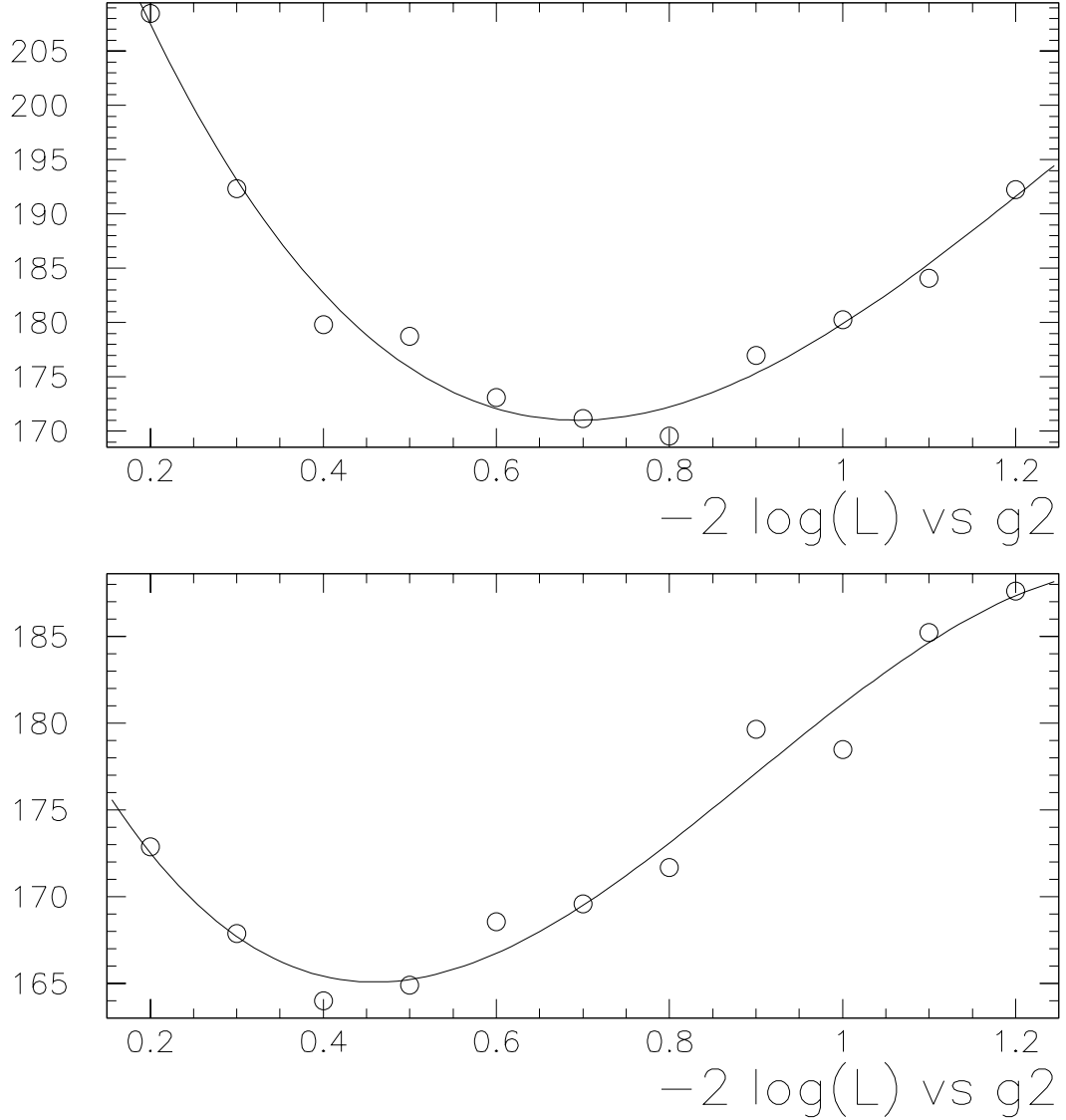
Figure 5.6: (Top) $-2\log(L)$ vs. g_2 for p_T^{ee} spectrum. The fit prefers $g_2 = 0.69^{+0.10}_{-0.09}$. (Bottom) $-2\log(L)$ vs. g_2 for $\Delta\phi^{ee}$ spectrum. The fit prefers $g_2 = 0.46^{+0.11}_{-0.10}$.

Skew parameter

As Figure 5.5 shows, varying g_2 changes the shape but not the normalization of the $p_T < 15$ GeV part of the p_T^Z spectrum. We can imagine at least two effects that could cause the observed ratio of high-p_T to low-p_T Z events to deviate slightly from the Ladinsky-Yuan calculation: First, the calculated ratio depends upon the QCD coupling constant $\alpha_s(M_Z)$, which must be determined from experiment; second, the event selection efficiency as a function of p_T may not be modeled perfectly in the simulation. It is useful to be able to constrain the size of these effects directly from
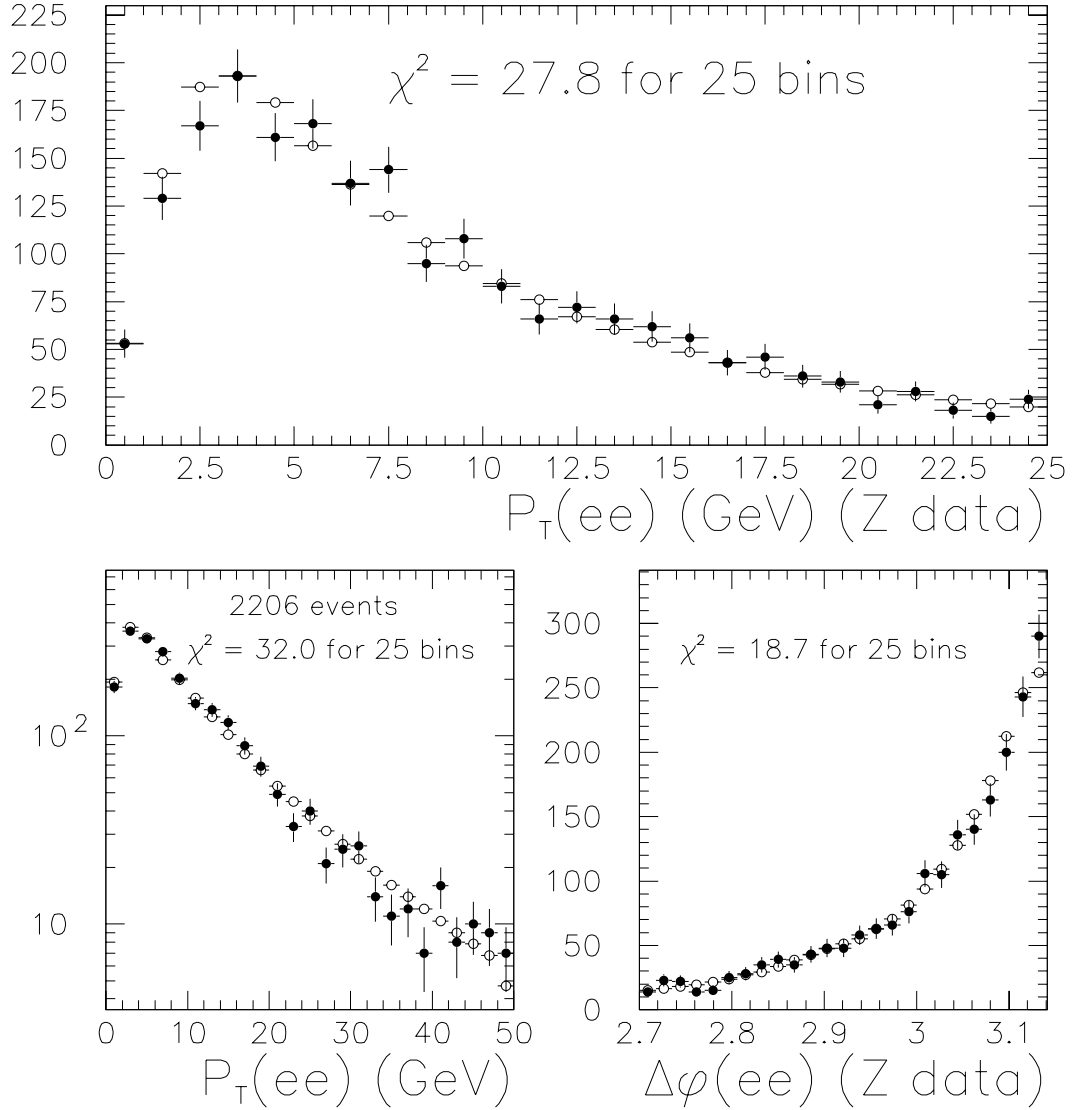
Figure 5.7: (Top) $Z \to ee$ p_T^{ee} spectrum for data (solid points) and simulation (open circles), using nonperturbative parameter $g_2 = 0.6$ and skew value -0.0028 GeV^{-1}. The KS confidence level is 13%. (Bottom left) Same as above, on a semilogarithmic scale, and with a larger range in p_T. KS=19%. (Bottom right) $\Delta\phi^{ee}$ spectra. KS=26%.

the Z data.

We introduce a "p_T skew parameter" s, with which we reweight the W and Z p_T spectra as follows:

$$\frac{dN}{dp_T} \to \frac{dN}{dp_T}(1 + sp_T) \tag{5.2}$$

Fitting the Z data (Figure 5.8), we find $s = -0.0028 \pm 0.0021$ GeV^{-1}. The data are consistent with no skew, but prefer to reduce the MC p_T spectrum at high p_T. We use $s = -0.0028$ GeV^{-1} by default in the W and Z simulation; in Chapter 7,

we vary s as a source of error in measuring , $_W$.

Reno [74] has noted that the ratio of W and Z p_T spectra can be predicted with much more confidence than the individual spectra. By reweighting the calculated Z p_T spectrum to match the data, then applying the same weighting function to the calculated W p_T spectrum, we leave the most reliable feature of the calculation—the ratio of W and Z spectra—unchanged.
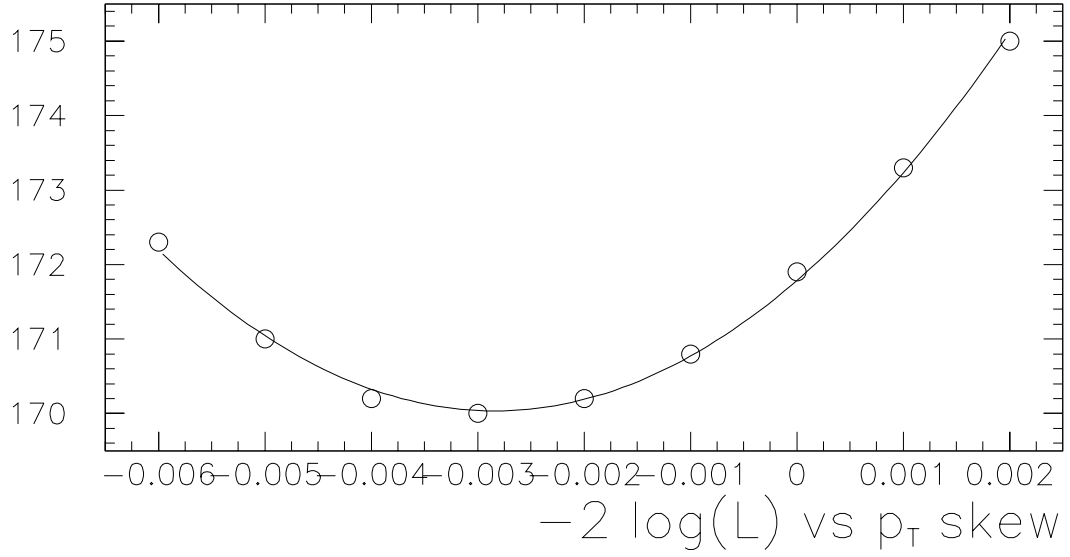
Figure 5.8: $-2\log(L)$ vs. Z p_T skew parameter s. A fit to $0 < p_T < 50$ GeV prefers $s = -0.0028 \pm 0.0021$ GeV^{-1}.

Mass dependence

Another W p_T effect that we need to consider is the dependence of the p_T spectrum on $\sqrt{\hat{s}}$, since TOYGEN uses the p_T spectrum for $\sqrt{\hat{s}} = M$ only. To include this effect, we apply a weight $F(p_T, \sqrt{\hat{s}})$ to the TOYGEN output. The function F is a fit by Mark Lancaster [75], of the form

$$F(p_T, \sqrt{\hat{s}}) = P_0 + P_1 \ p_T + P_2 \ p_T^2$$

$$P_i = A_i + B_i \ \sqrt{\hat{s}} + C_i \ (\sqrt{\hat{s}})^2 + D_i \ (\sqrt{\hat{s}})^3$$

to a large $W \to e\nu$ Monte Carlo sample generated using the Charlemagne program of Ellis *et al* [36, 37], which includes $\sqrt{\hat{s}}$ dependence in its W and Z p_T calculations. F is normalized so that $\frac{\int dp_T F(p_T, \sqrt{\hat{s}})}{\int dp_T} = 1$ and $F(p_T, M_W) = 1$, i.e. the weight does not change the p_T-integrated $\sqrt{\hat{s}}$ spectrum and does not change the p_T spectrum for $\sqrt{\hat{s}} = M_W$. Figure 5.9 shows the calculated variation of the W p_T spectrum with $\sqrt{\hat{s}}$.
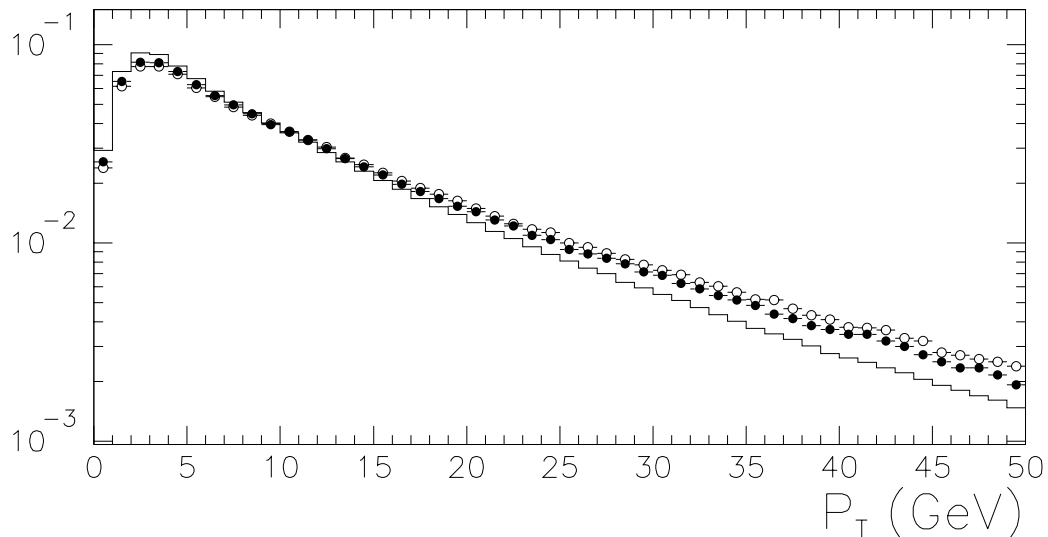
Figure 5.9: Simulated W p_T spectra, using $F(p_T, \sqrt{\hat{s}})$ weight function described in the text. We plot the true (generated) p_T for simulated events after all analysis requirements except $\not{E}_T > 25$ GeV and $u < 20$ GeV have been imposed. The histogram is for all $\sqrt{\hat{s}}$ values; the solid points are the $\sqrt{\hat{s}} > 100$ GeV subset; and the open circles are the $\sqrt{\hat{s}} > 120$ GeV subset. The spectra have been normalized to unit area.

5.5   Recoiling hadrons

Modeling the recoil measurement $\vec{u}$ accurately is important, because the $\vec{u}$ resolution is the largest component in the M_T resolution and (as we will show in Chapter 7) is a dominant systematic error in this analysis. An empirical model is required because a particle-level simulaton of $\vec{u}$ is difficult both theoretically and experimentally.[9]

Given a $\vec{p_T}^W$ or $\vec{p_T}^Z$ vector, the recoil model chooses a vector $\vec{u}$ of observed energy recoiling against the W or Z. To simplify the notation, we define $u_1 = \vec{u} \cdot \frac{\vec{p_T}}{|\vec{p_T}|}$ and define u_2 to be the perpendicular component. We assume that $\vec{u}$ is, on average, parallel to $-\vec{p_T}$, i.e. $\langle u_2 \rangle = 0$. We also assume that u_1 and u_2 fluctuate independently.

The recoil model we describe has three main ingredients: first, the shape of the resolution function that describes fluctuations of u_1 and u_2 about their mean values; second, the p_T-dependent mean of u_1 (denoted μ_1) by which the u_1 resolution function is translated; third, a p_T-dependent scale factor on the u_1 and u_2 resolution functions. Below, we first derive a shape for the resolution function based largely upon minimum-bias data, and then perform a fit in which this basic shape is translated and scaled to match the $Z \to ee$ data.

---

[9] The model described in this section closely follows earlier work by Andrew Gordon [69], but uses a completely different unsmearing method, and differs in many details of the fitting procedure and parameterization.

66

5.5.1 Shape of resolution function

We make an assumption, first used by the UA2 collaboration, that the $\vec{u}$ resolution in low-p_T W and Z events closely resembles the $\vec{u}$ resolution in minimum-bias events. Minimum-bias events have a broad distribution of ΣE_T, but for a given ΣE_T value, the $u_{x,y}$ resolution is well described by a Gaussian distribution, whose standard deviation we label σ_{MB}. The variation of σ_{MB} with ΣE_T is well described by a simple power law,

$$\sigma_{\mathrm{MB}}(\Sigma E_T) = 0.324 \text{ GeV} \left(\frac{\Sigma E_T}{1 \text{ GeV}} \right)^{0.577} \tag{5.3}$$

as shown in Figure 5.10. The minimum-bias $u_{x,y}$ distributions can thus be described by the resolution function

$$\frac{dN}{du_{x,y}} = \int d(\Sigma E_T) \, \frac{dN}{d(\Sigma E_T)} \, \frac{1}{\sigma_{\mathrm{MB}}(\Sigma E_T)} \, G\left(\frac{u_{x,y}}{\sigma_{\mathrm{MB}}(\Sigma E_T)} \right) \tag{5.4}$$

where $G(x) = \frac{1}{\sqrt{2\pi}} e^{-\frac{1}{2}x^2}$. The factor of $\frac{1}{\sigma_{\mathrm{MB}}}$ is for normalization. To model W and Z events, we replace $\frac{dN}{d(\Sigma E_T)}$ in Equation 5.4 with the ΣE_T distribution from the $Z \to ee$ data. As illustrated in Figure 5.11, this spectrum is well described by the gamma distribution

$$\frac{dN}{d(\Sigma E_T)} \propto \left(\frac{\Sigma E_T}{21.05 \text{ GeV}} \right)^{2.068} e^{-\Sigma E_T/21.05 \text{ GeV}} \tag{5.5}$$

Thus, we can define a resolution function, graphed in Figure 5.12,

$$S_{MB}(u_{x,y}) \propto \int d(\Sigma E_T) \, \left(\frac{\Sigma E_T}{21.05 \text{ GeV}} \right)^{2.068} \frac{e^{-\Sigma E_T/21.05 \text{ GeV}}}{\sigma_{\mathrm{MB}}(\Sigma E_T)} \, G\left(\frac{u_{x,y}}{\sigma_{\mathrm{MB}}(\Sigma E_T)} \right) \tag{5.6}$$

which we use as the shape of the $\vec{u}$ resolution in the W and Z data. Below, we scale the argument of S_{MB} as a function of p_T^Z to match the Z data.

5.5.2 Fit of resolution function to Z data

We expect μ_1 to be a smooth, monotonic function of p_T^Z, and we expect the u_1 and u_2 resolutions to increase slowly with p_T^Z. To turn these statements into a parametric description of the data, we perform an unbinned likelihood fit to the u_1 and u_2 distributions in the Z data as a function of p_T^{ee}. The likelihood function is

$$L = \frac{1}{\sigma_1 \sigma_2} \, S_{\mathrm{MB}}\left(\frac{u_1 - \mu_1}{\sigma_1} \right) \, S_{\mathrm{MB}}\left(\frac{u_2}{\sigma_2} \right) \tag{5.7}$$
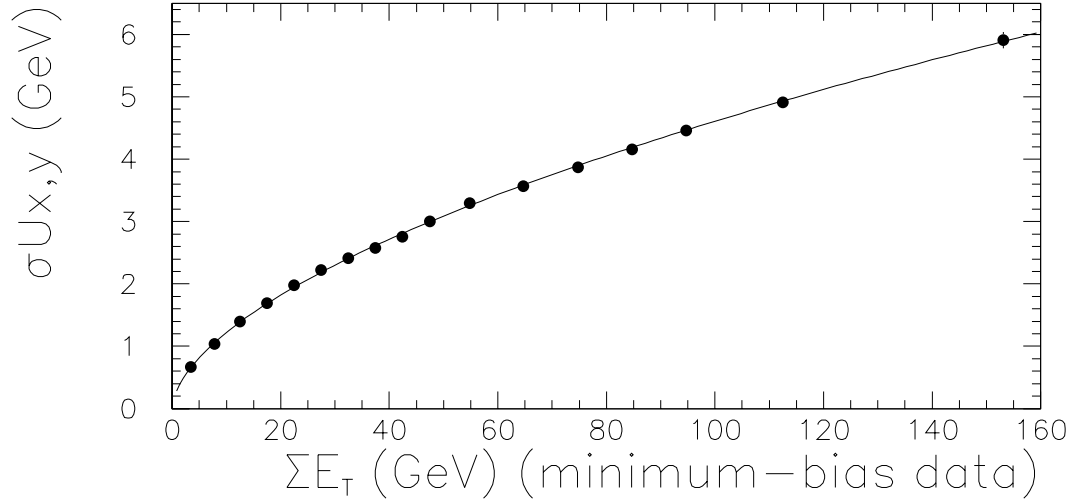
Figure 5.10: Observed $u_{x,y}$ resolutions vs. ΣE_T in minimum-bias data. The power law $\sigma_{x,y} = 0.324(\Sigma E_T)^{0.577}$ describes the data very well. (Data and fit courtesy of Mark Lancaster [73].)
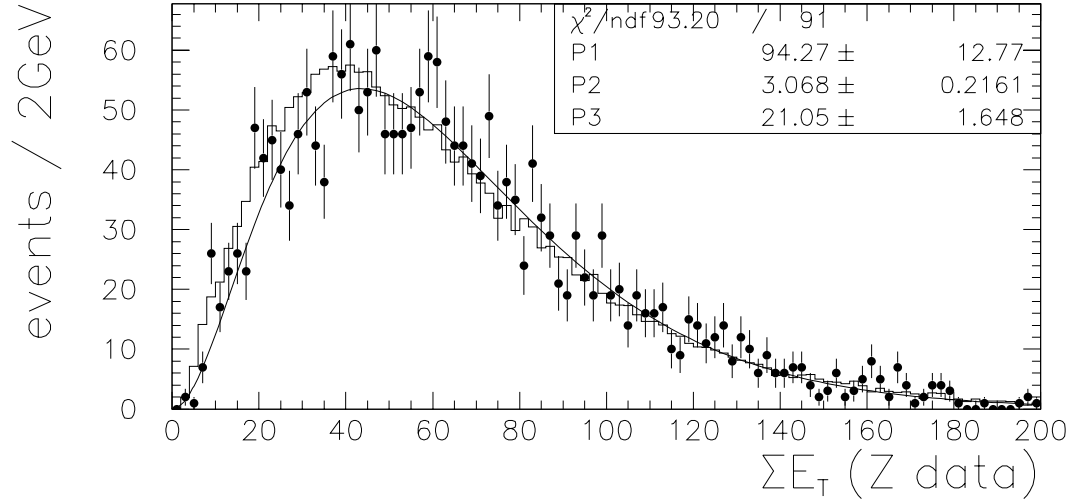
Figure 5.11: The data points are the ΣE_T spectrum of $Z \rightarrow ee$ data. The curve is a fit to the form $A(\frac{\Sigma E_T}{C})^{B-1}e^{-\Sigma E_T/C}$, a gamma distribution. The values $B = 3.068$, $C = 21.05$ GeV describe the data well. For comparison, the W ΣE_T spectrum, normalized to the number of Z events, is drawn as a histogram. The W and Z ΣE_T spectra are similar but clearly distinguishable. We use the Z spectrum because it has a lower background level and it is not subject to the bias of the $\not{E}_T > 25$ GeV and $u < 20$ GeV cuts applied in the W data.

where

$$
\begin{aligned}
\mu_1 &= \min\left(0,\ A + B\ p_T^{ee} + C\ (p_T^{ee})^2\right) \\
\sigma_1 &= D + E\ p_T^{ee}
\end{aligned}
\tag{5.8}
$$
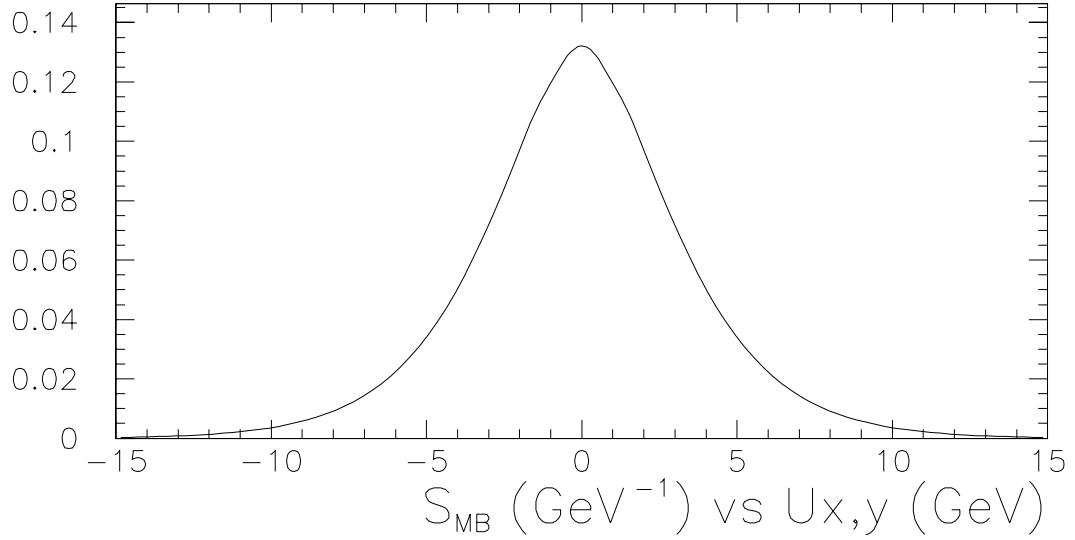
Figure 5.12: Resolution function S_{MB} (Equation 5.6).

$$\sigma_2 \;=\; F + G\, p_T^{ee}$$

Note that $\sigma_{1,2}$ are dimensionless; they are simply p_T-dependent scale factors for the argument of S_{MB}. Including parameter A allows μ_1 to reach zero at a p_T value that is comparable to the p_T resolution (≈ 1 GeV); events at very low p_T contain little information about μ_1, as the direction of the $\vec{p}_T$ vector is not well determined. A fit to the data yields these values:

$$
\begin{aligned}
A &= +0.713 \pm 0.077 \text{ GeV} & (5.9)\\
B &= -0.569 \pm 0.018 \\
C &= -0.00406 \pm 0.00068 \text{ GeV}^{-1} \\
D &= 0.928 \pm 0.030 \\
E &= 0.0244 \pm 0.0028 \text{ GeV}^{-1} \\
F &= 0.962 \pm 0.029 \\
G &= 0.0121 \pm 0.0024 \text{ GeV}^{-1}
\end{aligned}
$$

Figure 5.13 graphs the functions μ_1, σ_1, and σ_2, using the fitted parameters. As shown in Figures 5.14 and 5.15, this model provides an excellent description of the 2206 $Z \to ee$ events.

We have fitted μ_1 and $\sigma_{1,2}$ as functions of measured p_T^{ee} in the data. What we need in the simulation, however, are μ_1 and $\sigma_{1,2}$ as functions of true p_T^W or p_T^Z. Thus, some sort of "unsmearing" procedure is needed to undo the effect of p_T^{ee} measurement error in the data. The technique we use is to fit $\vec{u}$ in both the Z data and the Z simulation output as a function of smeared p_T^{ee} and to consider the ratio $R(p_T^{ee}) \equiv \frac{f^{\mathrm{data}(p_T^{ee})}}{f^{\mathrm{sim}(p_T^{ee})}}$ (where f refers generically to μ_1, σ_1, or σ_2) to be a p_T-dependent

69
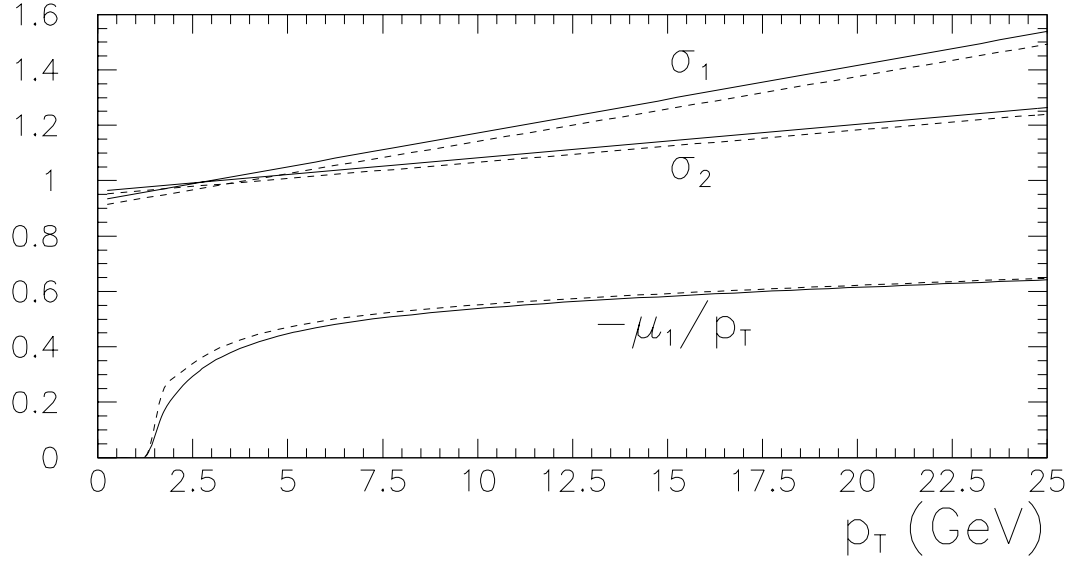
Figure 5.13: Recoil model response and resolution functions (Equation 5.8). We have plotted $-\mu_1(p_T)/p_T$ instead of $\mu_1(p_T)$ so that μ_1, σ_1, and σ_2 can be shown together. Note that σ_1 and σ_2 are dimensionless. The solid curves are the fits to the data, and the dashed curves are what is used as a function of true p_T in the simulation to match what is observed as a function of measured p_T in the data.

correction factor to be applied in the next iteration of the simulation. Whereas we derive the corrections $R(p_T)$ as functions of p_T^{smeared}, we modify the simulation by applying these same corrections as functions of p_T^{true}. (We make no attempt to convert $R(p_T^{\text{smeared}})$ into some related function $R'(p_T^{\text{true}})$; we just use the same function.) The procedure works because of two useful facts: first, once the iteration has converged, the fit parameters will be the same for data and simulation, i.e. A^{data}–G^{data} will approximately equal A^{sim}–G^{sim}, and each function $R \approx 1$; second, $p_T^{\text{smeared}}(ee)$ is a good approximation for $p_T^{\text{true}}(Z)$, i.e. the p_T^{ee} resolution is small compared to the $\vec{u}$ resolution, so $R(p_T^{\text{true}}) \approx R(p_T^{\text{smeared}})$. Then, if the fit returns parameters A^{data}–G^{data} for data and A^{sim}–G^{sim} for simulation, we modify μ_1, σ_1, and σ_2 in the simulation as follows:[10]

$$
\begin{aligned}
\mu_1 \;\;&\leftarrow\;\; \mu_1 \cdot \frac{A^{\text{data}} + B^{\text{data}} p_T^{\text{true}} + C^{\text{data}} (p_T^{\text{true}})^2}{A^{\text{sim}} + B^{\text{sim}} p_T^{\text{true}} + C^{\text{sim}} (p_T^{\text{true}})^2} \\
\sigma_1 \;\;&\leftarrow\;\; \sigma_1 \cdot \frac{D^{\text{data}} + E^{\text{data}} p_T^{\text{true}}}{D^{\text{sim}} + E^{\text{sim}} p_T^{\text{true}}}
\end{aligned}
\tag{5.10}
$$

---

[10] We note here two minor technical points: First, in fitting the MC output, we allow parameter A to float only in the first iteration; thereafter, we constrain A^{sim} to equal A^{data} to speed up the convergence of the fit. Second, we do not correct μ_1 in the region $|A + Bp_T + Cp_T^2| < 0.1$ GeV in which the correction factor is poorly defined.
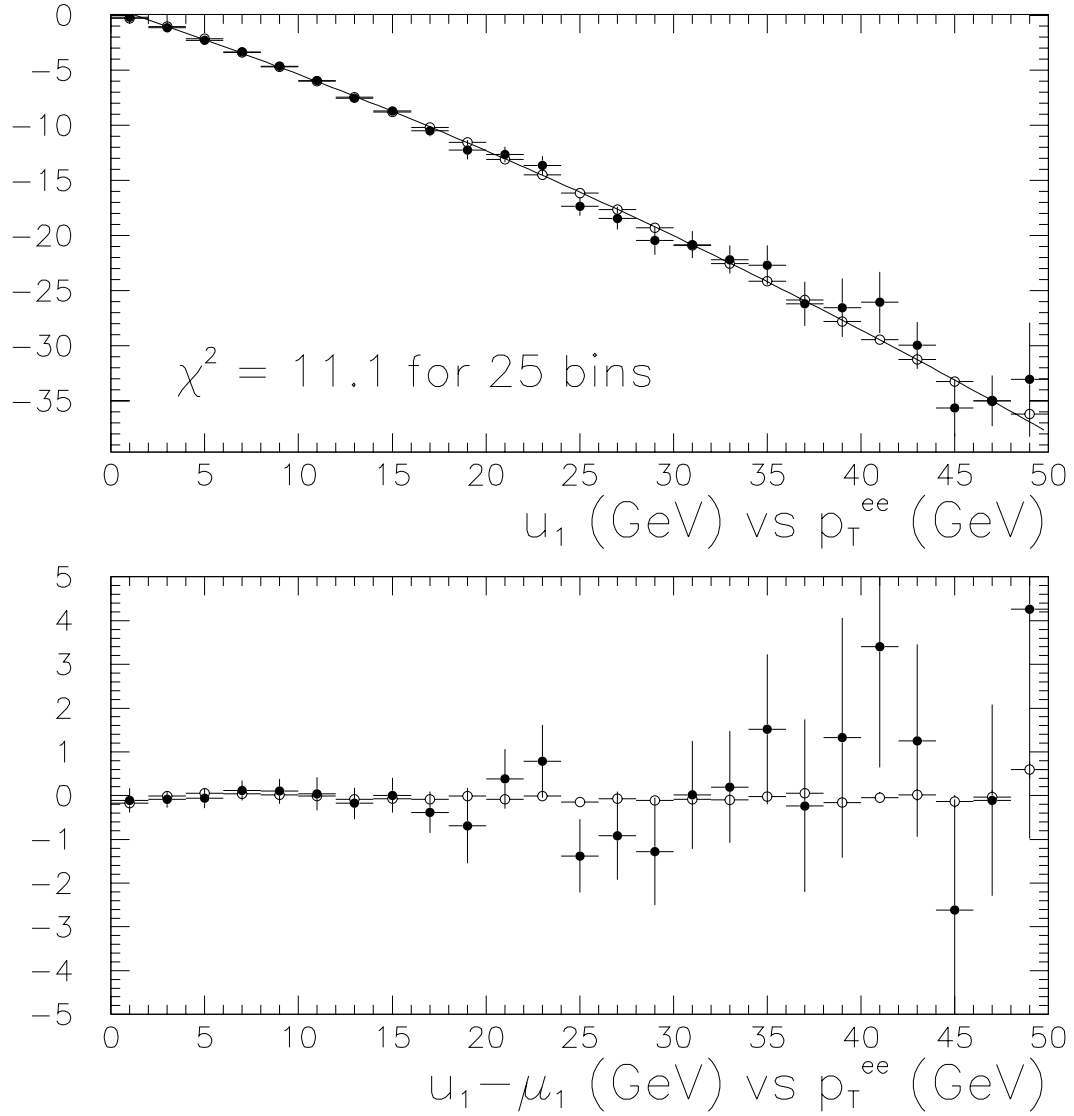
Figure 5.14: (Top) Mean of u_1 (component of recoil energy $\vec{u}$ parallel to $\vec{p}_T^{ee}$) vs. p_T^{ee} in Z events (solid points, data; open circles, simulation). The solid curve is the fit to the data ($\mu_1(p_T)$ in Equation 5.8). (Bottom) As above, but the fit to the data is subtracted from both data and simulation.

$$\sigma_2 \quad \leftarrow \quad \sigma_2 \cdot \frac{F^{\text{data}} + G^{\text{data}} p_T^{\text{true}}}{F^{\text{sim}} + G^{\text{sim}} p_T^{\text{true}}}$$

Before the first iteration, μ_1, σ_1, and σ_2 are just the curves fitted to the data; before the second iteration, μ_1, σ_1, and σ_2 are the data curves multiplied by the first iteration's correction factors. After two iterations, the simulation and data give consistent fit parameters ($\chi^2 < 0.001$).[11]

---

[11] We're tempted to call this procedure "unsmearing by perturbation." Its biggest virtue is that
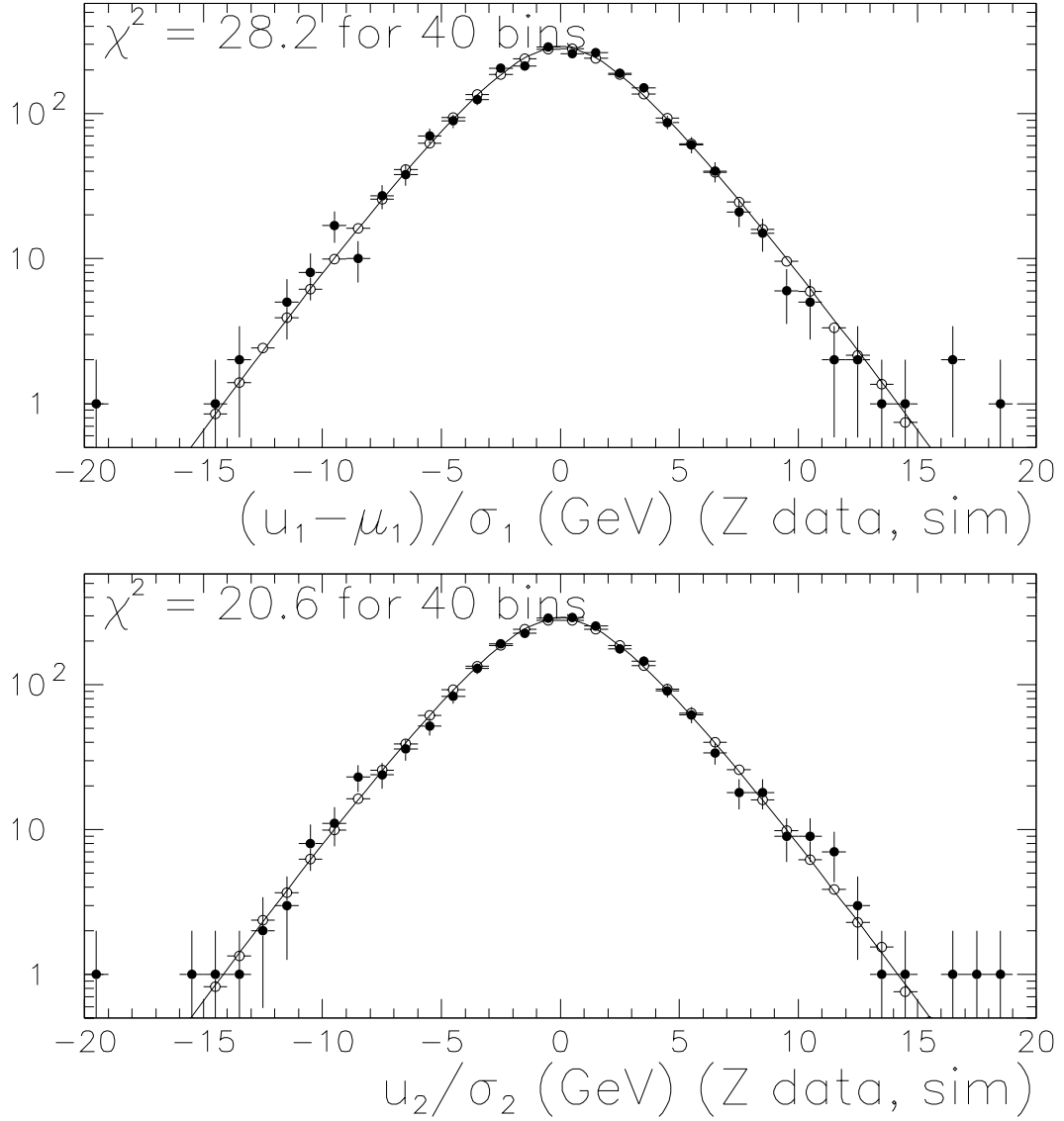
Figure 5.15: (Top) $(u_1 - \mu_1(p_T))/\sigma_1(p_T)$, for Z data (solid points) and simulation (open circles), where the μ_1 and σ_1 functions are from Equations 5.8 and 5.9. KS=16%. The curve is the min-bias resolution function S_{MB} (Equation 5.6). One of the 2206 data events lies outside the limits of the graph: the event has $M^{ee} = 107$ GeV, $p_T^{ee} = 19$ GeV, $u_1 = -53$ GeV, $\mu_1(p_T) = -12$ GeV. (Bottom) $u_2/\sigma_2(p_T)$ for Z data (solid points) and simulation (open circles), where the σ_2 function is from Equations 5.8 and 5.9. KS=79%. The curve is the min-bias resolution function. No events lie outside the limits of the graph. In both upper and lower plots, the shape is very well modeled over several orders of magnitude. Note that $\sigma_{1,2}$ are dimensionless.

---

it seems relatively foolproof.
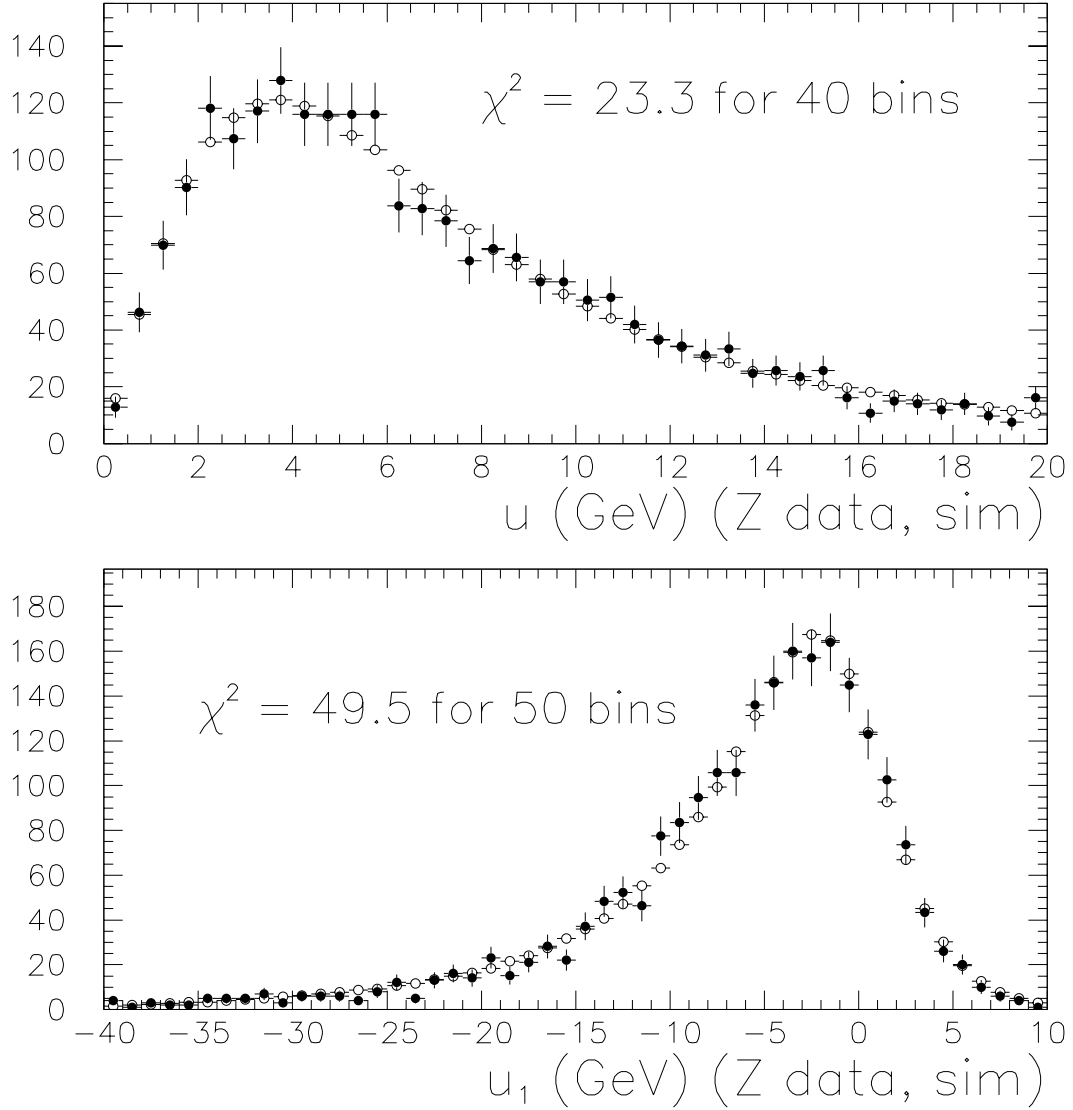
Figure 5.16: (Top) Recoil energy u for $Z \to ee$ data (solid points) and MC (open circles). KS=89%. (Bottom) Component u_1 of $\vec{u}$ along the $\vec{p}_T^{ee}$ unit vector, for $Z \to ee$ data (solid points) and MC (open circles). KS=75%.

5.5.3 Results of the recoil model

As shown in Figures 5.14–5.16, incorporating this model into the $Z \to ee$ simulation reproduces recoil distributions in the Z data very well.

Before we can sensibly compare the output of the recoil model, which is tuned from a sample of 2206 Z events, with the 49843-event W data sample, we need a mechanism for evaluating the effect of finite Z statistics on W Monte Carlo predictions. To assign a recoil model uncertainty to simulated W spectra, we use the covariance matrix from the model tuning procedure to throw multinormal septuplets

(A–G) of random numbers, producing a set of 54 alternative models that represent statistical variations from the fitted parameters, and generate a W dataset with each of these models.

Because the W sample is so much larger than the Z sample, the level of agreement between the W data recoil distributions and the simulated spectra varies considerably within the space of recoil model parameters that are consistent with the Z data. For instance, when comparing the u variable in the W data with the 54 simulated spectra, we find that χ^2 (for 40 bins) varies from 33 to 158, while the KS probability varies from 34% to $< 10^{-5}$. For the $u_\perp$ variable, χ^2 (for 40 bins) varies from 49 to 124, and the KS probability varies from 19% to $< 10^{-5}$. Of the 54 models, 3 have KS probability $> 5\%$ for both u and $u_\perp$, and 12 have KS probability $> 1\%$ for both; all of these 12 have $P(\chi^2) > 18\%$ in the recoil model covariance matrix.

The alternative set of model parameters that agrees best (best χ^2) with the u spectrum in the W data also agrees well with the central value of the Z fit: $\chi^2 = 6.4$ for 7 fitted parameters (A–G). The values of A–G are 0.704, -0.568, -0.00435, 0.919, 0.0263, 0.899, and 0.0148, respectively, with units as in Equation 5.9. We refer to this particular set of model parameters as the "W-data-preferred" parameters. A more formal procedure for choosing the W-data-preferred values would be to minimize a combined χ^2 that accounts for deviations from the Z fit and for disagreement with the u distribution in the W data. Since we demonstrate that a solution exists in which both χ^2 contributions are reasonable, we feel that the more formal procedure is not necessary.

In Chapter 7, we use the variation of fitted $,_W$ within these 54 alternative recoil models as a measure of systematic error, and we show that the difference between the central value of the Z fit and the W-data-preferred parameters is small in comparison with the quoted uncertainty.

Figures 5.17–5.19 compare simulated recoil spectra to the W data. We display the simulated spectra from the W-data-preferred model parameters. In the captions, we include information about the full range of model parameters.

5.6   Checking the simulation

In this section, we compare some predictions of TOYGEN and SSD with the data, and we compare some predictions of SSD with those of QFL.

5.6.1   Comparisons with the data

At the beginning of this chapter, we noted several important ingredients in the line-shape simulation. As we tuned the simulation's electron response, p_T^Z spectrum, and recoil response, we showed that the tuning produced good agreement between data
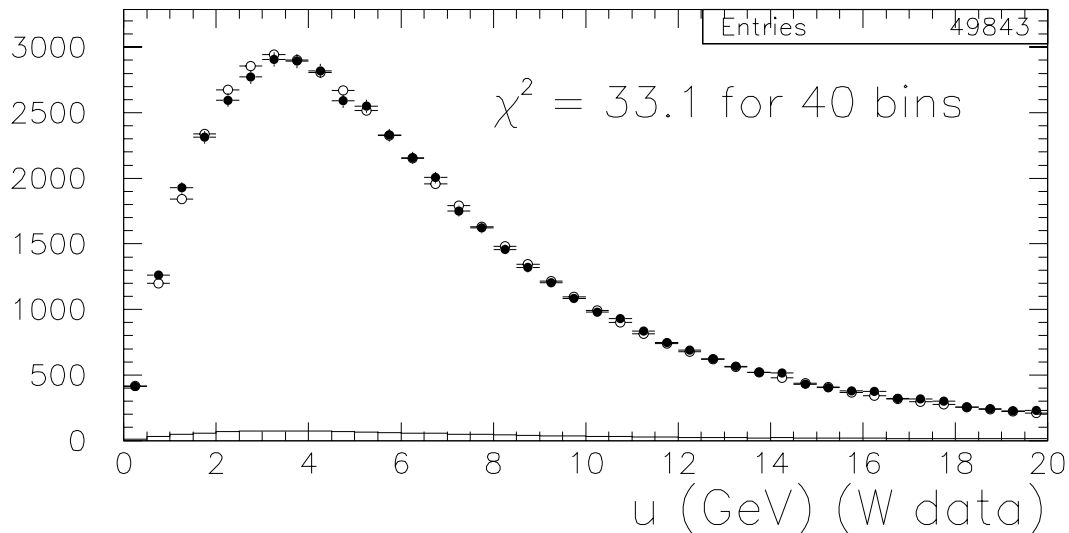
Figure 5.17: Magnitude of recoil energy, u, in W events. (Solid points, data, open circles, simulation.) Data mean and rms are 6.52 ± 0.03 GeV and 4.365 ± 0.014 GeV; MC mean and rms are 6.49 GeV and 4.33 GeV. KS=34%. The 54 model variations discussed in the text have mean 6.58 ± 0.05 GeV and rms 4.32 ± 0.015 GeV, where the uncertainty reflects finite Z statistics in tuning the model; the best Z fit has mean 6.56 GeV, rms 4.32 GeV, and $\chi^2 = 60.3$. In the W MC spectra, electron and photon quantities have been simulated with SSD, the track isolation cut has been simulated, and backgrounds have been added. The barely-visible histogram is the background shape.

and simulation. Here, we show the level of agreement between data and simulation in several other areas.

First, we consider geometric acceptance. Figure 5.20 shows the z-vertex distribution for W data and simulation. While there is room for improvement over the simple Gaussian model used in SSD, the agreement is adequate for this measurement. Figure 5.20 also shows the ϕ_0 distribution, folded into half of a 15° calorimeter wedge to improve the statistical power of the data. The simulation reproduces the sculpting effect that the calorimeter fiducial requirements have on the ϕ_0 distribution. Figure 5.21 shows the $|z|$ distributions of real and simulated W electrons at the CES and at the outer superlayer of the CTC, at which fiducial cuts in z are imposed. These plots give us confidence in both the modeling of the acceptance and the generation of W bosons with the correct angular distribution.

Because at moderate x ($x \approx \frac{1}{20}$ for Tevatron Z production) quarks are more likely to be found in the proton and antiquarks are more likely to be found in the antiproton, we expect Z bosons to have a net polarization. Because the weak interaction predicts both odd and even terms in $\cos\theta^*$ for the electrons in Z decay, we expect the angular distributions of e^+ and e^- to be distinct. Thus, comparing the $\cos\theta^*$ distribution for e^+ in data with the predictions for e^+ and e^- in the simulation, as we do in Figure 5.22, is an interesting check of boson production
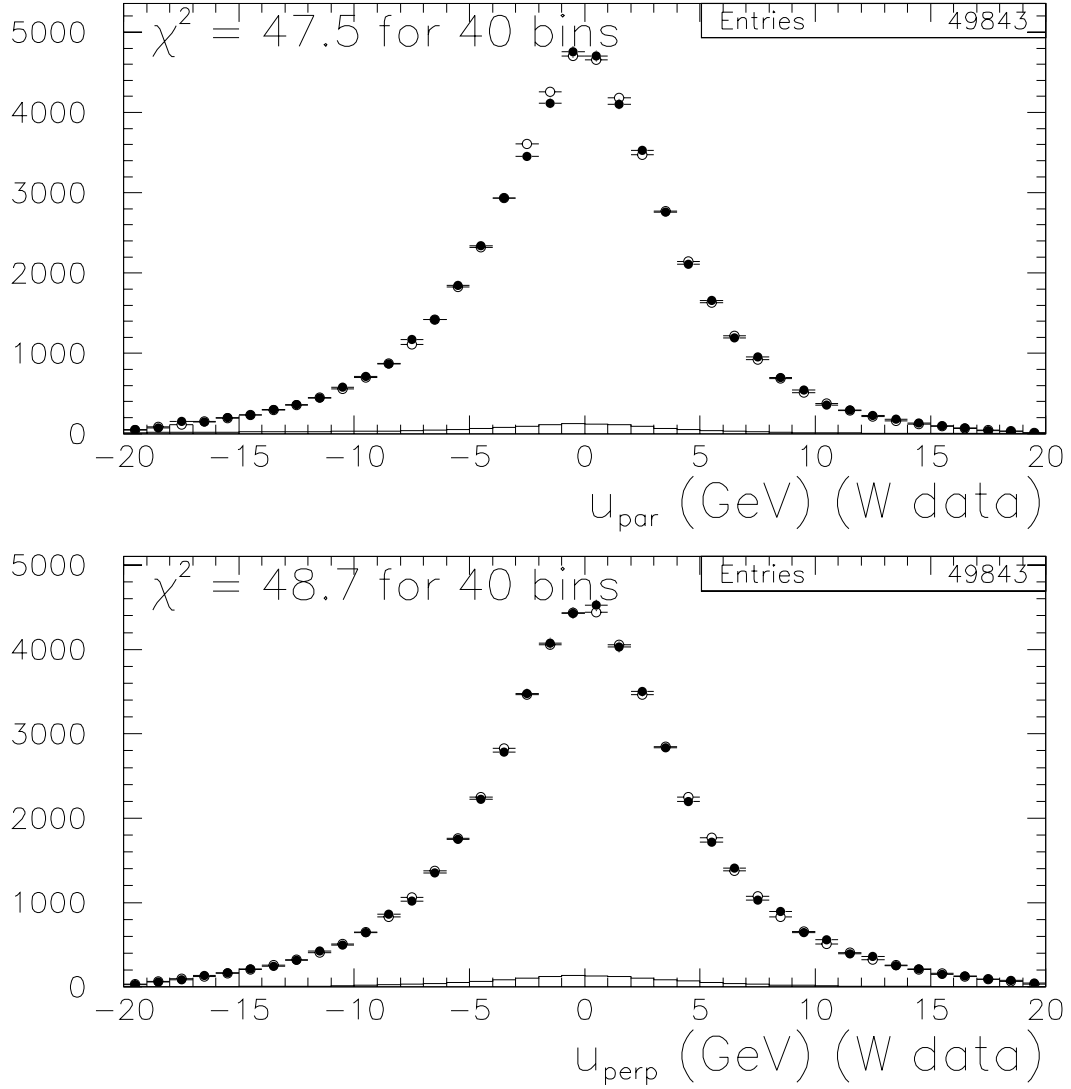
Figure 5.18: (Top) $u_{\parallel}$ (component of recoil parallel to electron direction). (Solid points, data; open circles, MC.) Data mean and rms are -477 ± 24 MeV and 5.44 ± 0.02 GeV. MC mean and rms are -486 MeV and 5.40 GeV. KS=23%. The 54 model variations have mean -495 ± 13 MeV (-430 MeV without BG), rms 5.44 ± 0.03 GeV; the best Z fit has mean -482 MeV, rms 5.44 GeV, and $\chi^2 = 47.2$. (Bottom) $u_{\perp}$ (component orthogonal to electron direction) for final recoil model parameters. (Solid points, data; open circles, MC.) Data rms is 5.64 ± 0.02 GeV. MC rms is 5.63 GeV. KS=19%. The 54 model variations have rms 5.69 ± 0.04 GeV; the best Z fit has rms 5.67 GeV, $\chi^2 = 68.2$.

and decay in TOYGEN. The e^+ data are in good agreement with the e^+ prediction and are clearly capable of distinguishing the e^+ and e^- predictions. Note that we have not divided out the acceptance for either data or simulation. The lower half of Figure 5.22 checks that Z bosons are produced with a reasonable rapidity distribution by comparing longitudinal momentum spectra for data and simulation.
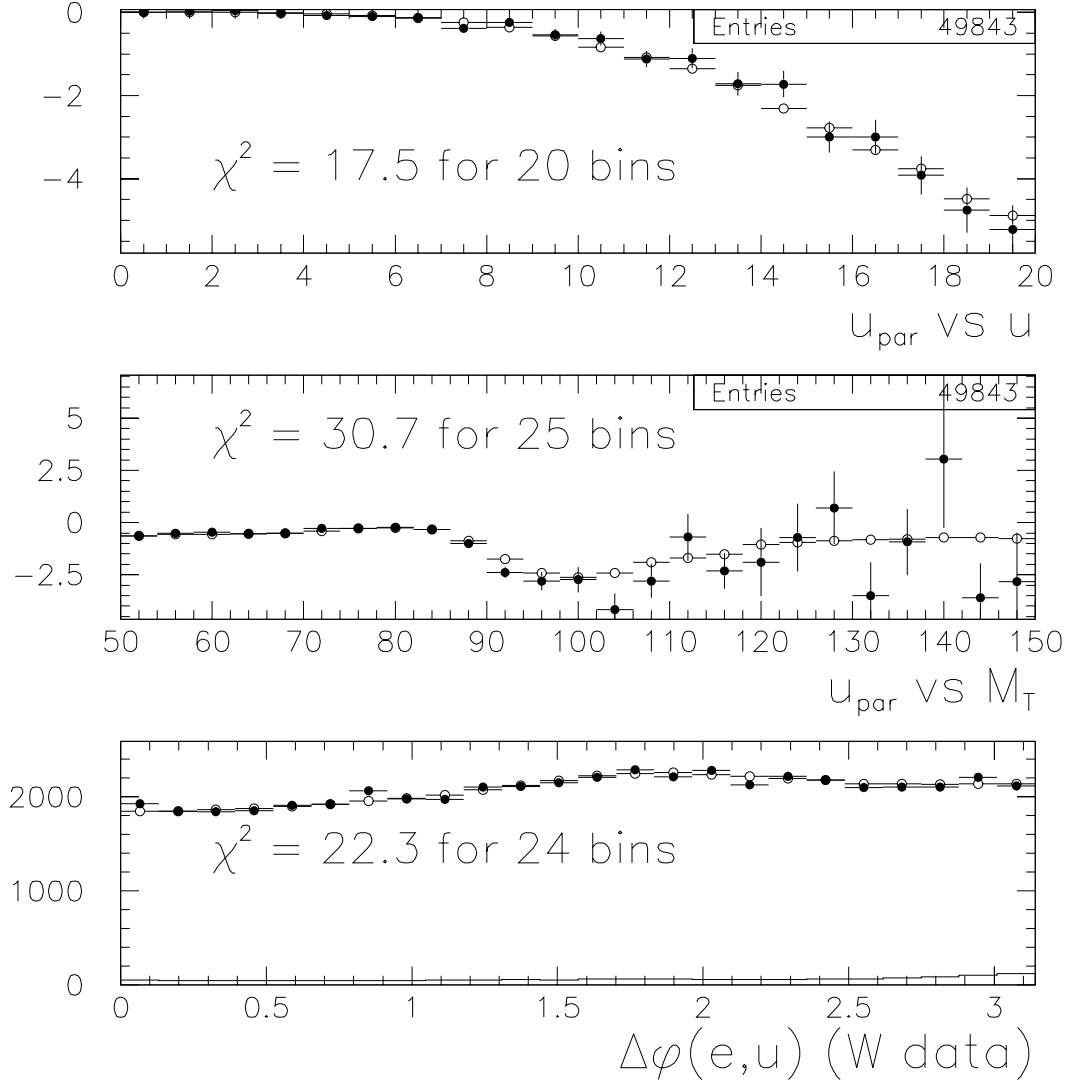
Figure 5.19: (Top) Mean component of recoil along electron direction as a function of total recoil energy. (Center) Mean component of recoil along electron direction as a function of transverse mass. In the region $M_T \approx 100$ GeV, the mean $u_\parallel$ decreases, indicating that many of these events are on-shell Ws that have $M_T > M_W$ because the electron is boosted and the W p_T underestimated. The shape is modeled reasonably well. (Bottom) Angle between electron and recoil energy vector. KS=49%.

Finally, the E_T and $\not{E}_T$ spectra in W events, shown in Figure 5.23, are sensitive to a wide range of simulation inputs, including electron energy resolution, the W p_T spectrum, the recoil model, and backgrounds (discussed in Chapter 6).

77
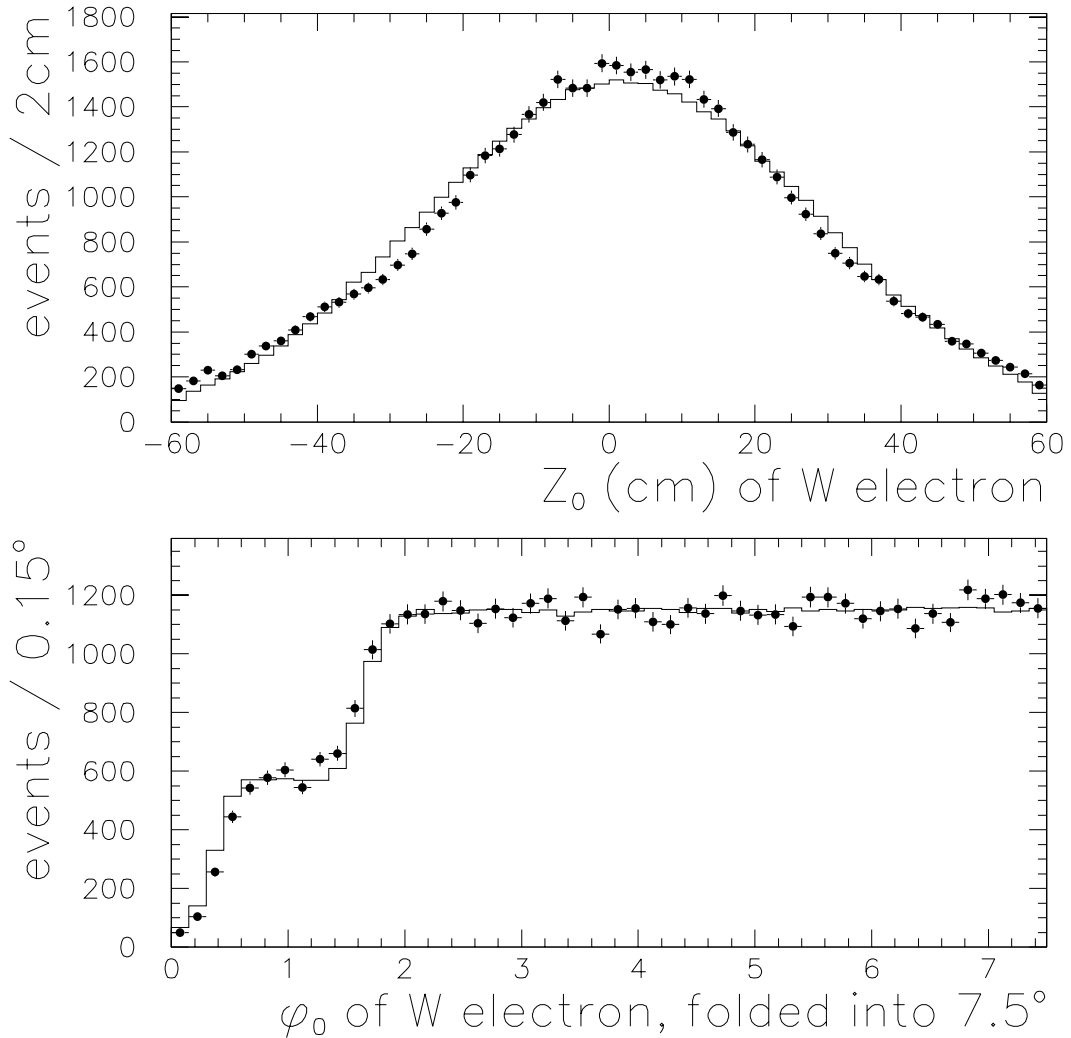
Figure 5.20: (Top) z-vertex distribution from W data (solid points) and SSD simulation (histogram). The simulation uses a Gaussian distribution, which is clearly not statistically compatible with the data, but which approximates the shape reasonably well. The simulation models the spread in z of $p\overline{p}$ collisions adequately for this measurement. (Bottom) ϕ_0 mod 15° of W electron (to match the 15° calorimeter segmentation), folded in half along the $\phi_0 = 7.5°$ axis. (Solid points, data; histogram, SSD simulation.) The electron ϕ_0 distribution is sculpted by the CEM fiducial requirement $|x_{\mathrm{cal}}| < 21$ cm (measured by the CES, at $r \approx 184$ cm), which eliminates the outer 12.5% of each 15° wedge. The ϕ_0 acceptance contributes to the p_T^Z acceptance at low p_T^Z. The KS probability is 17% while χ^2 is 108 for 50 bins, indicating that the shape is modeled well overall, but poorly in a few bins.

5.6.2 Checks with QFL

As a consistency check on the simulation of the electron variables, we fit M_Z, κ, and g_2 for a sample of approximately 160,000 $Z \rightarrow ee$ events (after all cuts) generated
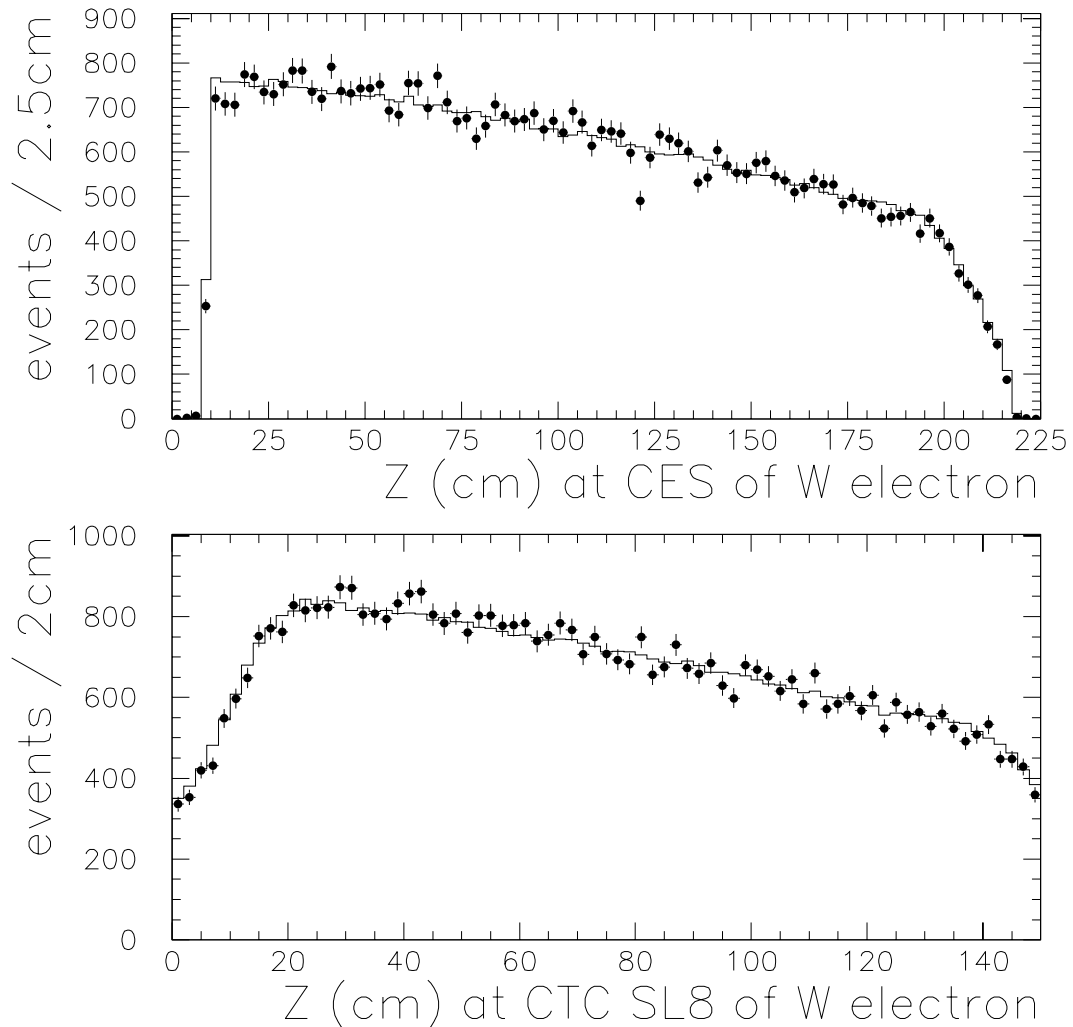
Figure 5.21: (Top) Distribution of $|z|$ at the CES ($r \approx 184$ cm) in W data (solid points) and SSD simulation (histogram). The shape is modeled well, except for the CES module boundary at $z \approx 121$ cm. χ^2 is 148 for 90 bins, while the KS probability is 36%. (Bottom) Distribution of $|z|$ at CTC superlayer 8 ($r = 130$ cm) in W data (solid points) and SSD simulation (histogram). χ^2 is 87 for 75 bins, and the KS confidence level is 46%. These plots show that the acceptance in z is modeled well at the radii at which CEM and CTC fiducial requirements are imposed.

with TOYGEN, simulated with QFL, and processed with the same analysis code used for the data. We set QFL's CEM constant term to 1.5% and we measure $\kappa = 1.54 \pm 0.03\%$. We use $g_2 = 0.6$ in the generator and measure $g_2 = 0.63 \pm 0.01$ by fitting the p_T spectrum and $g_2 = 0.585 \pm 0.014$ by fitting the $\Delta\phi$ spectrum.

Because QFL uses a more sophisticated model of calorimeter response than SSD, we must define what we mean by energy scale in QFL before we can compare Z masses in the two simulations. If we calibrate QFL using a sample of

79
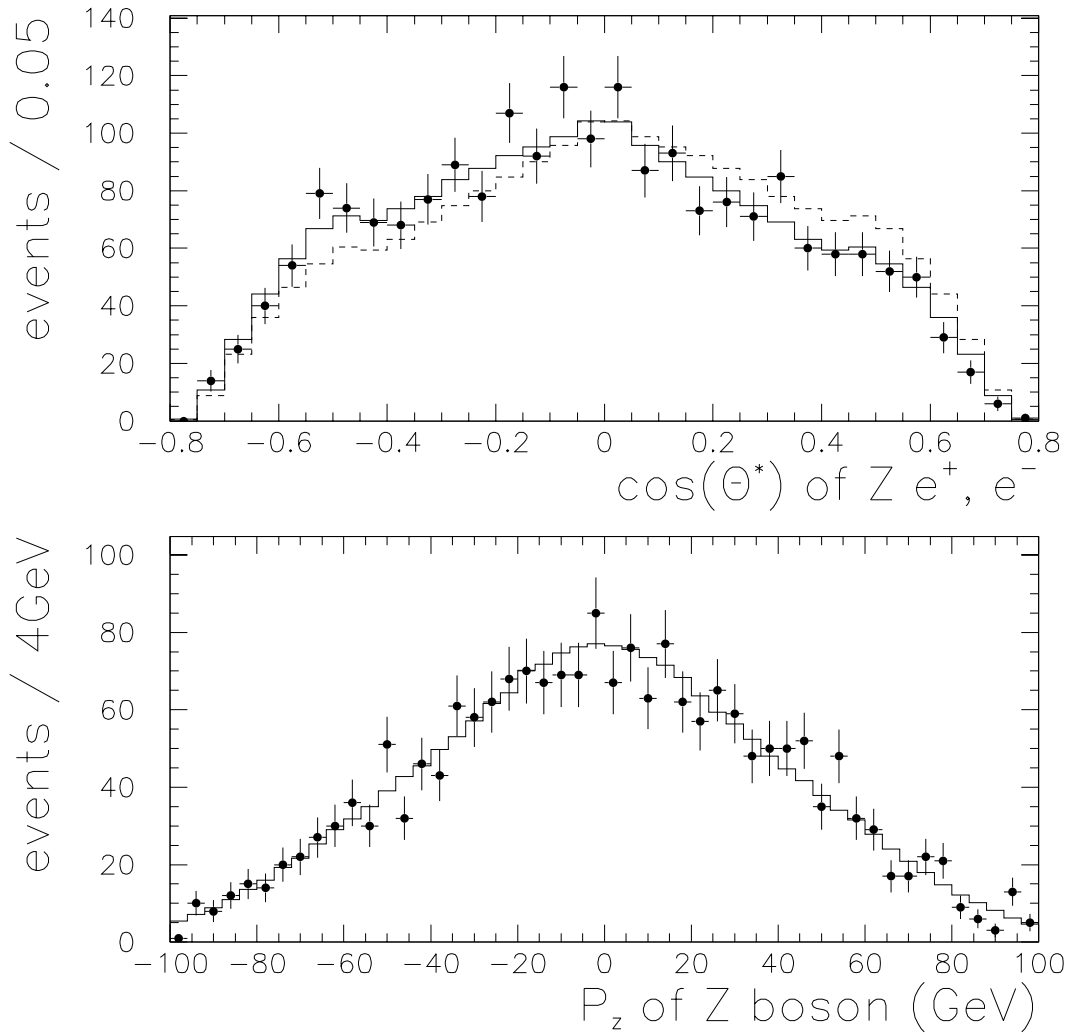
Figure 5.22: (Top) $\cos(\theta^*)$ (in the Z boson rest frame) for e^+ in Z data (solid points) and SSD simulation (solid histogram); the dashed histogram is the prediction for e^-. $\chi^2 = 26$ for 32 bins, KS $= 46\%$. The charge asymmetry is evident: if we compare the e^+ data to the e^- simulation, then $\chi^2 = 69$ and KS $< 10^{-5}$. (The distribution does not resemble textbook plots of $\cos(\theta^*)$ because the large acceptance effects have not been unfolded.) (Bottom) Z boson longitudinal momentum in data (solid points) and SSD simulation (histogram). $\chi^2 = 52$ for 50 bins, KS $= 62\%$. These plots suggest that the boson polarization, weak decay, and rapidity distribution have been properly implemented in TOYGEN.

$E = 40$ GeV electrons, disabling bremsstrahlung in the inner detector material, we
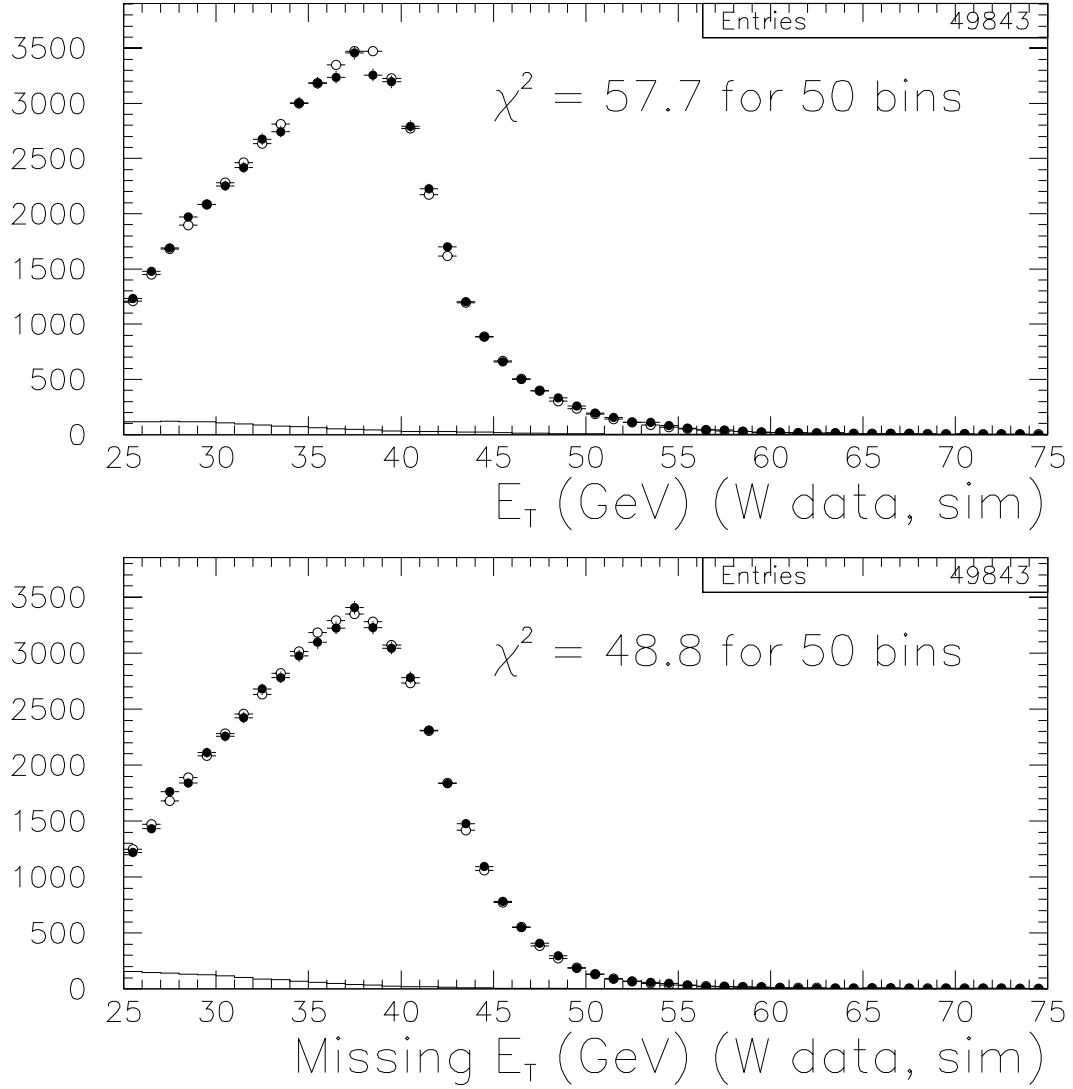
Figure 5.23: (Top) Electron E_T spectrum of W data (solid points) compared with simulation (open circles). KS=4%. (Bottom) $\not{E}_T$ spectrum of W data (solid) compared with simulation (open). KS=18%. Both of these plots are shown for nominal simulation input , $_W = 2.077$ GeV, not the final fitted value. The dribble is the background.

measure $M_Z^{\mathrm{QFL}}/M_Z^{\mathrm{SSD}} - 1 = -0.075 \pm 0.027\%$.[12] Using $E = 40$ GeV photons, disabling pair production in the inner detector material, we measure $-0.319 \pm 0.032\%$. In SSD, both electron and photon response are unity in the absence of inner-detector material. Once an electron from W or Z decay has traversed the inner detector,

---

[12] To calibrate QFL, we generate electrons (or photons) using a Gaussian distribution in z_0, a uniform distribution in ϕ, and an η distribution uniform in $[-1, 1]$. We then apply CEM fiducial requirements and response-map corrections and average E in the interval 35–45 GeV. Material effects are never disabled when simulating $Z \to ee$ events—only in the single-particle events used for checking QFL's internal energy scale.

about 10% of its energy is carried by photons on average. Thus, a fair comparison with SSD is $0.9 \times (-0.075\%) + 0.1 \times (-0.319\%) = -0.10 \pm 0.03\%$, which is well within the 0.2% uncertainty we assigned to the energy scale in Section 5.4.1.[13] In Chapter 7, when we fit Γ_W in $W \to e\nu$ events simulated with QFL as a further check, we will set QFL's energy scale such that QFL and SSD agree on M_Z.

---

[13] Allowing bremsstrahlung and pair production in the calibration samples of 40 GeV electrons and photons would change the electron result to $+0.204 \pm 0.029\%$ and the photon result to $-0.237 \pm 0.024\%$.

Chapter 6

Backgrounds

In this chapter, we discuss several event-selection criteria specifically designed to remove backgrounds from the $W \to e\nu$ sample, demonstrate that these criteria are effective for rejecting background, and estimate the sizes and kinematic shapes of backgrounds remaining in the $W \to e\nu$ sample.

6.1 $Z \to ee$

6.1.1 $Z \to ee$ removal

It is very improbable for a well-measured $Z \to ee$ event to fake the $W \to e\nu$ signature: $\not{E}_T > 25$ GeV is unlikely to arise from recoil resolution alone, and the presence of a second high-p_T electron makes $u < 20$ GeV unlikely.[1] One way to illustrate this point is to note that none of the 2206 $Z \to ee$ candidate events surviving cuts A–U of Table 4.1 is found among the 49843 $W \to e\nu$ candidate events of Table 4.5. Thus, we do not expect the W sample to contain $Z \to ee$ events in which two electrons, with energies measured by the calorimeter, form an invariant mass near M_Z.

Rather, we expect a $Z \to ee$ event to pass the $W \to e\nu$ selection if one of the electrons lands in a region of poor calorimeter response (see Section 3.2.6), so that its energy is badly undermeasured. In the region $|\eta| < 1.2$, covered by the CTC, we can find these events by searching for a track whose momentum can be combined with the first electron to form a mass near M_Z.

To prevent the Z removal from eliminating too many non-Z events, we impose several requirements on electron+track Z candidates. We consider all tracks that

---

[1] Recall (Section 3.4.3) that one electron is excluded from the $\vec{u}$ calculation when selecting W events and that two electrons are excluded when selecting Z events.

have $p_T^{\mathrm{BC}} > 15$ GeV, that have been fitted using both axial and stereo CTC information, and that are consistent with originating from the same z position along the beamline as the first electron. We also require $\Delta\phi(\mathrm{electron}, \mathrm{track}) > 3\pi/4$, which is equivalent to requiring that the reconstructed Z p_T not be too large. Figure 6.1 shows that this cut is about $96.4 \pm 0.5\%$ efficient.[2] We then require $75 < M(\mathrm{electron}, \mathrm{track}) < 105$ GeV. Requiring opposite charge, we remove 699 Z candidates. By looking at like-sign events, we estimate that 81 ± 9 of the 699 are fake. Figure 6.2 (Top) shows mass distributions for opposite-sign and like-sign combinations. The shape agrees well with a QFL simulation. Figure 6.2 (Bottom) shows the track positions extrapolated to the CEM and folded into a single 15° calorimeter wedge. Clearly most of the Z candidates' tracks are near azimuthal wedge boundaries, or in the 90° and 30° regions. We estimate residual Z contamination below.
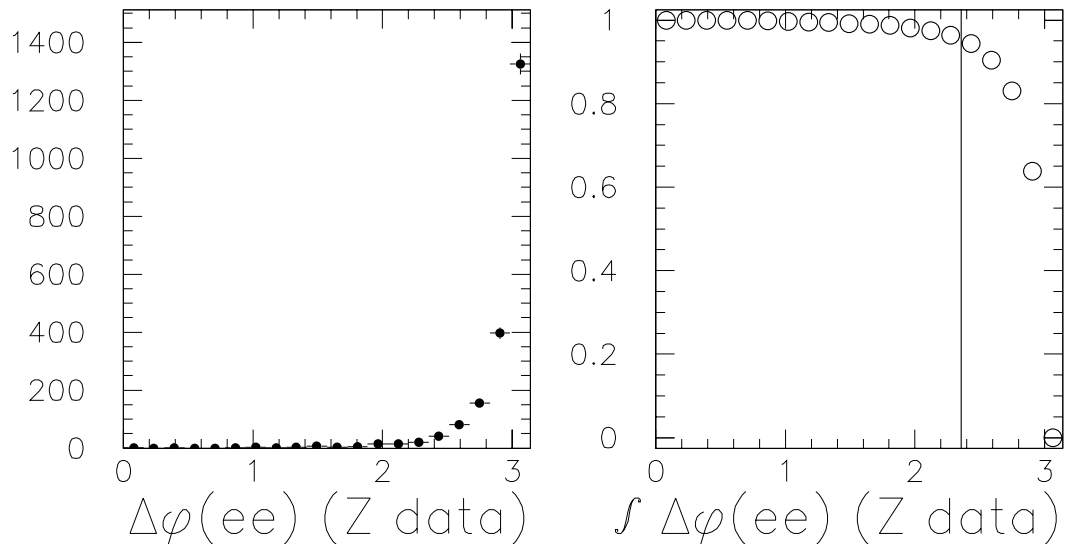
Figure 6.1: (Left) $\Delta\phi(ee)$ distribution for $Z \to ee$ data. Out of 2075 events, 75 have $\Delta\phi < 3\pi/4$. (Right) Integrated distribution.

6.1.2 Residual $Z \to ee$ background

Because most of CDF's calorimeter cracks, described in Section 3.2.6, are in the region $|\eta| < 1.2$, where the CTC can efficiently find high-p_T tracks, we expect in most cases to be able to find a lost Z electron's track in the CTC. To estimate the number of Z events remaining after the Z-removal procedure, we simulated 10^6 TOYGEN $Z \to ee$ events with QFL and ran both the Z and the W analysis codes

---

[2] We do this to reduce background from multijet events, which arises because the Z removal is applied before the electron ID cuts (see Table 4.5).

Region	OS data	LS data	OS-LS	MC
$|x| < 21$ cm, $|z| < 10$ cm	128	8	120	106
$|x| < 21$ cm, $210 < |z| < 280$ cm	138	20	118	89
$10 < |z| < 210$ cm	317	38	279	304

Table 6.1: Number of $Z \to$ electron + track candidates found in the $90°$ region, the $30°$ region, and the azimuthal boundaries between CEM wedges. Opposite-sign and like-sign combinations are listed separately, to provide a background estimate. The distribution matches a Monte Carlo prediction reasonably well.

on the output. We apply cuts A–U in Table 4.1 to both data and MC and normalize the MC to the 2206 data events.

Using this normalization factor, we scale the number of MC electron+track events found by the W analysis code and predict that 570 such events should be found in the data, to be compared with $699 - 81 = 618$ actually found in the data. The data and prediction agree at the 10% level, which is well within the uncertainty we assign below to the MC prediction.

We can argue in two ways that tracking efficiency (which may be optimistic in QFL, especially at high $|\eta|$) is not causing us to miss a large number of Z electrons in the $30°$ region. First, we look at the ratio of electron+track Z candidates in the $30°$ and $90°$ regions. (See Table 6.1 and Figure 6.3.) This ratio is 0.84 ± 0.02 in QFL and 0.98 ± 0.13 in the data. There is reasonably good agreement and no evidence of a deficit of events in the $30°$ region in the data. Second, we can make a crude estimate of tracking inefficiency in the $30°$ region by plotting tracking efficiency vs. η (as determined in Ref. [76]) and plotting the η distribution of Z candidates removed from the W data sample. As shown in Figure 6.4, the rapid falloff in tracking efficiency begins somewhat beyond the $30°$ region (i.e. we have efficient tracking into at least part of the PEM). This method estimates a negligible three Z events lost in the η region in which the tracking efficiency begins to fall.

By counting the number of MC $Z \to ee$ events that pass through the W analysis code without being flagged as Z candidates, we can estimate the number of $Z \to ee$ events remaining in the real W sample. The QFL simulation predicts 170 ± 85 events. As shown in Figure 6.5, about half of these events are predicted to arise from the $10°$ region ($|\eta| \approx 2.5$) between the PEM and FEM calorimeters. Because there is no charged particle tracking in this η region, the prediction is not trivial to test with data. Thus, we have assigned a large systematic uncertainty.

Using completely different methods, Andrew Gordon [00] predicts 32 lost Z events in the region $|\eta| < 1.2$ and 8 in $|\eta| > 1.2$. The differences are understandable. The prediction for $|\eta| < 1.2$ is lower because Andrew searches for tracks of $p_T^{\mathrm{BC}} > 10$ GeV and has no $M(e, \mathrm{track})$ and $\Delta\phi(e, \mathrm{track})$ requirements. If we apply these relaxed criteria to the simulation, we predict 20 lost Z events in $|\eta| < 1.2$.

Additionally, Andrew assumes a 7% tracking inefficiency in the 30° region; adding this assumption, we predict 30 events, in good agreement with Andrew's 32. The prediction for $|\eta| > 1.2$ is much lower because Andrew assumes perfect electron response in the 10° region, while QFL assumes a substantial region of poor response at the PEM-FEM boundary. The $Z \to ee$ events lost in the 10° region are not as important in this analysis as those lost in more central regions, as the former tend to have very low transverse mass.

Figure 6.6 shows some predicted properties of lost Z events. We predict that 57% of lost Z events, or 95 ± 50 events, have $65 < M_T < 100$ GeV, that 3.1% (5.3 ± 2.7 events) have $M_T > 100$ GeV, and that 1.6% (2.7 ± 1.4 events) have $M_T > 110$ GeV.

6.2   Multijet background

6.2.1   Track isolation

To discriminate between electrons from W and Z decay, which tend not to have other charged particles nearby, and electron candidates from non-electroweak sources,[3] we use the N_{cone} track isolation variable defined in Section 3.4.5. Figure 6.7 shows $\not{E}_T$ distributions in inclusive electrons (Table 4.4) for various values of N_{cone}; by inspection of the $\not{E}_T > 25$ GeV region, about 95% of Ws have $N_{\mathrm{cone}} = 0$ and an insignificant fraction have $N_{\mathrm{cone}} > 2$; in Section 5.3, we predicted that 0.05% of real $W \to e\nu$ events, or about 25 events, have $N_{\mathrm{cone}} > 2$. We require $N_{\mathrm{cone}} = 0$ to obtain a clean sample of W electrons.

Figure 6.8 shows the effect of a track isolation cut in the Z data (Table 4.2, cuts A–D). The figure illustrates that even after other ID requirements are imposed, events having $N_{\mathrm{cone}} > 2$ are dominated by background. Note that electron ID cuts are applied only to the "first" electron, to make the comparison between W and Z events as fair as possible. Figure 6.9 shows the effect of the track isolation cut when the other electron ID cuts (Table 4.2, cuts B, C, and D) are not applied. The figure demonstrates that the N_{cone} variable is a powerful discriminant against background, even in a relatively impure sample. In neither figure is there any evidence that real Zs remain in the $N_{\mathrm{cone}} > 2$ background sample.

Figure 6.10 shows the $\not{E}_T$ distribution for W candidates with $N_{\mathrm{cone}} = 0$ and > 2. Again we think we can safely say that the W contamination in the $N_{\mathrm{cone}} > 2$ sample is not large.

---

[3] We note some examples of these sources in Appendix C.

6.2.2 Residual QCD background

We estimate the number of dijet background events remaining in the W sample by extrapolating from the $N_{\mathrm{cone}} > 2$ region to the $N_{\mathrm{cone}} = 0$ region, using a sample of inclusive electrons with low $\not{E}_T$ to obtain the N_{cone} distribution for dijet events. We have two methods to estimate the M_T shape of these background events. The first method (described in Appendix C) uses a sample of photon conversion events to model the $\vec{E}_T$ and $\vec{u}$ distributions of the background. The second method just uses the M_T shape of the $N_{\mathrm{cone}} > 2$ events in the W sample. The two methods give consistent results.

In predicting the number of dijet background events remaining in the W sample, we assume that W candidates with $N_{\mathrm{cone}} > 2$ are pure background. We also assume that the N_{cone} shape of the dijet background remaining in the W sample is similar to the N_{cone} shape of inclusive electron events that have a small $\not{E}_T$. We use three subsamples of the inclusive electron sample (which is defined in Table 4.4) to estimate this N_{cone} shape: $\not{E}_T < 10$ GeV; 10 GeV $< \not{E}_T < 20$ GeV; and $\not{E}_T < 15$ GeV, $u < 30$ GeV. Using the numbers from Table 6.2, we infer that for every background event with $N_{\mathrm{cone}} > 2$, there are 1.3 ± 0.4 background events with $N_{\mathrm{cone}} = 0$.

Returning to the W sample, we apply all cuts from Table 4.5, but replace $N_{\mathrm{cone}} = 0$ with $N_{\mathrm{cone}} > 2$, and we find 347 events, five of which have $M_T > 100$ GeV and two of which have $M_T > 110$ GeV. (See Figure 6.11.) Thus, we expect 450 ± 110 total dijet background events.[4] If we use the M_T shape of the $N_{\mathrm{cone}} > 2$ events as the M_T shape of the background, we predict 6 ± 3 background events at $M_T > 100$ GeV and 3 ± 2 at $M_T > 110$ GeV. Using the M_T shape fit from the photon conversion data instead (see Figure 6.12), we predict 10 ± 3 events at $M_T > 100$ GeV and 5 ± 2 at $M_T > 100$ GeV. We will use the shape from the conversions and use 10 ± 4 and 5 ± 3 as the number of dijet background events with $M_T > 100$ GeV and $M_T > 110$ GeV respectively. As a check, we predict 200 ± 50 dijet background events ($0.56 \pm 0.14\%$) in the 35557 events in the region 65 GeV $\leq M_T < 100$ GeV, which is consistent with Andrew Gordon's estimate of $0.39 \pm 0.20\%$ [00].

Given an estimate of QCD backgrounds in the W sample, we can use the data in Table 6.2 to estimate the number of real W events rejected by the $N_{\mathrm{cone}} = 0$ cut in Table 4.5. We estimate 800 ± 150 dijet events in the $N_{\mathrm{cone}} = 1$ bin and 350 ± 50 in the $N_{\mathrm{cone}} = 2$ bin, leaving 1900 ± 150 W events in $N_{\mathrm{cone}} = 1$ and 450 ± 50 in $N_{\mathrm{cone}} = 2$. The inefficiency of the $N_{\mathrm{cone}} = 0$ cut for real W events is then $4.7 \pm 0.3\%$, consistent with both the $5 \pm 1\%$ found for Z electrons in Section 6.2.1 and the 5% (1.5% from tridents and 3.5% from the underlying event) found with SSD and the W list in Section 5.3.

---

[4] Using the W list estimate that 25 of these 347 events are from W decay would change the answer by only 7%, which is small compared with the 30% systematic uncertainty in determining the N_{cone} shape of the background.

Cuts	events	$N_{\text{cone}} = 0$	$N_{\text{cone}} = 1$	$N_{\text{cone}} = 2$	$N_{\text{cone}} > 2$	$\frac{N_{\text{cone}}=0}{N_{\text{cone}}>2}$
$\not{E}_T < 10$	37171	22.8%	37.4%	18.7%	21.0%	1.1
$10 < \not{E}_T < 20$	27419	24.5%	44.0%	15.5%	16.0%	1.5
$\not{E}_T < 15, u < 30$	34715	21.7%	45.4%	17.9%	15.1%	1.4
$\not{E}_T > 25, u < 20$	50582	93.9%	4.7%	1.2%	0.26%	360
Table 4.5 cuts	53643	92.9%	5.0%	1.5%	0.65%	140
veto EIA	3131	77.0%	10.0%	6.2%	6.8%	11

Table 6.2: (First four lines) Distribution of track isolation variable N_{cone} for three background-enriched samples and for a W-enriched sample, all selected from the inclusive electron dataset. We infer that for dijet background events, $\frac{N_{\text{cone}}=0}{N_{\text{cone}}>2} = 1.3 \pm 0.4$. (Last two lines) We also include, for reference, the N_{cone} distribution for the $W \to e\nu$ sample, selected with all cuts listed in Table 4.5 except N_{cone}, and for the subset of those events that fails the Level-3 inclusive electron trigger. We estimate a QCD background fraction of $0.4 \pm 0.1\%$ for the inclusive-electron W events, $0.9 \pm 0.2\%$ for the Table 4.5 W events, and $12 \pm 3\%$ for the Table 4.5 W events that fail the inclusive-electron trigger.

6.3 $W \to \tau\nu \to e\nu\nu\nu$

The process $W \to \tau\nu \to e\nu\nu\nu$ looks just like $W \to e\nu$, but with reduced E_T and $\not{E}_T$ and at a rate reduced by $B(\tau \to e\nu\nu)$. Calculating this background is simply a Monte Carlo exercise. To predict this rate, we use TOYGEN and QFL. We find $\frac{N(W \to \tau \to e)}{N(W \to e)} = 1.8 \pm 0.2\%$ for $M_T < 200$ GeV, or $0.7 \pm 0.1\%$ for $65 \text{ GeV} \leq M_T < 100$ GeV. We also find that 0.46% of these $W \to \tau \to e$ events have $M_T > 100$ GeV and 0.28% have $M_T > 110$ GeV.

Normalizing to $(49843 - 170 - 450)/1.018 = 48353$ (see Table 6.3) estimated $W \to e\nu$ events in the W data sample, we expect 870 ± 100 $W \to \tau \to e$ events in all, 4 ± 1 with $M_T > 100$ GeV, and 2.5 ± 1 with $M_T > 110$ GeV. Figure 6.13 shows the expected M_T shape of this background.

As a check, we predict $\frac{0.007}{1.007} \times 5718 = 40 \pm 5$ $W \to \tau \to e$ events (neglecting other backgrounds) in the $65 \text{ GeV} \leq M_T < 100$ GeV region of the Run Ia electron W mass sample. The value computed in that analysis is 45 events [77].

6.4 Cosmic rays

A few obvious cosmic rays found in an early hand-scan of $M_T > 100$ GeV events motivated us to impose an 0.5 cm cut on the electron track's impact parameter with respect to the beamline, d_{beam}. In fact most cosmic rays fail the $p_T^{\text{BC}} > 15$ GeV cut, so the d_{beam} cut has little effect.[5] If the $|d_{\text{beam}}| < 0.5$ cm cut is applied after all other cuts, it removes 0.2% of the W sample, consistent with an $0.23 \pm 0.08\%$ inefficiency measured in $Z \to ee$ tracks, illustrated in Figure 6.14.

We use the d_{beam} distribution to estimate residual cosmic ray contamination in the W sample. To do this, we remove the $|d_{\text{beam}}| < 0.5$ cm cut and replace the $p_T^{\text{BC}} > 15$ GeV cut with a $p_T > 15$ GeV cut, so that electrons with large impact parameter are allowed in the sample. Since about 0.22% of real W electrons will fail a $|d_{\text{beam}}| < 0.5$ cm cut, we go all the way out to $|d_{\text{beam}}| > 2.5$ cm to select a sample enriched in cosmic rays. We find 24 events passing cuts A–M in Table 4.5 (with d_{beam} removed and p_T^{BC} replaced by p_T). This subsample appears to be a combination of cosmic ray events and events with a dense jet, hence poor tracking resolution, near the "electron" track. After applying cuts N–R from Table 4.5, we have nine events with $|d_{\text{beam}}| > 2.5$ cm, all of which look like cosmic ray events. An example event is shown in Figure 6.15. Figure 6.16 shows d_{beam} and M_T distributions for the $|d_{\text{beam}}| > 2.5$ cm events.

---

[5] Consider a sample of cosmic rays having "infinite" momentum and a flat distribution of impact parameter. Since the beam constraint changes $\frac{1}{p_T}$ by roughly $0.05 \cdot d_{\text{beam}}$, a cosmic ray with $|d_{\text{beam}}| > 1.3$ cm will fail the p_T^{BC} cut.

Source	$M_T < 200$	$65 \leq M_T < 100$	$100 \leq M_T < 200$	$110 \leq M_T < 200$
$Z \to ee$	170 ± 85	95 ± 50	5 ± 3	3 ± 1.5
dijets	450 ± 110	200 ± 50	10 ± 4	5 ± 3
$W \to \tau \to e$	870 ± 100	250 ± 30	4 ± 1	2.5 ± 1
cosmic rays	0^{+1}_{-0}	0	0	0
total BG	1490 ± 170	545 ± 80	19 ± 5	10.5 ± 3.5
candidates	49843	35557	456	215

Table 6.3: Summary of background estimates.

If we make the conservative assumption that cosmic rays have a flat distribution in impact parameter[6] and the rather bold assumption that tracking efficiency does not vary rapidly with d_{beam} out to $|d_{\text{beam}}| \sim 15$ cm,[7] we can estimate the number of cosmic rays passing $|d_{\text{beam}}| < 0.5$ cm to be $9 \times \frac{0.5}{15-2.5} = 0.36$ events. We think it is safe to quote 0^{+1}_{-0} as the residual cosmic ray background.

6.5 Summary of backgrounds

We summarize the background estimates in Table 6.3 and Figure 6.17.

---

[6] For a finite range of incident angles, we might expect something more like $P(|d_{\text{beam}}|) \propto |d_{\text{beam}}|$.

[7] This is not as crazy as it may seem. A track with $p_T \approx \infty$, $d = 15$ cm has an aspect angle (angle with respect to the radial direction) at SL4 ($R \approx 82$ cm) of about $10°$—close to that of a 2 GeV track with $d = 0$. Also note the amusing fact that the absolute value of the former track's aspect angle *decreases* from the inner to the outer superlayers. (The search for tracks begins in the outer superlayers, and track segments with small aspect angles are more likely to be found.)
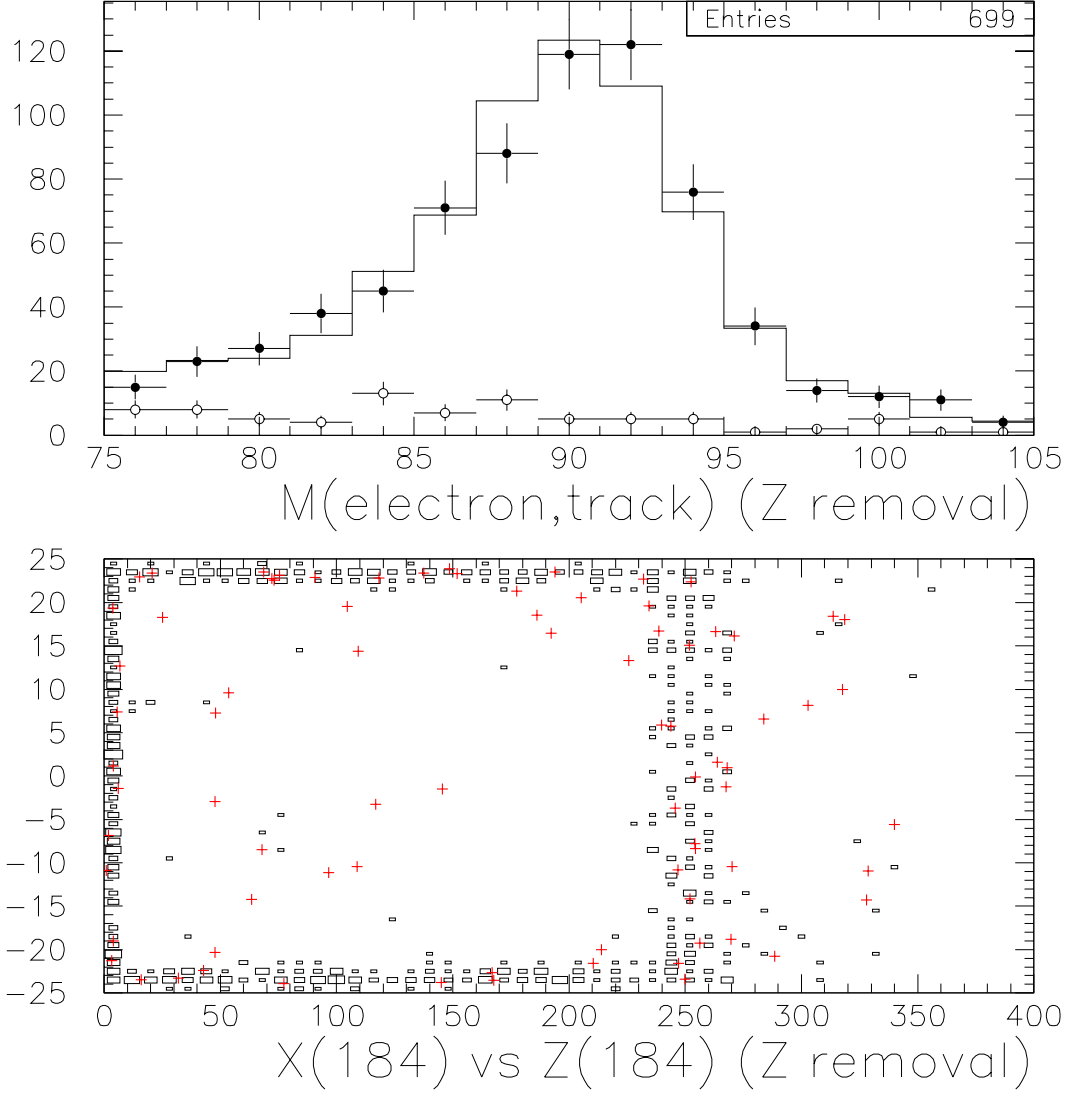
Figure 6.2: (Top) Invariant mass of first electron and high-p_T track of opposite sign (solid points) and same sign (open circles). There are 699 OS events and 81 LS events. The solid histogram is the mass spectrum predicted by the simulation (described in Section 6.1.2), normalized to 618 events and added to the 81 LS events in the data. χ^2 is 14.6 for 14 degrees of freedom. (Bottom) x vs. z (in CES local coordinates) for track that is second leg of Z candidate. The "box" histogram shows the OS candidates, and the crosses show the LS background. The OS events are predominantly from calorimeter wedge boundaries and the $\theta = 90°$ and $\theta \approx 30°$ regions. There is some excess of LS events in the crack regions, presumably from cases in which the $\not{E}_T$ is caused by a lost jet. We expect most such events to be eliminated by the electron ID cuts (which are after the Z removal in the event selection). Note that the z axis extends well beyond the physical length of the CEM so that high-η tracks can be conveniently plotted.
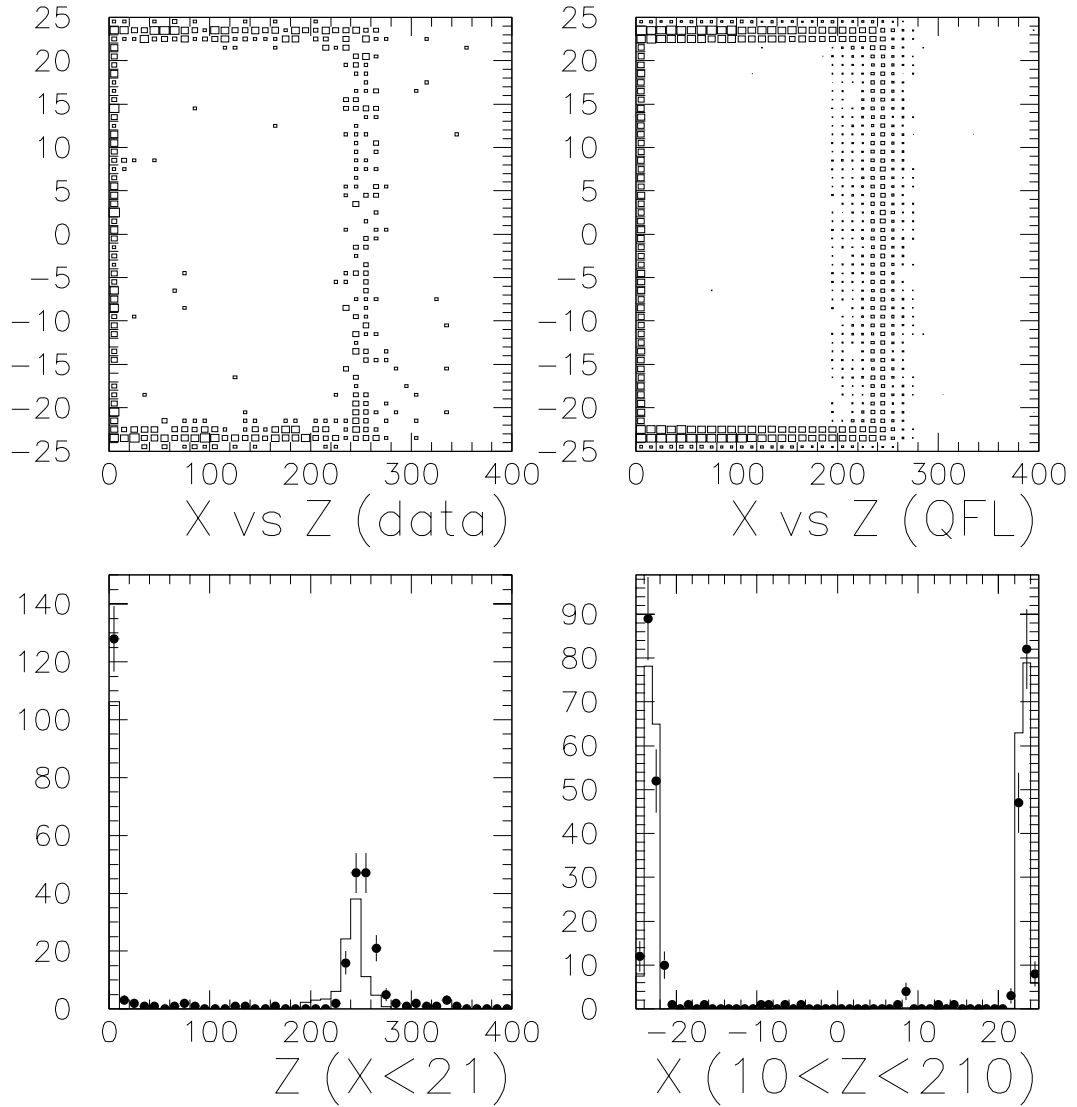
Figure 6.3: x vs. z (in CES local coordinates) for data and QFL Z-removal candidates. The points are the data; the histogram is a QFL simulation. The simulation is normalized to the 2206 Z data events, as described in the text.
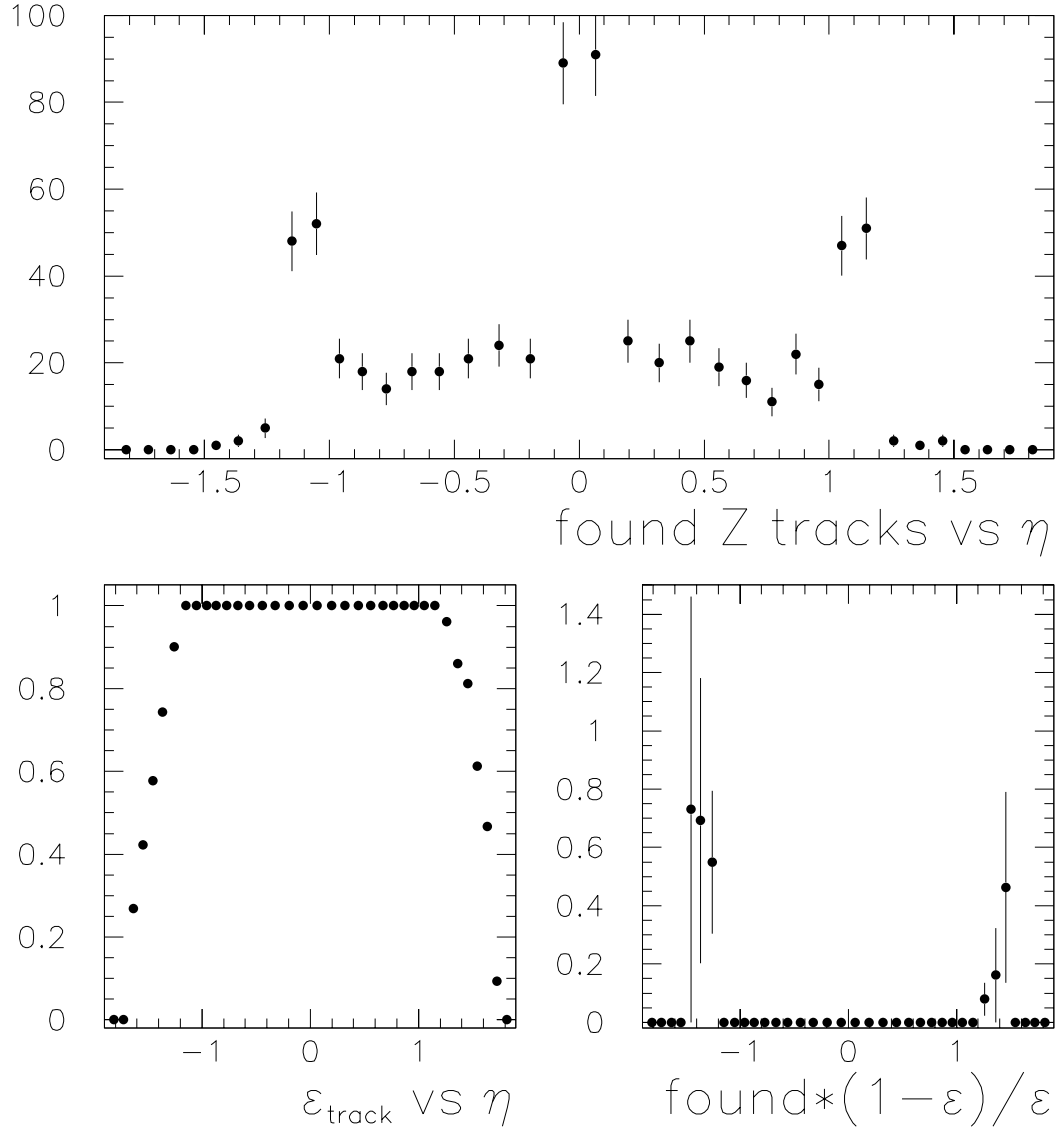
Figure 6.4: (Top) Detector η distribution of tracks found by Z-removal procedure. (Bottom Left) Tracking efficiency vs. η measured in Ref. [76]. The falloff in efficiency begins beyond the $30°$ region. (Bottom Right) We estimate about three Z candidates lost in the region in which $0 \ll \epsilon < 1$, by multiplying found candidates by $1/\epsilon - 1$ (which clearly says nothing about the region in which $\epsilon \ll 1$).
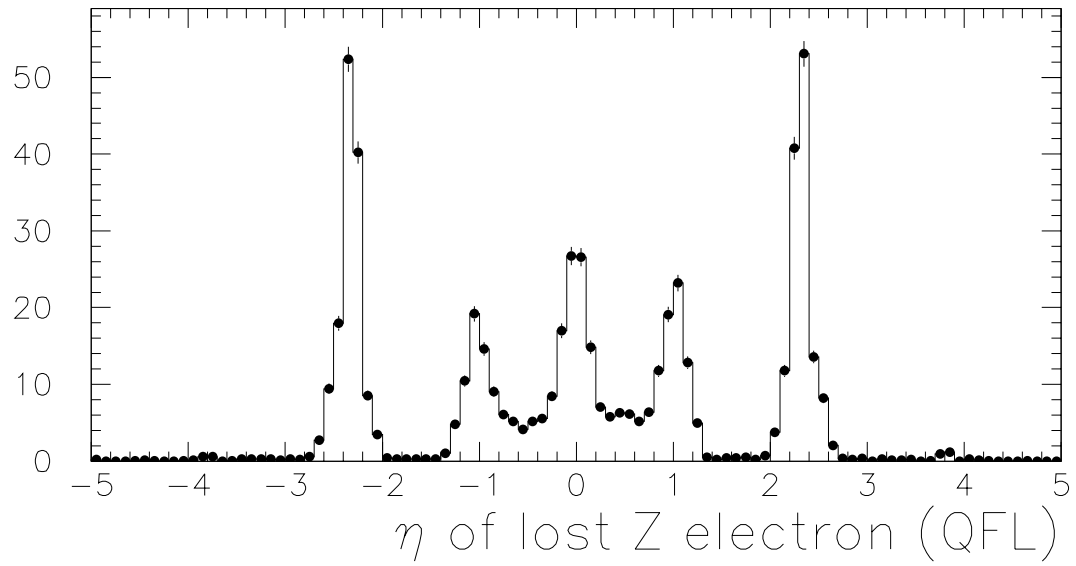
Figure 6.5: η distribution of lost Z electrons in QFL. The 90°, 30°, and 10° regions are evident. (The histogram is merely connecting the points, to guide the eye.)
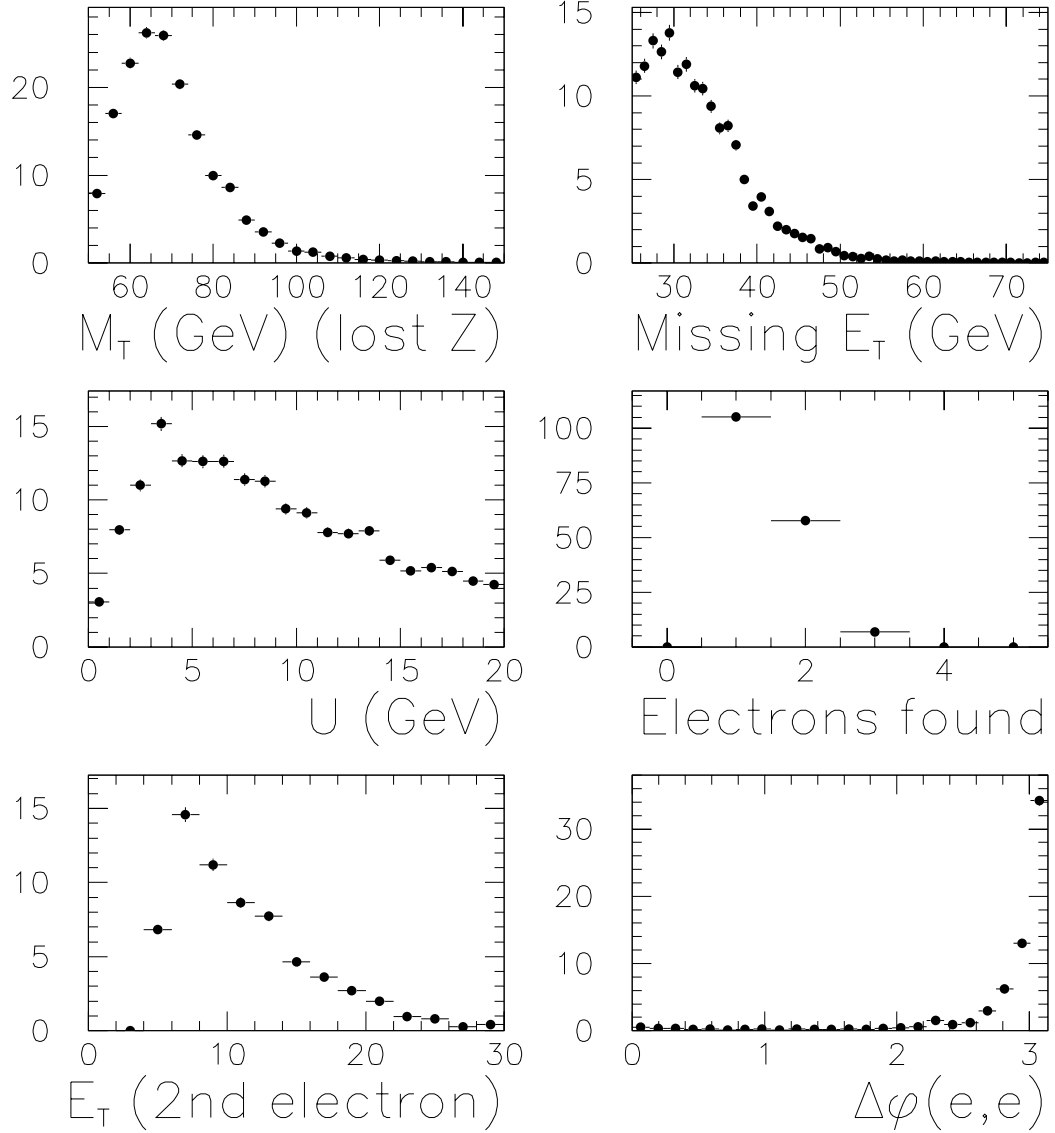
Figure 6.6: Shapes and sizes predicted by QFL for the remaining Z events lurking in the W sample. The quantities histogrammed are (a) transverse mass; (b) missing transverse energy; (c) magnitude of recoil energy (with only one electron subtracted); (d) number of reconstructed electron candidates; (e) transverse energy of the second electron, if it is reconstructed; (f) azimuthal angle between first and second electrons, if second is reconstructed.
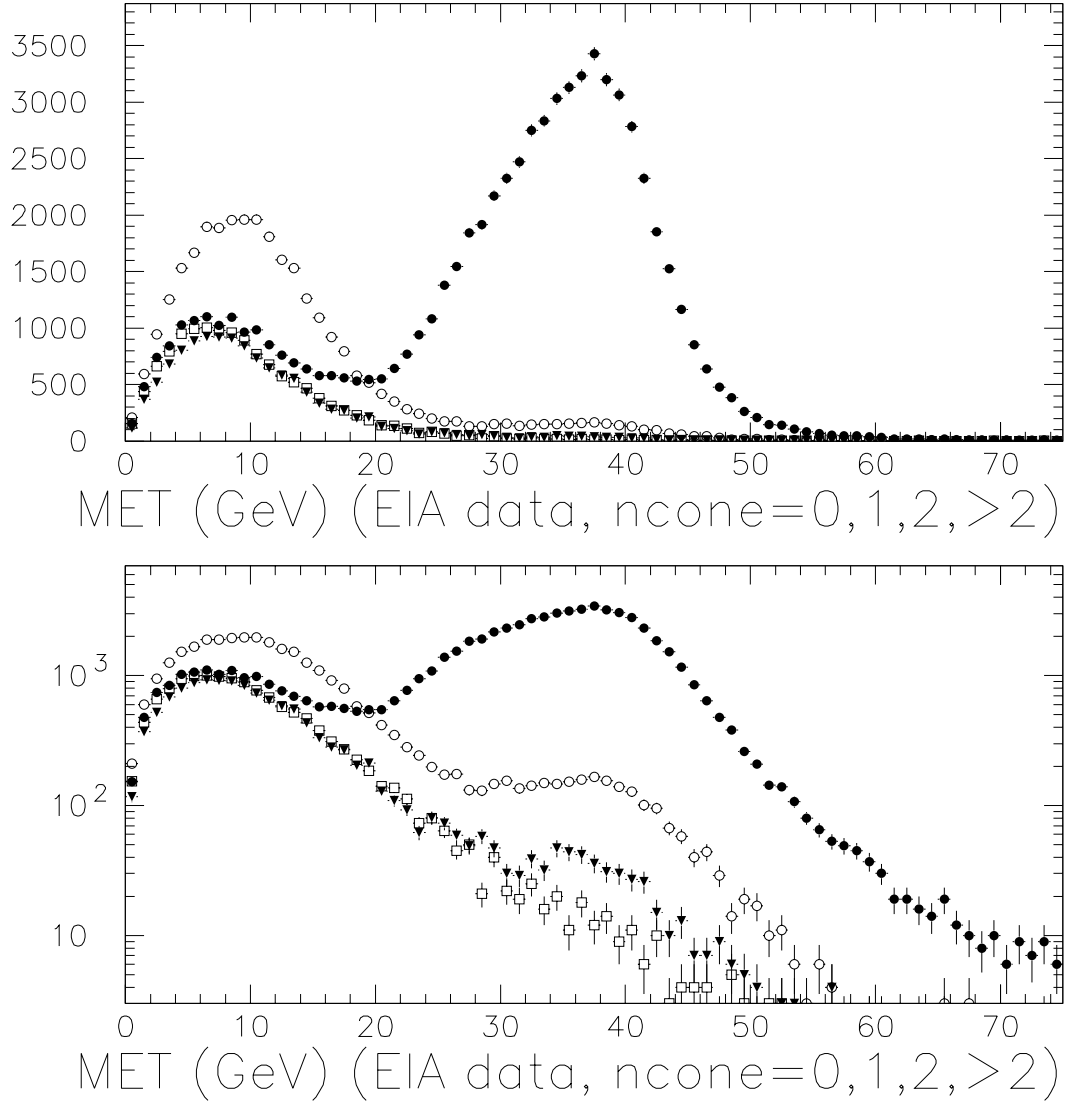
Figure 6.7: $\not{E}_T$ distributions from inclusive electrons (see Table 4.4), for $N_{\mathrm{cone}} = 0, 1, 2,$ and > 2 (solid circles, open circles, solid triangles, open squares, respectively).
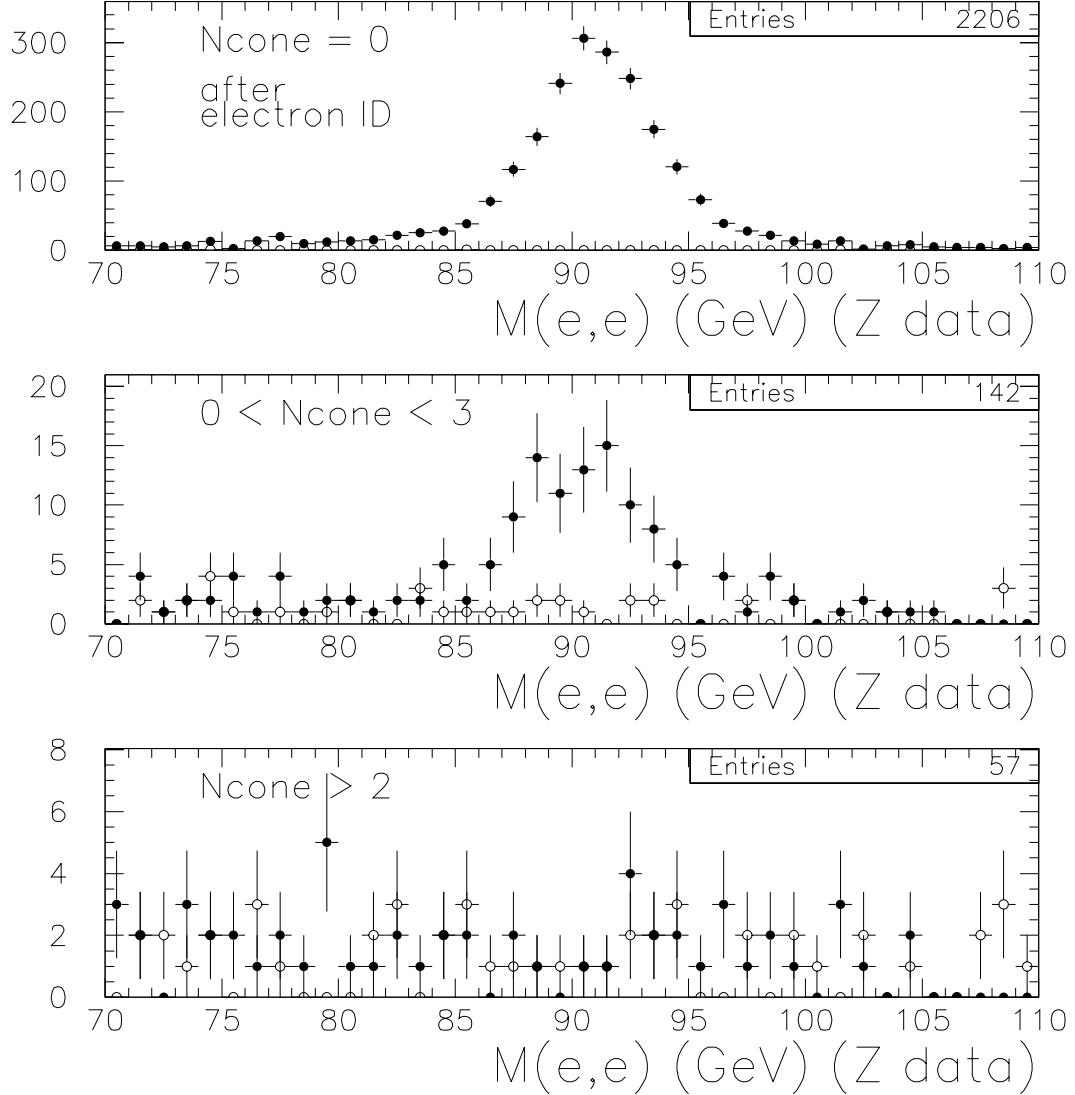
Figure 6.8: (Top) $Z \to ee$ mass distribution, for events in which the first electron passes ID cuts. Opposite sign pairs are the solid points and like sign pairs are the open circles. There are 2206 OS events and 8 LS events. (Center) Same as above, but $0 < N_{\mathrm{cone}} \leq 2$. There are 142 OS events and 38 LS events. (Bottom) Same as above, but $N_{\mathrm{cone}} > 2$. There are 57 OS events and 48 LS events. No significant number of Z electrons have $N_{\mathrm{cone}} > 2$; $5 \pm 1\%$ of Z electrons have $0 < N_{\mathrm{cone}} \leq 2$.

97
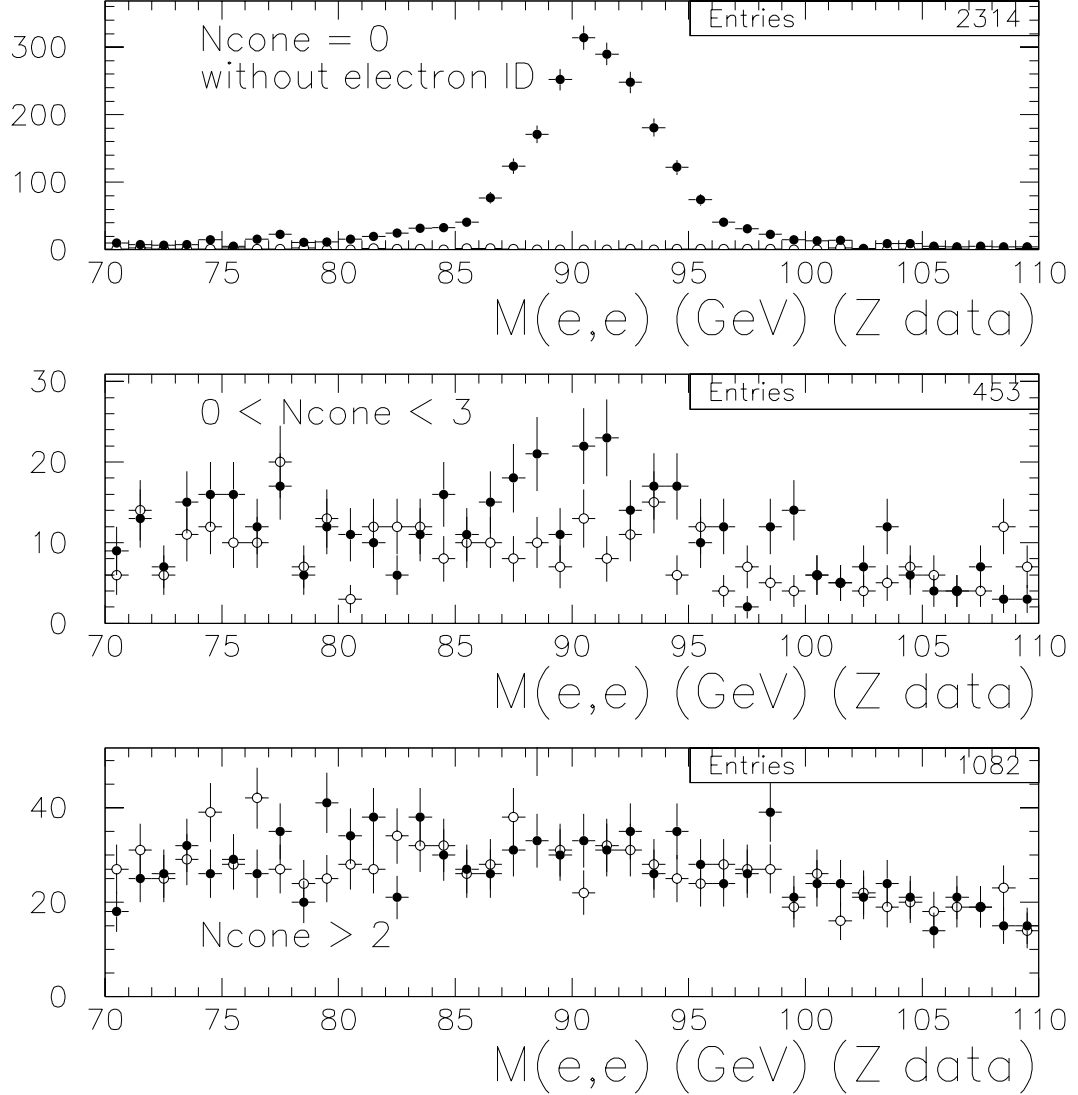
Figure 6.9: (Top) $Z \to ee$ mass distribution, for events in which the first electron passes $N_{\mathrm{cone}} = 0$ cut. (Other electron ID cuts are not applied.) Opposite sign pairs are the solid points and like sign pairs are the open circles. There are 2314 OS events and 39 LS events. (Center) Same as above, but $0 < N_{\mathrm{cone}} \leq 2$. There are 453 OS events and 346 LS events. (Bottom) Same as above, but $N_{\mathrm{cone}} > 2$. There are 1082 OS events and 1086 LS events. No significant number of Z electrons have $N_{\mathrm{cone}} > 2$; $5 \pm 1\%$ of Z electrons have $0 < N_{\mathrm{cone}} \leq 2$.
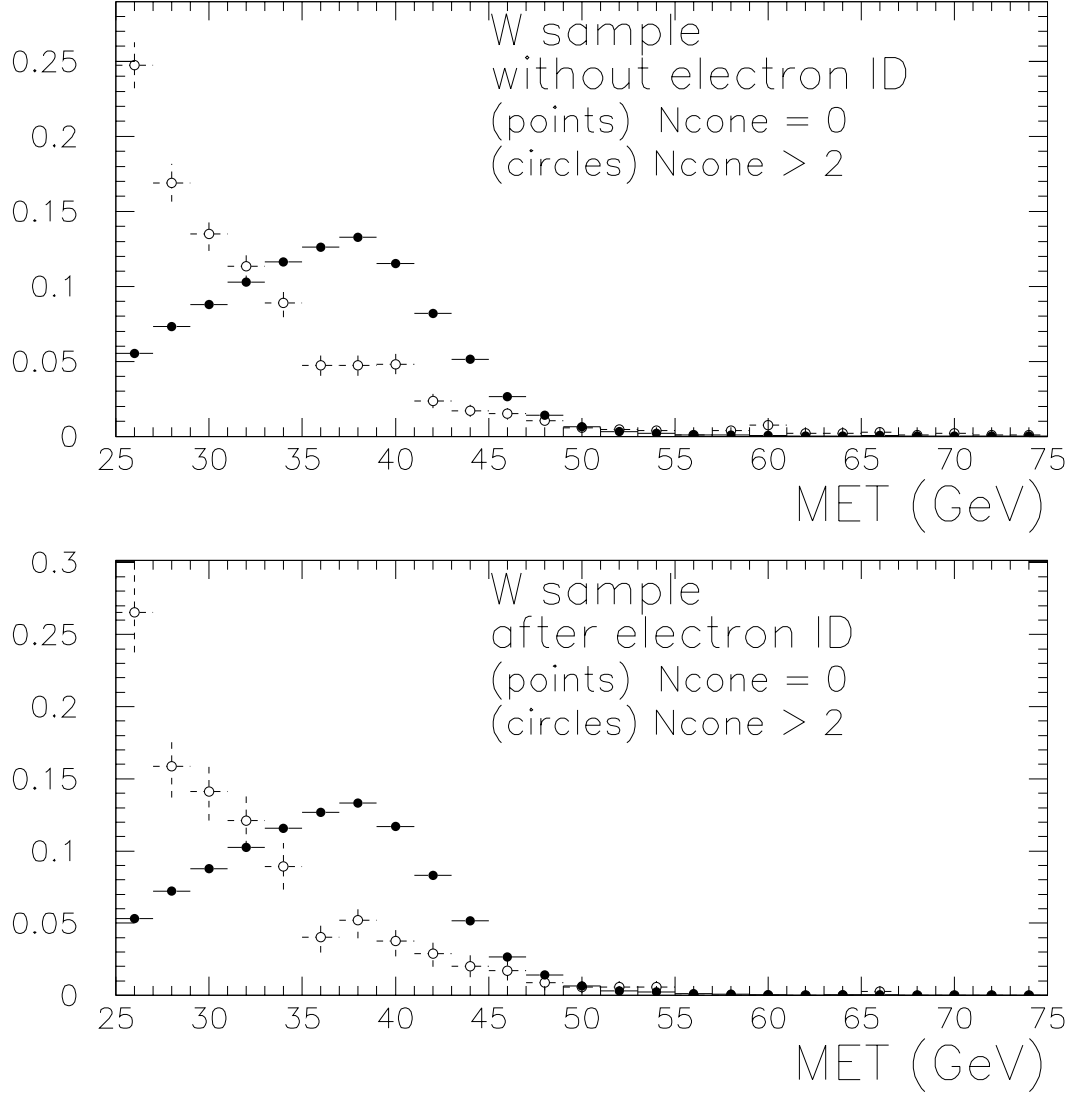
Figure 6.10: (Top) $\not{E}_T$ distribution for W candidates, without $E_{\text{hadron}}/E_{\text{EM}}$, $\Delta z_{\text{track,CES}}$, or χ_s^2 cuts. The solid points are the $N_{\text{cone}} = 0$ sample, which shows a clear Jacobian peak. The open circles are the $N_{\text{cone}} > 2$ sample, which shows no Jacobian peak. Both distributions are normalized to unity. (Bottom) Same as above, after the electron ID cuts have been applied.
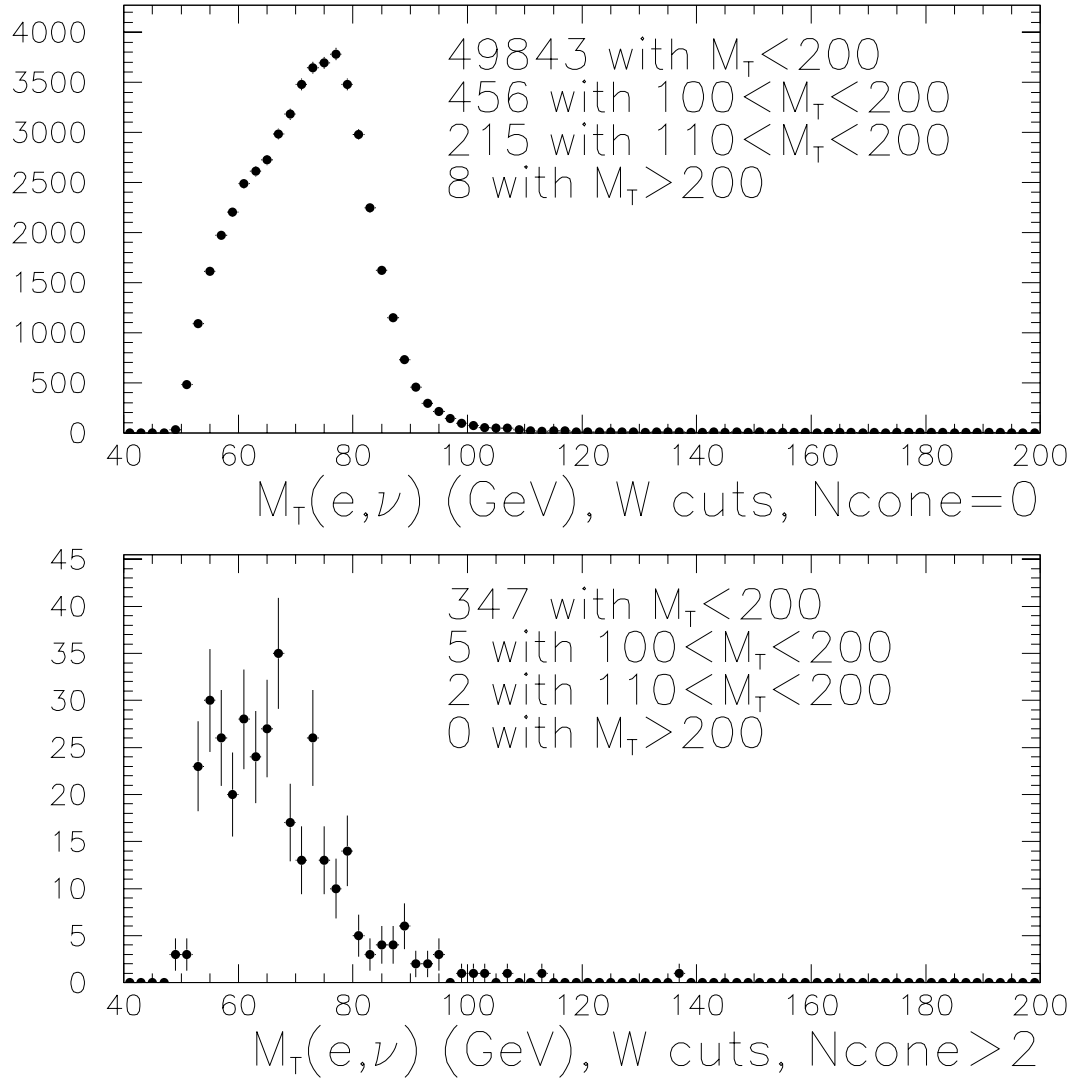
Figure 6.11: (Top) Transverse mass distribution for events passing all W cuts. (Bottom) Transverse mass distribution for events passing all W cuts, including $E_{\text{hadron}}/E_{\text{EM}}$, $\Delta z_{\text{track,CES}}$, and χ_s^2, but with track isolation $N_{\text{cone}} > 2$ instead of $N_{\text{cone}} = 0$.
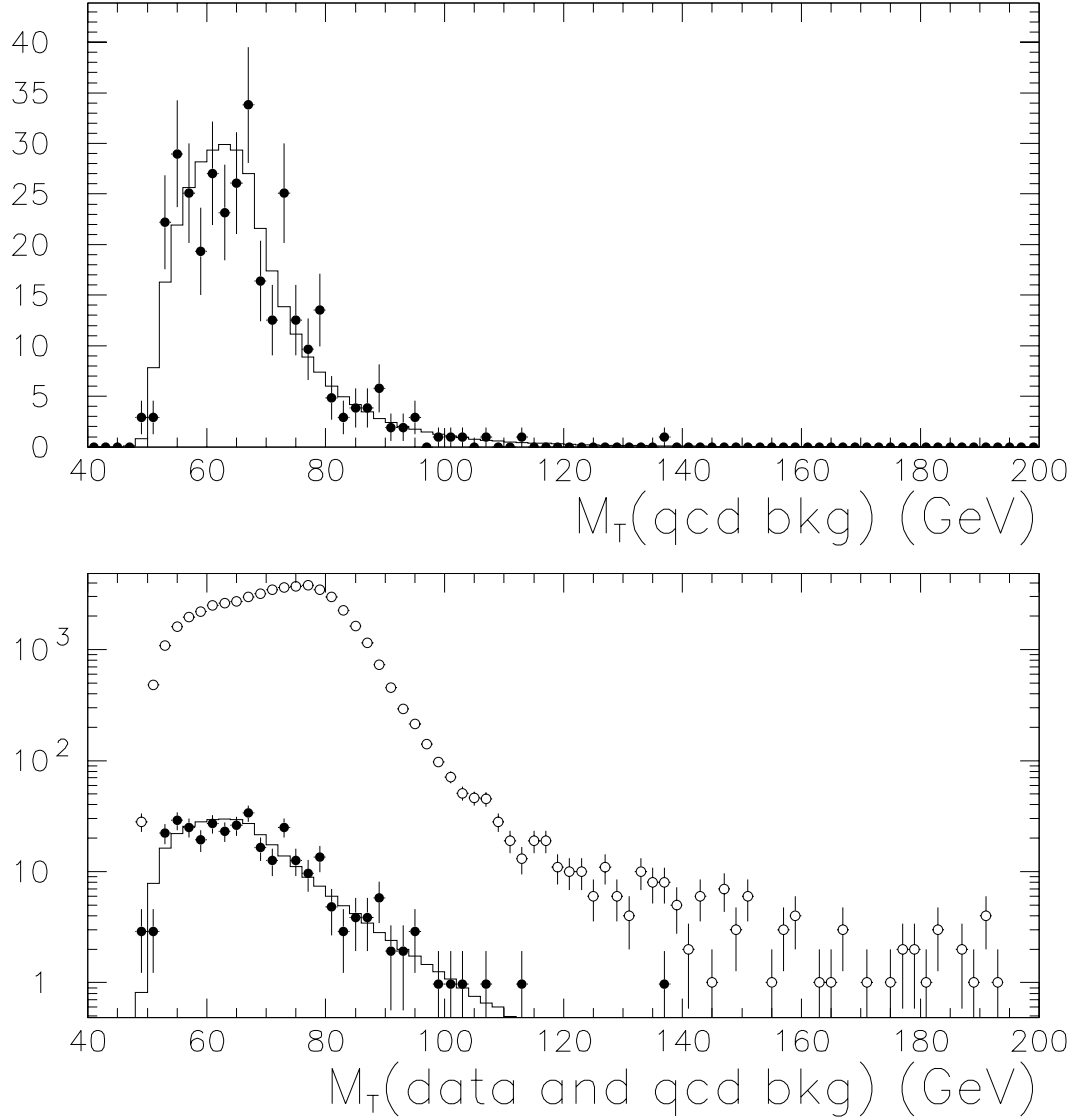
Figure 6.12: (Top) Histogram is M_T spectrum for QCD background predicted by fitting photon conversion data. Points are $N_{\mathrm{cone}} > 2$ data in W sample. The shapes agree very well. KS=45%. Both are normalized to the 450 background events expected in the data. (Bottom) $N_{\mathrm{cone}} = 0$ data, plus the above two plots, with a logarithmic y-axis.
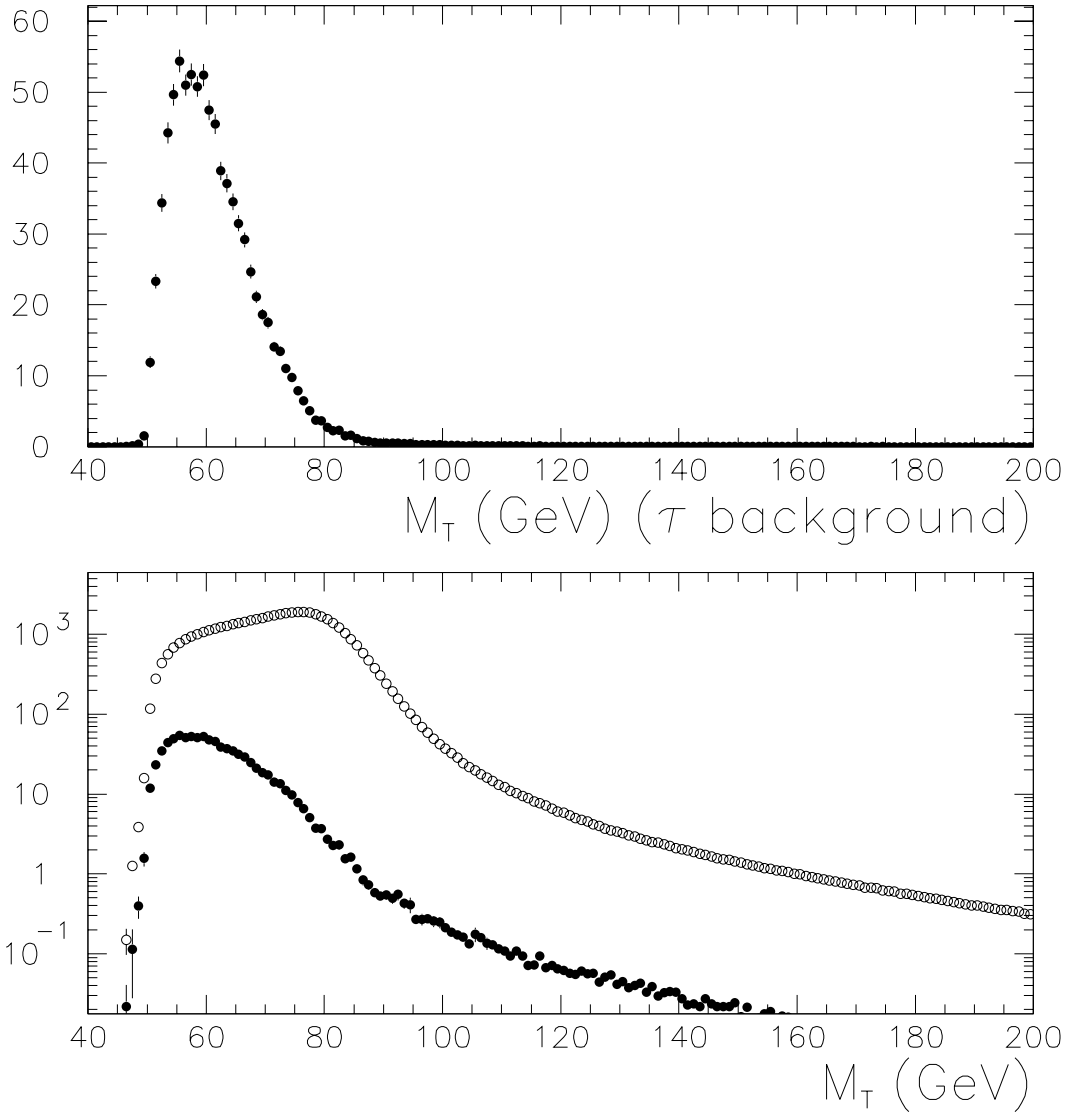
Figure 6.13: (Top) Transverse mass shape of $W \to \tau\nu \to e\nu\nu$ background. When normalizing to the size of the W electron dataset, we expect the size of this background to be 870 ± 100 events. (Bottom) Simulated $W \to e\nu$ signal and $W \to \tau\nu \to e\nu\nu$ background overlaid and normalized to the size of the data.
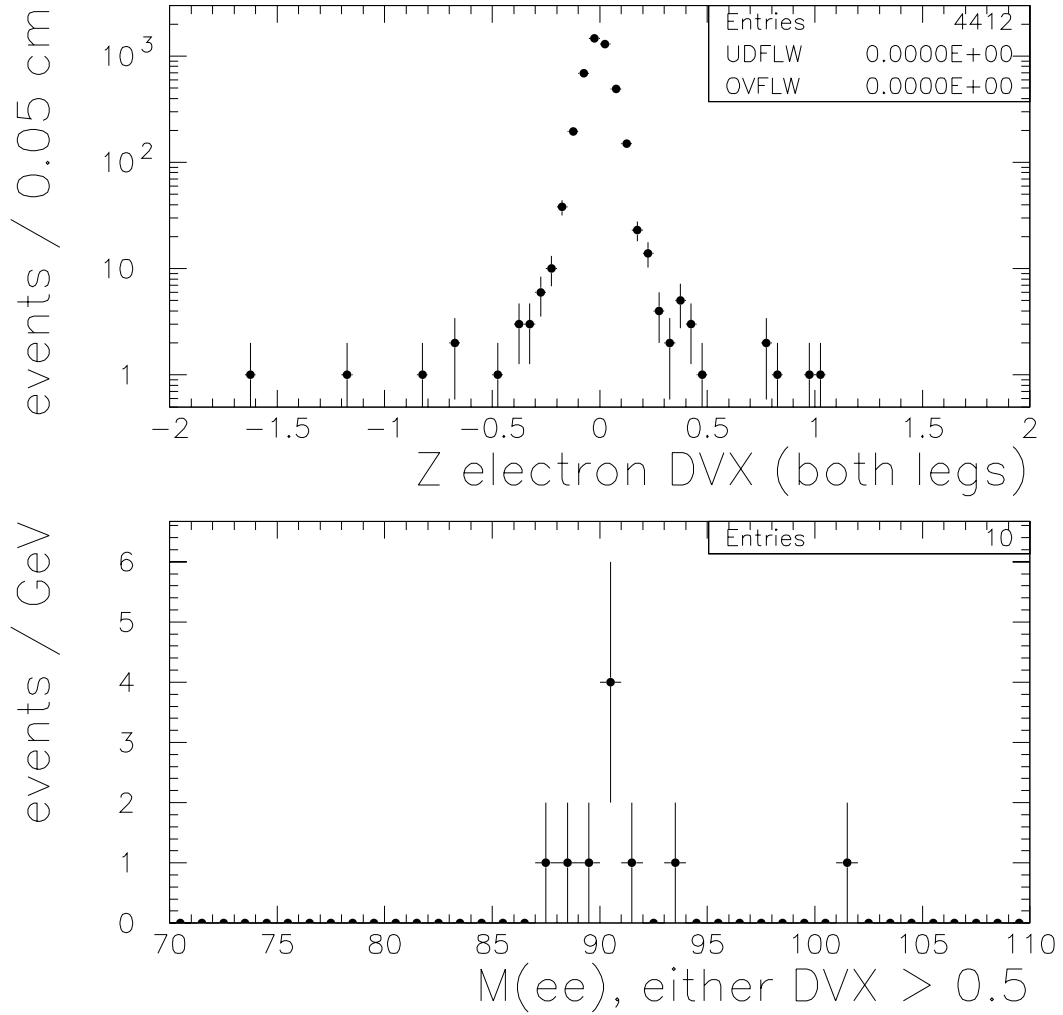
Figure 6.14: (Top) Impact parameter, d_{beam}, for both tracks in $Z \to ee$ events. Out of 4412 tracks in 2206 events, 10 (or $0.23 \pm 0.08\%$) have $|d_{\text{beam}}| > 0.5$ cm. (Bottom) Mass distribution for $Z \to ee$ events in which either leg has $|d_{\text{beam}}| > 0.5$ cm. Since the distribution is strongly peaked near M_Z, we conclude that the d_{beam} failures are dominated by real Z events.

103

```
Run 63171 Evt 414124                                    15OCT94   0:05:00

  Pt   Phi   Eta     Et(METS)=   30.5 GeV
-21.3  346 -0.21        Phi =  349.7 Deg         Emax =    31.3 GeV
 19.3  166  0.23     Sum Et =   44.0 GeV
 -0.8  156  0.82
  0.3   28  0.08
```
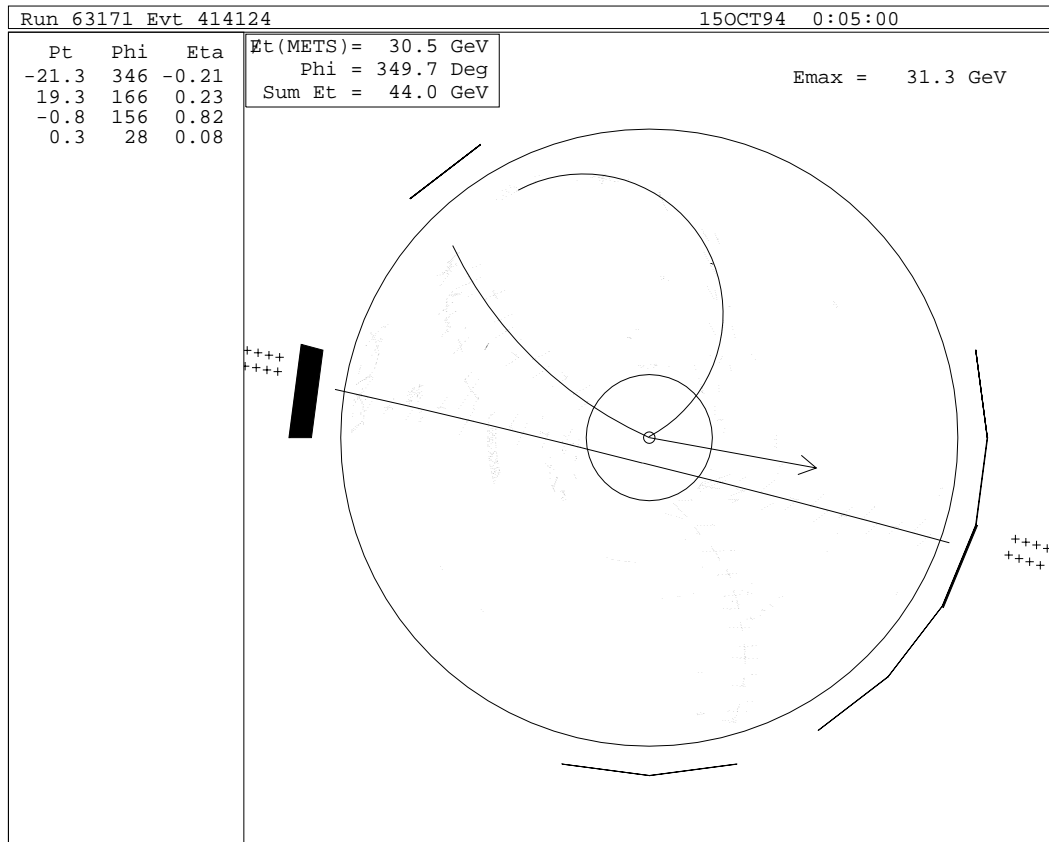
Figure 6.15: A cosmic ray candidate that survives all cuts except $|d_{\mathrm{beam}}|$ and p_T^{BC}.

104
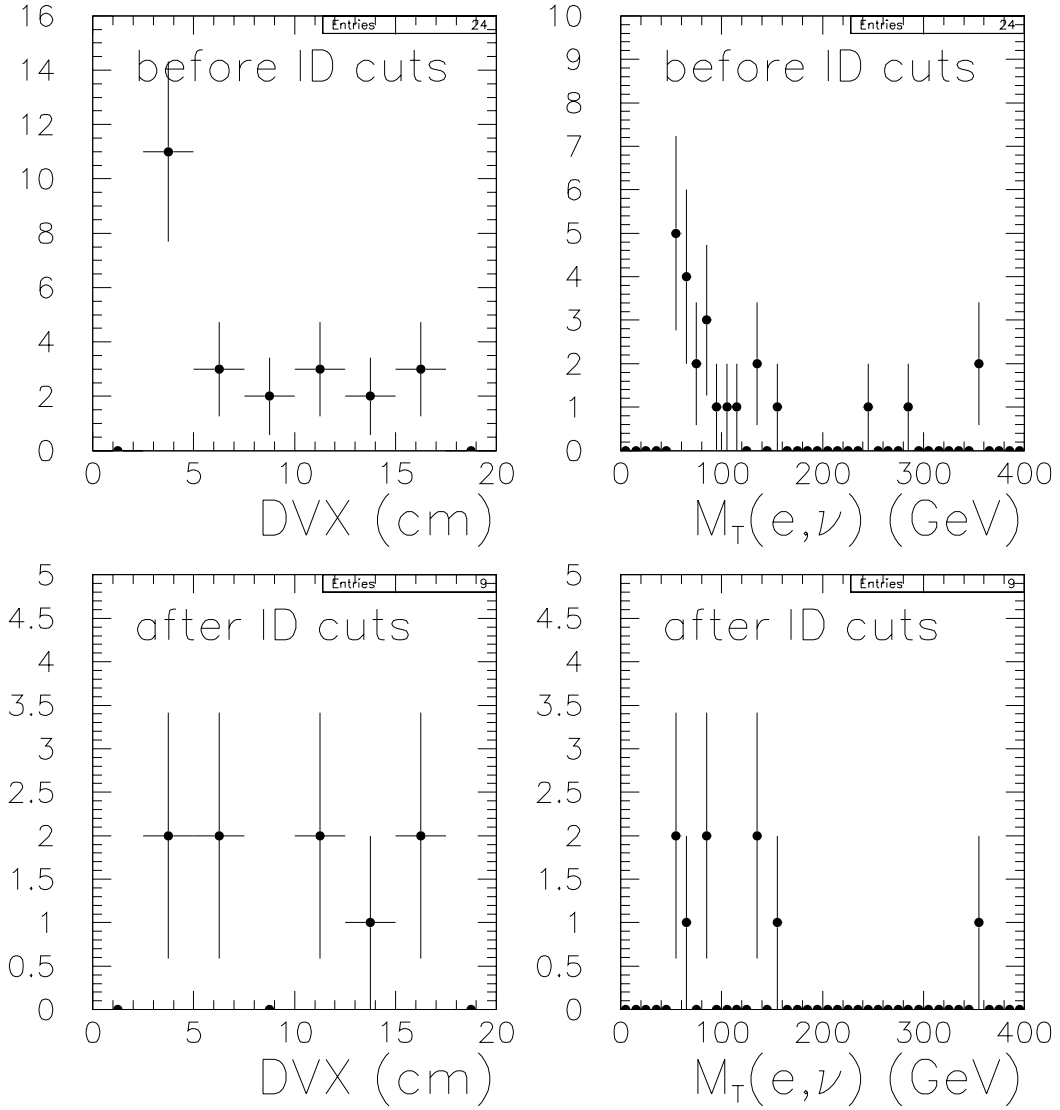
Figure 6.16: Impact parameter and transverse mass distributions for events with $|d_{\mathrm{beam}}| > 2.5$ cm. In the lower plots, all cuts in Table 4.5 are applied, except for the $|d_{\mathrm{beam}}|$ and p_T^{BC} cuts, as described in the text. For the upper plots, the last four cuts in Table 4.5 are also omitted.
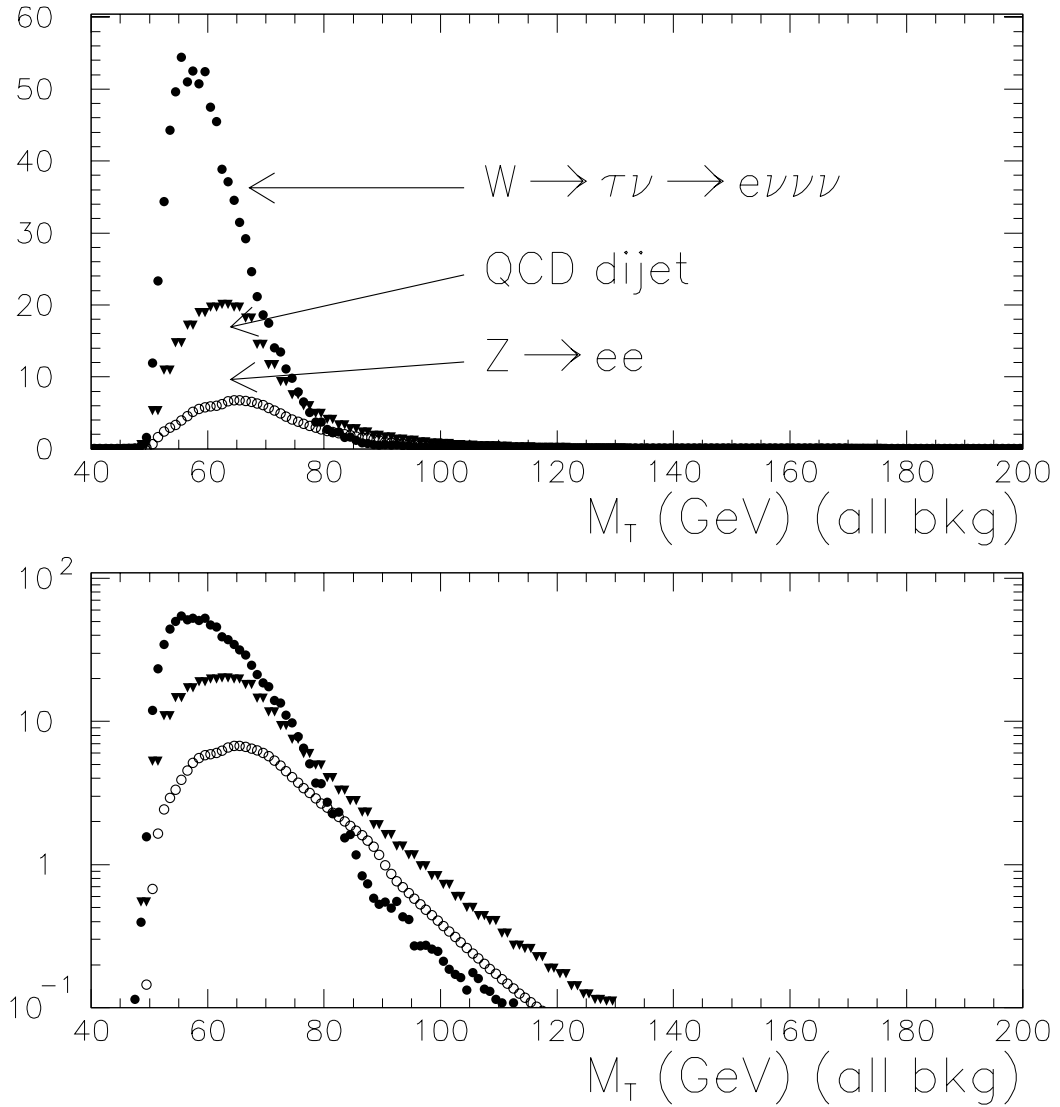
Figure 6.17: Shapes and sizes of predicted backgrounds, on linear and logarithmic scales.

Chapter 7

Extracting Γ_W from the Data

We now have all of the ingredients we need to make predicted M_T spectra for a range of Γ_W values. In this chapter, we extract a central value for the W width from the data and quantify sources of error.

7.1 Fitting for Γ_W

We use the simulation described in Chapter 5 to predict M_T spectra for $\Gamma_W = 1.5, 1.6, \ldots, 2.8$ GeV, normalize each spectrum to $49843 - 1490 = 48353$ expected signal events in the region $M_T < 200$ GeV, and add the 1490-event background shape (Figure 6.17, Table 6.3) to the predicted spectra.

We then perform a binned likelihood fit over the region $110 \leq M_T < 200$ GeV, in which we allow the contents of each data bin to fluctuate with Poisson statistics about the template bin contents. We fit a third-order polynomial to $-2\log(L)$ vs. Γ_W and find $\Gamma_W = 2.23 \pm 0.16$ (stat) GeV. The result is shown in Figure 7.1. Figure 7.2 shows the data with the best fit superimposed. The background size and shape are shown as well. A fit to the region $100 \leq M_T < 200$ GeV (not shown) yields the value $\Gamma_W = 2.27^{+.13}_{-.12}$ (stat) GeV.

7.2 Sources of error

To compute the effect of each source of systematic error, we generate Monte Carlo M_T spectra spanning the allowed range of that source of error (e.g. for $\pm 0.2\%$ in CEM energy scale) and fit those spectra to the original M_T templates. We do this separately for fits to $M_T > 110$ GeV, $M_T > 100$ GeV, and $M_T > 90$ GeV.

To compute the $\vec{u}$ model uncertainty, we use the 54 simulated W datasets, described in Section 5.5.3, in which the recoil model parameters are varied within the statistical errors of the fit to the Z data. The rms spread of Γ_W fitted from
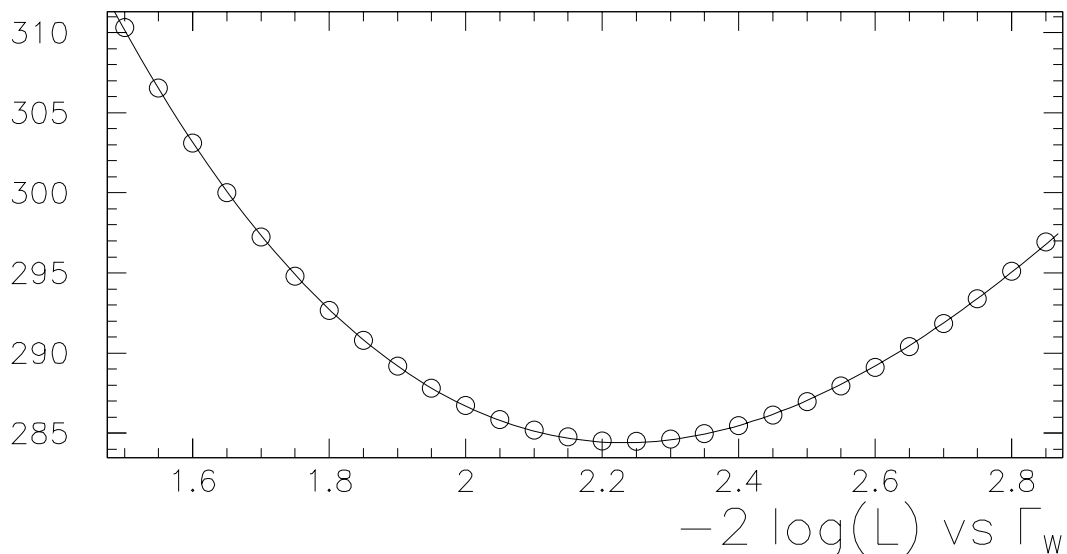
Figure 7.1: We perform a binned likelihood fit over the region $110 \leq M_T < 200$ GeV, where we allow the contents of each data bin to fluctuate with Poisson statistics about the template bin contents. We normalize the template to the total number of events in the $M_T < 200$ GeV region of the data before fitting. We fit a third-order polynomial to $-2\log(L)$ vs. Γ_W and find $\Gamma_W = 2.23 \pm 0.16$ (stat) GeV.

these MC datasets, 20 MeV for $M_T > 110$ GeV, 40 MeV for $M_T > 100$ GeV, and 65 MeV for $M_T > 90$ GeV, is the $\vec{u}$ model uncertainty due to finite Z statistics alone—a lower bound on the true uncertainty. Because the same Z sample is used both to fit the recoil model parameters and to decide what set of variables is needed for the fit, systematic effects due to choice of parameterization can only be revealed as discrepancies between the Z data and the Z recoil simulation. The excellent agreement observed between the Z data and the recoil model allows us only to rule out systematic effects larger than the statistical uncertainty. Thus, we inflate the statistical error by a factor 1.5 (rounded up from $\sqrt{2}$) to account for subtleties in the modeling that we may not yet have enough Zs to notice, resulting in a $(30, 60, 100)$ MeV uncertainty on Γ_W for the fit to $M_T > (110, 100, 90)$ GeV. The difference in fitted Γ_W between the W-data-preferred model parameters, discussed in Section 5.5.3, and the central value of the Z fit is $(5, 10, 35)$ MeV, which is much smaller than the quoted recoil model uncertainty, so we do not consider it as an additional source of error.

Andrew Gordon [78] has examined E/p distributions, comparing CEM energy scale and CTC momentum scale, for electrons from W and Z decays separately. He finds that the ratio of energy scales extracted from the Z and W samples is 0.9994 ± 0.0017, which (assuming linearity of the track momentum measurement) shows no evidence for CEM nonlinearity. Noting that $\langle E \rangle = 49.9 \pm 0.1$ GeV in the Z sample and $\langle E \rangle = 42.3$ GeV in the W sample, we extract a 1σ uncertainty on the ability to measure a CEM nonlinearity of $\frac{0.0017}{49.9-42.3} = 0.00022$ GeV^{-1}. A nonlinearity
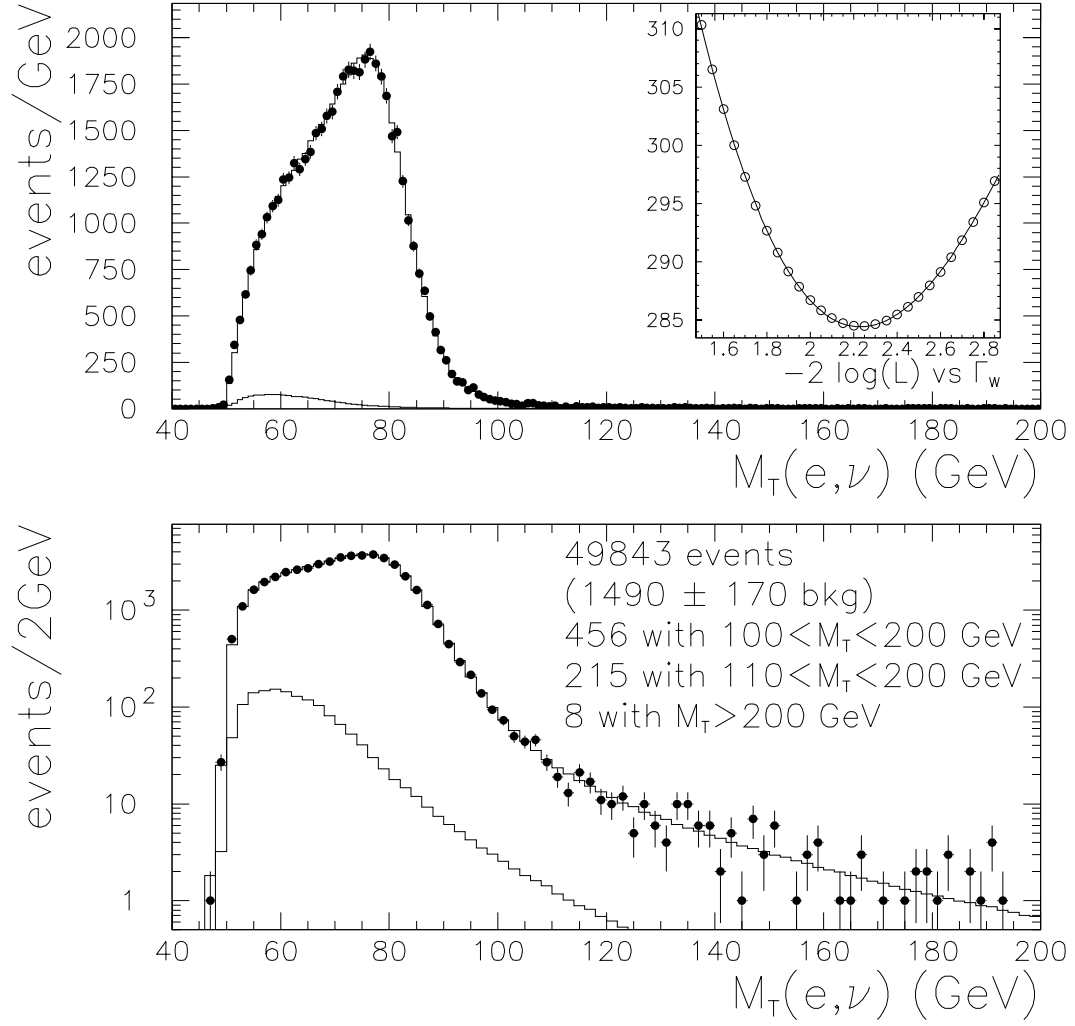
Figure 7.2: Data with best fit overlayed. The size and shape of the summed backgrounds are also shown. The KS fit confidence level is 78% for the entire $40 < M_T < 200$ GeV region, and 84% for the $100 < M_T < 200$ GeV region alone.

of 0 ± 0.00022 GeV^{-1} produces a $(40, 50, 60)$ MeV uncertainty on Γ_W for the fit to $M_T > (110, 100, 90)$ GeV.

Varying the CEM energy scale by $\pm 0.2\%$ yields a $(25, 40, 95)$ MeV uncertainty on Γ_W for $M_T > (110, 100, 90)$ GeV. Varying the background rates within the uncertainties quoted in Table 6.3 varies Γ_W by 40 MeV for $M_T > 110$ GeV and 30 MeV for $M_T > 100$ GeV. We have not quantified this source of error for $M_T > 90$ GeV.

We generated Monte Carlo samples using a variety of modern parton distribution functions. These distributions span a range of $\alpha_s(M_Z)$ values, which affects the Q^2 evolution of the structure functions, and hence the parton luminosity. The CTEQ-2M and CTEQ-2ML distributions are included because they do not incorporate the

PDF	$\alpha_s(M_Z)$	$M_T > 110$	$M_T > 100$	$M_T > 90$
MRS-R2	0.120	—	—	—
MRS-R1	0.113	+50 MeV	+40 MeV	+30 MeV
CTEQ-2M	0.110	+55 MeV	+40 MeV	+20 MeV
CTEQ-2ML	0.118	−5 MeV	−5 MeV	−15 MeV
CTEQ-4M	0.116	+15 MeV	+10 MeV	+5 MeV
CTEQ-5M1	0.119	+10 MeV	+5 MeV	0 MeV
min shift		−5 MeV	−5 MeV	−15 MeV
max shift		+55 MeV	+40 MeV	+30 MeV

Table 7.1: Observed shifts in $,_W$ when Monte Carlo samples generated with a variety of parton distribution functions are fit to templates generated with the MRS-R2 PDF. Fitting the data to templates generated with these PDFs would shift the fitted $,_W$ in the opposite direction.

measured CDF W charge/rapidity asymmetry. The α_s value is evidently a much more important effect than the W asymmetry constraint. Because the distribution of offsets, shown in Table 7.1, is asymmetric, we cover the observed variation by shifting the quoted , $_W$ value by the average of the maximum and minimum shifts and taking half of the maximum difference between shifts as a systematic uncertainty. We shift the $M_T > (110, 100, 90)$ GeV value by $(-25, -20, -10)$ MeV and assign an uncertainty of $(30, 25, 25)$ MeV.

Varying the W p_T skew parameter by ± 0.0028 GeV^{-1} changes , $_W$ by $(15, 30, 50)$ MeV for the fit to $M_T > (110, 100, 90)$ GeV. Varying the assumed value of the W mass by ± 110 MeV changes , $_W$ by $(10, 20, 50)$ MeV. Varying the CEM resolution and the g_2 parameter of the W p_T spectrum change the $M_T > 100$ GeV and $M_T > 110$ GeV results by less than 10 MeV; we have not evaluated these two sources of error for $M_T > 90$ GeV. Varying the g_3 parameter of the W p_T spectrum by ± 0.2 GeV^{-1} from its nominal value $g_3 = -1.5$ GeV^{-1} changes the fitted , $_W$ by $(< 10, < 10, 10)$ MeV.[1]

As a check of the electron and photon modeling in the SSD simulation, we simulated 5×10^6 $W \to e\nu\gamma$ events (1.3×10^6 events after all cuts) with QFL and fitted the resulting M_T spectrum with the SSD templates used to fit the data. We observe a shift of $(+15, +30, +30)$ MeV for $M_T > (110, 100, 90)$ GeV.[2] We include the magnitude of this difference as a source of error.

Table 7.2 summarizes the uncertainties in the measured , $_W$ that we have considered. We noted in Chapter 1 that the insight that makes this measurement feasible is to observe that many sources of systematic error decrease at high transverse mass, where there is good separation between on-shell and off-shell W bosons. Since the high-M_T region contains fewer events, however, one expects a larger statistical error at high transverse mass. Table 7.2 demonstrates that the $M_T > 100$ GeV region is near optimal for minimizing the total error on the measured W width: The statistical error rises from 100 MeV to 160 MeV as we move the left side of the fitting window from 90 GeV to 110 GeV, while the systematic error decreases from 175 MeV to 80 MeV.

We thus quote the $M_T > 100$ GeV fit, shifted -20 MeV for the PDF variation noted above, as the final result: , $_W = 2.25^{+0.13}_{-0.12}$ (stat) ± 0.11(syst) GeV.

---

[1] The LY fitted value is $g_3 = -1.5 \pm 0.1$ GeV^{-1}. We vary g_3 by twice the LY quoted error. We have learned very recently [79] that a new, preliminary analysis by Ladinsky and Yuan prefers $g_3 = -0.88$ GeV^{-1}, which would change , $_W$ by $(< 10, 10, 30)$ MeV. Since the change is negligible in comparision to other sources of error, we neglect it here.

[2] The uncertainty on this comparison due to Monte Carlo statistics is about 5 MeV, which is smaller than one might estimate by scaling the statistical error on the data, because of the manner in which weighted Monte Carlo events are generated.

Source	Variation	$M_T \geq 110$ Δ, (MeV)	$M_T \geq 100$ Δ, (MeV)	$M_T \geq 90$ Δ, (MeV)
$\vec{u}$ model	Z fit 1.5σ(stat)	30	60	100
CEM nonlinearity	± 0.00022 GeV^{-1}	40	50	60
CEM scale	1.0006 ± 0.0020	25	40	95
backgrounds	Table 6.3	40	30	*
W p_T (skew)	$-.0028 \pm .0028$ GeV^{-1}	15	30	50
$e^{\pm}, \gamma$ simulation	SSD vs. QFL	15	30	30
PDF	see text	30	25	25
M_W	80.356 ± 0.110 GeV	10	20	50
CEM resolution	$1.5 \pm 0.3\%$	< 10	< 10	*
W p_T (g_2)	0.6 ± 0.2 GeV^2	< 10	< 10	*
W p_T (g_3)	-1.5 ± 0.2 GeV^{-1}	< 10	< 10	10
all systematics		80	110	175
statistics		160	125	100
total		180	165	200

Table 7.2: Summary of uncertainties. Entries marked by an asterisk in the $M_T > 90$ GeV column have not been evaluated, but are expected not to be dominant sources of error. The $M_T > 100$ GeV fit clearly minimizes the total error.

Chapter 8

Conclusions

By fitting the transverse mass lineshape in $W \rightarrow e\nu$ events recorded in 90 pb^{-1} of 1.8 TeV $p\overline{p}$ collisions, we have measured the W boson total decay width, Γ_W, to a precision of 8%. The best individual measurements of Γ_W to date [42, 43], each of which has a precision of 4%, extract Γ_W by combining a measurement of the branching ratio $B(W \rightarrow e\nu)$ with a Standard Model calculation for $\Gamma(W \rightarrow e\nu)$. The measurement presented in this dissertation, $\Gamma_W = 2.25^{+0.13}_{-0.12}$ (stat) $\pm$ 0.11 (syst) GeV, is a factor of two more precise than the best direct measurement to date [22]. The result is consistent with the Standard Model prediction [20, 16], 2.09 ± 0.01 GeV, and with the average of other measurements [16], 2.07 ± 0.06 GeV. Figure 8.1 compares the result of this measurement with previous direct and indirect measurements and with the Standard Model prediction.

There are now two complementary methods to measure the W width: the direct method used in this dissertation and the R method described in Chapter 1. It is always desirable to show that consistent measurements of a given physical quantity can be made using a variety of experimental methods, with complementary sources of error.

This measurement also demonstrates our understanding of charged-current phenomena at $\hat{s} > M_W^2$. We understand the region well enough to model its M_T lineshape successfully, using only one free parameter, Γ_W, whose measured value is consistent with Standard Model predictions.

In making this measurement, we have produced independent background calculations, a recoil model, and fits for the Z mass, electron resolution, and Z p_T spectrum, as well as an independent simulation that models electron bremsstrahlung in the inner detector material. These by-products can be used for systematic checks of the CDF W mass analysis.

In future direct Γ_W measurements, it should be possible to observe Standard Model radiative corrections to the W width that cancel in the branching ratio $\frac{\Gamma(W \rightarrow e\nu)}{\Gamma_W}$, and hence are unobservable in the R measurement. In the data taking period scheduled to begin in the year 2000, CDF expects to record at least 2000 pb^{-1}

of data, exceeding the size of the data set used in this measurement by more than a factor of 20. If all errors scale as $1/\sqrt{N}$,[1] a 35 MeV precision may be possible from CDF's electron data alone. In addition, it should be possible for both CDF and DØ to make this measurement in both electron and muon channels, reducing the statistical error even further.

---

[1] The only source of error in this measurement not expected to scale statistically with the size of the CDF data set is from parton distribution functions.
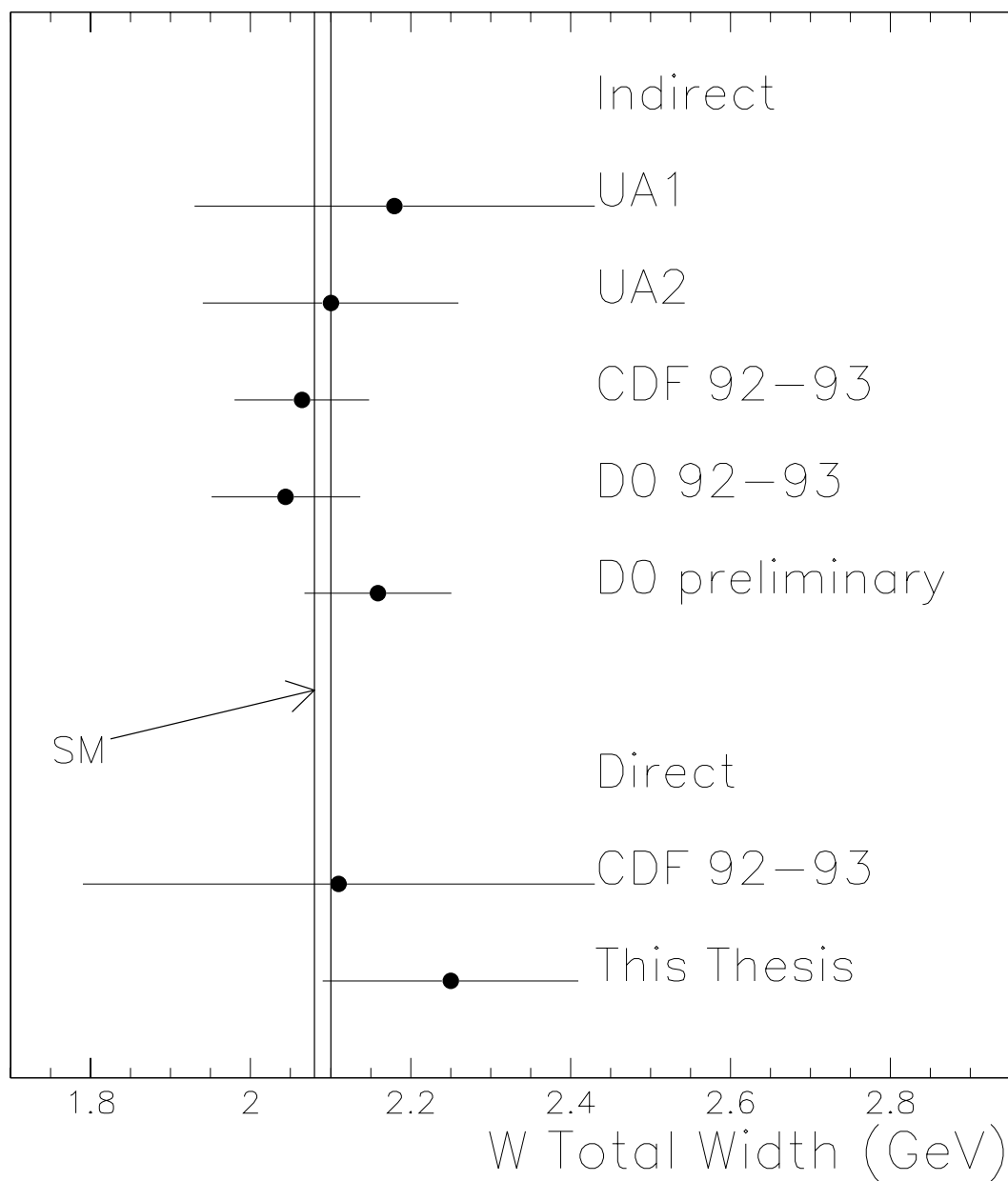
Figure 8.1: Comparison with other measurements.

Bibliography

[00] A. Gordon, Ph.D. thesis, Harvard University (in preparation).

[1] S. Glashow, *Nucl. Phys.* **22** 579 (1961).

[2] S. Weinberg, *Phys. Rev. Lett.* **19** 1264 (1967).

[3] A. Salam in *Elementary Particle Theory*, edited by N. Svartholm (Almquist and Wiksells, Stockholm, 1969), p. 367.

[4] W. Bardeen, H. Fritzsch, M. Gell-Mann in *Scale and Conformal Symmetry in Hadron Physics*, edited by R. Gatto (Wiley, New York, 1973), p. 139.

[5] D. Gross, F. Wilczek, "Asymptotically Free Gauge Theories," *Phys. Rev.* **D8** 3633 (1973).

[6] S. Weinberg, "Nonabelian Gauge Theories of the Strong Interactions," *Phys. Rev. Lett.* **31** 494 (1973).

[7] G. Baur *et al*, "Production of Anti-Hydrogen," *Phys. Lett.* **B368** 251 (1996).

[8] M. Kobayashi, T. Maskawa, "*CP* Violation in the Renormalizable Theory of Weak Interaction," *Prog. Theor. Phys.* **49** 652 (1973).

[9] N. Cabibbo, "Unitary Symmetry and Leptonic Decays," *Phys. Rev. Lett.* **10** 531 (1963).

[10] R. Cahn, G. Goldhaber, *The Experimental Foundations of Particle Physics*, (Cambridge University Press, 1989).

[11] C.S. Wu *et al*, "Experimental Test of Parity Conservation in Beta Decay," *Phys. Rev.* **105** 1413 (1957).

[12] R. Garwin, L. Lederman, M. Weinrich, "Observations of the Failure of Conservation of Parity and Charge Conjugation in Meson Decays: the Magnetic Moment of the Free Muon," *Phys. Rev.* **105** 1415 (1957).

[13] J. Friedman, V. Telegdi, "Nuclear Emulsion Evidence for Parity Non-Conservation in the Decay Chain $\pi^+ \to \mu^+ \to e^+$," *Phys. Rev.* **105** 1681 (1957).

[14] F.J. Hasert *et al*, "Observation of Neutrino Like Interactions without Muon or Electron in the Gargamelle Neutrino Experiment," *Phys. Lett.* **46B** 138 (1973).

[15] G. Arnison *et al* (UA1 Collaboration), "Experimental Observation of Isolated Large Transverse Energy Electrons with Associated Missing Energy at $\sqrt{s} = 540$ GeV," *Phys. Lett.* **122B** 103 (1983); "Intermediate-Vector-Boson Properties at the CERN Super Proton Synchrotron Collider," *Europhys. Lett.* **1** 327 (1986).

[16] R.M. Barnett *et al* (Particle Data Group), "Review of Particle Physics," *Phys. Rev.* **D54** 1 (1996) and 1997 off-year partial update for the 1998 edition at WWW location `http://pdg.lbl.gov`

[17] W.J. Marciano, A. Sirlin, "Radiative Corrections to Neutrino-Induced Neutral-Current Phenomena in the $SU(2)_L \times U(1)$ Theory," *Phys. Rev.* **D22** 2695 (1980).

[18] M. Swartz, "High Energy Tests of the Electroweak Standard Model," XVI International Symposium on Lepton-Photon Interactions (August, 1993).

[19] D.H. Perkins, *Introduction to High Energy Physics* (Third Edition) (Addison-Wesley, Reading, MA, 1987).

[20] J.L. Rosner, M.P. Worah, T. Takeuchi, "Oblique Corrections to the W Width," *Phys. Rev.* **D49** 1363 (1994).

[21] R.M. Barnett *et al* (Particle Data Group), "Review of Particle Physics," *Phys. Rev.* **D54** 1 (1996).

[22] F. Abe *et al* (CDF Collaboration), "Direct Measurement of the W Boson Width," *Phys. Rev. Lett.* **74** 342 (1995).

[23] V. Barger, A.D. Martin, R.J.N. Phillips, "Perpendicular $e\nu$ Mass from W Decay," Z. Phys. **C21** 99 (1983).

[24] J. Smith, W.L. van Neerven, J.A.M. Vermaseren, "Transverse Mass and Width of the W Boson," Phys. Rev. Lett. **50** 1738 (1983).

[25] S.E. Kopp, "A Measurement of the Ratio $R = \sigma \cdot B(p\overline{p} \to W \to e\nu)/\sigma \cdot B(p\overline{p} \to Z^0 \to e^+e^-)$ in $p\overline{p}$ Collisions at $\sqrt{s} = 1800$ GeV," Ph.D. thesis, University of Chicago (August, 1994).

[26] E. Eichten, I. Hinchliffe, K. Lane, C. Quigg, "Supercollider Physics," *Rev. Mod. Phys.* **56** 579 (1984).

[27] A.D. Martin, R.G. Roberts, W.J. Stirling, "Parton Distributions: a Study of the New HERA Data, α_s, the Gluon, and $p\overline{p}$ Jet Production," *Phys. Lett.* **B387** 419 (1996).

[28] V.D. Barger, R.J.N. Phillips, *Collider Physics* (Addison-Wesley, Reading, MA, 1987).

[29] F.A. Berends, R. Kleiss, J.P. Revol, J.P. Vialle, "QED Radiative Corrections and Radiative Decays of the Intermediate Weak Bosons Produced in Proton-Antiproton Collisions," *Z. Phys.* **C27** 155 (1985); F.A. Berends, R. Kleiss, "Hard Photon Effects in $W^{\pm}$ and Z_0 decay," *Z. Phys.* **C27** 365 (1985).

[30] P.B. Arnold, M. Reno, "The Complete Computation of High-p_T W and Z Production in Second-Order QCD," *Nucl. Phys.* **B319** 37 (1989).

[31] P.B. Arnold, R.P. Kauffman, "W and Z Production at Next-to-Leading Order: from Large q_T to Small," *Nucl. Phys.* **B349** 381 (1991).

[32] C. Davies, W.J. Stirling, "Nonleading Corrections to the Drell-Yan Cross-Section at Small Transverse Momentum," *Nucl. Phys.* **B244** 337 (1984).

[33] J. Collins, D. Soper, "Back to Back Jets in QCD," *Nucl. Phys.* **B193** 381 (1981); errata *Nucl. Phys.* **B213** 545 (1983); "Back to Back Jets: Fourier Transform from b to k_T," *Nucl. Phys.* **B197** 446 (1982).

[34] J. Collins, D. Soper, G. Sterman, "Transverse Momentum Distribution in Drell-Yan Pair and W and Z Boson Production," *Nucl. Phys.* **B250** 199 (1985).

[35] G.A. Ladinsky, C.P. Yuan, "Nonperturbative Regime in QCD Resummation for Gauge Boson Production at Hadron Colliders," *Phys. Rev.* **D50** 4239 (1994).

[36] R.K. Ellis, S. Veseli, "W and Z Transverse Momentum Distributions: Resummation in q_T-Space," *Nucl. Phys.* **B511** 649 (1998).

[37] R.K. Ellis, D.A. Ross, S. Veseli, "Vector Boson Production in Hadronic Collisions," *Nucl. Phys.* **B503** 309 (1997).

[38] F. Abe *et al* (CDF Collaboration), "Two Jet Invariant Mass Distribution at $\sqrt{s} = 1.8$ TeV," *Phys. Rev.* **D41** 1722 (1990).

[39] R. Ansari *et al* (UA2 Collaboration), "Measurement of the Standard Model Parameters from a Study of W and Z Bosons," *Phys. Lett.* **B186** 440 (1987).

[40] F. Abe *et al* (CDF Collaboration), "Measurement of the Ratio $\sigma(W \rightarrow e\nu)/\sigma(Z \rightarrow ee)$ in $\overline{p}p$ Collisions at $\sqrt{s} = 1.8$ TeV," *Phys. Rev. Lett.* **64** 152 (1990).

118

[41] J. Alitti *et al* (UA2 Collaboration), "An Improved Determination of the Ratio of W and Z Masses at the CERN $\overline{p}p$ Collider," *Phys. Lett.* **B276** 354 (1992).

[42] F. Abe *et al* (CDF Collaboration), "Measurement of the Ratio $\sigma \cdot B(W \to e\nu)/\sigma \cdot B(Z^0 \to e^+e^-)$ in $\overline{p}p$ Collisions at $\sqrt{s} = 1.8$ TeV, *Phys. Rev. Lett.* **73** 220 (1994).

[43] S. Abachi *et al* (DØ Collaboration), "W and Z Boson Production in $\overline{p}p$ Collisions at $\sqrt{s} = 1.8$ TeV," *Phys. Rev. Lett.* **75** 1456 (1995).

[44] DØ Collaboration, "DØ Results on W Boson Properties," submitted to the *International Europhysics Conference on High Energy Physics,* August 19–26, 1997, Jerusalem, Israel.

[45] P.H. Hansen, "LEP II Physics," CERN PPE/98-001, submitted to CERN School of Physics 1997, Menstrup, Denmark.

[46] R. Blair *et al* (CDF II Collaboration), "CDF II Technical Design Report," Fermilab-Pub-96/390-E (November, 1996).

[47] J. Marriner *et al*, "Run II Handbook," WWW document
`http://www-bd.fnal.gov/lug/runII_handbook/RunII_index.html`

[48] H. Wenzel, "The Primary Interaction Vertex," CDF Note 4066 (February, 1997).

[49] W. Badgett, P. Derwent, "Event z Vertex Cut Efficiency as a Luminosity Correction for Run Ia," CDF Note 2703 (July, 1994).

[50] F. Abe *et al*, "The CDF Detector: an Overview," *Nucl. Inst. Meth.* **A271** 387 (1988).

[51] F. Bedeschi *et al*, "Design and Construction of the CDF Central Tracking Chamber," *Nucl. Inst. Meth.* **A268** 50 (1988).

[52] G.W. Foster *et al*, "A Fast Hardware Track Finder for the CDF Central Tracking Chamber," *Nucl. Inst. Meth.* **A269** 93 (1988).

[53] P. Azzi *et al*, "SVX': the New CDF Silicon Vertex Detector," *Nucl. Inst. Meth.* **A360** 137 (1995).

[54] L. Balka *et al*, "The CDF Central Electromagnetic Calorimeter," *Nucl. Inst. Meth.* **A267** 272 (1988).

[55] D. Amidei *et al*, "A Two Level Fastbus Based Trigger System for CDF," *Nucl. Inst. Meth.* **A269** 51 (1988).

[56] E. Barsotti *et al*, "Fastbus Data Acquisition for CDF," *Nucl. Inst. Meth.* **A269** 82 (1988).

[57] R. Blair *et al*, "Trigger Cross-Sections for the 1991 Run," CDF Note 1467 (May, 1991).

[58] John Wahl, private communication about the 4 GeV prescaled $\times 40$ L1 calorimeter trigger.

[59] D. Amidei *et al*, "New Shower Maximum Trigger for Electrons and Photons at CDF," CDF Note 2740 (July, 1994).

[60] D. Glenzinski *et al*, documented on computer `fnald.fnal.gov` in file `cdf$w_z_data:[ana.val_1b]aaareadme.txt`

[61] K. Yasuoka *et al*, "Response Maps of the CDF Central Electromagnetic Calorimeter with Electrons," *Nucl. Inst. Meth.* **A267** 315 (1988).

[62] K. Yasuoka *et al*, "Performance of Response Maps of the CDF Central Electromagnetic Calorimeter with Electrons," CDF Note 399 (March, 1987).

[63] S. Kopp, J. Wahl, "Search for $W' \to e\nu$," CDF Note 2541 (June, 1994).

[64] F. Ukegawa, "Bottom Quark Production in 1.8-TeV Proton-Antiproton Collisions," Ph.D. Thesis, University of Tsukuba (September, 1991).

[65] L. Nodulman, K. Byrum, "CEM Calibration for 1b (but not 1c)," CDF Note 3477 (January, 1996).

[66] L. Nodulman, "On False Curvatures in 1b," CDF Note 4056 (February, 1997).

[67] UA2 `TOYGEN` Monte Carlo, unpublished.

[68] K. Einsweiler *et al*, "The Measurement of the W Mass in the Muon Channel," CDF Note 4064 (February, 1997).

[69] A. Gordon, "$W\ P_T$ Recoil Model for the 1B W Mass Measurement," CDF Note 3994 (December, 1996).

[70] W. Ashmanskas, "Direct Measurement of , $_W$ with Run Ib Electrons," CDF Note 4137 (August, 1997).

[71] M. Lancaster, "Lepton Resolutions for the Run 1B W Mass Analysis," CDF Note 4046 (February, 1997).

[72] D. Reher, "P_T^W and P_T^Z Modeling for Run 1B W Mass Analysis," CDF Note 4069 (February, 1997).

[73] M. Lancaster, "Recoil Modeling for the Run 1B W Mass Analysis," CDF Note 4048 (February, 1997).

[74] M.H. Reno, "Relative Distributions of W's and Z's at Low Transverse Momenta," *Phys. Rev.* **D49** 4326 (1994).

[75] M. Lancaster, private communication.

[76] Q. Fan, A. Bodek, "A Stand-Alone SVX Track-Finding Routine for High-p_T Tracks Originating from the Beam Position," CDF Note 3585 (March, 1996).

[77] F. Abe *et al* (CDF Collaboration), "Measurement of the W Boson Mass," *Phys. Rev.* **D52** 4784 (1995).

[78] A. Gordon, "Material and CEM Scale Calibration Using E/p from W Events," CDF Note 4013 (August, 1997).

[79] C.P. Yuan, private e-mail communication, May 8, 1998.

[80] Y.S. Tsai, "Pair Production and Bremsstrahlung of Charged Leptons," *Rev. Mod. Phys.* **46** 815 (1974); errata *Rev. Mod. Phys.* **49** 421 (1977).

[81] M.D. Peters, "A Measurement of B Meson Oscillations Using Inclusive Leptons in Proton-Antiproton Collisions at 1.8 TeV," PhD thesis, University of California, Berkeley (1997).

Appendix A

Details for CDF Physicists

This appendix contains various details that are important to fellow CDF physicists but unintelligible to the typical reader.

- **Run Ib Z electron dataset** means the EZA PAD dataset on `FNALD`, maintained by Andrew Gordon and documented in `CDF$W_Z_DATA:[ANA.VAL_1B]` `AAAREADME.TXT`. Similarly, **Run Ib inclusive electron dataset** and **Run Ib W electron dataset** refer to the EIA and EZA datasets, respectively.

- **No known detector problems** means that bit 0 is set in the status returned by `BADRUN`, indicating that the detector is in good working order, with the possible exception of the muon systems (which we do not use). The good run list is maintained by Dan Hennessey and Andy Beretvas. We use the version dated October 30, 1996.

- **Any $Z \to ee$ trigger** means `ELEA_CEM_22_Z`, `ELEA_CEM_22_Z_V1`, or `ELEA_PEM_20_Z`. **Central electron $Z \to ee$ trigger** means the first two of these three. Note that `ELEA_CEM_22_Z` was replaced by `ELEA_CEM_22_Z_V1` for runs 57899, 58146, and $\geq$58166, to remove the Level 3 had/EM cut.

- **Central electron reconstructed** means that an `ELES` bank exists with `REGELE = 0`. (No such bank is found in 0.001% of events passing the L3 W electron trigger; hand scanning reveals jets with had/EM fraction close to 0.125.)

- A CEM electron is in the **CEM fiducial volume** if `FIDELE` returns 0 for that electron. Regions removed are tower 9 (east and west), the chimney towers, $|z| < 9$ cm, and $|x| > 21$ cm.

- The **electron track** is the `QTRK` track whose number is given by `TRPELE` in the `ELES` bank; we usually beam constrain this track with `TRKSVC(0,0,0,-1)`.

FIDELE failure	data fraction	QFL fraction
ϕ cracks	5.4%	4.8%
90° crack	1.7%	1.1%
tower 9	0.7%	0.6%
Σ others	0.3%	0.2%
total	8.1%	6.7%

Table A.1: Distribution of FIDELE failure reasons for data and QFL W electrons. The CEM response in the crack regions may fall to zero faster in QFL than in the real detector; looking at E/p vs. position for the "second" (unbiased) electron in Z events may shed some light on CEM calorimeter cracks.

- **CTC fiducial volume** means track stays in CTC through SL8; in practice, we require $|z_0 + 130 \text{ cm} \cdot \cot\theta| < 150$ cm.

- $E_{\text{hadron}}/E_{\text{EM}}$ **consistent with electron** means HAD3ELE from the ELES bank is less than $0.055 + 0.045\frac{E}{100 \text{ GeV}}$.

- **Track/CEM position match (z-view)** means ZSTELE and ZEXELE from the ELES bank differ by less than 5 cm.

- **Transverse shower shape (z-view)** means CHSELE from the ELES bank is less than 20.

- In the Z removal (Section 6.1.1), "consistent with originating from the same z position" means that TRKSVC constrains the two tracks either to the same vertex or to two vertices less than 5 cm apart. Also note that in computing $M(\text{electron}, \text{track})$ we use ELES-bank information for the first electron and the beam-constrained track momentum for the second electron.

Appendix B

Detector Simulation

The SSD detector simulation, developed by this author, traces electrons, positrons, and photons through a simple model of the CDF detector.

We describe the detector as a set of thin surfaces. We currently implement two types of surface—"disk" and "shell"—though it is straightforward to add others. A disk $D(Z, R_1, R_2)$ is a locus $z = Z$, $R_1 < r < R_2$, and a shell $S(R, Z_1, Z_2)$ is a locus $r = R$, $Z_1 < z < Z_2$. A large portion of the Run I CDF detector can be described using these two surface types alone.[1] We make the simplifying assumption that all measurements and all interactions with detector material take place at these thin surfaces. Figure B.1 shows the SSD model of the Run I CDF detector. In the z-r plane of the figure, disks are vertical line segments, and shells are horizontal line segments.

We trace particles as helices (possibly with zero curvature) through the detector in steps. We step either through 30° in the particle's orbit[2] or to the first surface the particle intersects—whichever produces a shorter step.[3] Proper time, path length, turning angle, and amount of material traversed (in radiation lengths) are accumulated after each step. All of the interesting work of the simulation is performed by callback routines, which may be invoked before the first step and after each subsequent step. An arbitrary number of callbacks can be defined for any of the following occurrences: a new particle is about to be traced; a particle has just stepped 30°; a particle has just intersected a surface; a particle has just taken any step; a particle's trajectory has terminated. Termination occurs either when there is no surface to intersect in the forward direction (i.e. the particle escapes) or when termination is requested by a callback routine (as when a photon converts to e^+e^-

---

[1] Describing the muon system—which is beyond the scope of this document—would require two additional types: flat planes for the CMP and conic shells for the CMX.

[2] The 30° limit simplifies many calculations, e.g. by eliminating ambiguities about branches of transcendental functions and eliminating the need to check many expressions for singularities.

[3] If we implement particle decay in the future, then we will also consider the path length before decay as a possible step size.
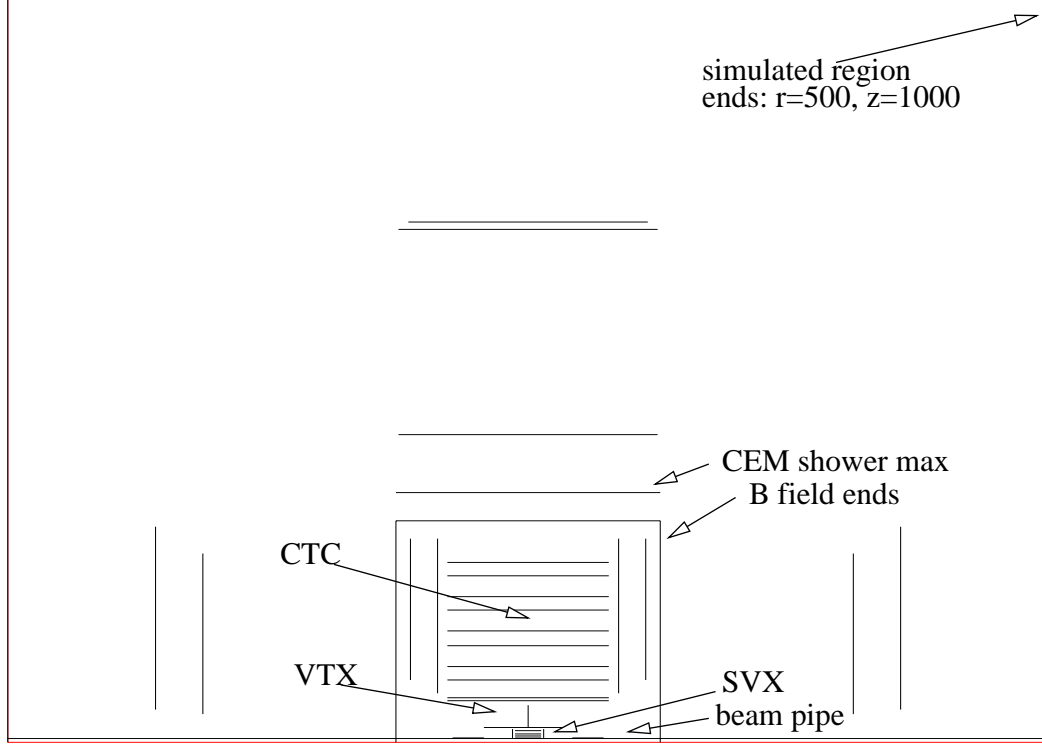
Figure B.1: CDF detector geometry in SSD simulation.

at a surface, an electron or photon reaches the calorimeter, or a particle has looped the maximum number of times).

While tracing a particle, we represent its geometrical state of motion as a "trajectory," which we define to be the particle's position, direction of motion, and curvature (defined as in the CDF helix parameterization): $x, y, z, \cos\varphi = \frac{p_x}{p_T}, \sin\varphi = \frac{p_y}{p_T}, \lambda = \cot\theta = \frac{p_z}{p_T}$. We swim a trajectory a distance s as follows:[4]

$$
\begin{pmatrix} x \\ y \end{pmatrix} \leftarrow \begin{pmatrix} x \\ y \end{pmatrix} + \begin{pmatrix} \cos\varphi & -\sin\varphi \\ \sin\varphi & \cos\varphi \end{pmatrix} \begin{pmatrix} \Delta x \\ \frac{\sin(2cs)}{1+\cos(2cs)}\,\Delta x \end{pmatrix}
$$

$$
\begin{pmatrix} \cos\varphi \\ \sin\varphi \end{pmatrix} \leftarrow \begin{pmatrix} \cos(2cs) & -\sin(2cs) \\ \sin(2cs) & \cos(2cs) \end{pmatrix} \begin{pmatrix} \cos\varphi \\ \sin\varphi \end{pmatrix}
$$

$$
\begin{aligned}
z &\leftarrow z + \lambda s \\
\lambda &\leftarrow \lambda \\
c &\leftarrow c
\end{aligned}
$$

---

[4] We define s to be arc length in the x-y plane, signed so that posigrade motion has $s > 0$.

where

$$\Delta x = \begin{cases} s & \text{if } c = 0 \\ \frac{\sin(2cs)}{2c} & \text{otherwise} \end{cases}$$

By requiring the plane of curvature to be the x-y plane, we implicitly require the magnetic field to be oriented along $\hat{z}$. The identity $1 - \cos\epsilon = \frac{\sin^2\epsilon}{1+\cos\epsilon}$ eliminates numerical problems for small turning angles, which are the usual case for all but the lowest-p_T tracks.

Finding the distance s at which a trajectory intersects a disk $D(Z, R_1, R_2)$ is straightforward: $s = (Z - z)/\lambda$. The trajectory never meets the disk if $s < 0$, if $\lambda = 0$ and $z \neq Z$, or if $R_1 < r < R_2$ is not satisfied after the particle swims a distance s. To find the distance s to a shell $S(R, Z_1, Z_2)$, we rotate x and y to the coordinate system in which $\varphi = 0$ and solve the equation $(x+\Delta x)^2 + (y+\Delta y)^2 = R^2$ for Δx using $\Delta y = \frac{2c(\Delta x)^2}{1+\sqrt{1-(2c\Delta x)^2}}$, which assumes that the turning angle $2|c|s$ is less than $90°$. The equation for Δx is

$$A \, (\Delta x)^2 + B \, \Delta x + C = 0$$

where

$$\begin{aligned} A &= 1 + 4cy + (2cr)^2 \\ B &= 2x(1 + 2cy + 2c^2(r^2 - R^2)) \\ C &= (r^2 - R^2)(1 + 2cy + c^2(r^2 - R^2)) \end{aligned}$$

In solving the quadratic equation, we take the well known precaution against truncation error, using solutions $-\frac{2C}{B+D}$ and $-\frac{B+D}{2A}$ for $B > 0$ and using solutions $\frac{-B+D}{2A}$ and $\frac{2C}{-B+D}$ for $B < 0$, where $D = \sqrt{B^2 - 4AC}$. We consider only solutions with turning angle $0 \leq 2|c|s \leq 45°$. We also require $Z_1 < z < Z_2$ after the particle swims a distance s. If two solutions remain, we choose the smaller s. In the most common case, $|cr| < |cR| \ll 1$, $x > 0$, $cy > 0$, so $A > 0, B > 0, C < 0$, and the chosen solution is $\Delta x = -\frac{2C}{B+\sqrt{B^2-4AC}}$. In practice, the turning angle test does not check s explicitly but instead requires $\Delta x \geq 0$, $|2c\Delta x| \leq \frac{1}{\sqrt{2}}$, and $(x+\Delta x)^2 + (y+\Delta y)^2 = R^2$, using the expression given above for Δy.[5] For solutions satisfying these conditions, the arc length is $s = \frac{\text{asin}(2c\Delta x)}{2c}$ for $c \neq 0$ or $s = \Delta x$ for $c = 0$.

To simulate an event, all final-state particles in the HEPEVT data structure[6] are loaded into SSD's list of particles to be simulated. Currently, only $e^{\pm}$, ν, and γ are processed; since neutrinos escape undetected, the simulation handles them correctly by ignoring them. An event z-vertex is chosen from a Gaussian distribution,

---

[5] The last test eliminates solutions with turning angles between $135°$ and $180°$, for which Δx is in range but for which the correct expression for Δy would be $\frac{1+\sqrt{1-(2c\Delta x)^2}}{2c}$.

[6] HEPEVT is a standardized interface through which HEP event generators communicate their output.

and the generated particles are translated to the interaction point.[7] All particles with $p_T > 50$ MeV are traced through the detector, step by step.

In addition to the particle's present trajectory, information stored while a particle is traced includes its initial position and momentum, its particle type (e, γ, etc.), the magnitude of its present momentum, the present magnetic field magnitude, and various book-keeping information, such as number of steps taken, path length traversed, and number of radiation lengths seen.

We take the magnetic field to be 14116 Gauss for $r < 149$ cm, $|z| < 254$ cm and zero elsewhere. Through the callback procedures of two disks and a shell that bound the region enclosed by the solenoid, the magnetic field is turned off, and the curvature set to zero, when a particle exits this region. Two disks and a shell bound the region $r < 500$ cm, $|z| < 1000$ cm; if a particle leaves this region, its path through the detector is terminated. A particle is also terminated if it turns so far in its orbit that its radius starts to decrease,[8] if its transverse momentum drops below 50 MeV by interacting in the detector material, or if it is an electron or photon that reaches the CEM (modeled as a shell at $r = 184$ cm, $|z| < 254$ cm). When a particle is terminated, its initial and final states are recorded in a data structure that can be written to disk with other program output.

The inner detector material is concentrated in a small number of shells: the beam pipe (1.6% X_0), four SVX layers (0.73% X_0 each), the VTX inner radius (which is segmented in z to accomodate the SVX) (0.5% X_0), and the VTX/CTC boundary (2.3% X_0).[9] We lump the CTC gas and wires into four surfaces, just inside of each stereo superlayer (2.1% X_0 total).[10] No material has been assigned to other surfaces.

When an electron or positron traverses a surface of finite material thickness, it may emit one or more bremsstrahlung photons. The mean number of bremsstrahlung photons emitted is $\frac{\#X_0}{\hat{p}\cdot\hat{n}}\, f(y_{\min}, Z)$, where $\#X_0$ is the surface thickness measured in radiation lengths,[11] $\hat{p}$ is the electron direction of motion, $\hat{n}$ is a unit vector normal to the surface at the point of incidence, $y_{\min}$ is the smallest fraction y of the electron's energy to be radiated to a single photon,[12] and Z is the number of protons

---

[7] The beam position in the x-y plane is straightforward to implement, but for now we use $(0, 0)$.

[8] We do this to save computing time. The simulation is in fact able to trace "loopers" through the detector.

[9] The X_0 values were estimated from values used in the QFL geometry.

[10] We think this value should be 1.8% (0.6% for the gas and 1.2% for the wires), but we use 2.1% for compatibility with Andrew Gordon's simulation.

[11] A radiation length is the distance over which a high-energy electron will radiate all but $1/e$ of its energy. The thickness of an elemental surface in radiation lengths is well approximated [21] by $Z(Z+1)\rho\Delta x \log(287/\sqrt{Z})/716.4A$, where ρ is the density in g/cm^3, Δx is the thickness in cm, Z is the number of protons per atom, and A is the atomic mass (g/mole).

[12] A cutoff is necessary because the number of radiated photons, $\int dy\, \frac{dN}{dy}$, diverges as $y \to 0$; the total energy fraction radiated, $\int dy\, y\, \frac{dN}{dy}$, converges without a cutoff, however. Up to percent-level

per atom. We use $y_{\min} = \frac{50 \text{ MeV}}{p_T^e}$. This mean can be calculated by a GEANT routine (GBRSGE) or a QFL routine (QBREMI, coded by R.G. Wagner). The actual number of photons is then drawn from a Poisson distribution with this mean. Each photon energy is then thrown by either a GEANT routine (GBREME) or a QFL routine (QBREMM). The electron momentum is reduced by the sum of the photon momenta. The photons, with momenta parallel to the electron momentum, are added to the list of particles to simulate.

When a photon traverses a surface of finite material thickness, it may convert into an e^+e^- pair. We use a GEANT routine (GPRSGG) to compute the pair-production cross-section $\sigma(Z, |\vec{p}_\gamma|)$, and calculate the conversion probability to be $1 - \exp(-\frac{\rho \sigma N_A}{A \hat{p} \cdot \hat{n}} \Delta x)$, where N_A is Avagadro's number and other quantities are as above.[13] If the photon converts, the energy sharing between e^+ and e^- is thrown by QFL routine QASSYM (which was modified from GEANT routine GPAIRG). The photon is terminated, and an electron and positron, with momenta parallel to the photon momentum, are added to the list of particles to be simulated.

When a charged particle traverses a surface of finite material thickness, it scatters elastically many times in the electric fields of nuclei and electrons. While the cumulative scattering angle after a very large number of scatters approaches a Gaussian distribution,[14] the angle after a moderate number of scatters is given by a Molière distribution, which has much longer tails. We throw a polar scattering angle θ from a Molière distribution using GEANT routine MLR, throw an azimuthal scattering angle ϕ from a flat distribution, and rotate the particle trajectory an angle θ from its incident direction of motion. Because we have not yet had an opportunity to test the multiple scattering implementation carefully, SSD simulation results presented in this dissertation are obtained with multiple scattering disabled.

Energy loss through ionization is not yet included. Also, several second-order effects within a single surface ought to be handled better: Multiple bremsstrahlung of an electron in one surface is allowed (since the number of photons is drawn from a Poisson distribution), but bremsstrahlung photons cannot convert in the surface in which they are created, and e^+e^- conversion pairs cannot radiate photons in the surface in which they are created. Since the thickest surface we implement is 2.3% X_0, these effects are small, but we have a plan in mind for handling them properly if we reuse the SSD simulation in the future.

Instead of simulating the VTX directly[15] we use a procedure from the QFL simulation to create a fake VTVZ data structure (which normally contains reconstructed z-vertex information), into which we write the simulated event z-vertex.

Z-dependent corrections, $\frac{dN}{dy} = \frac{1}{y}(\frac{4}{3}(1-y) + y^2)$ [80].

[13] At high energies (tens of GeV), the conversion probability is $1 - \exp(-\frac{7}{9} \frac{\#X_0}{\hat{p} \cdot \hat{n}})$.

[14] A popular rough approximation for the rms scattering angle is $\frac{15 \text{ MeV}}{p\beta} \sqrt{\#X_0}$.

[15] The ingredients already exist for a hit-level VTX simulation, but the questions such a simulation would address are not not pertinent to this dissertation.

We can simulate the CTC in two ways: at the hit level or at the track level. The hit-level simulation uses each CTC superlayer's callback procedure to determine each charged particle's position and direction of motion in each CTC superlayer. (Interactions in the detector material may occur between superlayers.) A CDF library procedure then simulates hits on drift chamber wires within that superlayer. After all particles have been traced, the usual CDF track reconstruction code finds and fits the particle trajectories.

For speed and simplicity, we normally use a track-level CTC simulation instead. The callback procedure for the innermost CTC superlayer converts each charged particle's trajectory into the five CDF helix parameters, using a CDF library procedure. These parameters are then smeared by adding a vector of five random numbers, distributed multinormally according to a covariance matrix. The covariance matrix calculation uses superlayer-by-superlayer hit patterns sampled from Run Ib W electron tracks and wire hit resolutions measured from residuals in Run Ib W electron track fits. To reproduce the beam-constrained $\frac{1}{p_T}$ resolution observed in the data, one must scale these hit resolutions by a factor 1.65; to reproduce the impact-parameter resolution, one must use a factor 2.0; for the z_0 resolution, the factor is 2.25.[16] As an ad-hoc method to reproduce these three resolutions simultaneously, we scale the hit resolutions by factors (2.25, 1.875, 1.50, 1.50, 1.50) in superlayers (0, 2, 4, 6, 8), and by a factor 2.25 in all stereo superlayers.

The callback routine for a shell at the CES radius ($r = 184$ cm, $|z| < 254$ cm) simulates electron and photon showers in the CEM by accumulating incident particle energies in a 20×24 array of CEM towers. Each incident electron or photon deposits its entire energy into the tower in which it lands at the CES radius. No particle-level shower simulation is performed, no leakage of any kind is simulated, and no response map is applied.[17] After all particles have been traced, each tower's energy E is smeared by $\frac{\sigma_E}{E} = \frac{13.5\%\sqrt{\text{GeV}}}{\sqrt{E\sin\theta}} \oplus 1.5\%$,[18] where θ is the polar angle measured from the detector origin to the center of the tower. The smeared energies are formatted into a TOWE data structure, which is then processed by the standard CDF electron reconstruction software.

The CES itself is not simulated. When CES data are not available, the electron reconstruction works properly but fills CES-related variables (shower x and z positions and shower-shape χ^2 values in the x and z views) with out-of-bounds values. We overwrite the CES x and z positions with the x and z positions of the track that the reconstruction code associates with the electron (creating a perfect

---

[16] The CDF reconstruction software multiplies CTC track parameter errors by a factor 2.0 before merging CTC tracks with SVX hit information.

[17] Consequently, we do not use the response map when analyzing SSD output. To be correct, we should apply the inverse response map in the simulation and then use the respose map when analyzing the output, but we expect this only to make a difference when an electron and a bremsstrahlung photon land far apart in the same tower.

[18] Tower energies smeared to negative values are truncated to zero.

position match) and overwrite the χ^2 values with zeros. We believe that a proper CES simulation can be implemented easily and profitably and may do this in the future.

A few other surfaces (for PEM, FEM, CHA, and CMU) are included in the geometry for future expansion, but they currently have no effect except to slow down the simulation.

Appendix C

QCD Background Model

An important component of this analysis is an understanding of the sizes and spectral shapes of the background processes that can mimic the $W \to e\nu$ signature. Backgrounds are even more important for this analysis than for the W mass analysis because we are measuring the tail of the W signal region. Here, we discuss a method, based on a parameterization of photon conversion events that pass the inclusive electron trigger, for determining the spectral shapes of dijet backgrounds in the high-p_T electron sample.[1]

The signature for an electron in CDF is an EM shower matched to a stiff track. Several processes allow jets to match this signature. Neutral pions are produced copiously in jets and decay almost exclusively to two photons. Since there is about 7% of a radiation length of material between the beamline and the CTC, each photon has a probability of about $\frac{7}{9} \cdot 7\% \approx 5\%$ to convert to an electron-positron pair; if one leg of the pair takes a large fraction of the photon energy, it leaves a track in the CTC that matches perfectly with an EM shower in the calorimeter. In addition, about 1% of π^0s decay promptly to $\gamma\, e^+ e^-$. A stiff π^+ in a jet can interact (e.g. $\pi^+ n \to \pi^0 p$) in the solenoid or early in the EM calorimeter to produce an EM shower matched to a high-p_T track. Random overlaps of charged and neutral pions are also possible. Finally, heavy flavor ($b\bar{b}$ and $c\bar{c}$) production is a QCD process (so its rate is much higher than the rates of electroweak processes) that can produce real electrons, since $(b, c) \to e\nu\ (c, s)$ about 10% of the time. In Section 6.2.2 we estimated the rate of these processes by exploiting the fact that these QCD processes are much more likely than electroweak processes to have a high track multiplicity near the electron candidate. In this appendix, we estimate the kinematic shapes of these processes by assuming that photon conversion events, which are readily identified, are representative of all QCD background events.

The study uses events selected from the inclusive electron dataset (Table 4.4). (Note that the inclusive electron trigger (`ELEA_CEM_18`) unfortunately imposes a

---

[1] This model was inspired by discussions with Andrew Gordon and Barry Wicklund.

131

few electron identification cuts that we either do not apply or apply more loosely in the W electron dataset, e.g. $|\Delta x| < 3$ cm, Lshr3 < 0.2, $\chi^2_s < 10$, so it is impossible for us to make a completely fair comparison with the W electron sample.)

We can then tag conversions by considering all tracks with $p_T > 1$ GeV[2] and charge opposite that of the electron as potential conversion partners. We consider a track a conversion partner if it satisfies $|\Delta \cot \theta| < 0.06$, $|S| < 0.3$ cm, $|\Delta z| < 5$ cm, $|\Delta \phi| < \frac{\pi}{4}$, -5 cm $< R_{\mathrm{conv}} < 45$ cm.[3] (Essentially we are requiring that there be a point at a physically reasonable radius at which the tracks meet and are parallel.)

Figure C.1 compares the $\not{E}_T$ spectra for inclusive electron events flagged and not flagged by the conversion finder. The W peak is evident in the unflagged sample. The agreement in shape at low $\not{E}_T$, while not perfect, suggests that the conversions represent the background reasonably well.

Close inspection reveals a small W peak in the conversion sample. This peak is the result of "tridents," electrons in which a bremsstrahlung photon from a W electron converts into an electron-positron pair. Since we do not want real W events to influence the background shape, we must subtract the tridents from the conversion sample. To perform the subtraction, we observe that a typical trident event has near the electron cluster one stiff track (the trigger electron) and two soft tracks from the converted photon. Frequently only one of the two soft tracks will be in the $p_T > 1$ GeV sample. We assume that in such events there is no charge correlation between the trigger electron and the one reconstructed leg of the conversion—that the two legs are equally likely to be found.[4] To eliminate the tridents, then, we look for both right-sign and wrong-sign conversion partners of the trigger electron; we assign a weight $+1$ if we find only a right-sign partner, a weight -1 if we find only a wrong-sign partner, and a weight 0 if we find both. Figure C.2 shows $\not{E}_T$ spectra for right-sign-only conversions, wrong-sign-only conversions, and weighted (right-sign minus wrong-sign) conversions. The subtraction seems to be effective at removing the W peak from the conversion sample.

Figure C.3 provides evidence that it is legitimate to interpret the LS conversions as tridents. Figure C.4 compares the E_T, $\not{E}_T$, and M_T spectra of weighted conversions and non-conversions, as additional evidence that the weighted conversions describe the background shape well.

So far we have been working with an inclusive electron sample in which no $\not{E}_T$ or $\vec{u}$ cuts have been applied. We would like to use the conversions to model the background that remains in the final W sample, which includes $\not{E}_T$ and $\vec{u}$ cuts.

---

[2] The p_T cut allows us to neglect tracking efficiency issues and to keep the micro-DST data files to a manageable size.

[3] These quantities are calculated by subroutine CNVCALC, written by W.J. Ashmanskas in early 1995, used extensively in Ref. [81], and likely to appear eventually in the CDF BOTTOM library.

[4] The CTC tracking efficiency does have a charge asymmetry, but since the trigger electron can have either charge, we expect this asymmetry to be washed out.
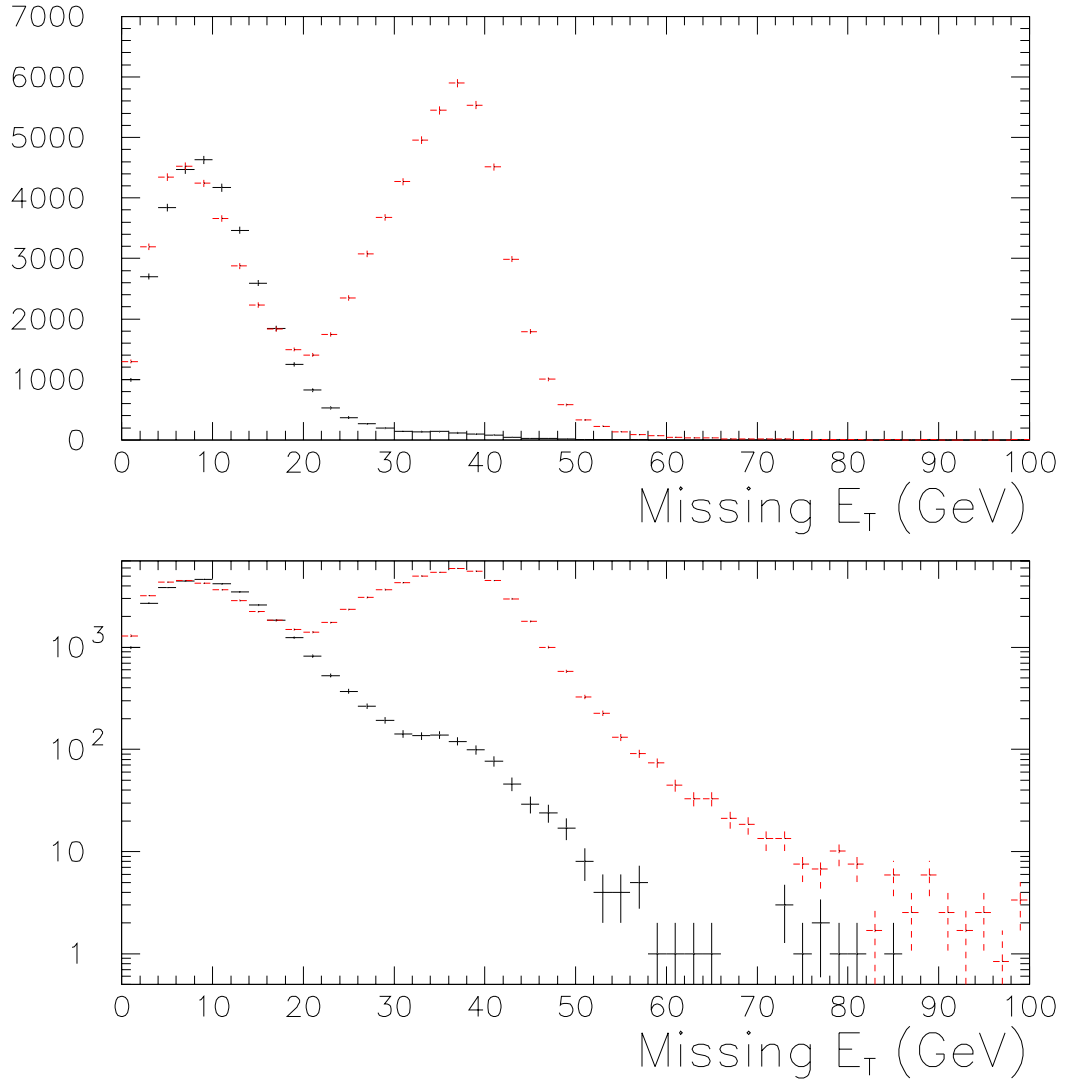
Figure C.1: (Top) $\not{E}_T$ spectra for events in which an opposite-sign conversion partner for the trigger electron is found (solid) and is not found (dashed). The shapes are rather similar at low $\not{E}_T$, giving us confidence that the conversion sample is representative of the multijet background. (Bottom) Same as above, on a semilogarithmic scale. Note the small W peak in the conversion sample.

Applying these cuts to the conversions, however, would leave very few events with which to model the background.

To increase the statistical power of the conversion sample, we assume that a multijet event fakes a W event through the random coincidence of two independent processes: number one, a jet produces a highly electromagnetic shower, satisfying the electron trigger; and number two, the hadronic energy in the event is mismeasured, causing large $\not{E}_T$. We assume that we can characterize the E_T spectrum of the conversion sample, then characterize the $\vec{u}$ distribution as a function of E_T, so
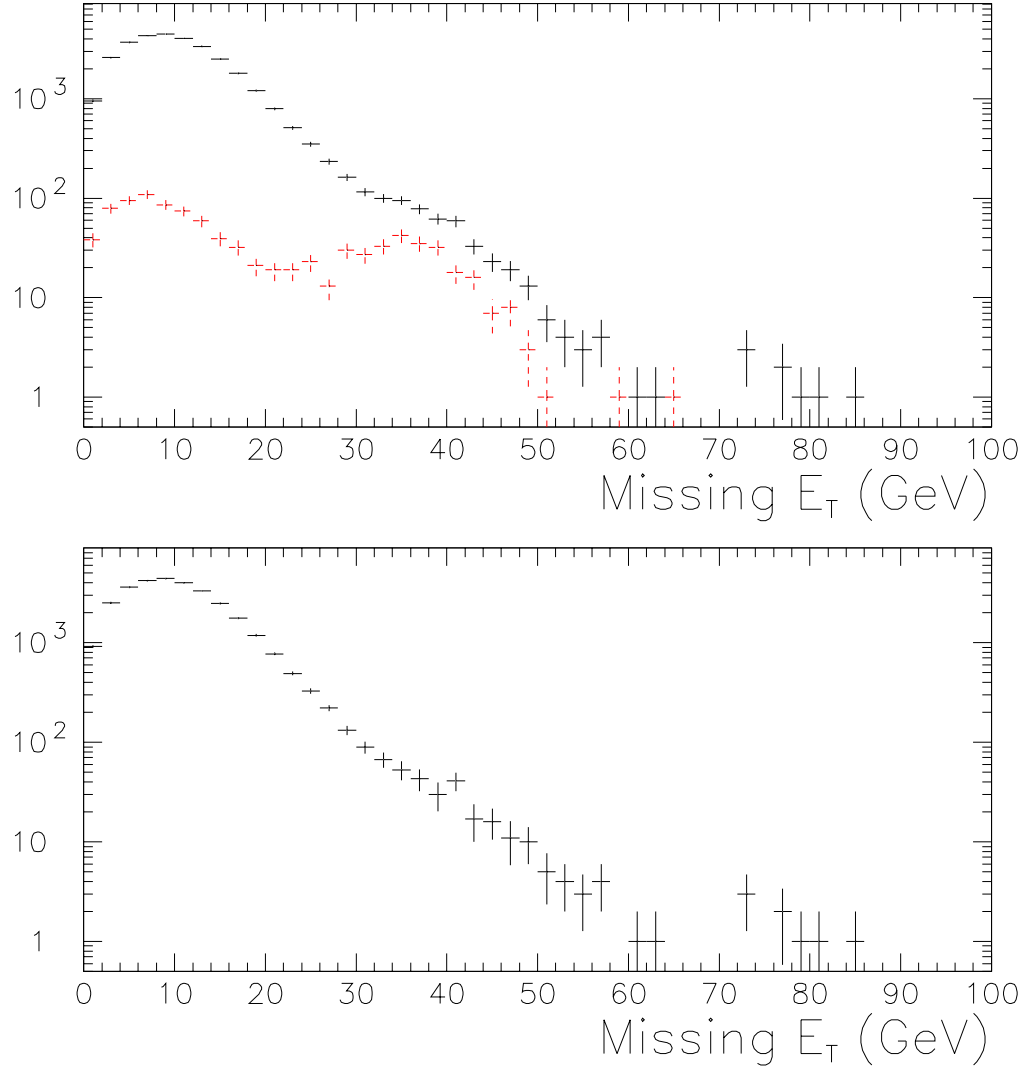
Figure C.2: (Top) $\displaystyle{\not}E_T$ spectra for OS (solid) and LS (dashed) conversions. We assume that tridents populate the OS and LS samples equally. (Bottom) $\displaystyle{\not}E_T$ spectrum for weighted conversion sample, in which OS pairs are given weight $+1$, LS pairs are given weight -1, and electrons for which both OS and LS partners are found are ignored. We expect this weighting to remove, statistically, the trident contribution. As expected, the W peak has disappeared.

that it is possible to generate observables E_T, $u_{\parallel}$, and $u_{\perp}$ in a simulation of the QCD background.

First we fit the E_T spectrum to the form

$$\frac{dN}{dE_T} = \exp\left\{A_1 + B_1 \cdot E_T\right\} + \exp\left\{C_1 + D_1 \cdot E_T\right\}, \qquad \text{(C.1)}$$

134

as shown in Figure C.5. Then we fit the mean and rms of $u_\parallel$ to the form

$$\mu_\parallel(E_T) = A_2 \cdot E_T + B_2 \cdot E_T^2 \tag{C.2}$$

$$\sigma_\parallel(E_T) = C_2 + D_2 \cdot E_T. \tag{C.3}$$

We can then define $x_\parallel \equiv \frac{u_\parallel - \mu_\parallel}{\sigma_\parallel}$ and fit the $x_\parallel$ spectrum to the form

$$\frac{dN}{dx_\parallel} = A_3 \cdot \exp\left\{-\frac{1}{2}\left(\frac{x_\parallel - B_3}{C_3}\right)^2\right\} + \tag{C.4}$$

$$D_3 \cdot \exp\left\{-\frac{1}{2}\left(\frac{x_\parallel - E_3}{F_3}\right)^2\right\} +$$

$$G_3 \cdot \exp\left\{-\frac{1}{2}\left(\frac{x_\parallel - H_3}{I_3}\right)^2\right\},$$

as shown in Figure C.6. We have assumed that the $x_\parallel$ shape is independent of E_T. Figure C.7 motivates this assumption by showing the data and fit results together in several E_T bins. Finally, we fit the $u_\perp$ distribution (which seems not to have a strong dependence on E_T) to the form

$$\frac{dN}{du_\perp} = A_4 \cdot \exp\left\{-\frac{1}{2}\left(\frac{u_\perp - B_4}{C_4}\right)^2\right\} + \tag{C.5}$$

$$D_4 \cdot \exp\left\{-\frac{1}{2}\left(\frac{u_\perp - E_4}{F_4}\right)^2\right\},$$

as shown in Figure C.8.

It is easy to turn this parameterization of the photon conversion data into a Monte Carlo program to generate "events" consisting of ordered triplets $(E_T, u_\parallel, u_\perp)$. We can apply to these events the E_T, $\not{E}_T$, and $\vec{u}$ cuts used to select W events and examine the properties of the Monte Carlo events that survive.

Figures C.9–C.11 show predictions of the Monte Carlo we have made from these fits to the conversion data and some comparisons with the input conversion data. In Figure 6.12 we compared the M_T shape predicted with this Monte Carlo to the M_T shape of events in the W sample having $N_{\text{cone}} > 2$. We use the distributions shown in Figure C.11 to compare simulated W-plus-backgrounds with the W dataset, as in Section 5.5.
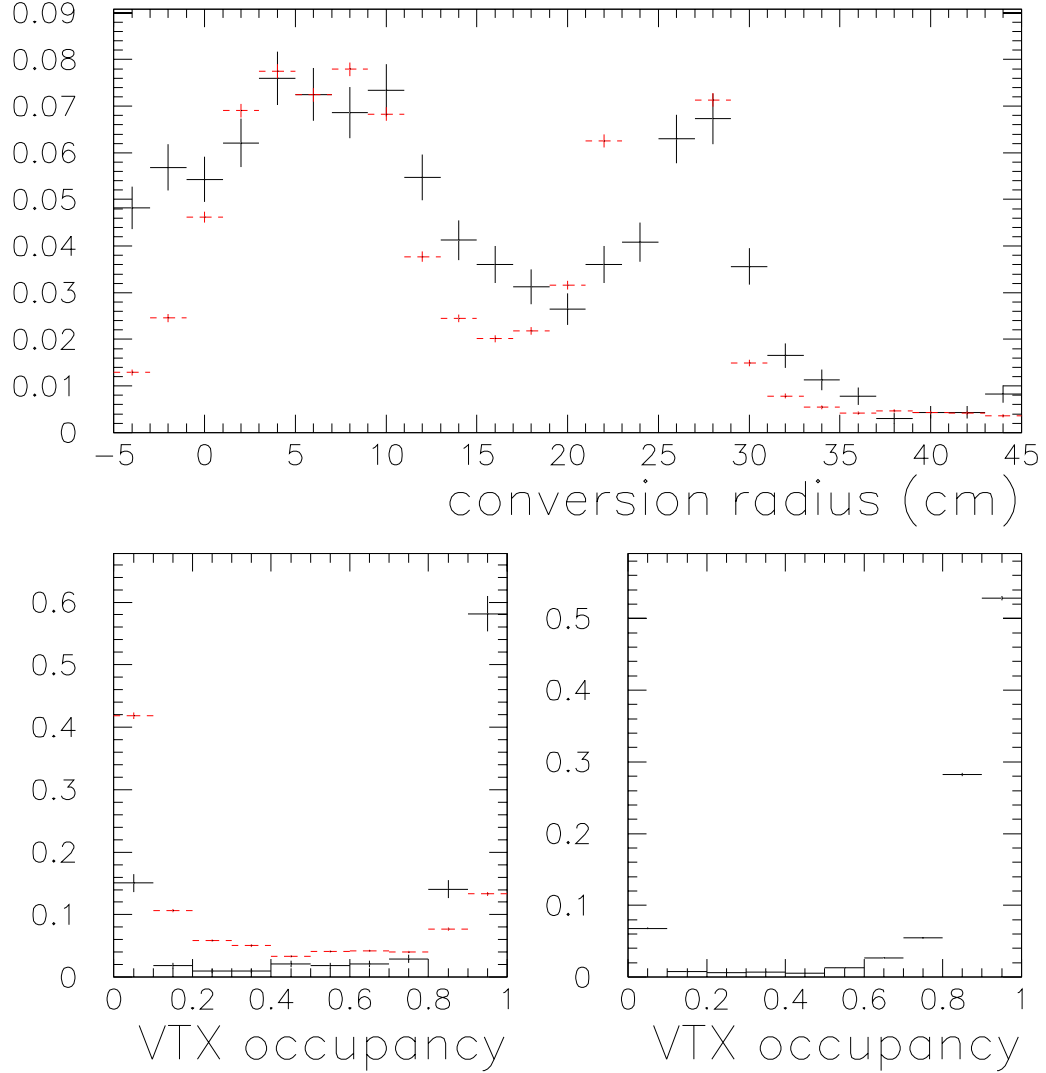
Figure C.3: (Top) Reconstructed radius of conversion for like-sign (solid) and opposite-sign (dashed) conversion partners of trigger electrons. Both spectra show peaks in the SVX region and the region between the VTX and CTC, indicating that both LS and OS pairs are the result of secondary interactions in the detector material. The R_{conv} resolution can be improved substantially with a constrained fit to the conversion hypothesis, but we chose not to use such a fit for this illustration. (Bottom left) Fraction of expected hits found in a road search of the VTX along the path of the trigger electron track, for LS (solid) and OS (dashed) conversion partners in which $R_{\text{conv}} > 20$ cm. (The outermost VTX sense wires are located at $r \approx 21$ cm.) (Bottom right) VTX hit fraction for events in which $\not{E}_T > 25$ GeV, which are dominated by real W electrons. The VTX confirms the expectation that in most OS conversions there is no electron charged track below R_{conv}, whereas in most LS conversions there is an electron charged track originating at the beamline. Together these plots give credibility to the trident interpretation of the LS conversions.
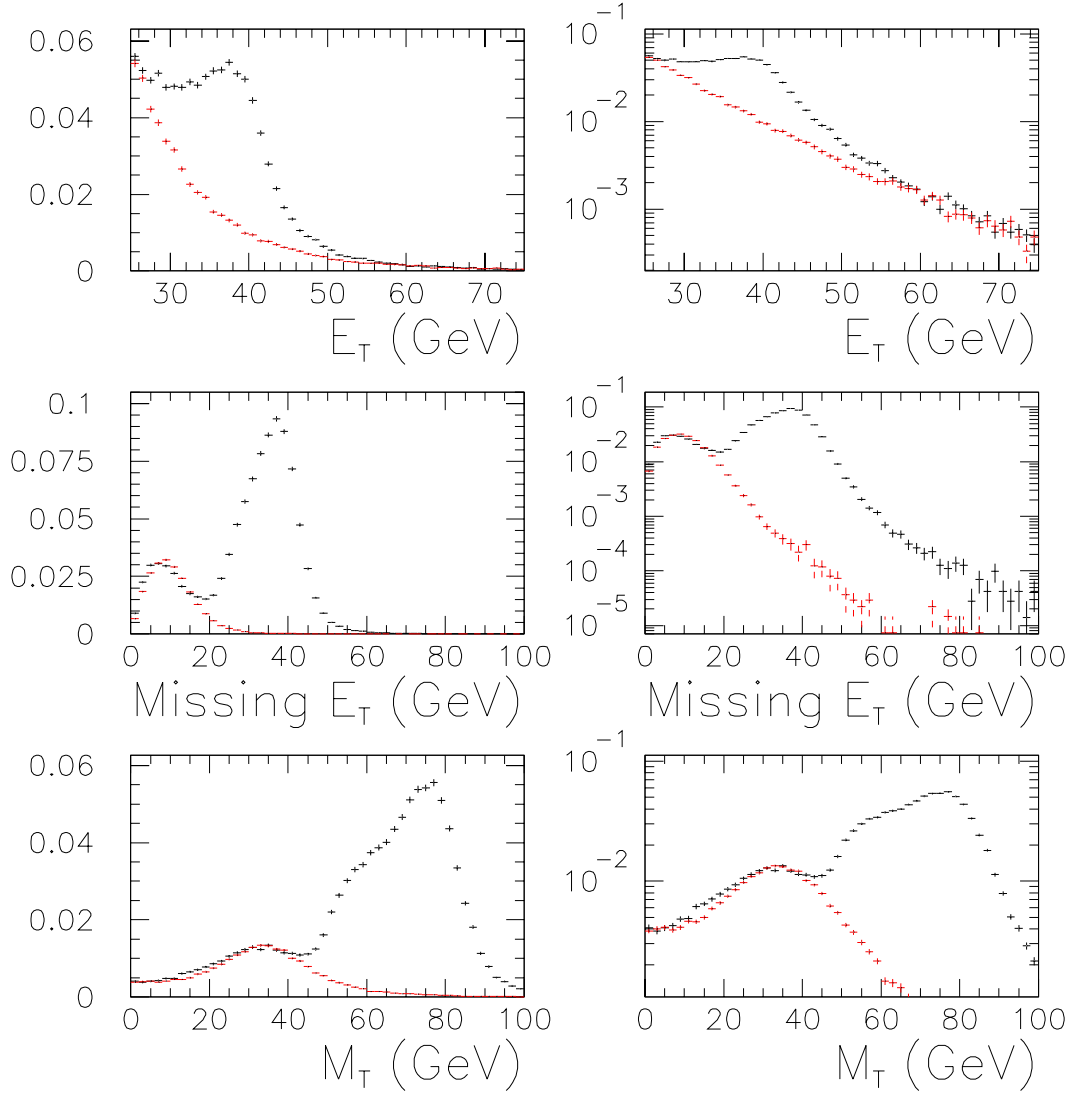
Figure C.4: E_T, $\not{E}_T$, and M_T spectra, on linear and semilogarithmic plots, for weighted conversion events (dashed) and events with $N_{\mathrm{cone}} = 0$ (solid). The $N_{\mathrm{cone}} = 0$ sample has a large W content, and we claim that the weighted conversions do a decent job representing the multijet background beneath the Ws.
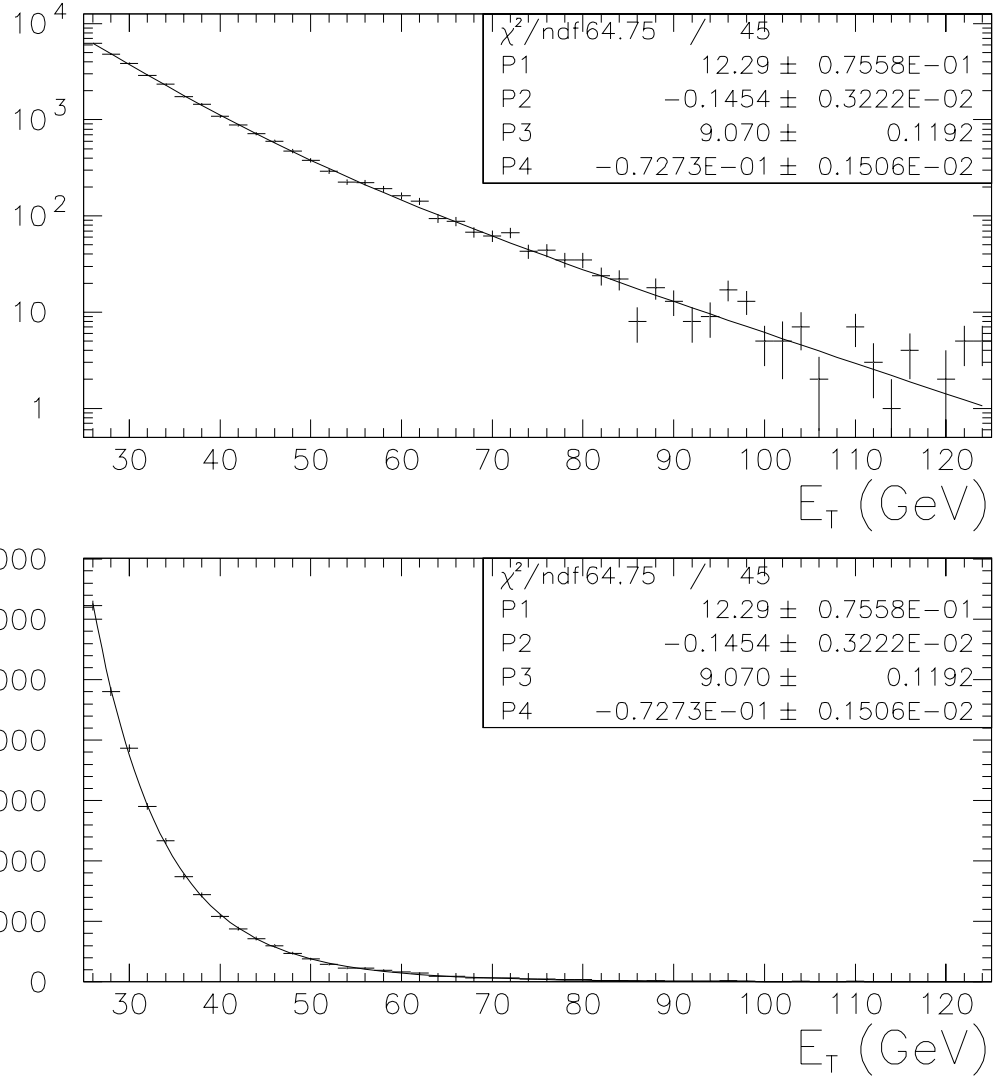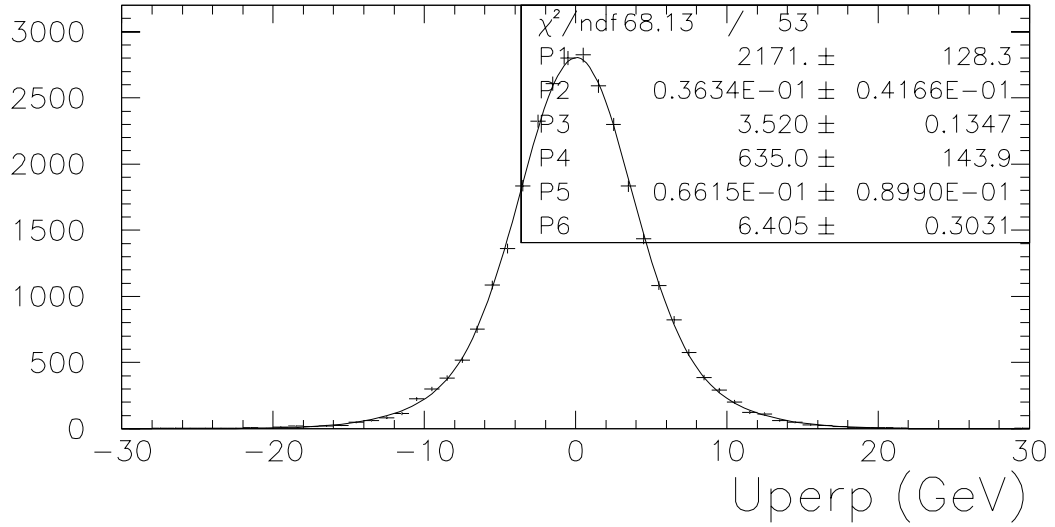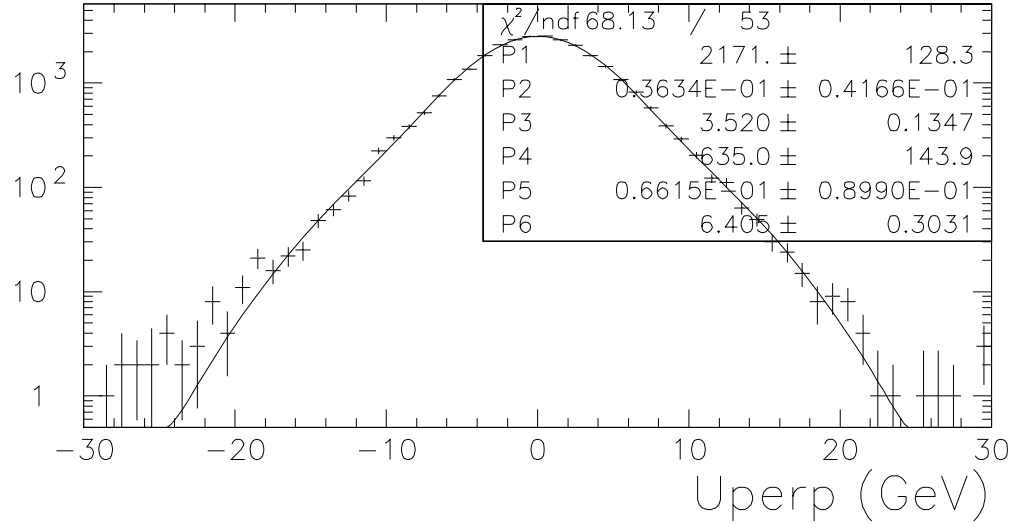
Figure C.5: We fit the E_T spectrum of the weighted photon conversion sample to the sum of two exponentials (see Eq. C.1). The result is shown on semilogarithmic and linear scales.

138
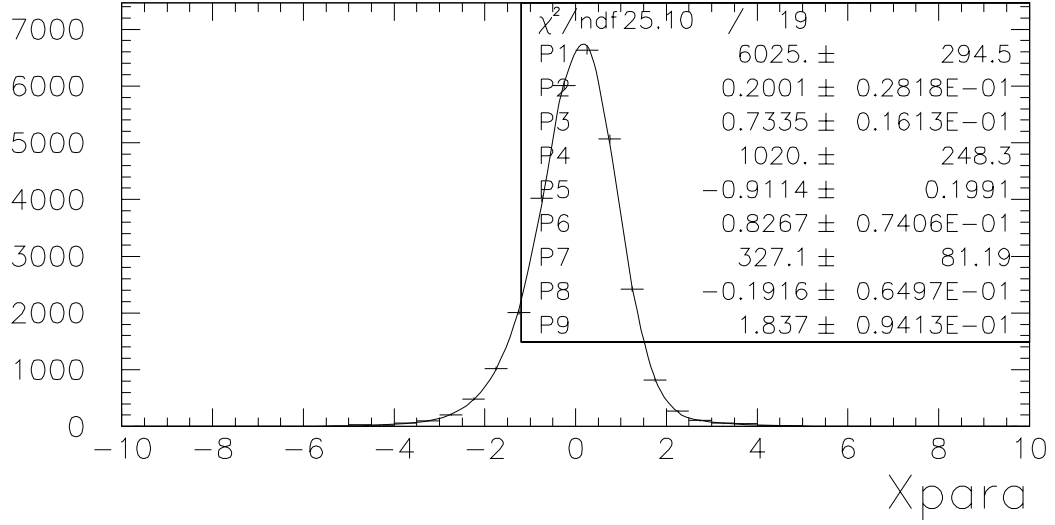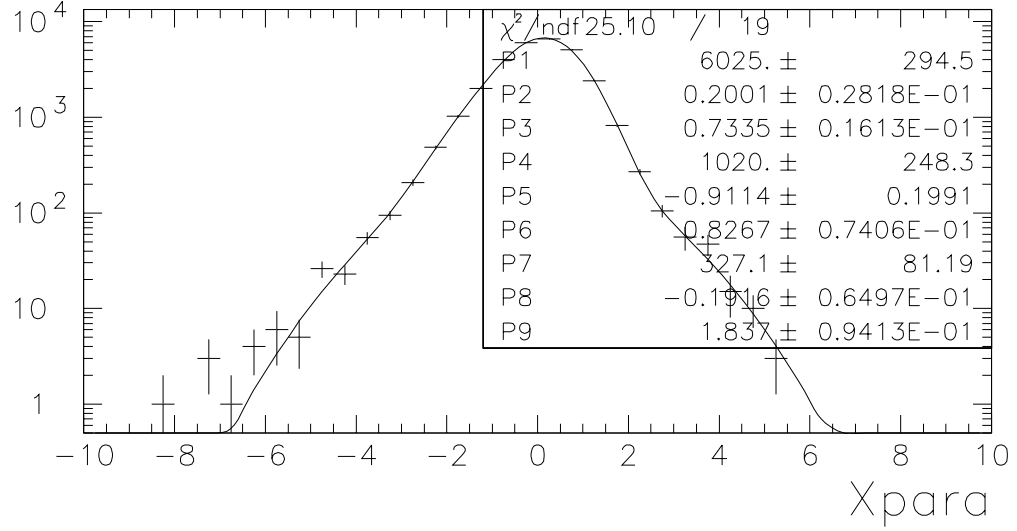
Figure C.6: We fit the spectrum of $x_{\parallel} \equiv \frac{u_{\parallel} - \mu_{\parallel}(E_T)}{\sigma_{\parallel}(E_T)}$ of the weighted photon conversion sample to the sum of three gaussian distributions (see Eq. C.4). The result is shown on semilogarithmic and linear scales.

139
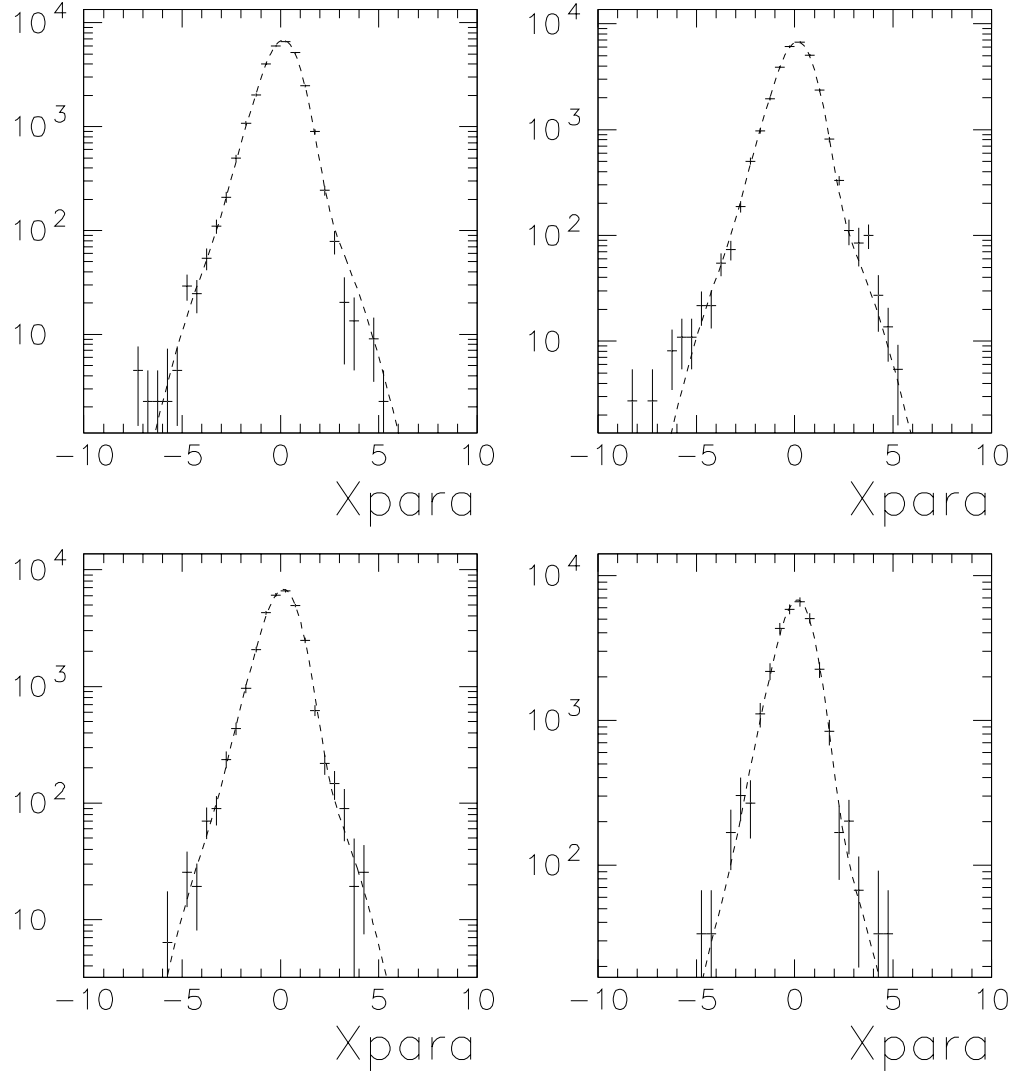
Figure C.7: We have assumed that the $x_{\parallel}$ shape of the weighted photon conversion sample is independent of E_T. Here we show the $x_{\parallel}$ distribution and the fit (see Eq. C.4) for 25 GeV $\leq E_T <$ 30 GeV (top left), 30 GeV $\leq E_T <$ 40 GeV (top right), 40 GeV $\leq E_T <$ 60 GeV (bottom left), and 60 GeV $\leq E_T <$ 100 GeV (bottom right). By eye, the fit describes the data well in all four E_T bins.

Figure C.8: We fit the $u_\perp$ spectrum of the weighted photon conversion sample to the sum of two gaussian distributions (see Eq. C.5). The result is shown on semilogarithmic and linear scales.
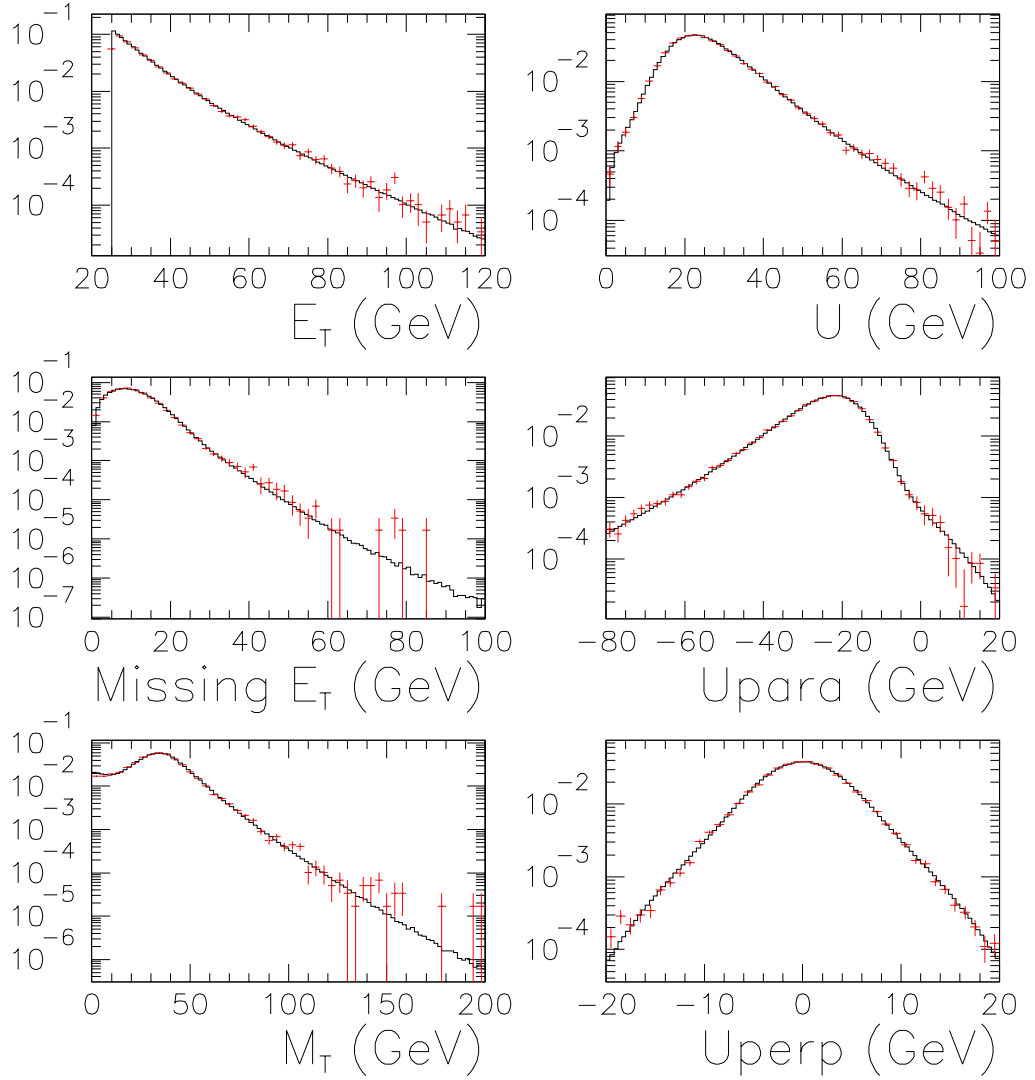
Figure C.9: Distributions of various kinematic variables coming out of the conversion-fit Monte Carlo (histogram), compared with weighted conversion data (points with errors). No $\not{E}_T$ or $\vec{u}$ cuts have been applied. These plots demonstrate that the fits (Eq. C.1–C.5) have been correctly turned into a Monte Carlo program.
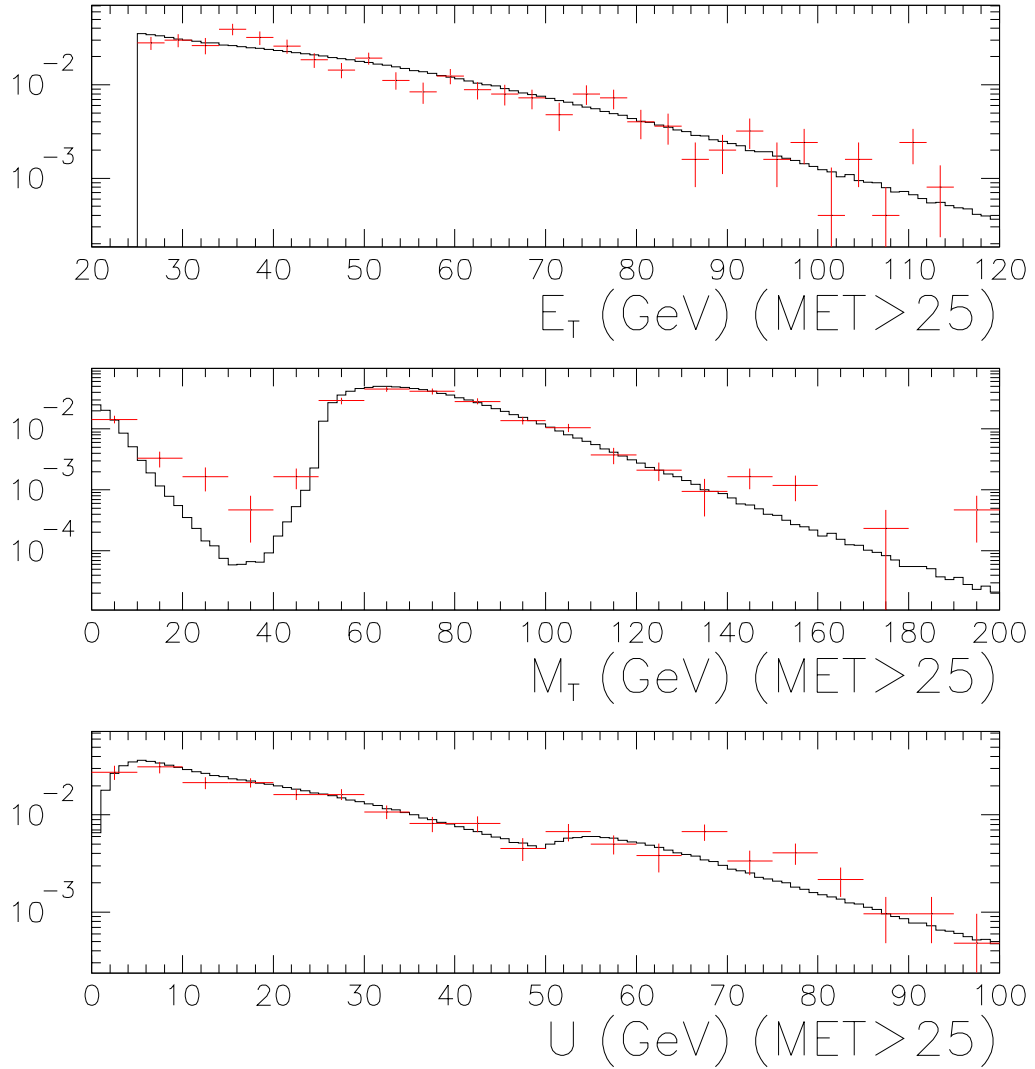
Figure C.10: Distributions of E_T, M_T, and $|\vec{u}|$ for Monte Carlo (histogram) and weighted conversion data (points with errors), after $\not{E}_T > 25$ GeV cut has been applied.
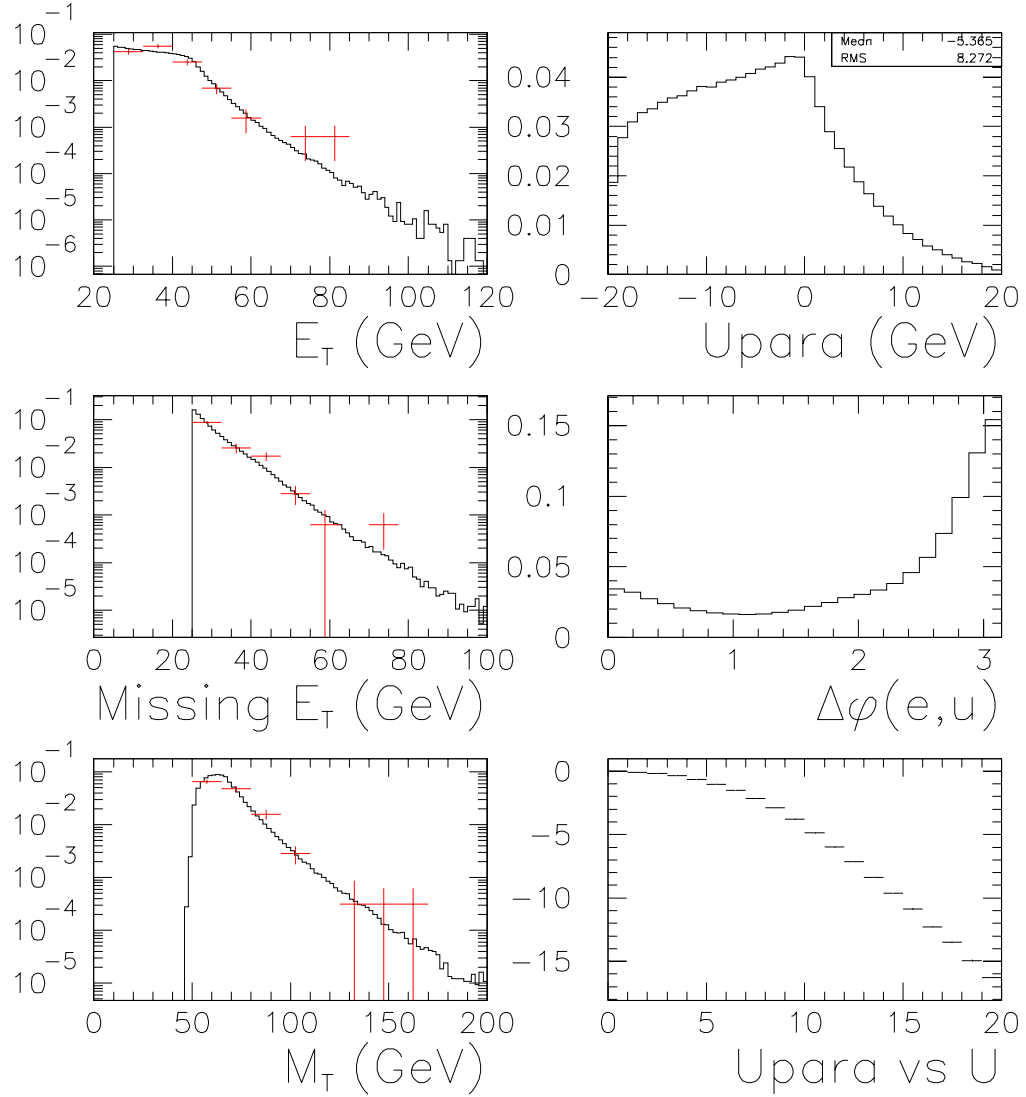
Figure C.11: (Left) Distributions of E_T, $\not{E}_T$, and M_T for Monte Carlo (histogram) and weighted conversion data (points with errors), after $\not{E}_T > 25$ GeV and $|\vec{u}| < 20$ GeV cuts have been applied. Agreement is good, but very few conversion events pass these $\not{E}_T$ and $|\vec{u}|$ cuts. The fact that these cuts leave so few events with which to characterize the background is the reason that we have factored the data into E_T and $\vec{u}(E_T)$ fits. (Right) Predictions of the Monte Carlo for $u_{\parallel}$, $\Delta\phi(\vec{E}_T, \vec{u})$, and $\langle u_{\parallel} \rangle$ vs. $|\vec{u}|$ for dijet background events passing $\not{E}_T > 25$ GeV and $|\vec{u}| < 20$ GeV cuts. These distributions are normalized to the expected background rate and added (along with distributions for other expected backgrounds) to W Monte Carlo distributions when comparing W data with expectations.

Appendix D

CTC Alignment

This appendix is a copy of a CDF internal note that Aseet Mukherjee and I have written. The note may be updated in the future. The latest version will always be available as CDF note 4456, archived electronically at `http://www-cdf.fnal.gov`

CTC Alignment for Run Ib

Bill Ashmanskas, *LBNL*
Aseet Mukherjee, *FNAL*

Abstract

We have derived new CTC `WPO` database constants using Run Ib $W \to e\nu$ data. In this note, we describe the alignment procedure and illustrate the results using $W \to e\nu$ and $J/\psi \to \mu\mu$ tracks.

D.1   Introduction

In the approximation that CTC drift trajectories are azimuthal, the CTC measures $\varphi_i = \phi(r_i) + \frac{s_i}{r_i} z(r_i)$ for each track at 84 radii r_i, where s_i is zero for axial layers and approximately $\pm \tan(2.5°)$ for stereo layers.

After naming the helix parameters $c, \phi_0, \delta, \lambda, z_0$ and defining $a = \frac{c}{1+2c\delta}$, $b = \frac{\delta(1+c\delta)}{1+2c\delta}$, $L = \sqrt{\frac{r^2-\delta^2}{1+2c\delta}}$, we can write $\phi(r) = \phi_0 + \mathrm{asin}(ar + b/r)$ and $z(r) = z_0 + \frac{\lambda}{c}\mathrm{asin}(cL)$. For the special case $\delta = 0$, the equations are somewhat simpler: $\phi(r) = \phi_0 + \mathrm{asin}(cr)$ and $z(r) = z_0 + \frac{\lambda}{c}\mathrm{asin}(cr)$.

A systematic error in φ_i can clearly bias the fitted helix parameters. For instance, an error of the form $\varphi_i \to \varphi_i + kr_i$ generates a "false curvature" $c \to c + k$, while an error of the form $\varphi_i \to \varphi_i + \epsilon s_i z(r_i)$ generates a "cot θ scale" $\lambda \to \lambda(1 + 2\epsilon \langle r \rangle)$ without scaling z_0. An error of the form $\varphi_i \to \varphi_i + \frac{d}{r_i}$ generates a "false impact parameter" $\delta \to \delta + d$.

The CTC internal alignment, introduced in Ref. [1], is intended to remove systematic errors of the form $\varphi_i \to \varphi_i + A_i + B_i z(r_i)$. The physical model for these misalignments is a coherent (i.e. ϕ-independent) twist of each endplate as a function of radius; an exaggerated example of such a twist is shown in Figure D.1. To allow different deformations in the east and west endplates, the φ offsets are given a linear slope in z.

The Run Ia alignment offsets ($A_i \pm 150 \text{ cm} \cdot B_i$) are shown in Figure D.2. (These are the same constants graphed in Figure 3 of Ref. [2].) Notice that the inner and
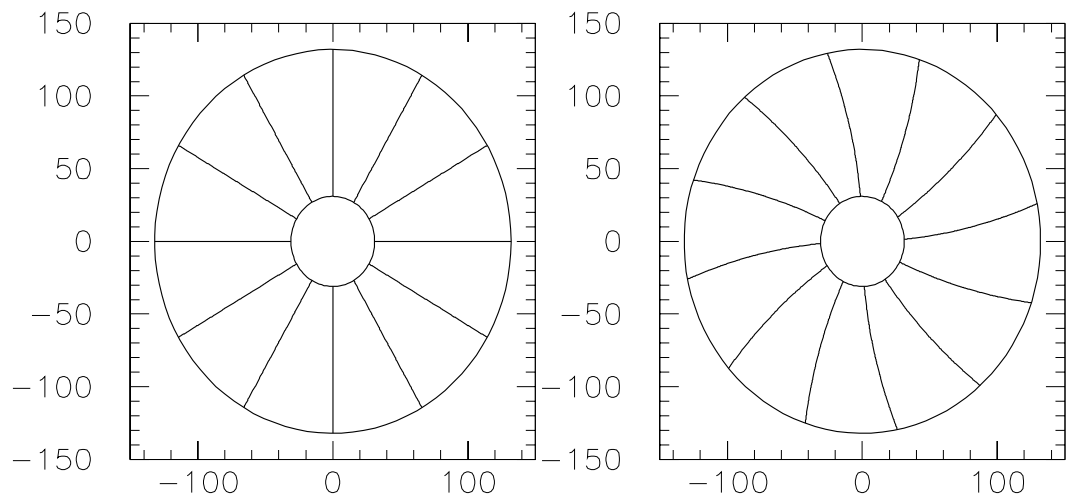
Figure D.1: A deformation of the CTC endplates of the form $\varphi \to \varphi + kr$ would transform the straight lines in the left figure into the curved lines in the right figure.
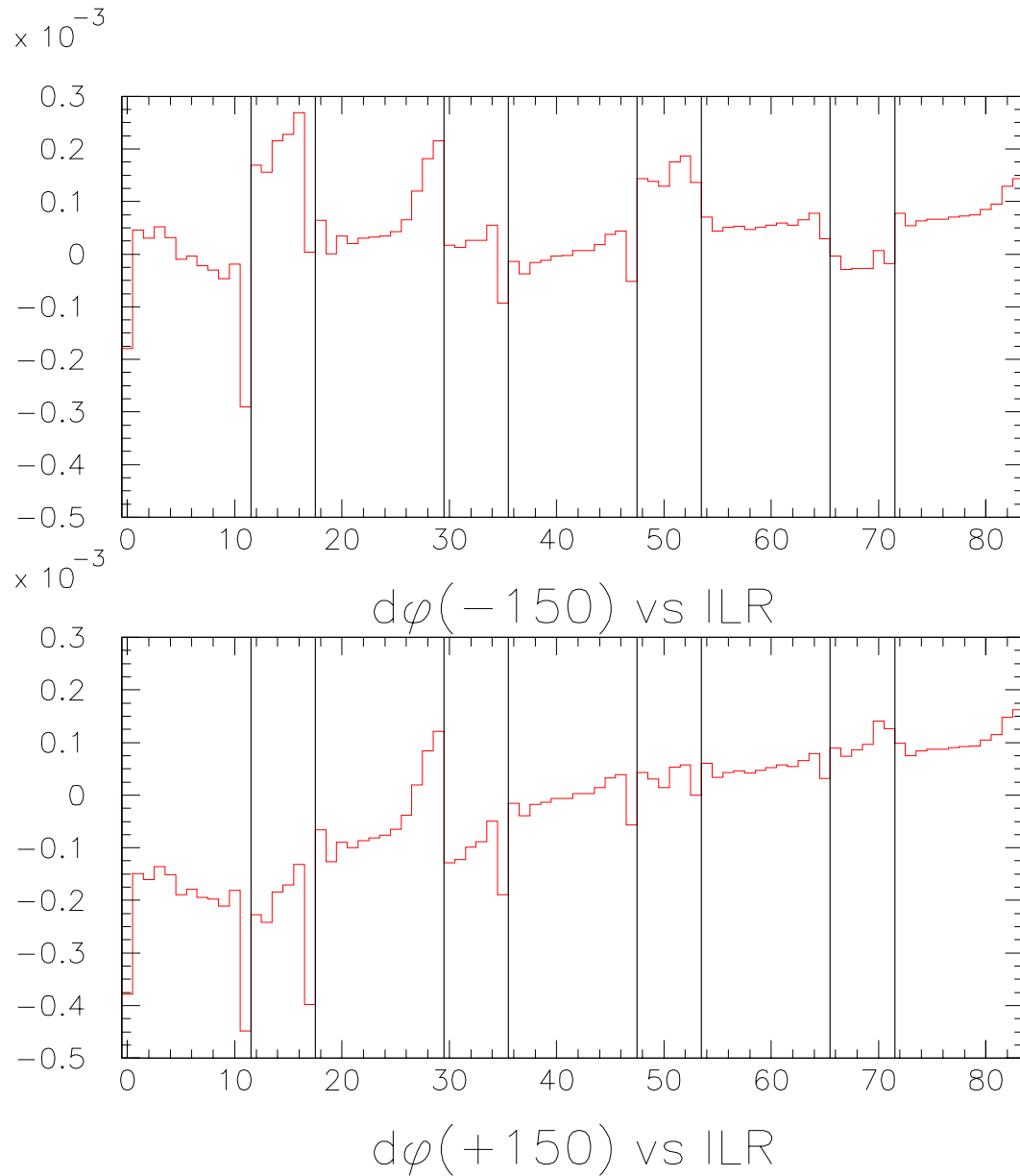
Figure D.2: Run Ia φ offset (radians) vs. CTC layer number. The upper figure shows the west endplate; the lower figure shows the east endplate. The $d\varphi$ values are calculated from the WPO constants for run 44600.

outer layers of some superlayers and the outer few layers of SL2 have displacements that vary too quickly to be physical features of the endplates. We believe that these features are caused by the small correlation between "alignment" and "calibration" in the CTC. Systematic effects in φ that are symmetric in drift sign (symmetric in $\varphi_{\text{track}} - \varphi_{\text{wire}}$) are typically labeled "alignment," while effects antisymmetric in drift sign are typically labeled "calibration." Because the CTC cells are not perfectly symmetric in drift sign, some drift model effects can be absorbed by the alignment constants. This crosstalk is most apparent for the inner and outer layers of a superlayer because the cells' asymmetry is largest at the radial boundaries and because these layers do not contribute to the drift model calibration.

A false curvature is evident in the east endplate's alignment in Figure D.2 (a difference of about 0.3 mrad from inside to outside); a much smaller effect (about 0.1 mrad) can be seen in the west endplate. Note that 0.2 mrad corresponds to a false curvature of $2 \times 10^{-6} \text{cm}^{-1}$, or a shift in $\frac{1}{qp_T}$ of about 1 TeV^{-1}.

False curvatures can be measured in the data by comparing $\frac{E_{\text{CEM}}}{p_{\text{CTC}}}$ distributions for positrons and electrons. After the Run Ia WPO alignment, there was no overall false curvature, but ϕ_0-dependent and z-dependent false curvatures were observed and removed with *ad hoc* corrections [2]. Both of these effects are surprising: The ϕ_0-dependent part should have been found in the BPO beam position calibration, and the z-dependent part should have been taken out in the WPO alignment.

Another strange result found in the Run Ia W mass analysis was that λ was apparently being measured 0.1% high [2]. If we take the nominal CTC stereo angles to be correct, then the alignment constants provide a straightforward explanation of this effect. Figure D.3 shows $r_i \frac{d\varphi_i}{dz}$, the effect of which is to scale the nominal stereo angle by $(-0.15\%, +0.07\%, -0.09\%, -0.11\%)$ in superlayers $(1, 3, 5, 7)$. Using these values and assuming equal hit usage on every stereo superlayer, λ would increase 0.10% if the CTC also fit z_0 and would increase 0.07% if z_0 were constrained from VTVZ data. We made a more careful check of the effect of the WPO constants on λ by refitting Run Ib electrons with a zeroed WPO file (as a baseline), and comparing the results to tracks refit using the Run Ia WPO; we found that the Run Ia WPO increased λ by 0.12% with no vertex constraint or 0.08% with a vertex constraint. We also tried a WPO file that was zeroed except to scale all stereo angles down by 0.1%; we found, as expected, that λ increased by 0.1% with or without a vertex constraint.

The nominal stereo angles (computed in CTCINI from constants in CTCGEO) do not reflect our best estimate of the chamber geometry, however, because they do not account for the endplate deflection reported in Ref. [3]. The nominal stereo angle $\left(r_i \frac{d\varphi_i}{dz} \right)$ for stereo layer i is $\pm \frac{2\pi r_i}{Z_{\text{max}} N_i}$, where the number of cells N_i is $(42, 60, 84, 108)$ for SL $(1, 3, 5, 7)$ and $2Z_{\text{max}} = 321.40$ cm is [3] "the free, unsupported length of the wires, without correcting for the deflection of the endplates." An FEA calculation[1] predicts that each endplate deflects inward by 0.112 cm $\cdot \left(\frac{r - 82.85 \text{ cm}}{55.15 \text{ cm}} \right)^2$. Also, the

---

[1] This calculation is suspected to be low by a factor of 1.7, however. See COT meeting minutes.
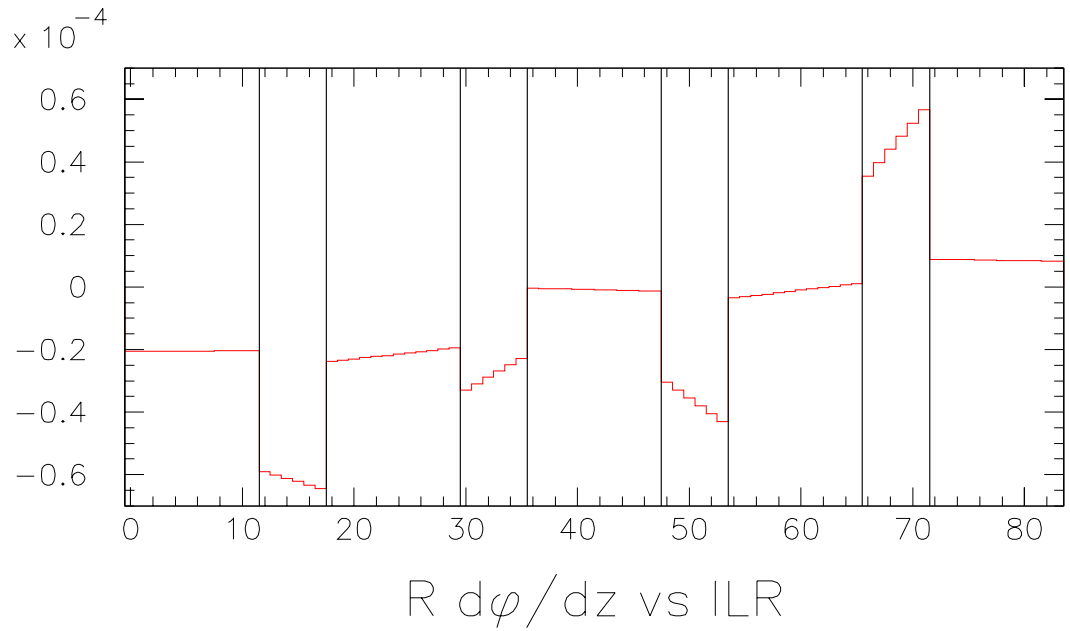
Figure D.3: From the Run Ia `WPO` alignment, we show $r_i \frac{d\varphi_i}{dz}$ ($= r_i B_i$) for each layer i. For stereo layers, these alignment offsets scale the effective stereo angle by a factor $\frac{r_i}{s_i} \frac{d\varphi_i}{dz}$. The shift of 0.5×10^{-4} in SL7 decreases SL7's effective stereo angle from its nominal value by 0.1%, which increases the effective length scale by 0.1%.

compressions of the inner and outer cylinders were reported to be 0.10 cm and 0.0075 cm respectively.[2] Using the values in Ref. [3] directly, we calculate $Z_{\max}(r)$ is

$$160.561 \text{ cm} + 0.023 \text{ cm} \cdot \left(\frac{r - 82.85 \text{ cm}}{55.15 \text{ cm}} \right) + 0.112 \text{ cm} \cdot \left(\frac{r - 82.85 \text{ cm}}{55.15 \text{ cm}} \right)^2 ,$$

to be compared with the nominal value 160.70 cm. At radii $(46.4, 69.9, 93.2, 116.5)$ cm, we calculate $Z_{\max}$ to be $(160.59, 160.56, 160.57, 160.62)$ cm, which means that we should increase the stereo angles by $(0.07\%, 0.09\%, 0.08\%, 0.05\%)$ from their nominal values. We find that refitting the Run Ib W electrons with a `WPO` file that is zeroed except to increase the stereo angles to the calculated values reduces `VTVZ`-constrained (unconstrained) λ by 0.06% (0.06%) with respect to a completely empty `WPO` file, or by 0.14% (0.18%) with respect to the Run Ia `WPO` file. As it turns out, a -0.14% λ scale factor is just the correction required by the Run Ib W mass analysis (see below).

The Run Ib W mass analysis has found an overall false curvature, a ϕ_0-dependent false curvature, a z-dependent false curvature, and a λ scale factor [4, 5]. The corrections used by the W mass group are the following:

$$\frac{1 \text{ GeV}}{q p_T} \to \frac{1 \text{ GeV}}{q p_T} - 0.000056 - 0.00040 \sin(\phi_0 - 3.0) - 0.00028 (\lambda + \frac{z_0}{81 \text{ cm}})$$

$$\lambda \to 0.9986 \lambda$$

It should be possible to remove all of these except the ϕ-dependent term with the `WPO` corrections. It should also be possible to understand the ϕ-dependent term by looking for other symptoms of a beam position problem. The goal of the alignment procedure is to eliminate the need for *ad hoc* track corrections, by including alignment corrections self-consistently into the track fits.

D.2   Alignment procedure

The CTC measures five helix parameters, $c, \phi_0, \delta, \lambda, z_0$. Since azimuthal wire misalignments can bias the helix parameters from their true values, the residuals of a helix fit with its parameters constrained to their true values can be used to extract azimuthal wire misalignments. The ideal values of the track parameters are of course not available, but we can constrain several of the parameters using information from external devices whose systematic errors are expected to be complementary to those of the CTC. For instance, a CEM scale error and a CTC false curvature are distinguishable for an equal number of e^+ and e^-. (This point is elaborated in Ref. [1].)

---

[2] We believe that Ref. [3] took the inner cylinder compression from a measurement and the outer can compression from a calculation.

Cut	# pass	% fail
Initial $W \to e\nu$ selection	48772	—
CTC hit data available on disk	48044	1.5
Passes VTX road search	46236	3.8
`TRKSVC` succeeds for refit track	45846	0.8
$0.8 < \frac{E}{p} < 1.2$	40000	12.8
c constraint $\chi^2 < 100$	39780	0.6

Table D.1: Events passing successive selection cuts.

For any primary track, we can constrain z_0 to a `VTVZ` vertex (measured by the VTX) and δ to the beamline (measured by the CTC or the SVX). The $\frac{E}{p}$ distribution for electrons is sharply peaked and should be independent of charge. Thus, for particles known to be electrons, we can constrain $\frac{\sqrt{1+\lambda^2}}{|c|}$ to be proportional to E measured by the CEM. Imposing these constraints leaves only ϕ_0 and λ to be fit by the CTC.

In principle, we could also constrain ϕ_0 using SVX hits, leaving the CTC to fit only λ. In practice, this would significantly reduce our acceptance, would make the CTC alignment dependent upon the SVX wedge-to-wedge alignment, and would only provide additional information if the alignment were fitting ϕ-dependent φ offsets, as in a cell-by-cell alignment of the CTC. Not using the SVX has the further advantage that the alignment averages over the same acceptance as the W mass measurement.

We use the W electrons as a large, clean sample of primary electrons. We begin with the 48772 events passing all cuts in Table 1 of Ref. [6]. Of these events, 48044 are available in the W mass MPAD sample on disk in Berkeley. We then perform a VTX road search, to reduce (non-primary) conversion backgrounds, so that the beam constraint makes sense; search the `CTCE` bank for hits lying in a road around the `QTRK` track trajectory; refit these hits to extract new track parameters and a new covariance matrix; impose the z_0 and δ constraints with `TRKSVC`; make an $\frac{E}{p}$ cut, so that the curvature constraint makes sense; and constrain c using the CEM energy. The cuts are summarized in Table D.1. 39780 electrons are used in the alignment.

We accumulate the residuals, Δ_i, for each refit, c, δ, z_0-constrained track, as a function of z, separately for e^+ and e^-.[3] For each layer i, we produce five sums over all positrons—$\sum 1$, $\sum \Delta$, $\sum z$, $\sum z\Delta$, $\sum z^2$—and five corresponding sums over all electrons. For each track, only layers used in the fit and having residuals less than 0.1 cm contribute to the sums. From these sums, we make 168 linear fits:

---

[3]Schematically, the residual Δ_i is $r_i(\varphi^{\text{track}}(r_i) - \varphi_i^{\text{hit}})$; in practice, the residual is calculated along a straight drift trajectory.

$\Delta_i^+/r_i = a_i^+ + b_i^+ z$; $\Delta_i^-/r_i = a_i^- + b_i^- z$.[4] We then average the $+$ and $-$ with equal weight: $a_i = \frac{1}{2}(a_i^+ + a_i^-)$; $b_i = \frac{1}{2}(b_i^+ + b_i^-)$. Equal weighting of $+$ and $-$ reduces the correlation between an energy scale bias and CTC misalignments [1].

We can then add the a_i and b_i values to the WPO constants A_i and B_i to produce improved constants. Before doing so, however, we need to remove unwanted degrees of freedom from a_i and b_i. For instance, $A_i \rightarrow A_i + \alpha$ would add a meaningless offset α to ϕ_0 of all CTC tracks. (The offset is meaningless because in practice the CTC defines $\phi = 0$ for CDF.) In the past, this degree of freedom was removed by freezing SL4 (the average of east and west) in the alignment. For Run Ib, we decided instead to freeze SL8.[5] To minimize changes to the CDF coordinate system, we forced $\sum_{\mathrm{SL8}} r_i A_i$ to agree with the Run Ia alignment instead of constraining it to zero.

A relative rotation of the two endplates, $B_i \rightarrow B_i + \beta$, is meaningful, and should appear as a λ-dependent false curvature. While this degree of freedom has not been constrained in the past and arguably does not need to be constrained, we decided in the Run Ib alignment to force $\sum_{\mathrm{SL8}} r_i B_i$ to zero. The justification for this choice is that a relative rotation of the two endplates is ruled out most reliably (from a survey during chamber construction) at the outer radius of the chamber [7].

We noted earlier that in a stereo layer i, B_i changes the effective stereo angle s_i by a factor $1 + \frac{r_i}{s_i} B_i$. In the past, the only constraint on the stereo angles in the alignment was that z_0 was fixed from VTVZ. This choice has two consequences worth noting. First, the CTC z scale is inherited from the VTX z scale. Second, changes in B_i that scale λ but leave the z axis unchanged (after averaging over λ), such as $B_i = \gamma s_i r_i$, are unconstrained. Another unwanted degree of freedom is $A_i = \kappa s_i r_i$, which adds a constant offset to λ but not to z_0.

In the Run Ib alignment, we have forced $\sum_{\mathrm{SL7}} r_i B_i$ and $\sum_{\mathrm{SL1}} r_i B_i$ to agree with the calculated endplate deflection, and have allowed superlayers 3 and 5 to float. Fixing SL7 alone would be sufficient to eliminate degree of freedom γ from the previous paragraph; fixing SL1 as well eliminates dependence on the VTX length scale. We will see below that using the calculated endplate deflection eliminates the need for a λ scale factor in the $J/\psi \rightarrow \mu\mu$ data. To remove degree of freedom κ noted in the previous paragraph, we freeze $\sum_{\mathrm{SL7}} r_i A_i$ to its Run Ia value.

Since the VTX length scale can, depending on one's choice of constraints, contribute to the CTC stereo alignment, it is important to know that the VTX itself is properly aligned. In particular, the east and west halves of the VTX are installed separately, so the $z \approx 0$ boundary is the most likely point at which a discrepancy may arise between clean-room survey data and beam data. The upper plot in Figure D.4 shows $\langle z_{\mathrm{CTC}} - z_{\mathrm{VTVZ}} \rangle$ as a function of z_{VTVZ} for W electrons, using the

---

[4] The fits are actually done to Δ, not to Δ/r. We put in the factor $1/r$ because it is convenient to describe misalignments in terms of φ offsets.

[5] The choice is somewhat arbitrary. Compelling arguments can be made for freezing SL8, SL4, or SL0. We chose SL8.

Run Ia CTC alignment. There is clear evidence of a misalignment at $z \approx 0$. While the correct way to fix this problem (which we will do if time allows) is to update the VTX `WPO` database and rerun `V2VERT`, in the interest of expediency, we have made the following *ad hoc* correction in `TRKSVC`:

```
vrtxyz(3) = vrtxyz(3)+0.0370
vrtxyz(3) = vrtxyz(3)+sign(0.0840,vrtxyz(3))
```

The middle plot in Figure D.4 shows that $\langle z_{\mathrm{CTC}} - z_{\mathrm{VTVZ}} \rangle$ vs. z looks more continuous across $z = 0$ after this kludge has been applied, though perhaps the constants could be fine-tuned a bit more. The lower plot makes the same comparison using the new CTC alignment. It is interesting to note that the VTX z_0 scale seems to be $0.18 \pm 0.02\%$ longer than the CTC z_0 scale that emerges from the alignment. At the moment, we have no explanation for this effect.

In our first pass through the alignment, we began with a zeroed `WPO` file. We iterated the alignment procedure, using the residuals to update the `WPO` constants each time, until the constants converged to stable values. Figure D.5 shows that the constants settle down to stable values after several iterations.

D.3   Results

Figure D.6 (top) shows residuals Δ_i for each layer i for the muon tracks in $J/\psi \to \mu\mu$ events, using the new Run Ib alignment derived from $W \to e\nu$ events. The mean residual is within a few microns of zero in most layers, and within ten microns of zero in all layers. The lower figure shows these residuals signed by drift direction, $\mathrm{sign}(\phi_{\mathrm{hit}} - \phi_{\mathrm{wire}})$; residuals signed in this manner are sensitive to the drift velocity calibration. The inner layers show symptoms of a calibration problem.

While we were working on this alignment, Alan Sill derived an improved set of CTC calibration constants (`PRO` and `TMS` databases) for Run Ib data [8]. Once the new calibration constants were available, we repeated the alignment procedure. Figure D.7 shows the same residuals as Figure D.6, using the new calibration. Alan's new constants clearly improve the drift-sign-weighted residuals in the inner superlayers.

An unphysical feature of the initial alignment results, illustrated in Figure D.8 (top), was that the alignment in SL0 had changed considerably between Run Ia and Run Ib. Apparently, some of the calibration problems were being absorbed by the alignment constants. As Figure D.8 (bottom) shows, this feature is no longer present in the alignment once the new calibration constants are used. This is an example of the small cross-talk between alignment and calibration in the CTC that we mentioned in Section D.1.
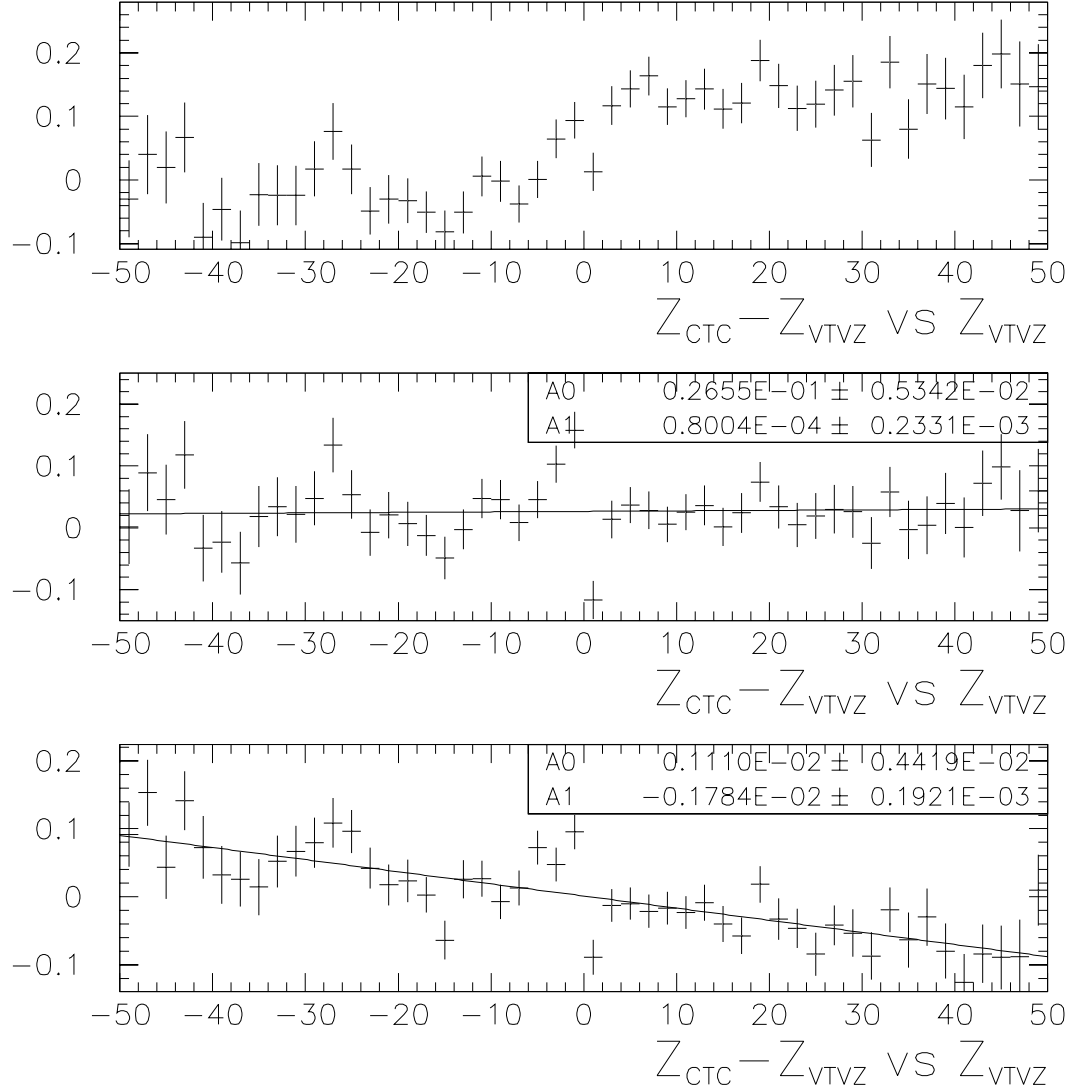
Figure D.4: (Top) $\langle z_{\mathrm{CTC}} - z_{\mathrm{VTVZ}} \rangle$ vs. z_{VTVZ}, using Run Ia CTC `WP0`. (Center) After tweaking `VTVZ` to remove discontinuity. (Bottom) Using new CTC `WP0` constants. Only tracks with $|z_{\mathrm{CTC}} - z_{\mathrm{VTVZ}}| < 5$ cm are included in the average.
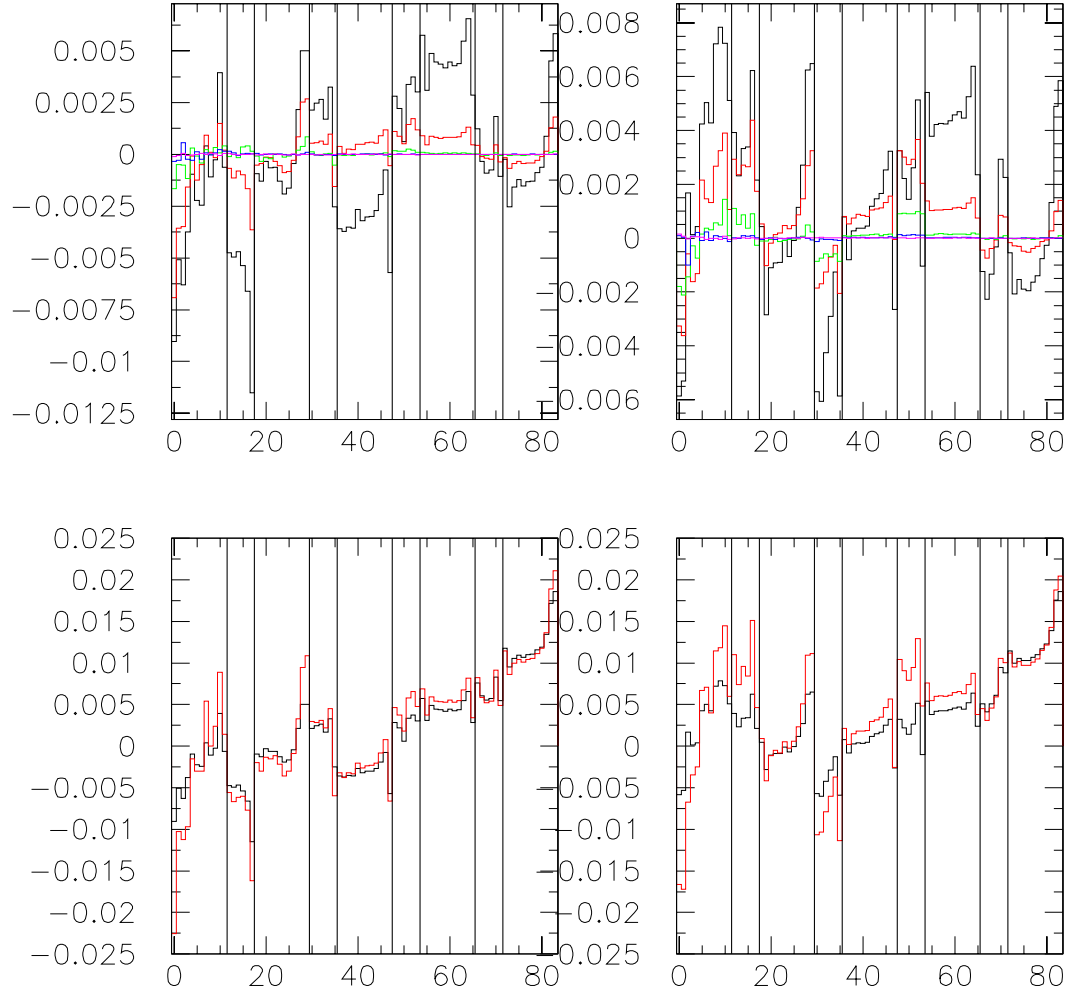
Figure D.5: (Upper left) One iteration's differential change $r_i \Delta \varphi_i$ in alignment for west endplate, in cm, by layer i, after 1, 2, 4, 8, and 16 iterations. (Upper right) Same for east endplate. (Lower left) Net alignment of west endplate, $r_i(A_i - 150 \text{ cm} \cdot B_i)$, in cm, after one iteration and after 20 iterations. (Lower right) East endplate, $r_i(A_i + 150 \text{ cm} \cdot B_i)$.
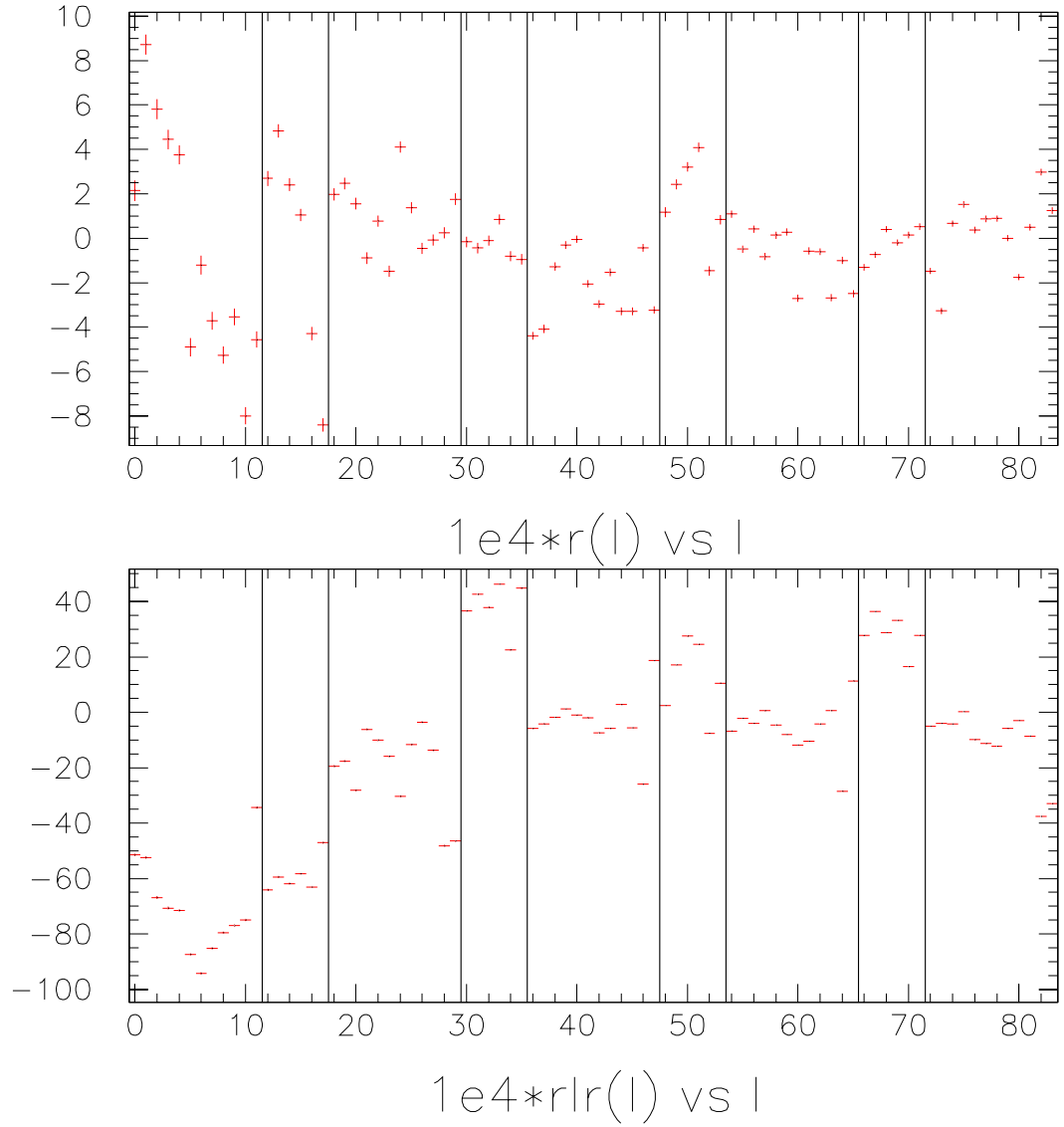
Figure D.6: (Top) Mean residual Δ_i (μm) by layer i, in $\psi \to \mu\mu$ sample, using new alignment (`WPO`) but original drift-velocity (`PRO` and `TMS`) calibration. (Bottom) $\psi \to \mu\mu$ residuals weighted by drift sign. The alignment looks fine, but there is clearly a calibration problem in the inner superlayers and perhaps in the outer stereo superlayers.
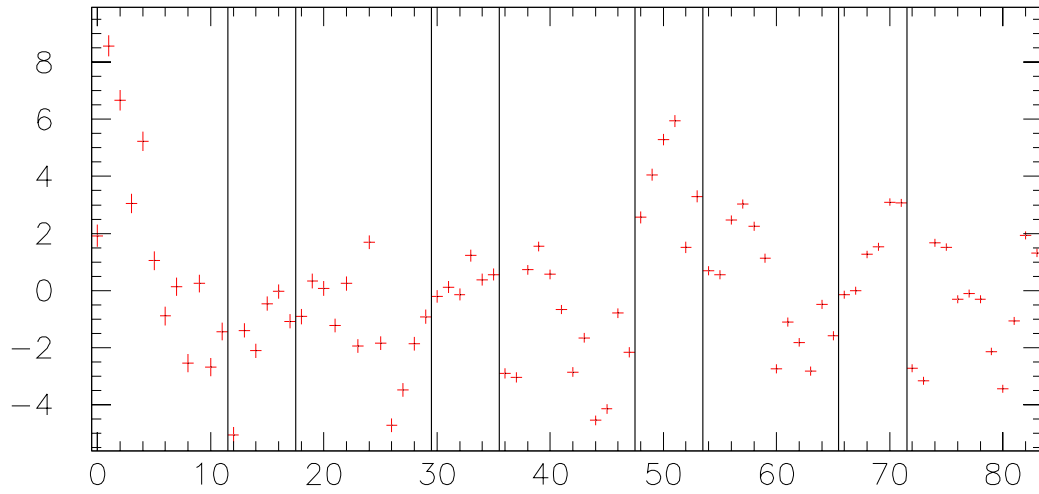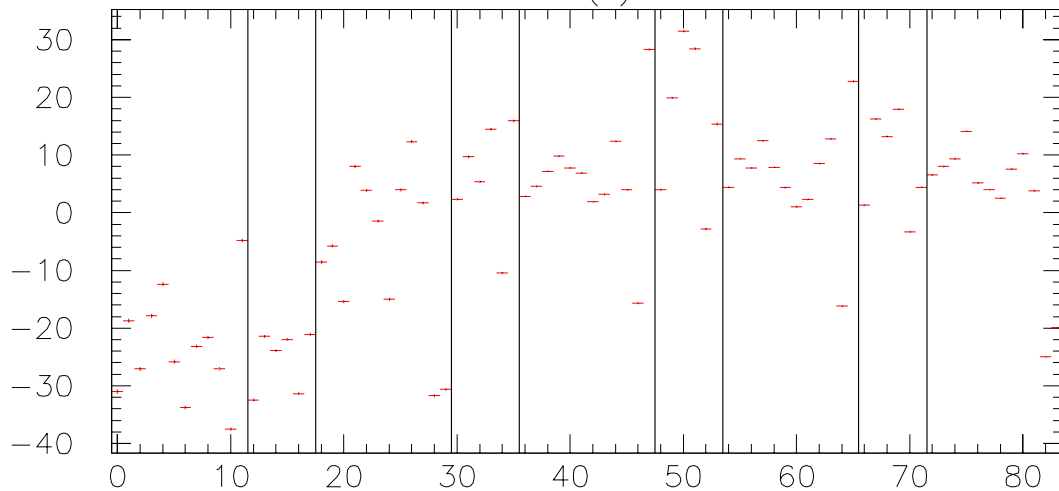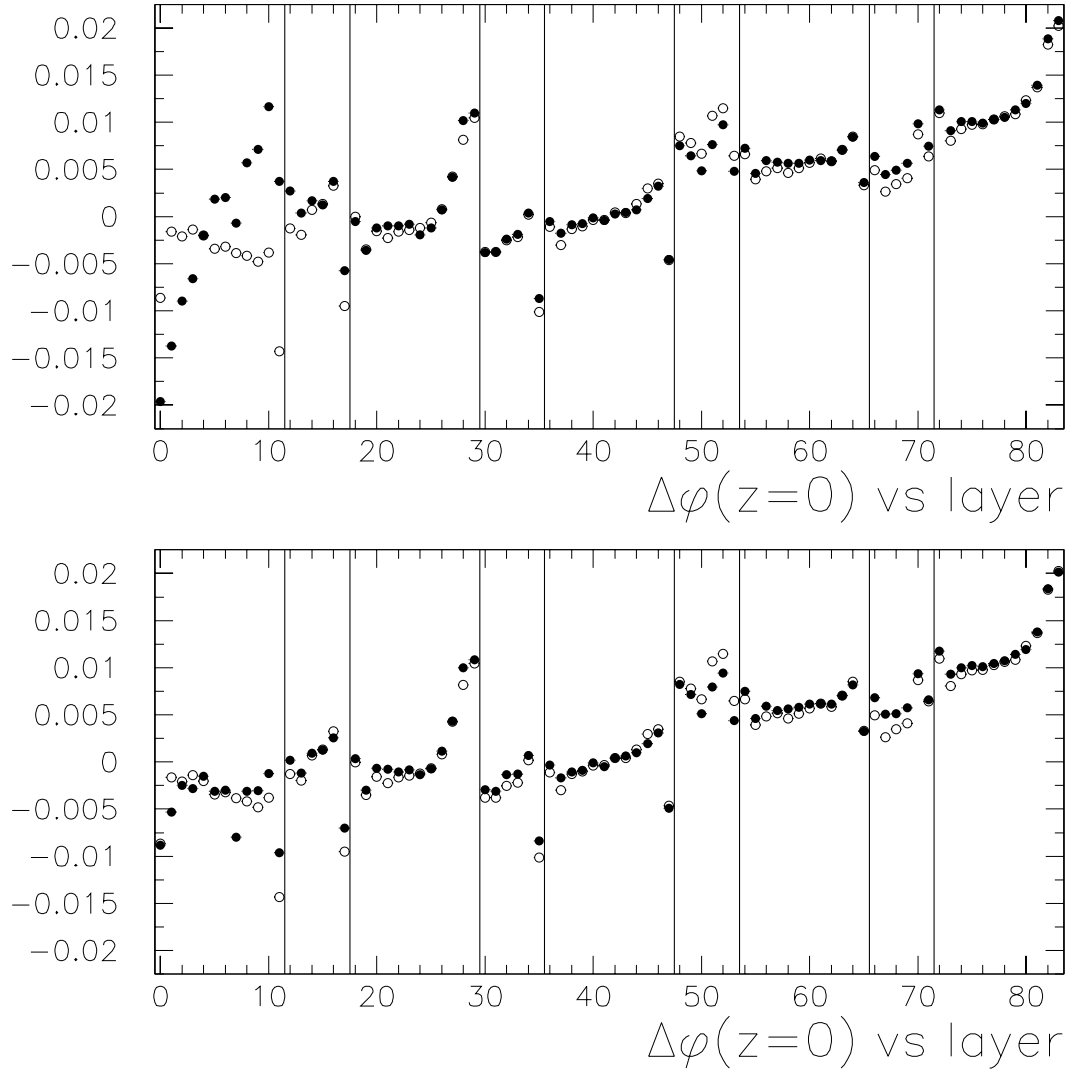
Figure D.7: (Top) Mean residual Δ_i (μm) by layer i, in $\psi \to \mu\mu$ sample, using Alan's new `PRO` and `TMS` calibrations and the corresponding new `WPO`. (Bottom) $\psi \to \mu\mu$ residuals weighted by drift sign. The calibration problem in the inner superlayers is substantially better than in Figure D.6.

Figure D.8: (Top) $\Delta\varphi$ (averaging east and west) for Run Ia alignment (open circles) and Run Ib alignment (solid points), using original Run Ib CTC calibration. (Bottom) Run Ia alignment (open circles) compared with a Run Ib alignment that uses Alan Sill's new Run Ib CTC calibration (solid points). When the new calibration is used, the alignment constants for SL0 move back toward their Run Ia values.
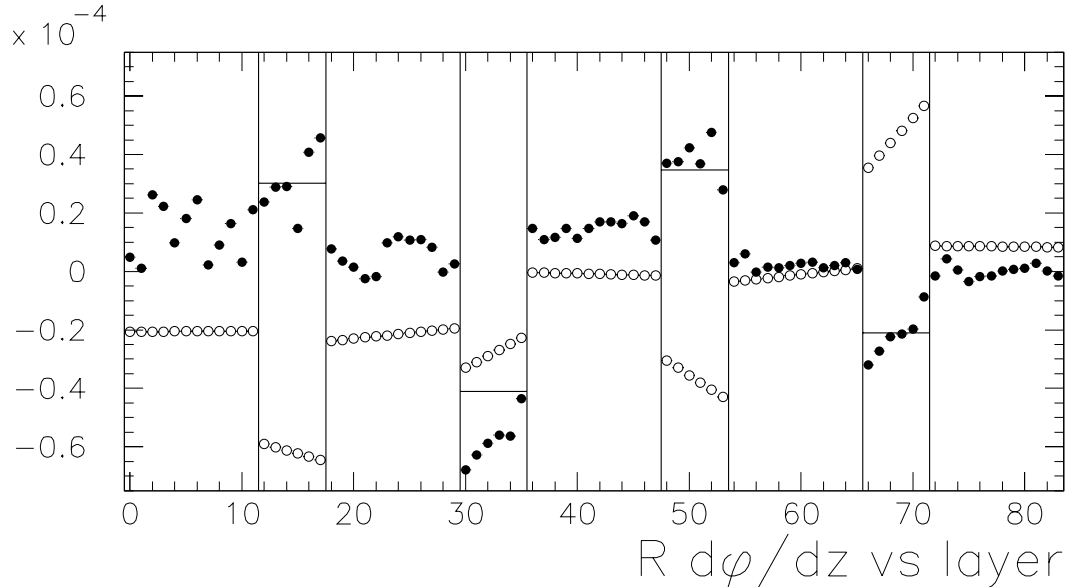
Figure D.9: For Ib alignment (solid points) and Ia alignment (open circles), we show $r_i \frac{d\varphi_i}{dz} (= r_i B_i)$ for each layer i. The horizontal line segments show the values implied by the calculated endplate deflection in the stereo layers. The Ib alignment constrained SL1 and SL7 to agree with the calculation, and constrained SL8 to zero.

Figure D.9 shows $r_i \frac{d\varphi_i}{dz}$ for each layer i for the Run Ia and Run Ib alignment constants. The results are rather different, largely because in Run Ib we have forced the stereo angles in SL1 and SL7 to agree with the calculated endplate deflection.

Using $W \to e\nu$ events, Figure D.10 shows the residuals Δ_i by layer i using the Run Ia alignment and the old calibration; using no alignment and the old calibration; and using the new alignment and new calibration. After the alignment, the mean residual is consistent with zero in each layer.

The goal of this alignment was to eliminate *ad hoc* corrections to CTC track parameters. Table D.2 shows false curvatures in the data using the old and the new alignments. We expected to be able to remove all but the ϕ_0-dependent one, and we did so. This is an improvement over Run Ia, in which the z-dependent false curvature remained. We do not yet understand why this effect was removed in Run Ib and not in Run Ia.

Another improvement made by the Run Ib alignment is that we have eliminated the need for a λ scale factor, by incorporating the calculated endplate deflection in the stereo alignment. Figure D.11 shows ψ mass vs. $\Delta\lambda$, for Run Ia and Run Ib alignment constants. In the W mass analysis, a scale factor on λ is varied until this profile agrees with a Monte Carlo prediction, which is approximately flat. Using the old alignment, a λ scale factor of 0.9986 is needed; using the new alignment,

160
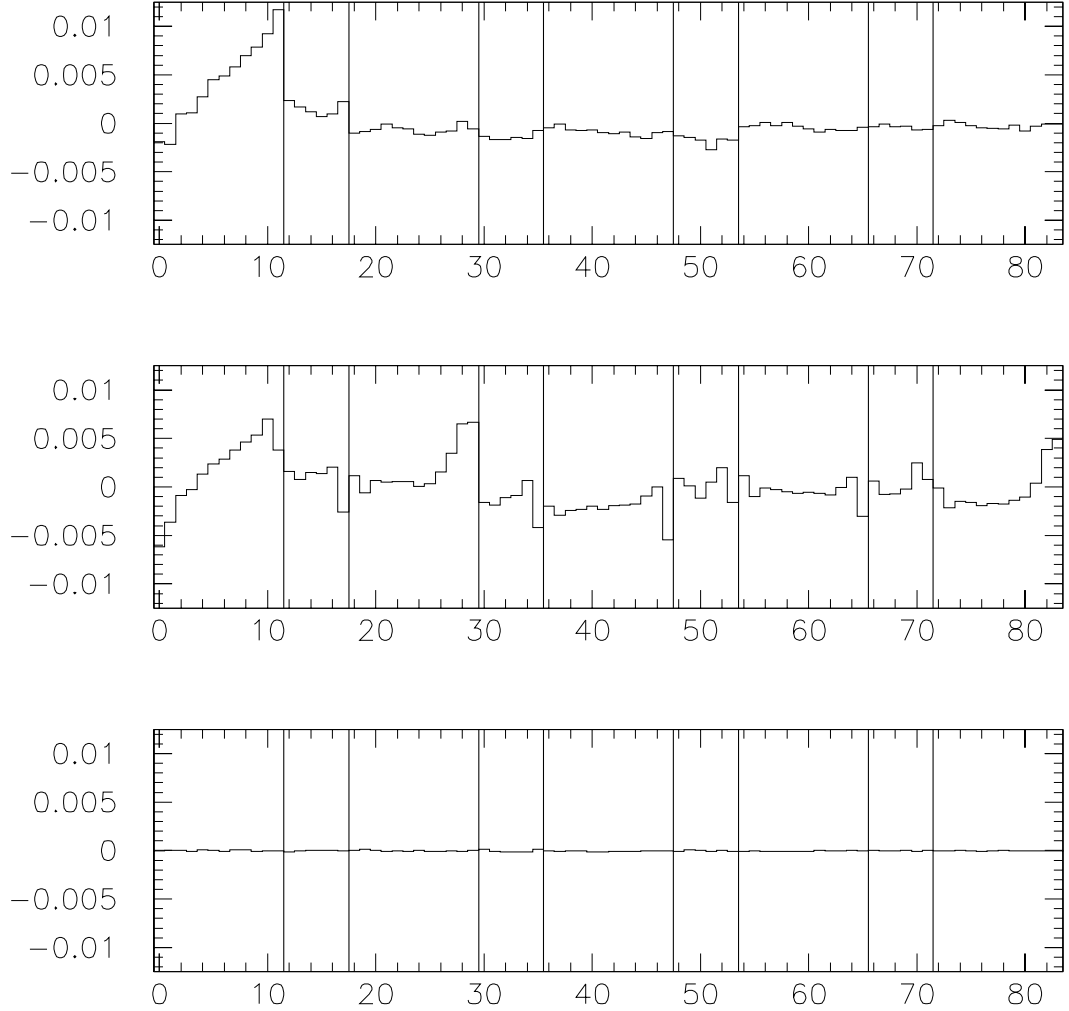
Figure D.10: (Top) Mean residual Δ_i (cm) by layer i, in $W \rightarrow e\nu$ sample, using Run Ia `WPO` and original `PRO` and `TMS` calibrations. (Center) Using zeroed `WPO` and original calibrations. (Bottom) Using new `WPO` and Alan's new calibrations.

| False $\frac{1}{qp_T}$	LJN	us, old `WPO`	us, new `WPO`
overall	$.000056 \pm .000008$	$.000044 \pm .000009$	$.000002 \pm .000006$
λ	$.00028 \pm .00002$	$.00024 \pm .00001$	$-.00001 \pm .00001$
$z_0/187/.00028$	2.3 ± 0.3	2.6 ± 0.2	0.2 ± 0.2
$\sin(\phi_0 - 3.0)$	$.00040 \pm .00002$	$.00033 \pm .00001$	$.00032 \pm .00001$

Table D.2: False curvatures (LJN cm = GeV = 1 unit convention) in Ib W electrons, using Ia `WPO` and using Ib `WPO`. We also list the values extracted by LJN, to show that there is a strong correlation between what we're measuring and what he's measuring.
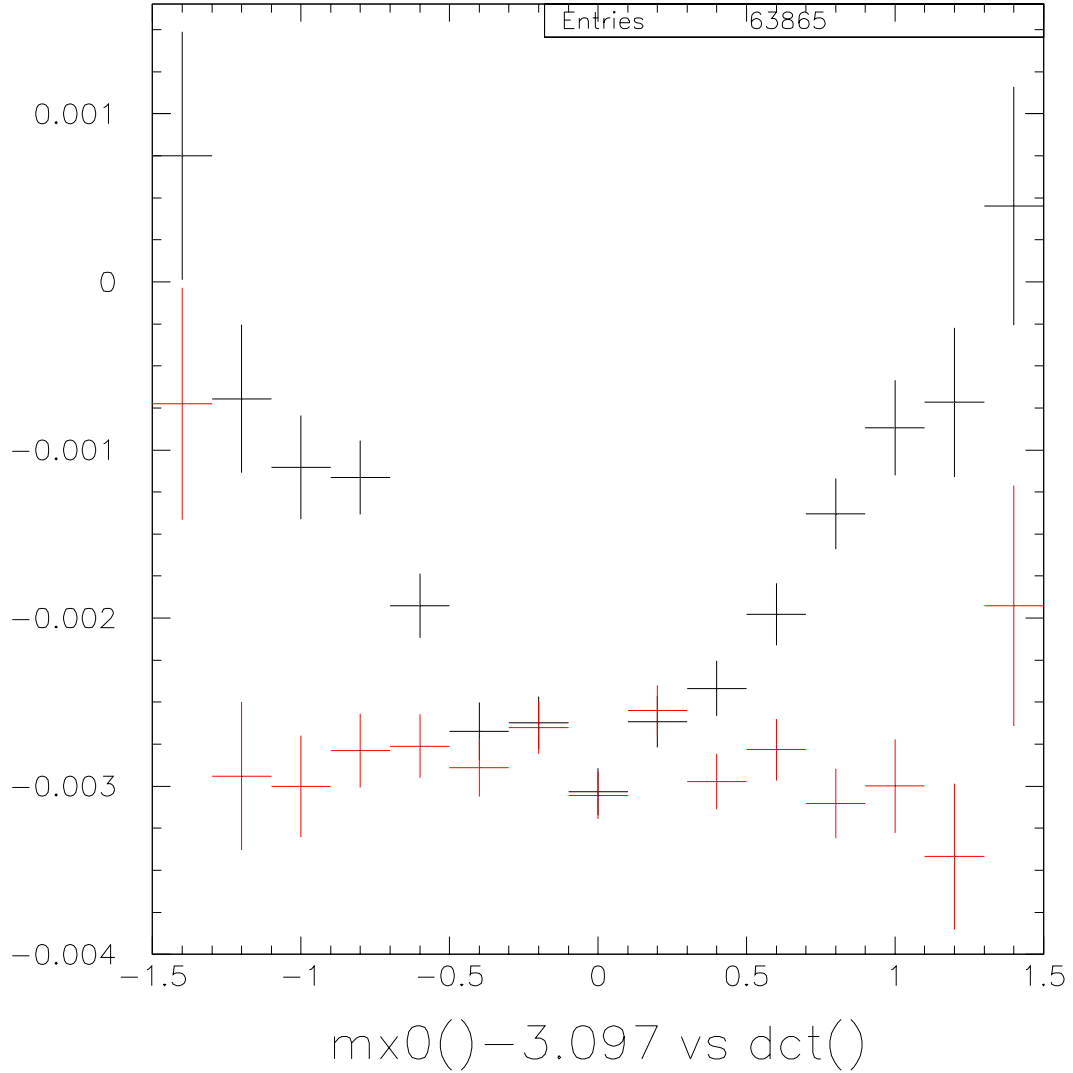
Figure D.11: ψ mass vs. $\Delta\lambda$, using Ia alignment (black) and using Ib alignment in which both SL1 and SL7 stereo angles are constrained to calculated endplate deflection (red). This re-alignment also used Alan Sill's new CTC calibration constants. The latter is nearly flat, indicating that the required λ scale factor appears to be very close to unity after including the calculated endplate deflection in the alignment.

the required scale factor is consistent with unity.

Figure D.12 illustrates one improvement made by the alignment and another improvement made by the calibration. Before aligning, there is not only a bias in the CTC curvature measurement but also in the impact parameter measurement. A false impact parameter causes primary tracks to appear to converge to a circle in the x-y plane instead of a point. The alignment removes this bias. The figure also
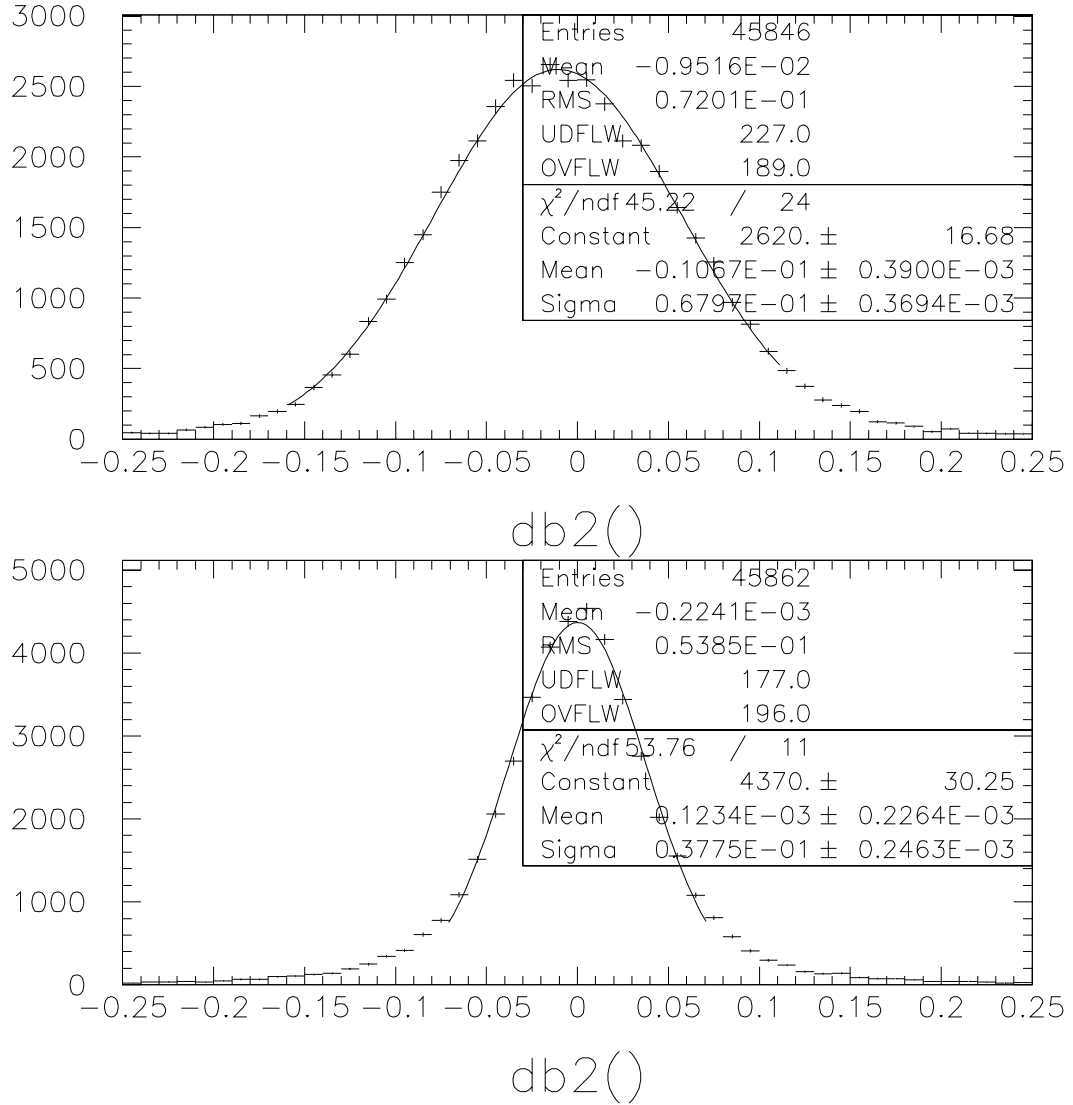
Figure D.12: CTC impact parameter with respect to SVX beamline. (Top) Before aligning or re-calibrating. There is a false impact parameter of about 100 μm (i.e. tracks converge to a circle instead of to a point), and the resolution is about 680 μm. (Bottom) After aligning and re-calibrating. The false impact parameter is reduced to ~ 2 μm (consistent with zero) by the alignment, and the resolution is improved to 380 μm (a 45% improvement) by the calibration.

shows that the CTC impact parameter resolution is improved by nearly a factor of two by Alan's recalibration.

163

D.4 SVX/CTC global alignment

A problem that remains (indeed that the present `WPO` alignment is not intended to address) is the apparent false curvature that is proportional to $\sin(\phi_0 - 3.0)$. This false curvature corresponds, approximately, to taking a track originating at (x, y) and constraining it to come from the point $(x + 63\ \mu\text{m}, y - 9\ \mu\text{m})$. Such a problem could occur if the SVX beamline were offset $(+63\ \mu\text{m}, -9\ \mu\text{m})$ in (x, y) with respect to the CTC origin. The putative beam-position offset is large enough that one should be able to find other evidence for it; so far we have found very little.

Figure D.13 shows the false curvature, inferred by comparing p_T and E_T measurements, as a function of ϕ, before and after beam-constraining the electron track. The false curvature appears only to be present after the beam constraint, as one would expect if the problem were the result of a beam-position problem. Figure D.14 compares the beam position used in the CTC beam constraint with the beam position obtained by explicitly loading the SVX `BPO` database; there is some scatter, but the bias is only 1-2 μm. Figure D.15 looks at CTC and SVX impact parameters, for J/ψ muons, with respect to the SVX beamline; there is not much evidence for a sinusoidal offset.

Figure D.16 compares the CTC-derived entry in the CTC `BPO` database with the SVX-derived entry, run by run. There is a $+21\ \mu$m offset in x, a $-24\ \mu$m offset in y, and a lot of scatter ($\approx 40\ \mu$m rms) in both directions. This is a fairly large offset, but it differs by a factor of two in magnitude and 40° in direction from the effect we're looking for.
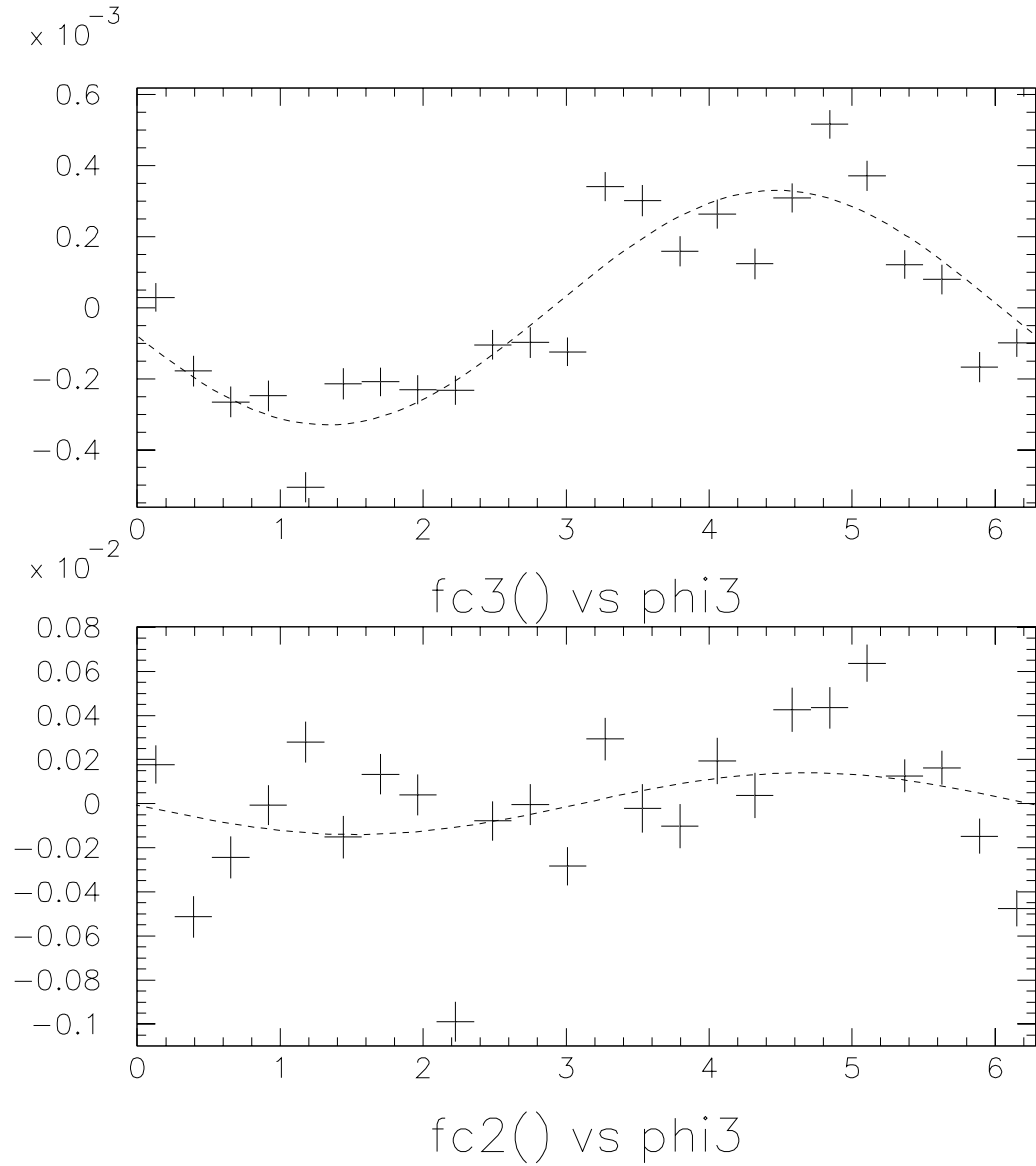
**Figure D.13:** $\left\langle q(\frac{1}{p_T} - \frac{1}{E_T}) \right\rangle$ vs. ϕ. Upper plot is after beam constraint; lower plot is before beam constraint. The curve is $A\sin(\phi_0 - 3.0)$, with A determined by linear regression.

165
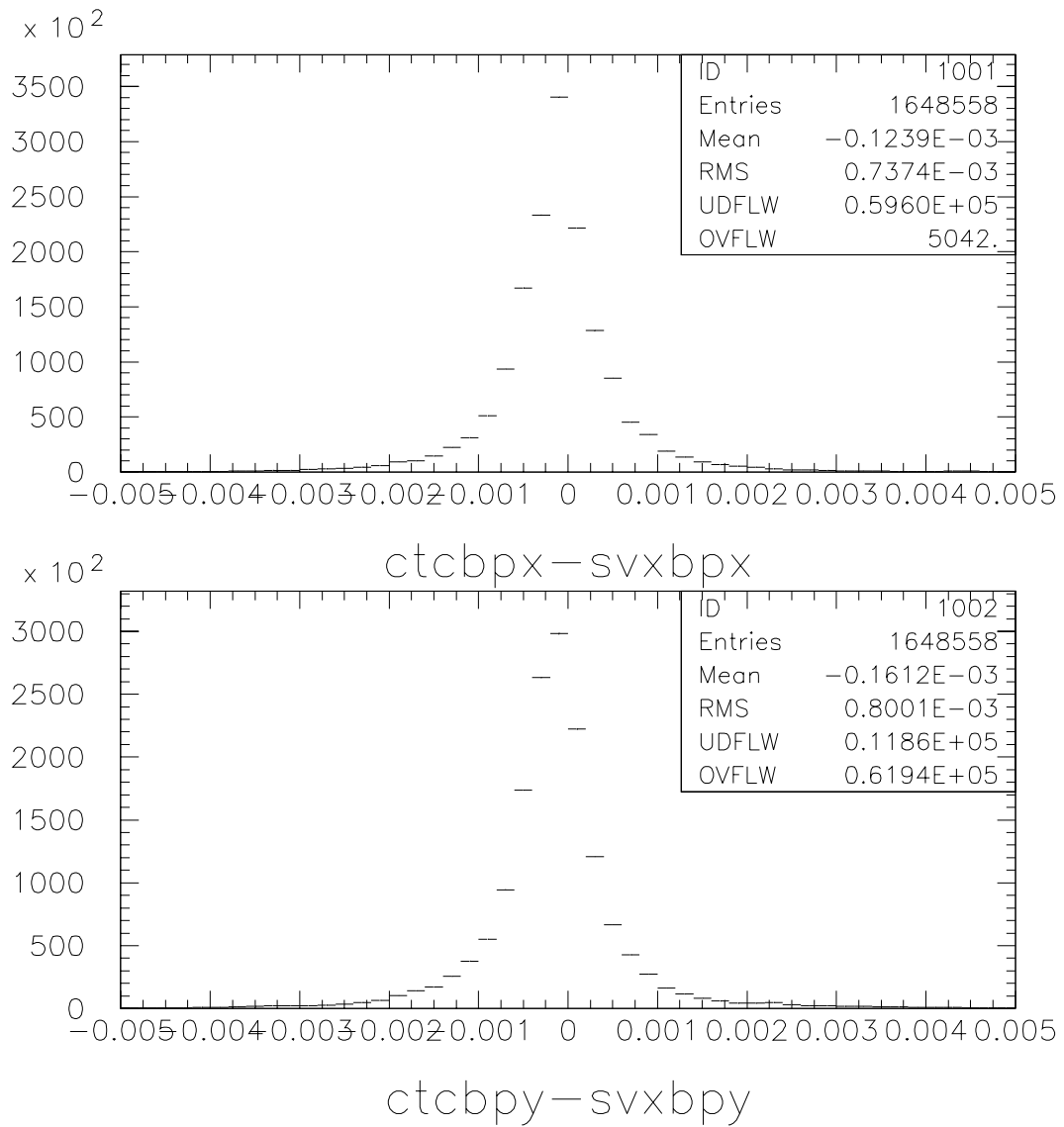
Figure D.14: Difference between output of `SVGEBP` and contents of `XBEAM,YBEAM` in `CTCALB` common block. This shows that the beam position used by `TRKSVC` is on average within 2 μm of the SVX beam position. (A separate question is whether the beam positions fitted by CTC and SVX agree.)
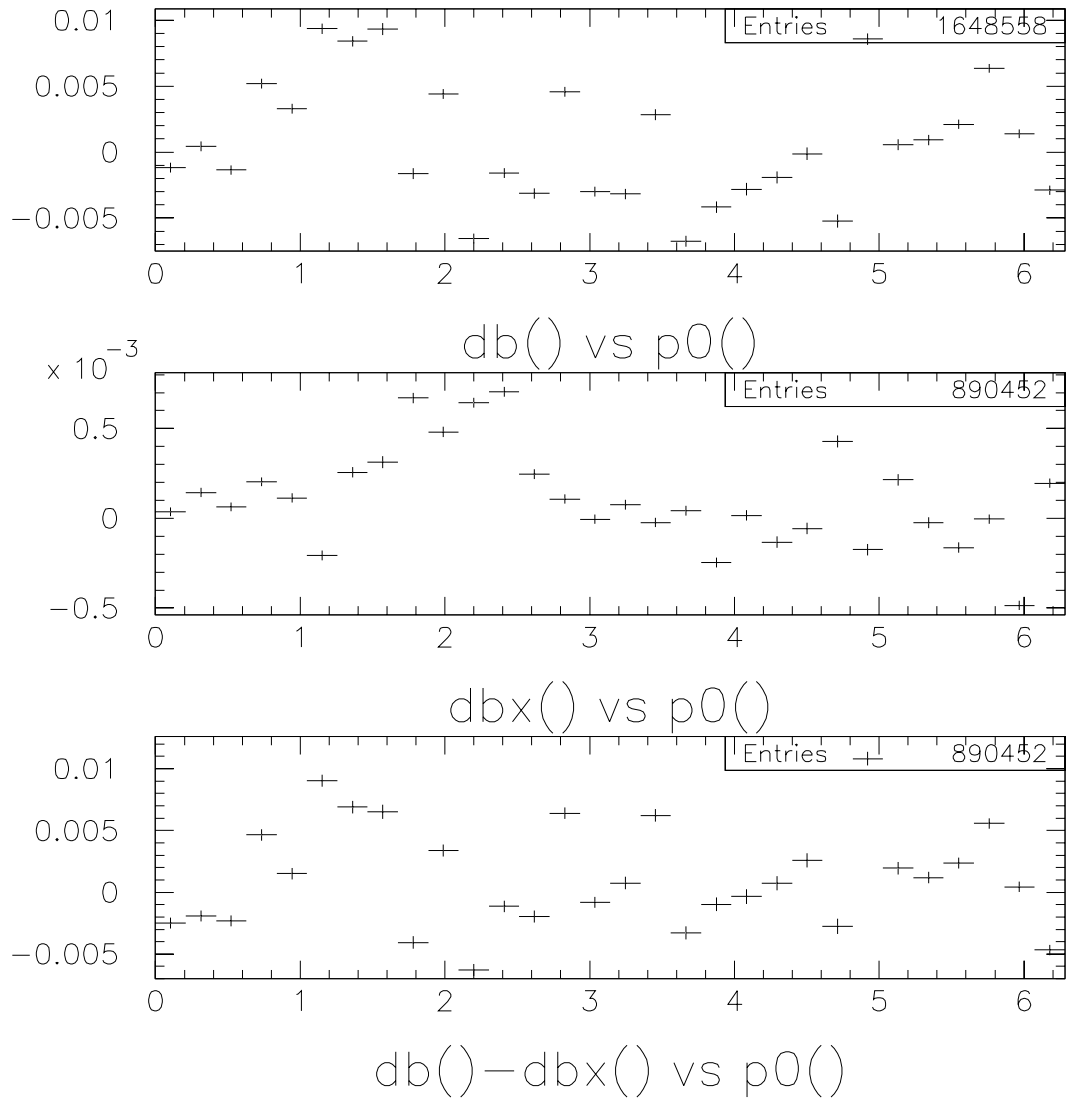
Figure D.15: (Top) Mean CTC impact parameter (cm) with respect to SVX beamline vs. ϕ, from J/ψ data. (Center) Mean SVX impact parameter with respect to SVX beamline vs. ϕ. (Bottom) Difference between CTC and SVX impact parameters vs. ϕ. There is no obvious global SVX/CTC misalignment (which would appear as a sinusoidal offset of magnitude $\approx 60~\mu$m), but CTC SL0 cell scatter makes it hard to say for sure.

167
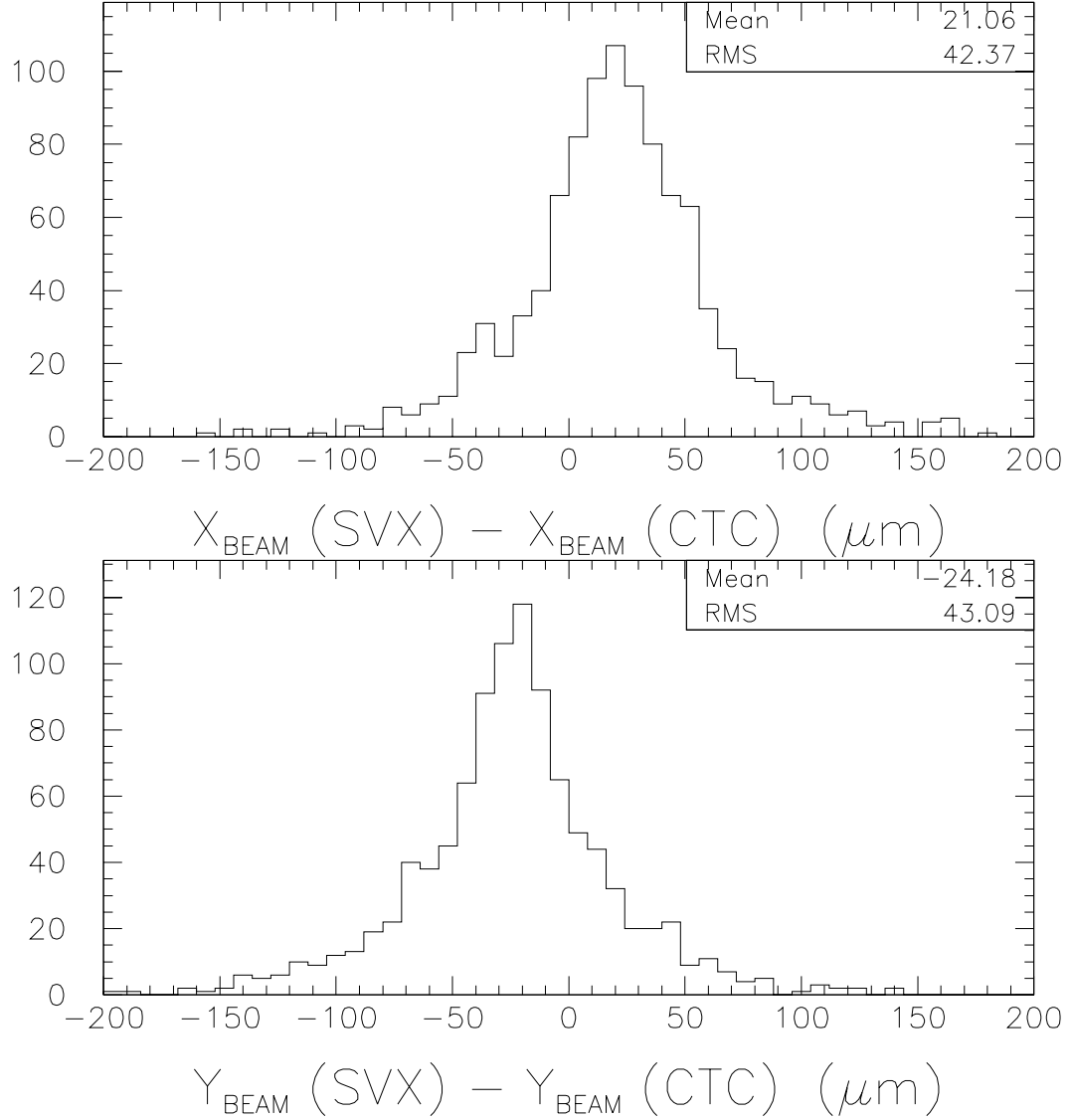
Figure D.16: Difference between beam position fitted by SVX and beam position fitted by CTC, in x and y projections. There is one entry per Run Ib run. An offset of $(+21 \ \mu\text{m}, -24 \ \mu\text{m})$ would produce a false $\frac{1}{qp_T}$ of $+0.00017 \sin(\phi_0 - 2.3)$, while the effect we're trying to explain is $+0.00033 \sin(\phi_0 - 3.0)$ (or an offset of $(+63 \ \mu\text{m}, -9 \ \mu\text{m})$).

D.5　Bibliography

[1] A. Mukherjee, "CTC Calibration and Alignment," CDF Note 1002 (August, 1989).

[2] F. Abe *et al*, "Measurement of the W Boson Mass," *Phys. Rev.* **D52** 4784 (1995).

[3] F. Bedeschi *et al*, "Design and Construction of the CDF Central Tracking Chamber," *NIM* **A268** 50 (1988).

[4] L. Nodulman, "On False Curvatures in 1b," CDF Note 4056 (February, 1997).

[5] Y.K. Kim, "A Determination of the Momentum Scale for the Run Ib W Mass Measurement," CDF Note 3972 (February, 1997).

[6] W. Ashmanskas, "Direct Measurement of $,_W$ with Run Ib Electrons," CDF Note 4137 (August, 1997).

[7] R.W. Kadel, private communication.

[8] A. Sill, CDF note in preparation.